

APPLICATION OF A CRYSTAL SEPTUM TO REPLACE A MAGNET
IN A CHARGED PARTICLE BEAM
AND
STUDY OF DECHANNELING AND FEEDING-IN EFFECTS
IN A SINGLE SILICON CRYSTAL

by

Ranjith Laxman Wijayawardana

A Dissertation

Submitted to the State University of New York at Albany

in Partial Fulfillment of

the Requirements for the Degree of

Doctor of Philosophy

in

Physics

1985 - May

Albany - New York

State University of New York at Albany

COLLEGE OF SCIENCE AND MATHEMATICS

The dissertation submitted by

Ranjith Wijayawardana

under the title

Application of a Crystal Septum to Replace a Magnet
in a Charged Particle Beam and Study of Dechanneling
and Feeding-in Effects in a Single Silicon Crystal

has been read by the undersigned. It is hereby recommended for acceptance to the Faculty of the University in partial fulfillment of the requirements for the degree of Doctor of Philosophy.

Chih Reel Sun
(Signed)

5/23/85
(Date)

Richard A. Connors
(Signed)

5/23/85
(Date)

M. S. Lee
(Signed)

5/23/85
(Date)

Walter M. Dubin
(Signed)

5/23/85
(Date)

John J. Lawrence
(Signed)

5/23/85
(Date)

Recommended by the Department of Physics

Ned Auer, Chairman
(Signed)

Recommendation accepted by the Dean of Graduate Studies for the Graduate Academic Council.

(Signed)

(Date)

ACKNOWLEDGEMENTS

Throughout the entire research program I was fortunate to have the guidance of Prof. C. R. Sun. As my thesis advisor he always provided patient advice, constant encouragement and helpful suggestions. During two and half years stay at the Fermi National Accelerator Laboratory Dr. R. A. Carrigan, who served as the co-advisor also helped immensely. The discussions I have had with him and the constant guidance and knowledgeable advice he provided have been most valuable. Without their kind assistance the research reported herein would not have been possible and I would like to take this opportunity to place in record my deep gratitude and sincere thanks to both of them.

Professors W. M. Gibson and A. Inomata have given me advice and encouragement throughout my carrier as a graduate student at State University of New York at Albany. They were kind enough to serve on my thesis advisory committee too. I have benefited much from my discussions during the experiment with Dr. S. I. Baker of Fermi National Accelerator Laboratory. I am most grateful to them for their valuable support.

At different stages of this study I have received assistance in the form of discussions and suggestions from Dr. J. S. Forster Chalk

River Nuclear Laboratories, Atomic Energy of Canada, Prof. J. A. Ellison of University of New Mexico and Dr. I. J. Kim of State University of New York at Albany. Prof. S. Alam of State University of New York at Albany acted as a member of thesis advisory committee. I wish to thank all of them sincerely. I thankfully acknowledge the friendly assistance given by Ron Schailey of Fermi National Accelerator Laboratory during various stages of the experiment. Thanks are also due to my fellow graduate student V. Tanikella for his friendly cooperation during the experimental phase.

This research was performed as part of the experimental high energy physics program supported by the Department of Energy and conducted jointly by State University of New York at Albany, Fermi National Accelerator Laboratory, Chalk River Nuclear Laboratories and University of New Mexico. I would also like to acknowledge the assistance provided to me during my stay in U.S.A. by Institute of International Education under the Fulbright Scholarship program.

I extend my deep thanks to my parents for their love, patience and encouragement.

ABSTRACT

First part of this thesis describes the first application of a crystal septum to replace a magnetic septum at the Fermilab Meson area M-Bottom secondary beam line. As a result the maximum momentum of the beam that could be transmitted to the experimental area was raised from the magnetic septum limit of 225 GeV/c to the full primary beam momentum of 400 GeV/c. Transmission properties of the crystal septum has been studied at energies of 60, 100 and 200 GeV/c. Beam properties at 200 GeV/c with the crystal septum operation has also been studied.

The second part consists of a study of planar (110) and axial $\langle 112 \rangle$ feeding-in and dechanneling effects in a single silicon crystal. Three surface barrier semiconductor detectors along the crystal were used to measure the energy loss of the charged particles. For each particle incident and outgoing angles and the energy losses in the three crystal mounted detectors were recorded on magnetic tapes. Channeled particles were identified by their low energy losses. Data was acquired at energies of 30, 60, 100 and 200 GeV for planar channeling and 60 and 100 GeV for axial channeling. Feeding-in effects were observed for both

planar and axial cases. The basic probabilistic equation was used to derive a simple theoretical model which contains the characteristic dechanneling and feeding-in lengths. The dechanneling lengths have been calculated for both planar and axial channeling and the incident angle dependence of feeding-in has been studied for planar channeling at above all energies.

CONTENTS

Acknowledgements	i
Abstract	iii
References	viii
Chapter	Page
1. INTRODUCTION	1
Crystal Septum	2
Feeding-in and Dechanneling	3
PART 1	
2. CLASSICAL THEORY OF BENDING	6
2.1 Introduction	6
2.2 Planar Channeling	6
2.2.1 Continuum Potential	6
2.2.2 Motion of a Charged Particle	8
2.2.3 Phase Space Representation	10
2.2.4 Phase Space Density	13
2.3 Bending of Planar Channeled Particles	16
2.3.1 Equation of Motion	16
2.3.2 Dechanneling due to a Constant Curvature	19
3. DESCRIPTION OF THE BEAM LINE	22
3.1 Introduction	22
3.2 Beam Line Transport System	22
3.3 Beam Tuning	27
3.4 Regular Secondary Beam Properties	28
3.5 Calculation Of Beam Element Parameters	32
3.5.1 Computer Program 'TRANSPORT'	32
3.5.2 Computer Program 'DECAY TURTLE'	33
4. EXPERIMENTAL SET UP IN THE M-BOTTOM PIT	35
4.1 Introduction	35
4.2 Apparatus Set Up	37
4.2.1 Drift Chambers	37
4.2.2 Scintillation Detectors	43
4.2.3 Surface Barrier Semiconductor Detectors	45
4.3 Trigger System	49
4.4 Data Acquisition System	52
5. CRYSTAL SEPTUM	55
5.1 Introduction	55
5.2 Crystal	55
5.3 Bending Device	60
5.4 Septum Stand	65
5.5 Septum Control System	68
5.6 Septum Crystal Scanning Set Up	70
5.7 Setting the Bending Angle	72

5.8 Through-put Studies of the Septum Crystal	77
5.8.1 Bending Efficiency (f_b)	77
5.8.2 Capture Efficiency (f_c)	81
5.8.3 Spatial Acceptance (f_s)	87
5.8.4 Angular Acceptance (f_a)	87
5.8.5 Transmission Fraction (f_T)	87
6. SCANNING OF CRYSTALS	89
6.1 Introduction	89
6.2 Energy Loss Scanning Method	89
6.3 Efficiency Tests	92
6.4 Kim Scan Method	97
6.5 Some Important Points About Scanning	99
7. CRYSTAL SEPTUM OPERATION	100
7.1 Introduction	100
7.2 Crystal Septum Installation Procedure	100
7.2.1 Base Plate Alignment	100
7.2.2 Background Studies in FEH	101
7.2.3 Decision to Use Kim Technique	103
7.2.4 Preparations to Use Energy Loss Technique	104
7.2.5 Installation	106
7.3 Input Beam for Crystal Septum Applications	106
7.4 Operation at 200 GeV/c	108
7.4.1 Crystal Alignment	108
7.4.2 Beam Divergence and Width Studies	110
7.4.3 Momentum Studies	113
7.4.4 Momentum Recombination and Focusing	122
7.4.5 Beam Intensity Studies	125
7.5 Operation At 400 GeV/c	130
7.5.1 400 GeV/c Beam in M-Bottom Beam Line	130
7.5.2 Momentum Recombination and Focusing	134

PART 2

8. THEORY OF DECHANNELING AND FEEDING-IN	141
8.1 Introduction	141
8.2 Derivation of the Probabilistic Equation	142
8.3 Derivation of the Basic Equation	143
8.4 Analysis of the Basic Equation	145
8.5 Alternative Method of deriving Basic Equation	147
8.6 Dechanneling	148
8.6.1 Planer Dechanneling	150
8.6.2 Axial Dechanneling	153
8.7 Initial Channeled Fraction	154
9. STUDY OF DECHANNELING AND FEEDING-IN	158
9.1 Introduction	158
9.2 Data Acquisition	158
9.3 Algorithm	159
9.3.1 Determination of Channeled Particles	159
9.3.2 Calculation of Dechanneling Lengths	172

9.3.3 Calculation of Feeding-in Lengths	174
9.4 Results and Calculations	175
9.4.1 Dechanneling Lengths	199
9.4.2 Feeding-in Lengths	200
9.4.3 Channeled Fractions	204
9.5 Conclusion	209

REFERENCES

- [1] J.Lindhard, Mat. Fys. Medd. Dan. Vid. Selsk. 34, No. 14 (1965).
- [2] D.S.Gemmell, "Channeling and Related Effects", Rev. Mod. Phys. 46 (1974) 129.
- [3] J.A.Ellison, Phy. Rev. B13 (1976) 1880.
- [4] J.A.Ellison, Phy. Rev. B18 (1978) 5948.
- [5] J.A.Ellison and S.T.Picraux, Phy. Rev. B18 (1978) 1028.
- [6] J.A.Ellison, Phy. Rev. B12 (1975) 4771.
- [7] D.V.Morgan, "Channeling" (Wiley and Sons, New York, 1973)
- [8] E.N.Tsyganov, Fermilab TM-682, TM-684, Batavia, 1976.
- [9] A.F.Elishev et al., Phys. Lett. 88B (1979) 387.
- [10] J.Bak et al., Phys. Lett. 93B (1980) 505.
- [11] S.M.Salman, "Deflections of High Energy Channeled Particles by Elastically Bent Silicon Single Crystals", State University of New York at Albany (1982).
- [12] J.A.Ellison and S.T.Picraux, Phys. Lett. 83A (1981) 271.
- [13] J.A.Ellison, Nucl. Phys. B206 (1982) 205.
- [14] H.Kudo, Nucl. Instr. Meth. 189 (1981) 609. Conference on Atomic Collisions in Solids, Bad Iburg, Germany (1983).
- [15] R.A.Carrigan, W.M.Gibson, C.R.Sun, E.N.Tsyganov, Nucl. Inst. Meth. 194 (1982) 205.
- [16] R.A.Carrigan, Fermilab-pub-80/45-exp (may,1980).
- [17] J.F.Bak et al., Nucl. Inst. Meth. B242 (1984) 1.
- [18] "Review of Particle Properties", Phy. Lett. April 1984.
- [19] H.W.Atherton et al., CERN 80-07.

- [20] K.L.Brown et al., "Transport - a Computer Program for Designing Charged Particle beam Transport System", SLAC-91, Rev.2, UC-28 (I/A) also CERN-73-16 and NAL-91.
- [21] D.C.Carrey et al., "Decay Turtle - a Computer Program for Simulating Charged Particle beam Transport Systems, Including Decay Calculations", SLAC-246, UC-28 (I/A).
- [22] F.Sauli, Nucl. Inst. Meth. 156 (1978) 147.
- [23] H.Daum, Nucl. Inst. Meth. 152 (1978) 541.
- [24] F.Sauli, CERN 77-09.
- [25] A.Breskin et al., Nucl. Inst. Meth. 124 (1975) 189.
- [26] Birks, "The Theory and Particle of Scintillation Counters", (Pergamon, New York).
- [27] U.Fano, Annu. Rev. Nucl. Scie. 13 (1963) 1.
- [28] G.L.Miller, W.M.Gibson and P.F.Donavon, Annu. Rev. Nucl. Scie. 12 (1962) 189.
- [29] J.A.Ellison et al., Nucl. Instr. Meth. B2 (1984) 9.
- [30] W.M.Gibson et al., Contributions to the 10th International Conference on Atomic Collisions in Solids, Bad Iburg, Germany (July 1983).
- [31] S.I.Baker et al., Phys. Lett. 137B (1984) 129.
- [32] R.J.Roark. "Formulas for Stress and Strain", (McGraw-Hill, New York, 1954) p. 121.
- [33] S.Timoshenko and J.Goodier, "Theory of Elasticity", 2nd ed. (McGraw Hill, New York, 1951).
- [34] M.M.Frochet, "Photo Elasticity", (Wiley, New York, 1948) Vol.2, p.104.
- [35] R.A.Carrigan, FN-362-Fermilab (1982).
- [36] R.A.Carrigan et al., Phy. Rev. Lett. 31 (1973)
- [37] G.Bellettini et al., Phy. Lett. 14 (1965) 164. 1088.
- [38] R.A.Carrigan, Phy. Rev. Lett. 24 (1970) 168.
- [39] R.A.Carrigan et al., Phy. Rev. Lett. 24 (1970) 683.
- [40] J.V.Allaby et al., Phy. Lett. 28B (1968) 67.

- [41] V.Bartenev et al., Phy. Rev. Lett. 29 (1972) 1755.
- [42] G.Barbiellini et al., Phy. Lett. 39B (1972) 663.
- [43] E.Bonderup et al., Radi. Eff. 12 (1972) 261.
- [44] S.U.Campisano et.al., Radi. Eff. 13 (1972) 156.
- [45] L.C.Feldman and B.R.Appleton, Phy. Rev. B8 (1973) 935.
- [46] M.J.Pedersen et.al., Atomic Collisions in Solids, 1973 Gatlinburg Conf. ed. by S.Datz et.al. (Plenum Press, 1975), Vol.2, p.863.
- [47] H.Esbensen and J.A.Golovshenko, Nucl. Phy. A298 (1978) 832.
- [48] E.Uggerhoj, Phys. Sscri. 28 (1983) 331.
- [49] J.Lindhard and V.Nielsen, idid 38 (1971) no.9.

CHAPTER 1

INTRODUCTION

When a charged particle beam is incident nearly parallel to a low-index crystal axis or plane there is a significant difference in the motion of the particles. This phenomenon is called 'channeling'. For the past 10-15 years this has been an interesting area of both theoretical and experimental research.

Basic concepts of channeling were first published by Lindhard [1] in 1965. In 1974 Gemmell [2] reviewed the channeling and related effects of the passage of charged particles through crystals. Ellison has done more detailed analysis and calculations to study the behavior of planar channeled particles [3,4,5,6]. His approach was based on the classical equation of motion of a charged particle due to the continuum potential of the channel. In addition, a book edited by Morgan [7] gives detailed treatment both of the theory and applications of channeling.

The steering mechanism of charged particles by bent crystal planes using channeling was first proposed by Tsyganov [8]. This remarkable behavior was first observed at Dubna with 8.4 GeV/c protons [9], later at CERN with 12 GeV/c [10] and recently (1982) at Fermilab up to 180 GeV/c [11]. Ellison has done further theoretical work on dechanneling of charged particles due to curved planes. His

calculations led him to a universal curve which determines the dechanneling fraction due to a bent channel of constant curvature [12,13]. Kudo [14] has also done somewhat similar work for silicon and germanium including the effect due to other near by crystal planes. Several aspects of bending of charged particles by bent crystals were discussed in the papers [15,16] by R. Carrigan et al.

Crystal Septum

After the experimental success of bending of charged particles by bent crystals, a crystal septum was considered for operation in the Fermilab M-Bottom secondary beam line. This beam line was constructed at an angle of 8.25 milliradians relative to the incident primary beam. The secondary beam is bent by two conventional septum magnets each of 3.05 meters length and operating at 9.6 kG at 200 GeV/c. The beam line transport system will be discussed in Chapter 3. The magnetic septum had been originally designed to transmit particles of momentum only up to 225 GeV/c into the experimental area even though the accelerator then was capable of running at 400 GeV/c. Therefore the M-Bottom beam line was limited mostly to experiments of energy below 225 GeV.

One aspect of the present experimental program was to replace this magnetic septum by a bent silicon crystal to transmit the regular secondary beam into the beam line. The demonstration crystal which was 0.8 mm thick, 12.0 mm wide and 27.0 mm long was bent along the crystal length by a bending device. The other aspect of the experimental program was to feed 400 GeV/c particles into the existing beam line.

The classical theory of bending will be discussed in the next

Chapter (Chapter 2). A brief discussion of the M-Bottom beam line is given in Chapter 3. The experimental set up used in M-Bottom pit for different tests of the crystal prior to the installation in the septum position is discussed in Chapter 4. Setting the correct bend in the crystal has to be done prior to installation. Chapter 5 details this and studies carried out to understand the transmission properties of the septum crystal. Crystal alignment is the other important part of this application. It is impossible to perform the regular energy loss scanning technique at the location of the crystal septum because of the high background due to the other beam lines. Different scanning methods relevant to septum alignment were tested in the experimental pit. These studies are discussed in Chapter 6. Chapter 7 is devoted to a discussion of the installation and operation of the crystal septum at energies of 200 and 400 GeV. The observed beam properties at 200 GeV are also presented in this chapter. Beam tuning plays an important role in getting the maximum possible yield in experimental locations. 'TRANSPORT' program runs for momentum recombination and focusing the beam in the pit and 'DECAY TURTLE' program runs to calculate the beam intensities are discussed in this chapter. Results will be compared with the observations made for septum operation.

Feeding-in and Dechanneling

Dechanneling was first described theoretically by Lindhard [1]. The reverse process is called feeding-in or rechanneling where random incident particles are trapped in channels due to multiple scattering. This effect is normally assumed to be negligible in theoretical

calculations. The first observations of feeding-in effect [17] in planar and axial channeling shows that this effect is not negligible and has some influence in channeling phenomena. The second part of this thesis deals with planar and axial feeding-in and dechanneling studies. This experiment was done in the Fermilab Meson area M-Bottom beam line using the experimental set up which was used for the septum studies. The relevant theory is discussed in Chapter 8 and the results are presented in Chapter 9.

PART 1

CHAPTER 2

CLASSICAL THEORY OF BENDING

2.1 Introduction

This chapter reviews the basic theory of the channeling of charged particles. The continuum potential with the Lindhard approximation to the screening function will be used to discuss the motion of a planar channeled particle. Phase space arguments will be used under statistical equilibrium assumption made by Lindhard[1] to understand the behavior of channeled particles. The following discussions are based on Ellison's approach for derivation of the theory.

2.2 Planar Channeling

2.2.1 Continuum Potential

Channeling of a particle along a major crystal plane is basically governed by the potential due to the nearby planes of atoms. The continuum potential due to the plane of atoms at a distance x from the plane can be written as the summation of individual contributions due to all the atoms in the plane.

$$U(x) = Nd_p \int_0^{\infty} 2\pi r Y\{\sqrt{(y^2+r^2)}\} dr \quad 2.1$$

where r is the radial distance from isolated atoms along the plane, N

is the atomic density of the crystal and d_p is the separation between the atomic planes. The potential $Y(r)$ which describes the interaction between the incident particle (atomic number Z_1) and an isolated atom (atomic number Z_2) when they are at a separation r , can be written as an expression of the form

$$Y(r) = \frac{Z_1 Z_2}{r} e^2 \phi(r/a) \quad 2.2$$

where e is the electronic charge, $\phi(r/a)$ is the screening function. $a = .8853 a_0 (Z_1^2 + Z_2^2)^{-1/2}$ is the screening distance, where a_0 is the Bohr radius. Most commonly used potentials are based on Moliere and Lindhard approximations to the screening functions. The Moliere approximation to the screening function is

$$\phi(r/a) = 0.1 \exp(-6.0r/a) + 0.55 \exp(-1.2r/a) + 0.35 \exp(-0.3r/a) \quad 2.3$$

and the Lindhard approximation to the screening is

$$\phi(r/a) = [1 - r/(r^2 + C^2 a^2)^{1/2}] \quad 2.4$$

where C is a standard constant which he sets equal to $\sqrt{3}$. Using the Lindhard approximation the continuum potential at a distance x from the plane can be written as [1]

$$U(x) = 2\pi Z_1 Z_2 e^2 N_d \{ (x^2 + C^2 a^2)^{1/2} - x \} \quad 2.5$$

For relativistic particles the critical angle for planar channeling can be derived[1] by considering the closest distance of approach as

$$\theta_{c,p} = [4\pi Z_0 Z_2 e^2 N d_p a / E]^{\frac{1}{2}} \quad 2.6$$

where E is the energy of the particle. For the axial case the critical angle is given by

$$\theta_{c,a} = [4Z_1 Z_2 e^2 / E d_a]^{\frac{1}{2}} \quad 2.7$$

where d_a is the atomic spacing along the corresponding axis.

2.2.2 Motion of a Charged Particle

The actual motion of a charged particle is very complicated to write because of the thermal vibrations of the crystal atoms and the interaction with electrons. But ignoring these effects and assuming the continuum potential approximation, the equation of motion can be approximated by using Newtonian mechanics. Let us now consider the motion of a charged particle between two crystal planes as shown in Figure 2.1. If the continuum approximation is assumed to be valid and the longitudinal velocity of the particle (in the z -direction) is constant, then the motion reduces to a two dimensional problem in which the motion can be written as [5]

$$\frac{d^2x}{dz^2} = \frac{-1}{2E} \frac{d}{dx} V(x) \quad 2.8$$

where E is the relativistic energy of the particle and x is measured from the point midway between the planes. $V(x)$ is the potential experienced by the particle due to both atomic planes such that

$$V(x) = U(d_p/2+x) + U(d_p/2-x) \quad 2.9$$

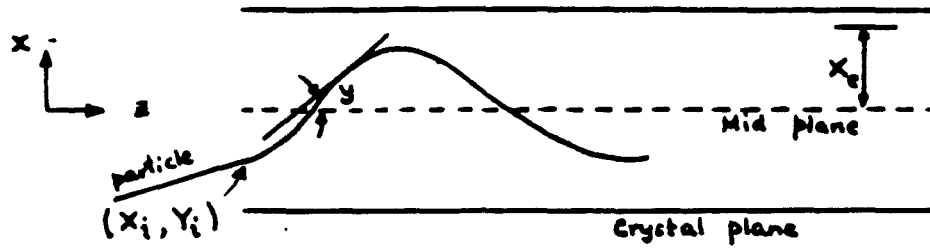


Figure 2.1 Planar channeling of a charged particle between two crystal planes. The initial normalized position and momentum are X_1 and Y_1 .

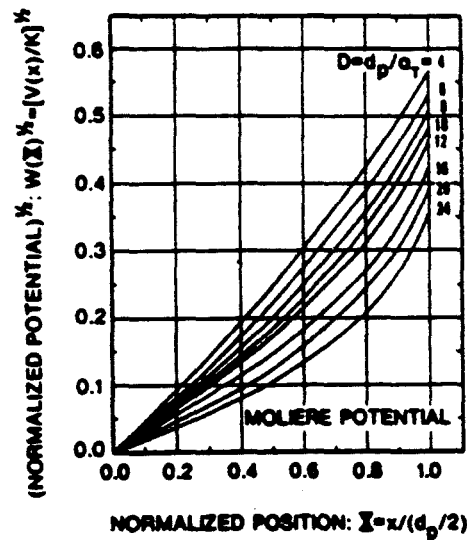


Figure 2.2 Universal curves of $(W^{\frac{1}{2}})$ versus normalized position X for the Moliere potential obtained from reference [5]. The different curves are for different normalized separations D .

Here $U(y)$ is the planar continuum potential. For convenience the following notation will be used for defining the normalized distance and normalized planar separation:

$$X = 2x/d_p \quad \text{and} \quad D = d_p/a \quad 2.10$$

For the Lindhard potential

$$V(x) = K \left\{ \left[\left\{ (1+X)^2 + \frac{12}{D^2} \right\}^{\frac{1}{2}} - (1+X) \right] + \left[\left\{ (1-X)^2 + \frac{12}{D^2} \right\}^{\frac{1}{2}} - (1-X) \right] \right\} \quad 2.11a$$

or

$$V(x) = K W(X, D) \quad 2.11b$$

where $W(X, D)$ is the normalized form of the continuum potential, X is the normalized position in the channel, D is the normalized planar spacing, K is the parameter scaling the magnitude of the potential which is given by

$$K = \pi Z_1 Z_2 e^2 N d_p \quad 2.12$$

The normalized potential versus normalized position is shown in Figure 2.2 for the Moliere potential [13].

2.2.3 Phase Space Representation

If we define the normalized position along the channel as $Z=2z/d_p$, the equation of motion (equation 2.8) becomes

$$\frac{d^2 X}{dZ^2} + \frac{K}{2E} W'(X, D) = 0 \quad 2.13$$

where the prime denotes differentiation with respect to the first argument X . This equation can be written as two first order equations

$$\frac{dX}{dZ} = (K/E)^{\frac{1}{2}} Y \quad 2.14a$$

$$\frac{dY}{dZ} = -\frac{1}{2}(K/E)^{\frac{1}{2}} W'(X,D) \quad 2.14b$$

If $y(z)$ is the angle the particle trajectory makes with the plane at a distance z , the transverse velocity of the particle is $v_t = v \sin y(z) \approx v dx/dz$ and the corresponding transverse energy is $E_t = E[y(z)]^2$. The corresponding energy of an equivalent two dimensional system transverse to the particle motion is defined as the transverse energy. Since dx/dz is related to transverse momentum, equation 2.14a defines the normalized transverse momentum Y and the solutions of equation 2.14 are of the form

$$X = \phi_1(Z, X_i, Y_i) \quad 2.15a$$

$$Y = \phi_2(Z, X_i, Y_i) \quad 2.15b$$

where X_i and Y_i are the initial normalized coordinates of the channeled particles. Further equation 2.13 can be written in the form

$$\frac{d}{dX} \left[\left\{ \sqrt{\frac{E}{K}} \frac{dX}{dZ} \right\}^2 + W(X,D) \right] = 0 \quad 2.16$$

which implies that the motion is governed by a conservation law and the conservation of transverse energy will be given by the equation

$$Y^2 + W(X,D) = e \quad 2.17$$

where $e (=E_t/K)$ is the normalized transverse energy.

These potentials $(W(X,D))$ are symmetric (i.e. $W(X)=W(-X)$), therefore the solutions $X(Z, X_i, Y_i)$ are periodic functions, and the

transverse motion of each particle has a uniquely associated amplitude A where the amplitude is given by the equation

$$W(A,D) = e \quad 2.18$$

The wavelength Q of the oscillation depends on the amplitude A such that $Q(A,D)$ is a monotonically decreasing function of A where $Q(A,D)$ can be written as [5]

$$Q(A,D) = \int_0^A [W(A,D) - W(X,D)]^{-\frac{1}{2}} dX \quad \text{for } A \neq 0 \quad 2.19a$$

$$= \pi [2W''(0,D)]^{\frac{1}{2}} \quad \text{for } A = 0 \quad 2.19b$$

where W'' is the second derivative of W with respect to X and the wavelength can be written as [5]

$$\lambda = 2d_p \left(\frac{E}{K}\right)^{\frac{1}{2}} Q(A,D) \quad 2.20$$

For each amplitude A , equation 2.14 defines a curve in phase space (X,Y) which are called integral curves. The integral curve 'e' in Figure 2.3 shows the path in phase space of an arbitrary particle which has an amplitude A . For standard potentials like Lindhard and Moliere these integral curves form a family of concentric ovals about the origin. When a beam of particles is channeled through a plane in a crystal, they move in phase space along the integral curves in the clockwise direction. The larger amplitude particle moves faster around its own integral curve.

For example, curve 'a' in figure 2.3 represents the initial positions and velocities ($t=0$) of the particles incident parallel to

the crystal plane and 'b' and 'c' represent the positions and velocities at some depths at time t_1 and t_2 into the crystal.

Let us define the critical distance of approach to be x_c such that normalized critical distance $X_c = 2x_c/d_p$. For a particle to be channeled through the plane its amplitude A must be less than or equal to X_c ($A \leq X_c$). The critical transverse energy is defined by

$$E_c = V(x_c) \quad 2.22$$

and any particle which has a transverse energy $E > E_c$ is assumed to be dechanneled.

2.2.4 Phase Space Density

All the information for the continuum model planar channeled particles is contained in the phase space density $\sigma(Z, X, Y)$. Let $\sigma_0(0, X_i, Y_i)$ be the initial phase space density and $\sigma(Z, X, Y)$ be the phase space density at a depth Z . By the Liouville theorem in classical mechanics it can be shown [4] that σ is a constant along the curves in X, Y, Z space determined by equation 2.14. i.e.

$$\sigma(Z, X, Y) = \sigma_0(0, X_i, Y_i) \quad 2.23$$

Since the equation 2.14 does not depend explicitly on Z , the phase space point (X, Y) must move back to (X_i, Y_i) in $-Z$ units if we reverse the motion of particles. Hence the inverse relation of equation 2.15 is

$$X_i = \phi_1(-Z, X, Y) \quad 2.24a$$

$$Y_1 = \phi_2(-Z, X, Y) \quad 2.24b$$

and the phase space density at (X, Y, Z) can be rewritten as

$$\sigma(Z, X, Y) = \sigma_0 \{0, \phi_1(-Z, X, Y), \phi_2(-Z, X, Y)\} \quad 2.25$$

Since ϕ_1 and ϕ_2 are periodic, equation 2.23 tells us that for a fixed X and Y phase space density σ is also a periodic function of Z with the same wavelength and therefore the statistical equilibrium phase space density $\bar{\sigma}$ is the depth average of σ over one period.

$$\bar{\sigma}(X, Y) = \frac{1}{\lambda} \int_0^\lambda \sigma_0 \{0, \phi_1(-Z, X, Y), \phi_2(-Z, X, Y)\} dZ \quad 2.26$$

Once the phase space density is evaluated, spatial density $\bar{\rho}_s$ and momentum density $\bar{\rho}_m$ can be written as

$$\bar{\rho}_s(X, D) = 2 \int_0^{[e_c - W(X)]} \bar{\sigma}(X, Y, D) dY \quad 2.27a$$

$$\bar{\rho}_m(X, D) = 2 \int_0^{X_y} \bar{\sigma}(X, Y, D) dY \quad 2.27b$$

where e_c is the critical transverse energy and $W(X_y) = e_c - Y^2$.

For Moliere or Lindhard potentials there are no solutions to ϕ_1 and ϕ_2 in terms of elementary functions. Therefore, equation 2.26 can not easily be solved analytically. In a channeling experiment or in reality the initial spatial density is uniform and the initial momentum density is Gaussian. For an example let us assume a parallel incident beam of initial momentum distribution

$$\sigma_0 = \frac{1}{2} \delta(Y - Y_0) \quad 2.28$$

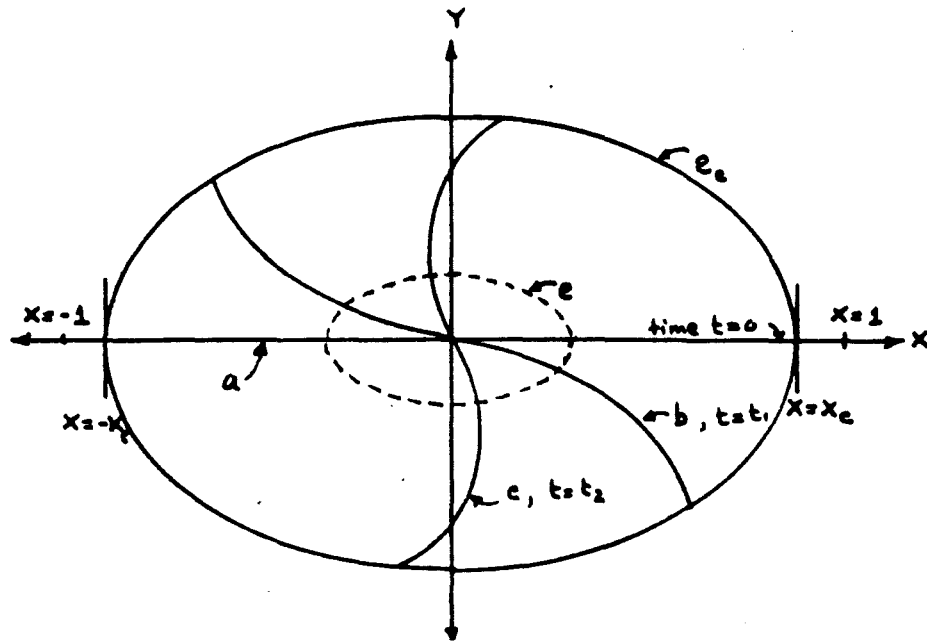


Figure 2.3 Phase flow at various crystal depths (curves a, b and c) for particles incident parallel to the plane. e is an integral curve for an arbitrary particle.

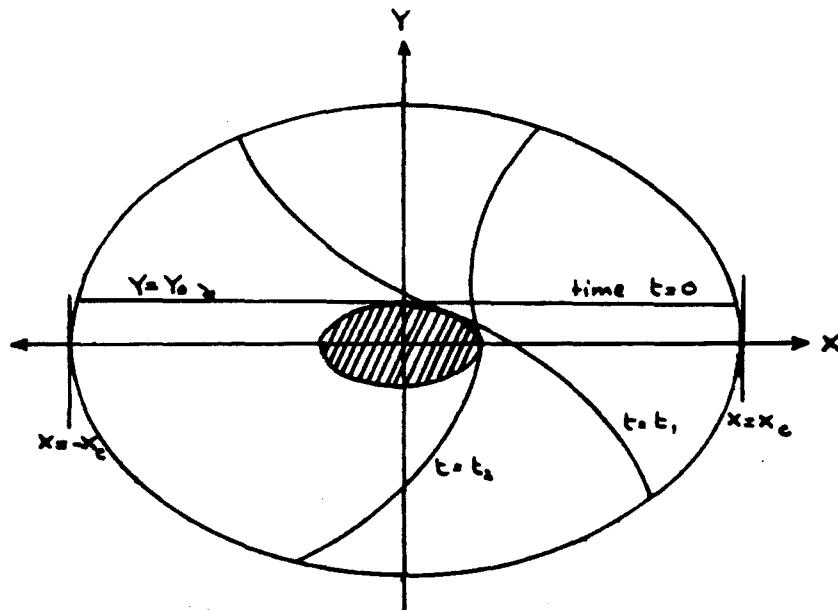


Figure 2.4 Phase flow at various crystal depths for particles incident at an angle to the plane. These particles never enter the darked region defined by $E > Y_0^2$.

where δ denotes the Delta function and Y_0 is the incident angle. An initial spatial distribution of $1/2$ is assumed between planes $(-1 < X < +1)$. Now equation 2.26 can be reduced to the simple form [5]

$$\bar{o}_0 = 0 \quad \text{for } e < Y_0^2 \text{ and } e > W(A_c) \quad 2.29a$$

$$= [2Q(A, D) W'(X_1)]^{-1} \text{ for other values of } e \quad 2.29b$$

where A is the amplitude corresponding to transverse energy e , $A_c (= X_c)$ is the critical amplitude for channeling and X_1 is defined by $W(X_1) = e - Y_0^2$. Any particle is considered to be dechanneled if its amplitude is greater than or equal to the critical amplitude. It is easily seen that once A_c is chosen \bar{o} depends only on Y_0 and D .

Figure 2.4 shows the phase flow in the phase plane for various depths for particles starting along the line $Y = Y_0$. The particles never enter the region where $E < Y_0^2$.

2.3 Bending of Planar Channeled Particles

The characteristics of planar channeled particles were discussed before. Steering of charged particles by bent planes will be discussed below.

2.3.1 Equation of Motion

Let us now consider a charged particle, channeled between two crystal planes and entering a bent region of curvature $k(z)$ as shown in Figure 2.5. If \bar{x} and \bar{z} are two perpendicular axes in the lab frame as shown in Figure 2.5 then the curvature of the central plane is defined by $\bar{x} = f(\bar{z})$ and the the curvature $k(z)$ can be written as

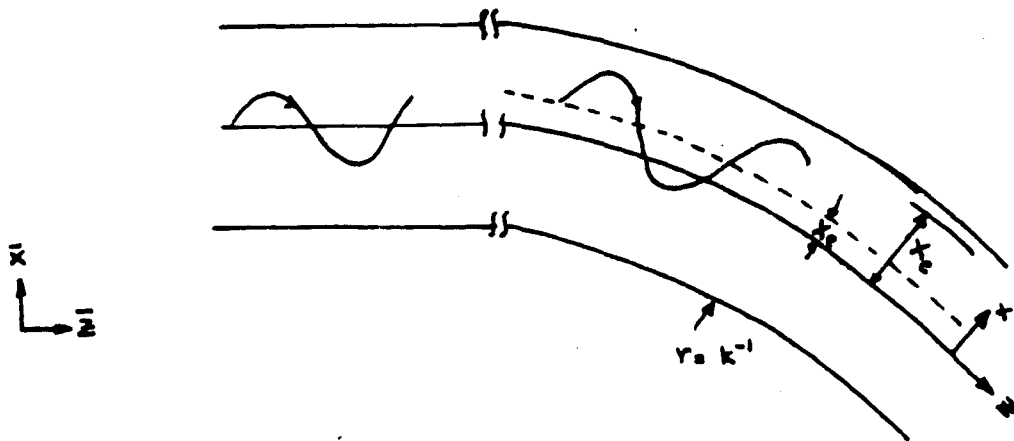


Figure 2.5 Planar channeling of a charged particle between two bent crystal planes of constant curvature k . X_c is the critical distance for channeling and X_e is the distance of the equilibrium plane from the center of the channel.

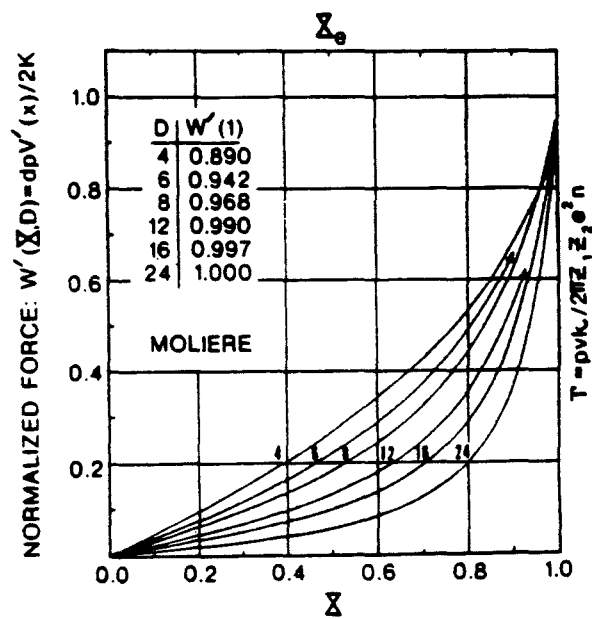


Figure 2.6 Universal curves of W' versus normalized position X for use in determining X_e for a given k or Γ (obtained from reference [13]).

$$k(z) = f''(\bar{z}) / (1 + f'(\bar{z})^2)^{3/2}. \quad 2.30$$

Introducing the generalized coordinate (x, z) where z is the arc length along the central plane and x is the distance perpendicular to the central plane, the Lagrangian for a particle in a curved channel can be written [12] as

$$L = \frac{m}{2} \left((dx/dt)^2 + (1 - xk)^2 (dz/dt)^2 \right) - V(x) \quad 2.31$$

where m is the mass of the particle and $V(x)$ is the continuum potential. Using $dz/dt = (2E/m)^{1/2}$ and for relatively smaller curvatures $1 \gg dk(z)$ the equation of motion will be reduced to [12]

$$\frac{d^2x}{dz^2} + \frac{1}{2} \frac{V'(x)}{pV} = k(z) \quad 2.32$$

Using the normalized definitions in equation 2.10 the above equation can be written [13] as

$$\frac{dX^2}{dZ^2} + \frac{K}{pV} (W'(X, D) - \Gamma) = 0 \quad 2.33$$

where $\Gamma = pvk/2\pi Z_1 Z_2 e^2 N$. A particle is defined to be rechanneled by the bend if $-X_c < X(Z) < X_c$ for all z and is dechanneled if $X(Z) \geq X_c$ for some z . The X_c is related to the critical transverse energy for channeling by $E_c = V(x_c)$.

The equilibrium solution $X = X_e$ of equation is defined by

$$W'(X_e, D) = \Gamma \quad 2.34$$

The non-negative geometrical parameter X_e depends only on the two physical parameters D and Γ , and is a monotonically increasing function

of Γ . The equilibrium path is shown by the dashed line in Figure 2.5. The universal curves of the normalized potential are shown in Figure 2.6. For a given k or Γ the equilibrium position can be determined from Figure 2.6.

The equation of motion (equation 2.33) has an associated conservation law given by

$$Y^2 + W(X,D) - \Gamma X = e \quad 2.35$$

where $Y = (E/2K)^{1/2} dX/dZ$ and e is the normalized transverse energy. Equation 2.35 implies that e is constant along a given solution as in the case of $\Gamma=0$ (section 2.2.3). The solutions define a set of concentric ovals about $X=X_e$ and $Y=0$ in the phase plane as shown in Figure 2.7. The motions of the particles are periodic and oscillate around $X=X_e$. As the particle moves down the unbent channel, it moves clockwise along the phase space curve 'c'. When it enters the bent channel at 'L', it changes its motion from 'c' to 'd' and starts to oscillate around $X=X_e$. This arbitrary particle, according to the Figure 2.7, will be dechanneled at 'M'. If the particle moves along the phase space curve 'e' in the unbent region and enters the bend region at N, then it continues channeling along the phase space curve 'f' in the bend region.

2.3.2 Dechanneling due to a Constant Curvature

In Figure 2.7 the phase space of the particles before entering the bent channel is represented by the region inside the curve 'a' and they oscillate around the center $X=0$. As they enter the bent channel, the

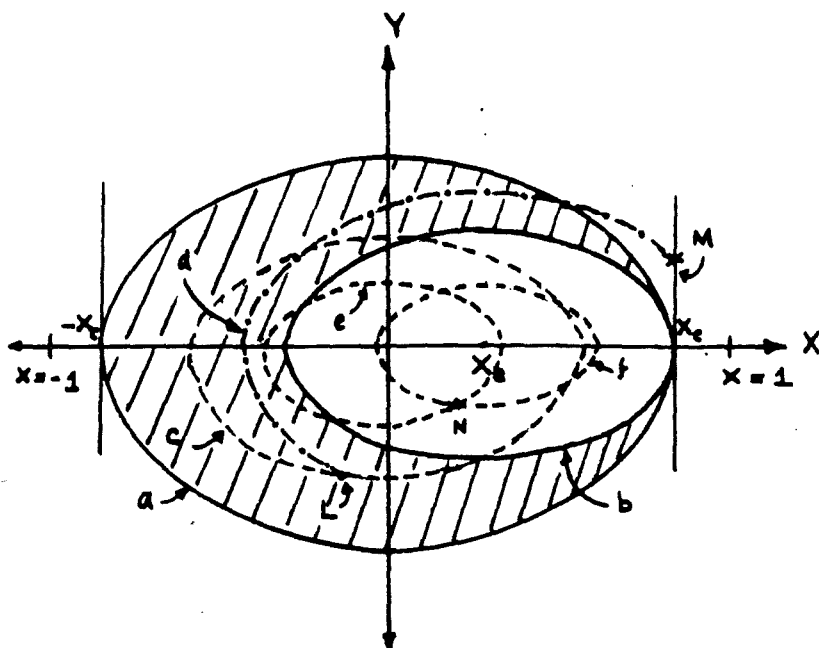


Figure 2.7 Phase flow at various crystal depths for planar channeled particles (ovals centered at $X=0$) and bent crystal planes (ovals centered at $X=X_e$).

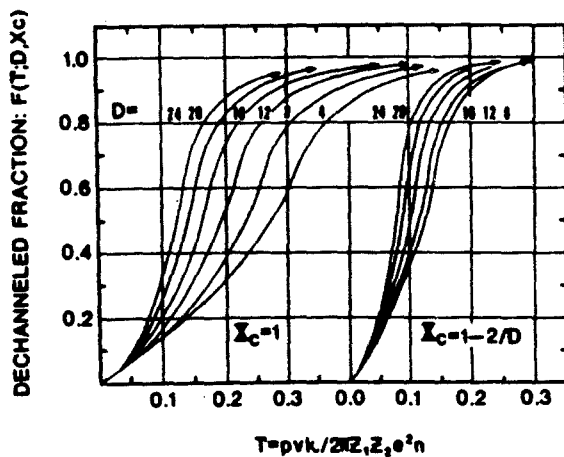


Figure 2.8 Universal curves of F versus Γ for the two cases $X_c=1$ and $X_c=1-2/D$ using the Moliere potential (obtained from reference [13]).

oscillation center shifts to $X=X_e$ and the region inside the curve 'b' represents the phase space of bent channeled particles. Therefore, the particles in the region a-b are dechanneled at the bend and the dechanneled fraction F can be written as

$$F = \iint_{(a-b)} o(X,Y) dX dY \quad 2.36$$

As discussed in section 2.2.4, there are no analytical solutions available for o and, therefore, no analytical solution can be found for F. Ellison[13] has done some computations of Γ using the Moliere potential and has obtained the universal curves for dechanneling fractions. These curves are shown in Figure 2.8 for different values of D.

CHAPTER 3

DESCRIPTION OF THE BEAM LINE

3.1 Introduction

The purpose of the crystal septum application was to show that a bent crystal could be used to replace a magnetic element in a beam line to bend a charged particle beam. The Meson area M-Bottom (Meson Bottom) secondary beam line was used for this demonstration. The two septum magnets (MB2D) which are located about 160 feet downstream of the production target deflect the secondary beam by 8.9 milliradians in the downward direction. It was suggested to replace the above septum magnets by a bent crystal to operate the beam line. This chapter describes the M-Bottom beam line and its normal beam properties.

3.2 Beam Line Transport System

During the period of this experiment the primary beam of the main accelerator was 400 GeV/c protons. Figure 3.1 shows the schematic of the M-Bottom beam line elements. The primary proton beam which is bent vertically downward by 1.46 milliradians by the MC1D bending magnet is incident horizontally on an aluminum production target. The target can be remotely adjusted to cause 0.1% to 4.0% of the incident protons to interact in it. The M-Bottom beam line is a secondary beam line which has been designed to accept secondary particles produced at an angle

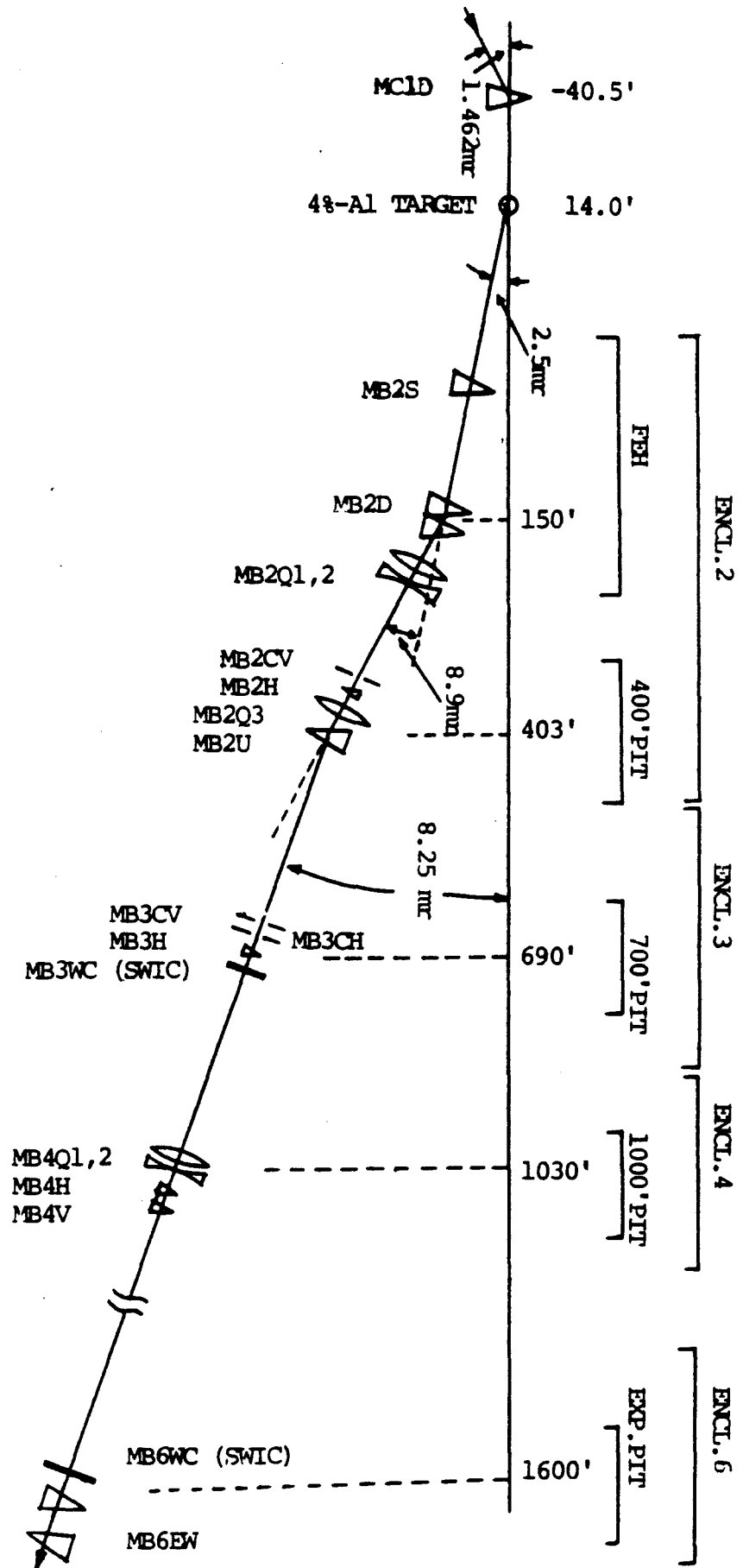


Figure 3.1 Schematic of the M-Bottom beam line.

2.5 milliradians. This beam angle was largely set by the septum character of the MB2S and MB2D magnets. They were specially built to get as close as possible to the primary beam direction. Clearly a crystal septum could get much closer so that secondary beam lines of smaller beam angles would be possible. This beam is deflected downward by 8.9 milliradians by the MB2D septum magnets for normal operation. The magnetic septum consists of two dipole magnets each 3.05 m long and operating at a maximum field of 9.6 kG at a momentum of 225 GeV/c. The septum magnets are located in enclosure-2 which is called Front End Hall (FEH). Because of the magnetic septum limit this beam line can not normally be operated at energies higher than 225 GeV.

Another vertical upward bending magnet (MB2U) at 400 feet downstream of the target brings the beam back at 8.25 milliradians relative to the horizontal direction and sends it through the M-Bottom beam line to the experimental location about 1600 feet downstream of the production target. Table 3.1 shows the component floor layout and gives a description of all the elements in the beam line.

The quadrupole triplet MB2Q1, MB2Q2 and MB2Q3 in the beam transport system gives the first stage of point to point focusing and momentum recombination at the horizontal (MB3CH) and vertical (MB3CV) collimators at an intermediate position about 600 feet from the production target. The second quadrupole doublet MB4Q1 and MB4Q2 gives the final point to point focusing and momentum recombination at the experimental location.

Table 4.1 M-Bottom component floor layout and their nominal values for 200 GeV secondary beam. 'B' in column six represents the magnetic fields of dipole magnets in kGauss and magnetic field gradients of quadrupole magnets in kGauss per inch. Respective current settings are shown in the last column.

Z	X	Y	ELEMENT	POWER	B/(KG)	CURR.
feet	inch	inch		SUPPLY	(KG/IN)	(AMPS)
-40.5	0.00	0.00	BENDING MAGNET	MC1D	16.000	880.0
-14.0	0.00	0.00	EPB 0.1%-4% TARGET	MBTGT		
94.3	0.00	-.27	R1 SEPTUM ELEC.MODE	MB2S		1400.0
133.4	0.00	-.37	PB CONV. ELEC. MODE	MB2MT		
138.5	0.00	-.39	SEPTUM MAGNET 4-2-123	MB2D	9.518	3210.0
155.4	0.00	-.51	SEPTUM MAGNET 4-2-123	MB2D	9.518	3210.0
192.5	0.00	-.92	NEUTRAL BEAM DUMP	MB2BD		
245.6	0.00	-1.53	QUAD 3Q120	MB2Q1	-3.145	60.3
256.6	0.00	-1.66	QUAD 3Q120	MB2Q2	4.125	79.0
379.5	0.00	-3.06	VERT COLLIMATOR	MB2CV		
384.2	0.00	-3.11	HORI VERNIER 4-4-30	MB2H		
392.0	0.00	-3.20	QUAD 3Q120	MB2Q3	-1.372	26.3
403.0	0.00	-3.32	EPB DIPLOE 5-1.5-120	MB2U	6.926	672.0
649.4	0.00	-5.36	VACUUM BEAM STOP	MB3BS		
656.8	0.00	-5.42	VERT COLLIMATOR	MB3CV		
661.7	0.00	-5.46	HORI COLLIMATOR	MB3CH		
691.0	0.00	-5.70	HORI VERNIER 4-4-30	MB3H		
665.7	0.00	-5.49	VACUUM SWIC	MB3WC		
1020.3	0.00	-8.42	QUAD 3Q60	MB4Q1	-3.882	74.3
1026.8	0.00	-8.47	QUAD 3Q60	MB4Q1	-3.882	74.3
1034.1	0.00	-8.53	QUAD 3Q60	MB4Q2	3.801	72.8
1040.6	0.00	-8.59	QUAD 3Q60	MB4Q2	3.801	72.8
1046.6	0.00	-8.63	HORI VERNIER 4-4-30	MB4H		
1050.1	0.00	-8.66	VERT VERNIER 4-4-30	MB4V		
1598.0	0.00	-13.18	AIR SWIC	MB6WC		
1700.1	-.01	-14.03	EPB DIPOLE 5-1.5-120	MB6EW	12.005	1165.0
1711.1	-.07	-14.12	EPB DIPOLE 5-1.5-120	MB6EW	12.005	1165.0
1761.1	-.60	-14.53	EPB DIPOLE 5-1.5-120	MB6EW	-12.005	1165.0
1772.5	-.66	-14.62	EPB DIPOLE 5-1.5-120	MB6EW	-12.005	1165.0

Figure 3.2 shows the beam optics of the M-Bottom beam line for a 200 GeV/c secondary beam. The solid lines are the paths of two rays which are starting from the target on the axis of the beam line with

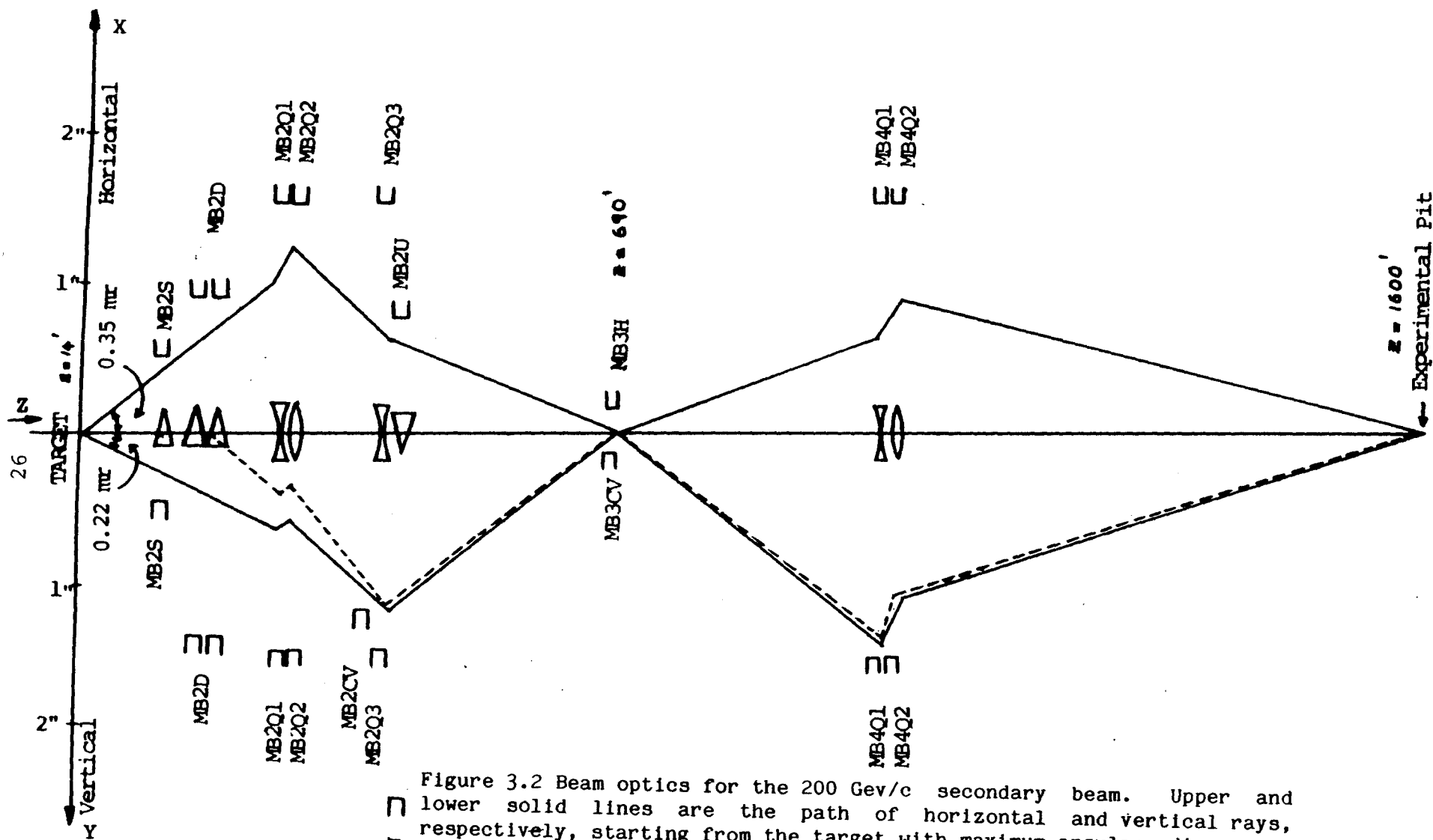


Figure 3.2 Beam optics for the 200 GeV/c secondary beam. Upper and lower solid lines are the path of horizontal and vertical rays, respectively, starting from the target with maximum angular divergence (on momentum off axis). The broken line is the momentum dispersion for a $\pm 4\%$ change in momentum (off momentum on axis). The apertures are drawn according to the scale.

maximum horizontal and vertical angular divergence of 0.35 and 0.20 milliradians, respectively. The maximum horizontal and vertical angular acceptance of the system is determined by the apertures of the MB2S dipole magnet and the quadrupole doublet (MB4Q1 and MB4Q2), respectively. The broken line shows the momentum dispersion for a $\pm 4\%$ change of momentum. The momentum dispersion is limited to $\pm 4\%$ by the vertical apertures of the MB4Q1 and MB4Q2 quadrupole magnets.

The MB2D and MB2U are the momentum selection magnets in regular operation. MB2D can only be operated up to 225 GeV/c while MB2U can be operated up to 500 GeV/c. In crystal septum operation (in the absence of MB2D), the MB2U dipole magnet would be the momentum selection magnet in the beam line and the maximum possible beam momentum would be 500 GeV/c. Four beam trim magnets (MB2H, MB3H, MB4H and MB4V) are available at different positions along the beam for beam position tuning.

3.3 Beam Tuning

The user has complete access to control all the elements in the beam line downstream of the production target through the beam line control system called Experimental Physics Interactive Control System (EPICS). For beam tuning the currents of all magnets (quadrupoles and dipoles) have to be set to their correct values for a given energy. These values are calculated by the computer program TRANSPORT (section 3.5.1) by requiring the necessary focusing and momentum recombination. The calculated currents of all magnets together with other devices and their specifications are stored in a file called

'PAGE FILE' for a given energy. Stored values of devices can be set at once by calling the 'PAGE FILE', using a control command. In addition to that, control commands can be used to change the device currents and collimator sizes. Fine adjustments can be done by tuning quadrupoles and verniers (trim magnets). Two segmented wire ion chambers (SWICs) MB3WC and MB6WC are located in the beam line at the first focus and the experimental pit to assist fine tuning. Horizontal and vertical beam profiles at the SWIC positions can be monitored at the end of each spill via a television screen in the control room.

3.4 Regular Secondary Beam Properties

The normal accelerator cycle time was 40 seconds and the spill time was 5 seconds (5 second flat top) during the 400 GeV/c operation of the accelerator. At 800 GeV/c operation the cycle time was the same and the spill time was 20 seconds (20 second flat top). The primary beam intensity at the production target is of the order of 1.0×10^{11} particles per spill. This primary beam produces about 1.6×10^9 π^+ particles per spill due to the interaction with the aluminum target (2.5 cm long). A π^+ production cross section of 12 millibarns was used in the above calculation. It was assumed that the total p-p cross section is 40 millibarns [18], 90% of the products is pions in the GeV range and one-third of the pions is π^+ . According to the empirical model given in reference [19], the secondary particle production yield at an angle θ per unit solid angle ($d\Omega$) per unit fractional momentum (dp/p) is given by

$$\frac{d^2N}{d\Omega dp/p} = A \left[\frac{B}{p_0} e^{-Bp/p_0} \right] \left[\frac{2Cp^3}{2\pi} e^{-C(p\theta)^2} \right] \quad 3.1$$

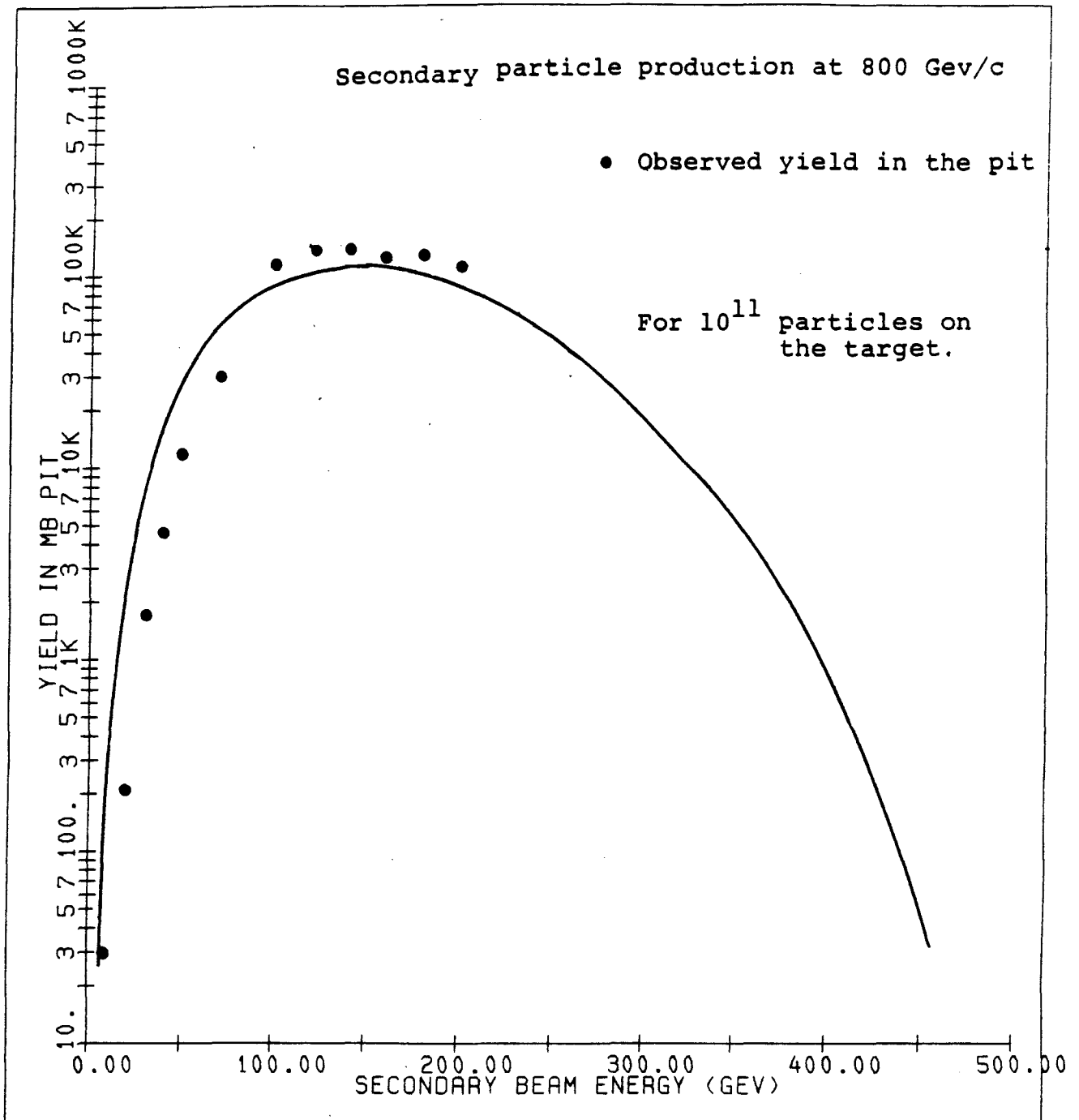


Figure 3.3 The circles represent the observed secondary particle yield in the experimental pit for 1.0×10^{11} particles incident on the target. The solid line is the calculated yield using the empirical formula given in equation 3.1.

where p_0 is the primary beam momentum in GeV/c, p is the secondary beam momentum in GeV/c and θ is the production angle. A, B and C are constants which depend on the kind of the particle and the primary energy. For π^+ production at 400 GeV/c, $A=1.2$, $B=9.5$ and $C=5.0$ are the best fit values for the above empirical formula from the experimental data in reference [19].

Figure 3.3 shows the observed yields in the experimental pit at 800 GeV/c primary beam momentum. The data was obtained over a range of secondary beam momentum in the M-Bottom pit. The 400 GeV/c values of A, B and C were used to calculate the yield at 800 GeV/c and the results are also shown in Figure 3.3. The flux was calculated over a solid angle of 0.2 microsteradian around the 2.5 milliradian production angle. The horizontal and vertical beam divergence of 0.35 and 0.20 milliradian, respectively, were used to calculate the solid angle of 0.2 microsteradian. Decay of π^+ has also been taken into account.

The Cerenkov detector located at the upstream end of the experimental pit was used to find the hadron composition in the beam. The primary beam momentum at the time was 400 GeV/c. Figure 3.4 shows threshold curves made at a beam energy of 200 GeV. The relative counts in the upstream counter in the Cerenkov chamber was plotted against the gas pressure of the chamber. Calculated hadron composition at this energy is about 27% protons, 61% pions and 2.1% kaons.

At 200 GeV/c the observed beam divergence is about 100 microradians (half width) in both horizontal and vertical directions and the beam size is about 1.0 inch in diameter.

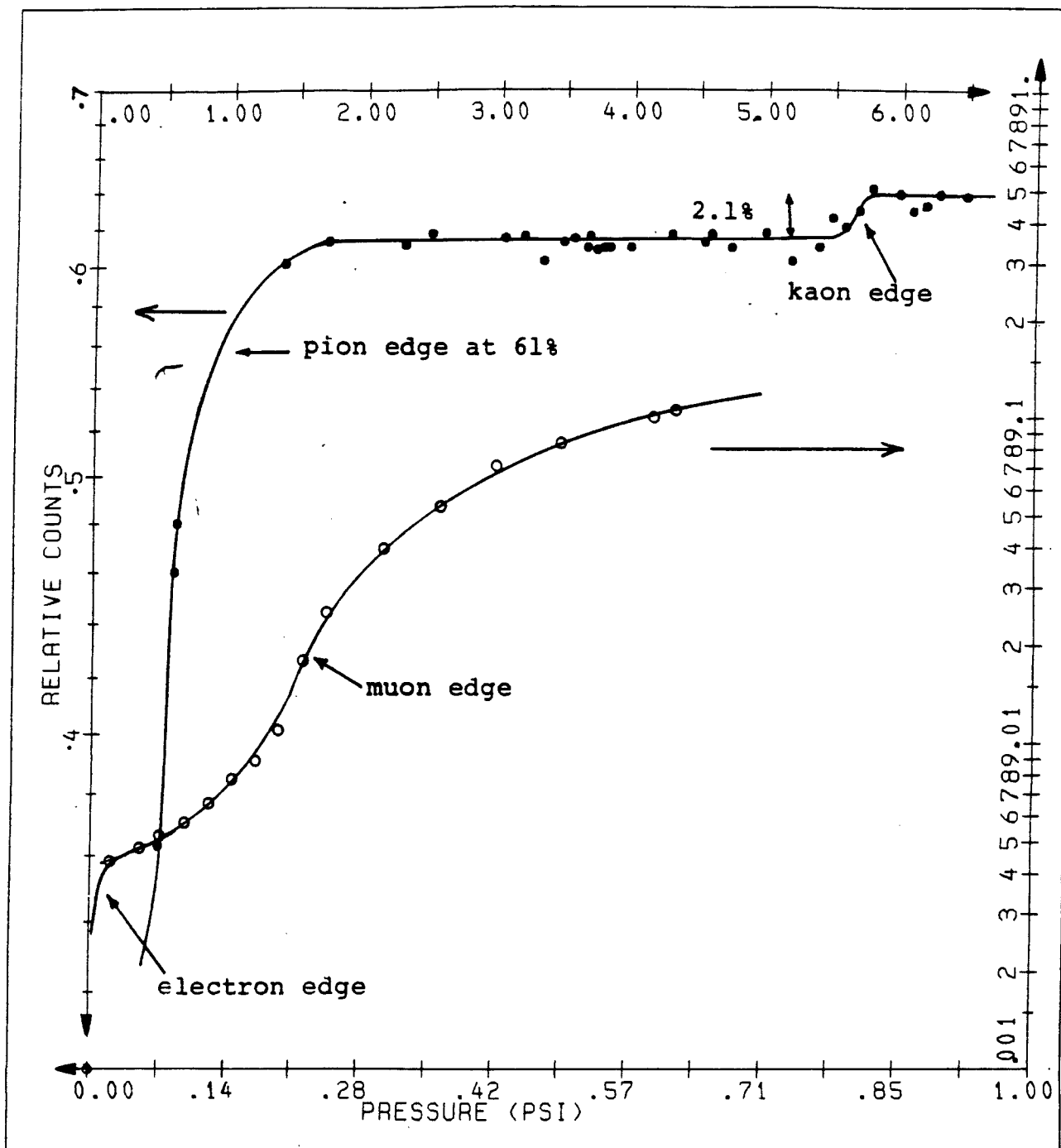


Figure 3.4 Cerenkov threshold curves at a secondary beam momentum of 200 GeV/c.

3.5 Calculation of Beam Element Parameters and Beam Characteristics

The following discussion covers the two programs that beam line designers use to calculate element parameters and characteristics when designing a beam line transport system. These two programs will be used in Chapter 7 to calculate beam parameters and to compare with the observed values. The input beam for the crystal septum mode will be discussed in section 7.3 of Chapter 7.

3.5.1 Computer Program 'TRANSPORT'

The computer program 'TRANSPORT' [20] is used to calculate the beam element parameters in a beam line transport system. This is a first and second order matrix multiplication program. At any position in the beam line an arbitrary charged particle is represented by a single column vector of six components which is called the 'coordinate vector'. These components are the horizontal and vertical positions and divergences, path length difference and fractional momentum deviation of the charged particle. Elements in a beam line such as dipole and quadrupole magnets and drift spaces are represented by square matrices (6x6) which are called 'transfer matrices'.

Passage of a charged particle through a component of the beam line is represented by the multiplication of transfer matrix and the coordinate vector. If X_0 is the coordinate vector of the input beam then the coordinate vector X_1 after passing through the first element is given by

$$X_1 = R_1 X_0$$

where R_1 is the transfer matrix of the first element. If there are n elements in the beam transport system with transfer matrices R_1, R_2, \dots, R_n then the coordinate vector at the end of the beam line is given by

$$X_n = R_n \dots R_2 R_1 X_0 \quad 3.3$$

Provision has been made to impose various constraints according to the need of the user when calculating the parameters in the elements of the beam transport system. These constraints are momentum recombination, horizontal and vertical focusing, horizontal and vertical parallel and so on. For an existing beam line, magnetic fields (e.g. quadrupoles) can be calculated according to the given constraints at any position of the beam. When designing a beam line the positions of magnets and collimators can also be calculated in order to get the desired characteristics of the beam one needs.

3.5.2 Computer Program 'DECAY TURTLE'

DECAY TURTLE (Trace Unlimited Rays Through Lumped Elements) is another computer program [21] designed to simulate charged beam transport systems. It allows one to examine chromatic aberration and the effects of nonlinearities in magnetic fields and to evaluate the effects of slits and apertures. In DECAY TURTLE, provision has been made to include particle decay, following the parent particles and up to two kinds of daughter particles through the beam line. In order to use the DECAY TURTLE program one has to calculate the The number of rays one wishes to run through the system can be set in the input data. The beam phase space of these arbitrarily generated rays can be

examined at any point in the system. The distributions of components of the coordinate vector can be represented by one or two dimensional histograms.

CHAPTER 4

EXPERIMENTAL SET UP IN THE M-BOTTOM PIT

4.1 Introduction

The purpose of this chapter is to discuss the basic experimental set up used in the M-Bottom experimental pit, located at the downstream end of the beam line. This set up has been used for the following parts of this experimental program

1. aligning the septum crystal before installation,
2. setting up the correct bend angle in the septum crystal,
3. studying the through-put of the septum crystal at different energies,
4. studying scanning techniques and
5. studying the feeding-in and dechanneling properties of unbent crystals made with several detectors.

Chapter 5 deals with the bend angle set up and the through-put studies of the septum crystal. Crystal alignment and scanning techniques will be discussed in Chapter 6. Feeding-in and dechanneling studies will be examined in Chapters 8 and 9.

Apparatus set up, detectors and data acquisition will be discussed in this chapter. A detailed description of the detectors can be found in reference [11].

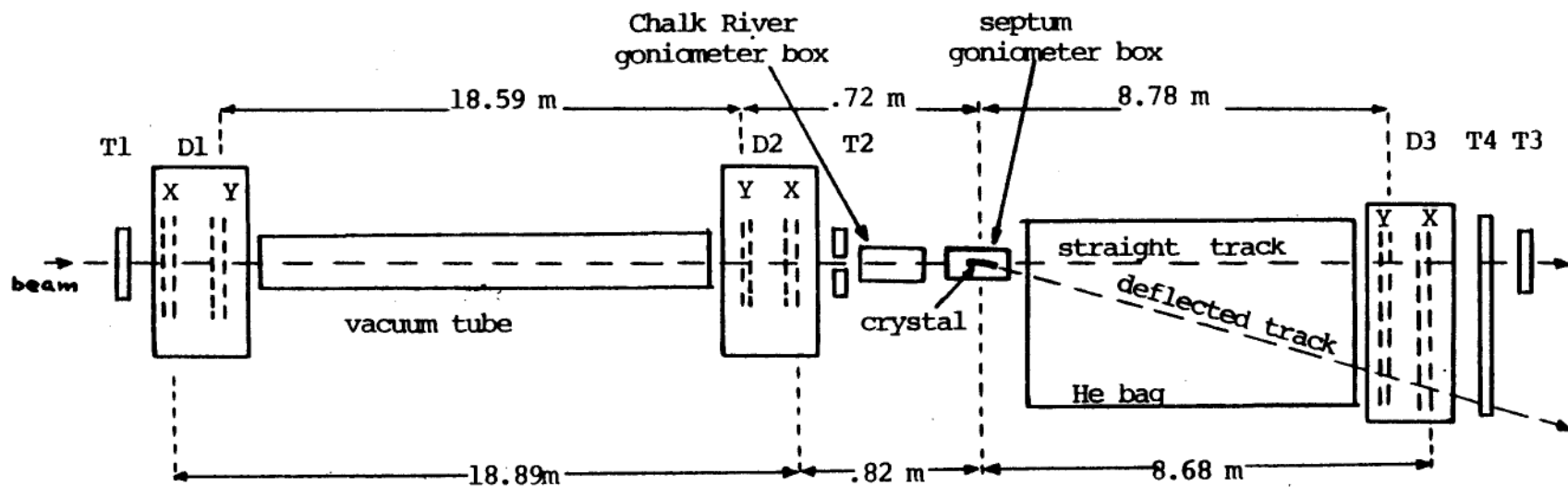


Figure 4.1 Experimental set up used in M-Bottom pit for the crystal studies. Upper numbers indicate the distances between Y sense wire planes of drift chambers and lower numbers for X sense wire planes.

4.2 Apparatus Set Up

Figure 4.1 shows the schematic of the apparatus set up which was located in the upstream end of enclosure-6 (the experimental pit) of the M-Bottom beam line. D1, D2 and D3 are three drift chambers and T1, T2, T3 and T4 are four scintillation detectors. Detector T2 has a hole of 1.0 mm by 5.0 mm and has been used as a veto to the trigger system to require particles passing through the crystal. Very close to the downstream end of the drift chamber D2 is the Chalk River goniometer box which was used for feeding-in and dechanneling studies. Next to this is the septum stand.

A vacuum pipe between D1 and D2 and a helium bag between the crystal and D3 were used to reduce the multiple scattering of particles in the range where the measurements were taken. Without the helium bag the angular width of multiple scattering is 15 microradians and with the helium bag it reduces to 2.6 microradians, leading to 26 micrometers resolution at drift chamber D3 at 200 GeV/c. The angular width due to the multiple scattering is inversely proportional to the momentum of the particles.

4.2.1 Drift Chambers

Each drift chamber has two horizontal sense wire planes and two vertical sense wire planes to measure y and x coordinates, respectively, of the charged particle tracks as shown in Figure 4.2. Each sense wire (anode wire) is surrounded by a set of cathode wires. Figure 4.3 shows a drift chamber wire plane of two sense wires. High voltages are applied to field wires to produce the electric field

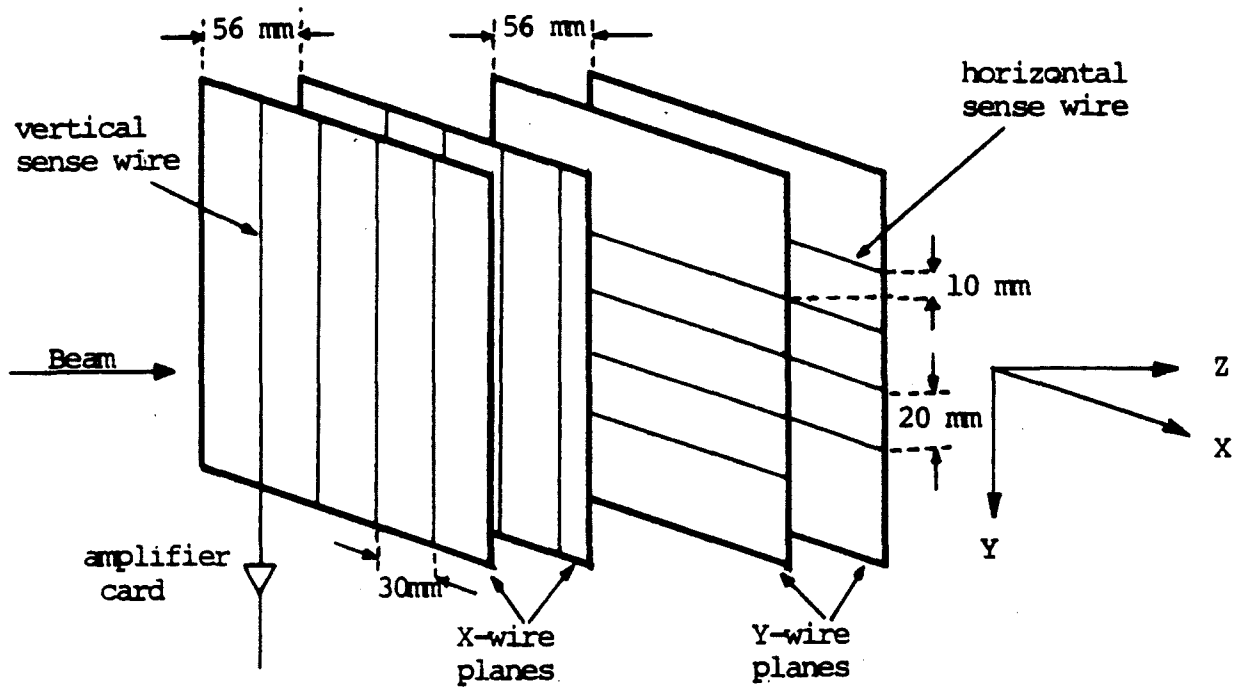


Figure 4.2 Schematic diagram of the two X and two Y planes in a drift chamber module. The signal (sense) wires are shifted by half of the distance between them in alternative planes.

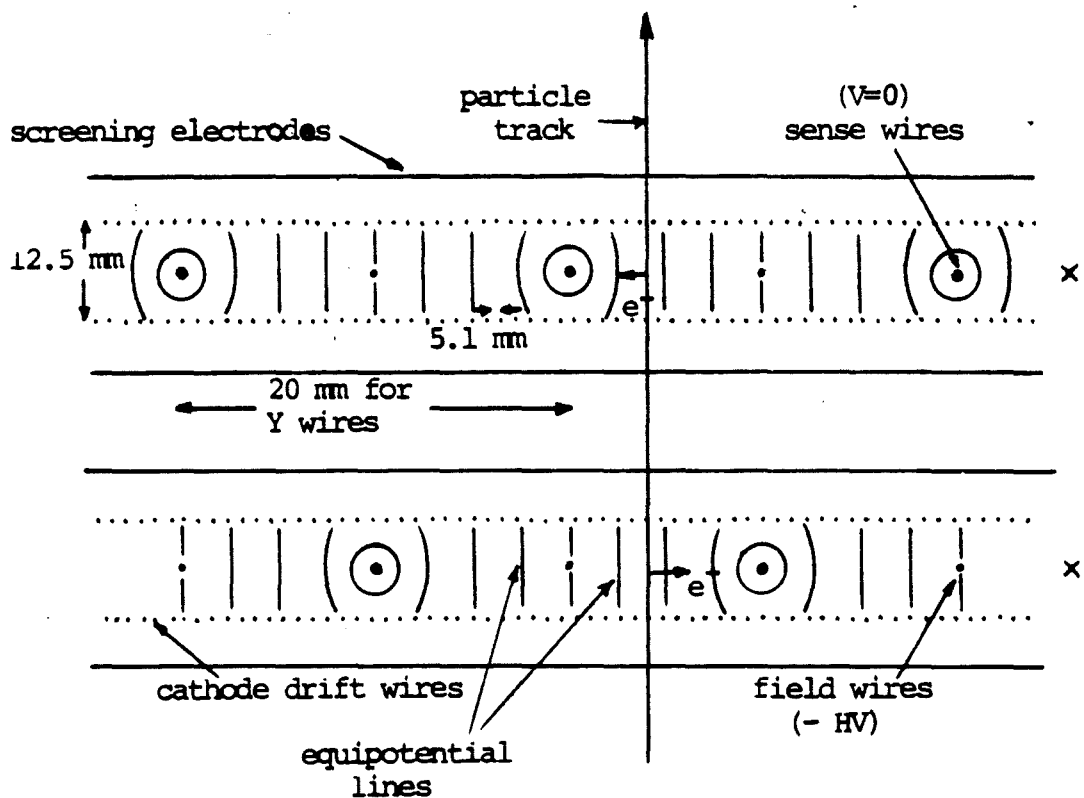


Figure 4.3 Two wire planes of a drift chamber module showing the relative positions of the sense wires. All the wires are perpendicular to the paper and the beam direction is upward. The equipotential surfaces are also shown.

necessary to collect the charges produced by ionization. Cathode wires are connected to uniformly decreasing potentials starting from ground in front of the anode. The equipotential surfaces are shown in Figure 4.3. A gas mixture of 50% argon and 50% ethane bubbled through ethyl alcohol at atmospheric pressure was made to flow through the drift chambers for better ionization and collection [22,23,24,25].

Passage of a charged particle ionizes the gas molecules and creates electrons and ions. These electrons are drifted towards the nearest sense wire (anode wire) by the electric field surrounding it as shown in Figure 4.3. Multiplying the time of flight by the drift velocity, the distance to the track of the charged particle from the corresponding sense wire can be found. An independent measurement of the drift velocity had been done in the previous experiment [11] and the measured value of 0.0505 mm/ns will be used in calculations.

The time of flight is measured by an electronic unit called 'Time to Digital Converter' (TDC- LeCroy model 2228A, 8-channel). Collection of the charged particles creates an electric signal at the sense wire. Each sense wire signal is amplified by a separate amplifier circuit to an analog signal of -5.0 Volts. These signals are sent to separate channels of several TDC modules in the CAMAC crate through low impedance cables. These units start counting when a fast coincidence (section 4.3) occurs in the logic (corresponds to the time at which the ionization is produced), stop when the sense wire signal reaches the unit (corresponds to the time at which the charge is collected at the sense wire) and convert the time difference to a digital number. All the channels of all the TDC units were calibrated for zero counts and

conversion factors (counts to time). The zero count is defined as the digital number that the TDC unit registers if an ionization occurs right next to the sense wire. The conversion time of a TDC channel is about 100 nanoseconds and the time resolution is of the order of 0.5 nanosecond. Details of the TDC calibration are given in reference [11].

Table 4.1 Drift chamber parameters.

Draft Chamber	Number Wires /pln	Wire Separ. mm	Operating High Voltage	Efficiency		Resolution μM
				Jan. run	June run	
D1	x = 4	30.2	3400	87%	93%	200
	x' = 4	30.2	3500	84%	88%	
	y = 4	20.0	3000	68%	91%	300
	y' = 4	20.0	3050	65%	91%	
D2	x = 4	30.2	3200	95%	93%	300
	x' = 4	30.2	3200	93%	95%	
	y = 4	20.0	3200	94%	96%	300
	y' = 4	20.0	3200	96%	96%	
D3	x = 11	60.4	4350	61%	92%	500
	x' = 10	60.4	4450	78%	95%	
	y = 11	20.4	2850	87%	92%	250
	y' = 10	20.4	2850	86%	94%	

The minimum time difference between two successive events that the drift chamber can resolve is of the order of 100 nanoseconds. The event rate of the experiment is of the order of 1.0×10^6 per second which is well within the time resolution of the detectors.

The operating high voltages were established by making voltage curves as shown in Figure 4.4. The percentage of single hits for each

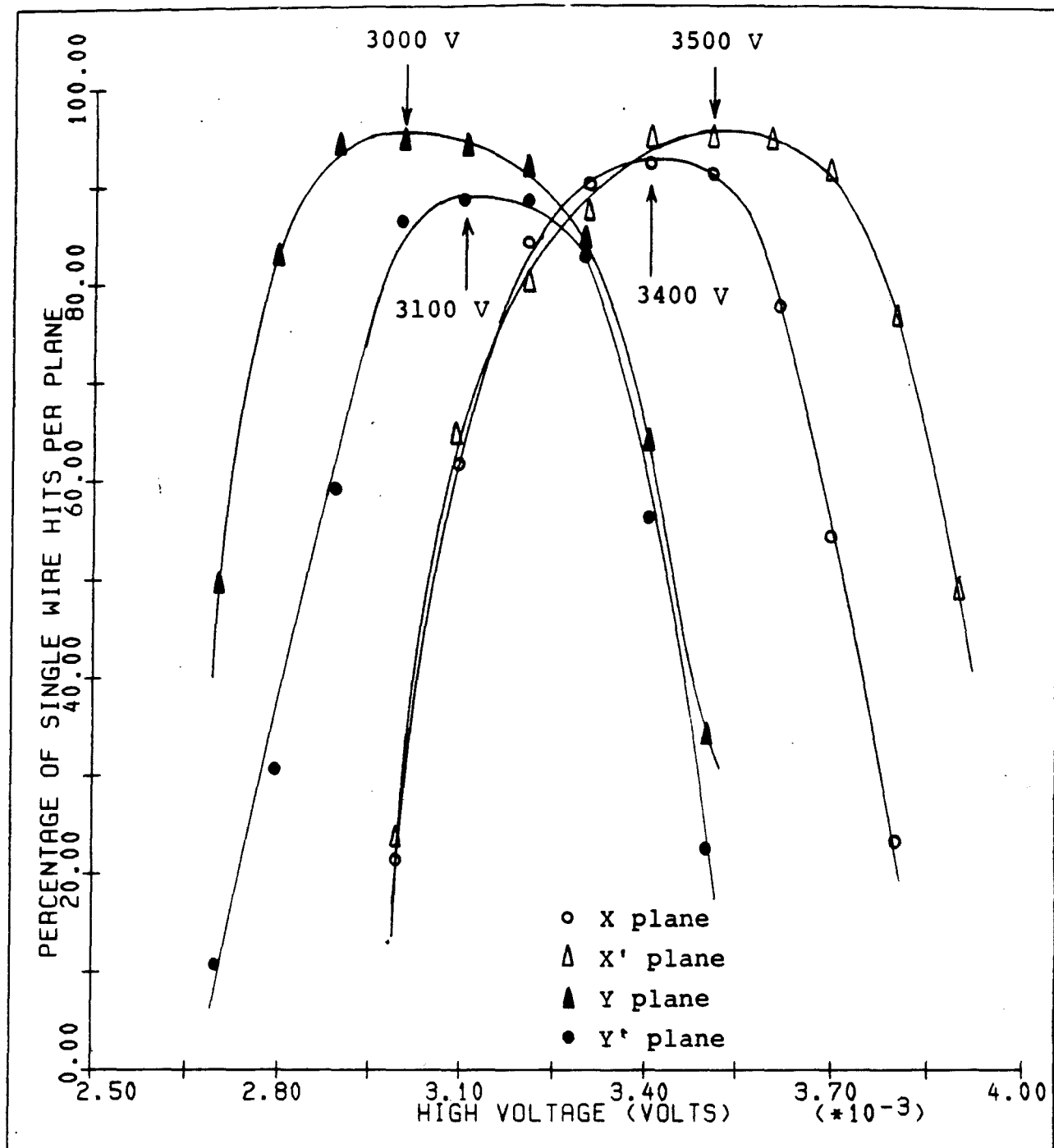


Figure 4.4 Voltage curves of drift chamber D1. The percentage of single hits per plane were plotted against the applied high voltage.

wire plane is plotted against the applied high voltage. Table 4.1 shows the sense wire configuration, operating high voltages, efficiencies and resolution of sense wire planes. The efficiency of a wire plane was defined as the percentage of single wire firings. The overall good event percentage in the January run was 10% and the June run was 42%. A good event was defined as an event which has one wire fired in all twelve drift planes. The January run was for the septum crystal through-put studies and June run was for the feeding-in studies.

4.2.2 Scintillation Detectors

The basic principle of a scintillation detector [26,27] is the following. When a charged particle passes through the detector, electrons in the scintillation material get excited. When they decay to the ground state, photons are emitted. The photomultiplier tube collects this light and produces an electrical signal proportional to the amount of light collected, by electron multiplication in a series of dynodes. Figure 4.5 shows the base circuit used to operate the photomultiplier tubes. This signal is transferred to the fast logic by cables with 50 ohm impedance. The cable lengths have been adjusted such that all signals due to a beam particle passing through all three detectors, reach the coincidence unit in the counting room at the same time. The fast coincidence for the computer trigger is selected from these scintillation detector signals. Normally, scintillation detectors have resolution of the order of a few nanoseconds.

Table 4.2 shows the dimensions of all the scintillation detectors

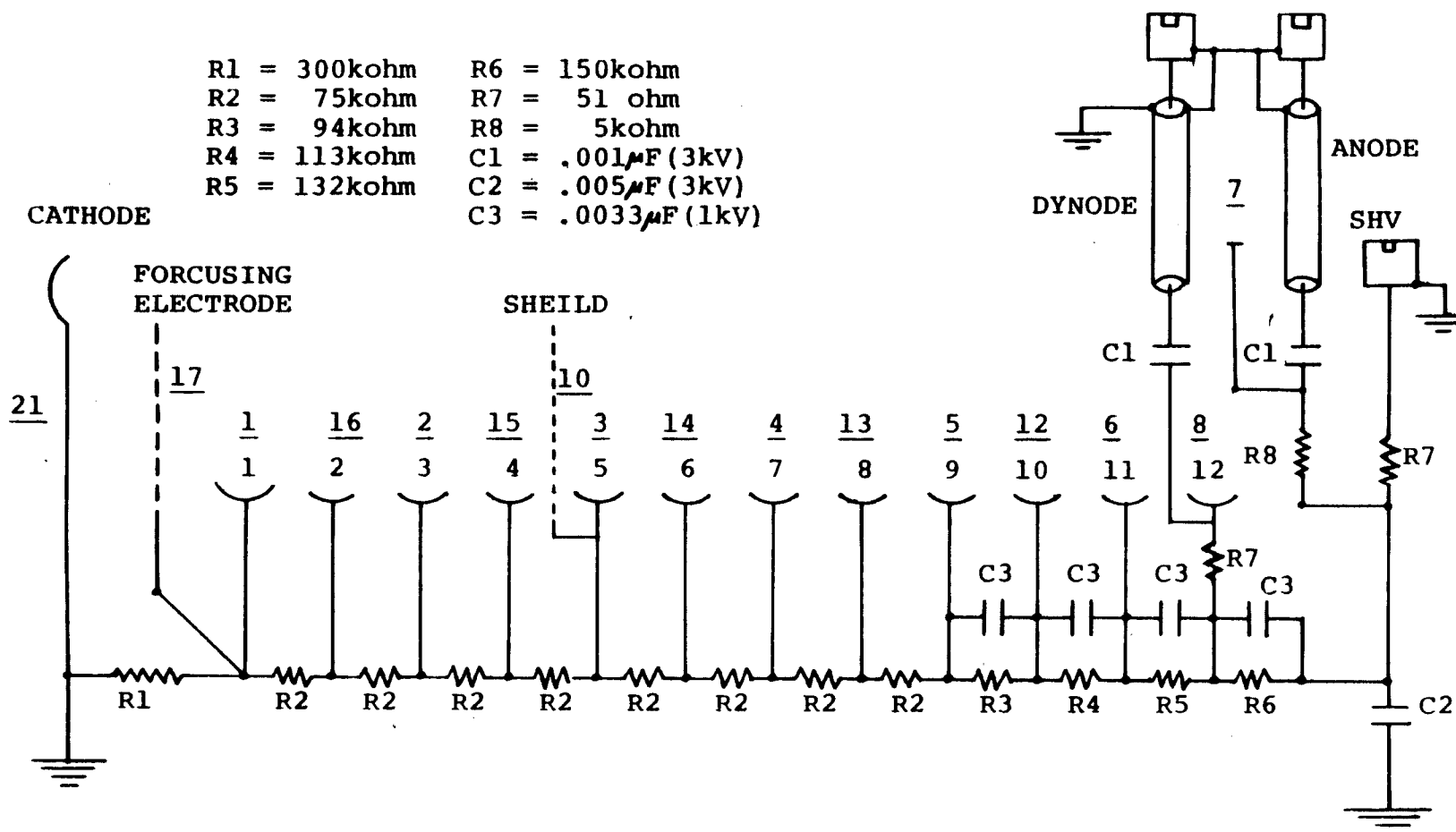


Figure 4.5 Photomultiplier base circuit used in scintillation detectors. The underlined numbers indicates the pin numbers of the photomultiplier tube (RCA 8575).

used and corresponding photomultiplier tube high voltages. The high voltages of the photomultiplier tubes have been set to their optimum values by making voltage plateau curves.

Table 4.2 Scintillation detector parameters

Scintillation Detector	Dimension mm×mm	High Voltage
T1	50x50 (2"x 2")	+1460
T2	50x50 (2"x 2") (1.x 5. mm hole)	+1420
T3	50x50 (2"x 2")	+1420
T4	178x710 (7"x 28")	-1620
T5	2 x 2 mm	+1500
T6	50x50 (2"x 2")	+1450
T7	2 x 2 mm	+1500

4.2.3 Surface Barrier Semiconductor Detectors

The silicon crystal used for the septum application had a surface barrier semiconductor detectors [28] incorporated directly in the crystal to measure the energy loss of the charged particles passing through the detector. The detector is a diode consisting of an extremely thin (less than one micrometer) p-type layer on the sensitive face of the n-type silicon crystal. The two electrical contacts to this diode are made (1) to the p-type surface through a thin (approximately 40 $\mu\text{g}/\text{cm}^2$ thick) gold film and (2) to the n-type silicon on the back surface through a non-rectifying aluminum metal contact.

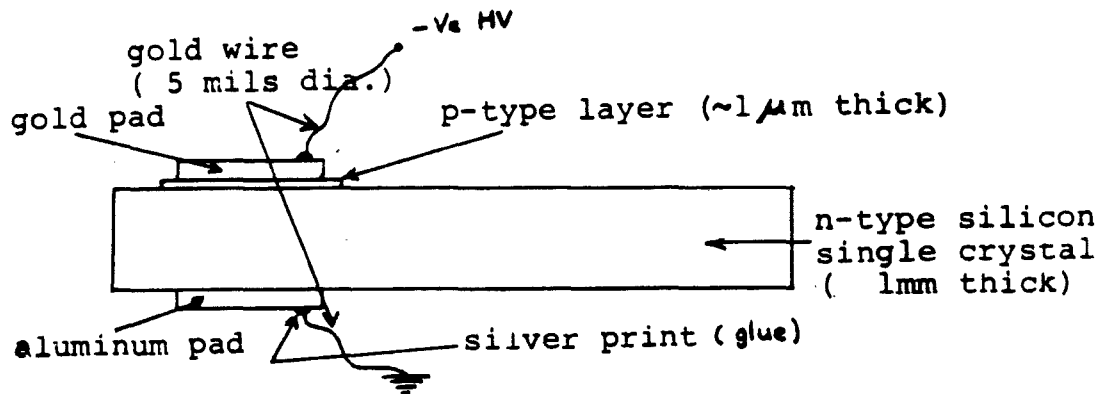


Figure 4.6 Schematic diagram of a crystal with a surface barrier semiconductor detector. The electrical contacts to the diode are made through the gold and aluminum pads. Aluminum side is grounded and a reverse bias voltage (negative) is applied to the gold side to operate the detector.

The schematic of a typical crystal with a detector is shown in Figure 4.6.

The description of detector operation is as follows. When a charged particle passes through the detector it loses energy by creating electron and hole pairs at a rate of 3.6 electron volts per electron-hole pair for silicon and 2.9 electron volts for germanium. When a reverse bias voltage is applied externally to the electrodes (aluminum grounded and negative voltage on gold), electrons and holes are attracted towards opposite electrodes under the influence of the electric field. For silicon the minimum bias voltage necessary to deplete the detector can be calculated from the following equation

$$t = 0.5(P_n V_b)^{\frac{1}{2}} \quad 4.1$$

where P_n is the room temperature n-type resistivity in ohm/cm, V_b is the applied bias in volts and t is the thickness of the detector. The resulting net current represents the energy loss of the charged particle passing through the detector. The charge collection by the gold electrode which gives a negative pulse signal is amplified by a preamplifier at the first stage. Figure 4.7 shows the electronic set up used for crystal detector signal amplification.

The fast signal is generated by the Timing Filter Amplifier as soon as the charge collection has been started by the detector. This signal was used to trigger the data acquisition system. The amplifier signal is very slow (about 2 microseconds latter) and its pulse height is proportional to the total charge collected. This signal was used for energy loss information for charged particles passing through the

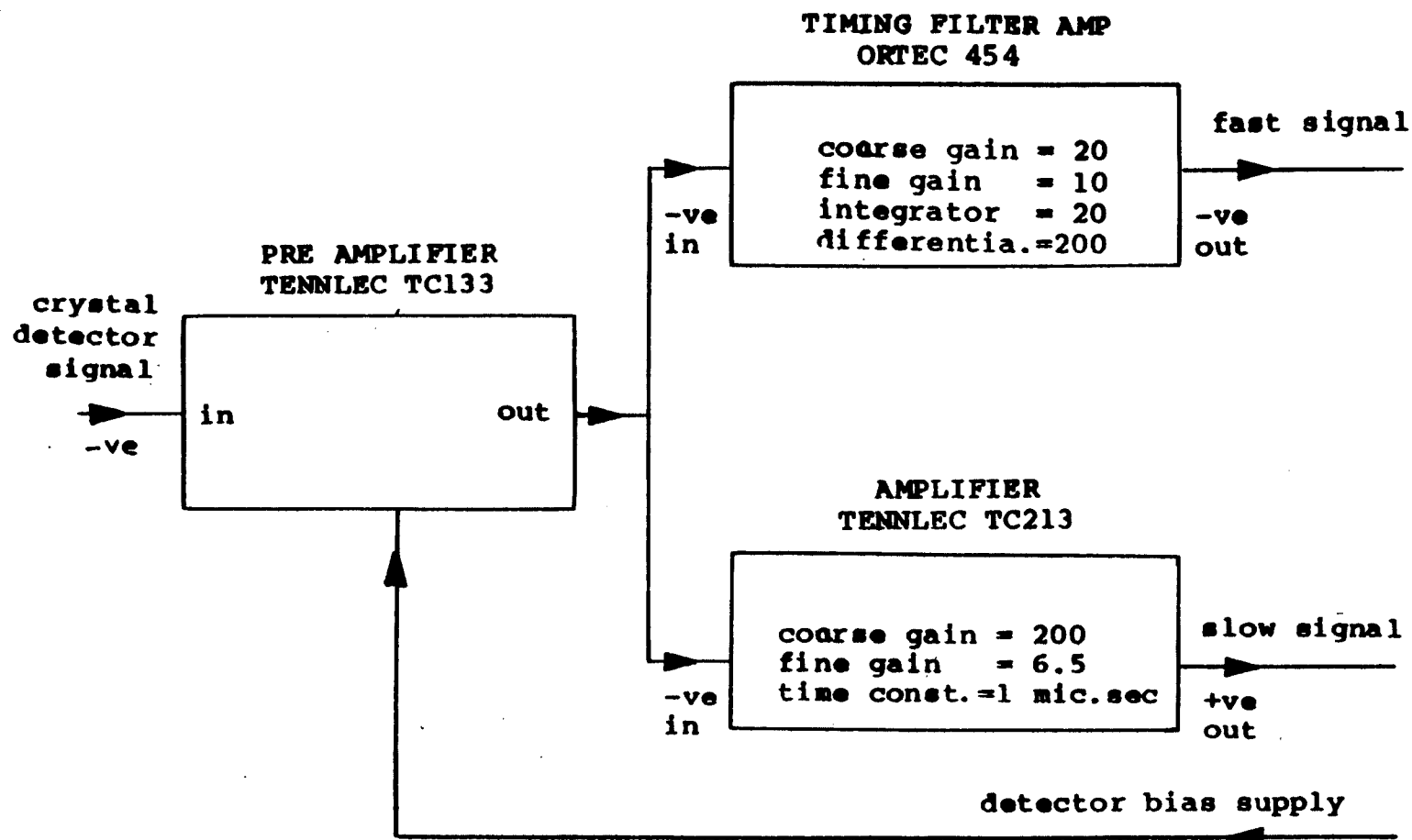


Figure 4.7 Electronic set up used to amplify the crystal detector signal. Fast signal was used for data triggering and slow signal was used for energy loss information of beam particles.

crystal at the detector.

The pulse height of the slow signal is converted to a digital value by a CAMAC unit 'Analog to Digital Converter' (ADC- Ortec model AD811, 8-channel).

4.3 Trigger System

Figure 4.8 shows the block diagram of the fast and slow logic of the trigger system used for

1. Drift chambers only mode.
2. Drift chamber and crystal mode.
3. Crystal scan mode.

The trigger system was developed to accomplish all three modes in one logic system. The "drift chamber only" mode was used without the crystal for alignment of scintillation detectors and drift chambers. The event trigger is produced by the coincidence of the fast trigger counters T1 and T4.

The second "drift chamber and crystal" mode was used for data acquisition. Scintillation detector signals and the crystal fast signal were used to trigger the detection system on particles through the crystal. The coincidence signal was $T1 \cdot \overline{T2} \cdot T4 \cdot X$, where X denotes the crystal fast signal and $\overline{T2}$ denotes the anti-coincidence of the T2 signal. TDC counts of drift chamber sense wires, the ADC value as well as counts of the crystal detectors and several scaler values were recorded for each event.

The "crystal scan" mode was used to trigger the system when scanning crystals to locate the planes or axes. In scanning only upper

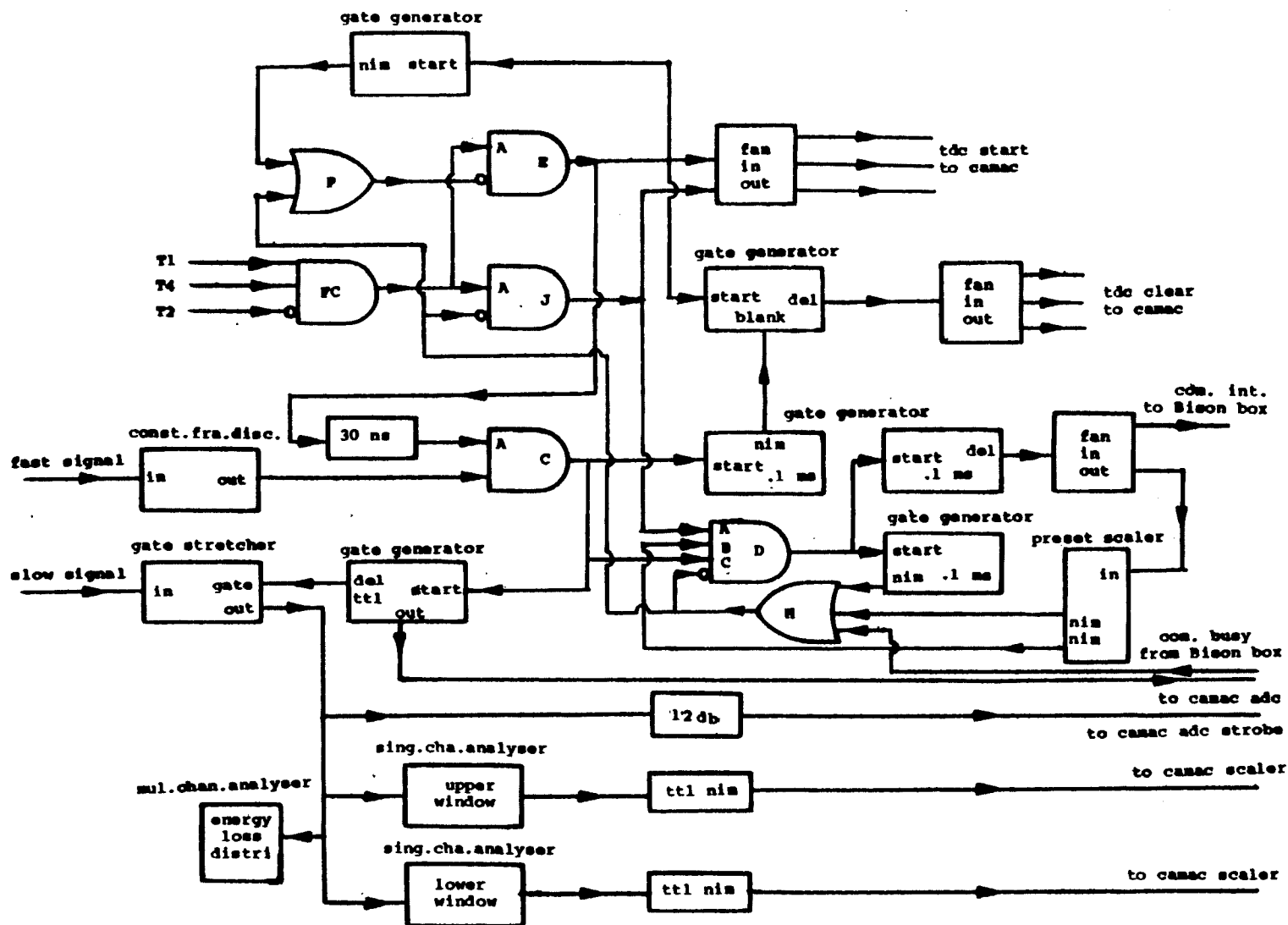


Figure 4.8 Logic diagram of trigger system used for data acquisition and scanning of crystals.

window counts, lower window counts and crystal orientation are recorded. The trigger used for scanning was $T1.\overline{T2}.T4.X$. Window settings and different triggers used for scanning will be discussed in Chapter 6. Table 4.3 gives the changes to be done in the fast logic when switching modes in the trigger system shown in Figure 4.8.

Table 4.3 Changes need to be done in the fast logic when switching modes of the event trigger.

1. Drift chamber only mode
 - a. select fast coincidence in unit 'FC'
 - b. disable input 'A' of unit 'E'
 - c. enable input 'A' of unit 'J'
 - d. enable only input 'A' of unit 'D'
2. Drift chamber and crystal mode
 - a. select fast coincidence in unit 'FC'
 - b. enable input 'A' of unit 'E'
 - c. disable input 'A' of unit 'J'
 - d. enable only input 'C' of unit 'D'
3. Crystal scan mode
 - a. select fast coincidence in unit 'FC'
 - b. enable only input 'B' of unit 'D'
 - c. disconnect unit 'H' input from preset scaler
 - d. connect upper window counts to input of preset scaler
 - e. connect computer busy TTL gate to 'reset' of preset scaler

4.4 Data Acquisition System

Figure 4.9 shows the block diagram of the data acquisition system. The computer was a PDP-11/34 processor with 28K words of core memory and 100K words of upper memory. Other peripheral devices used were

1. user terminal to communicate with the computer (decwriter 11 - Digital Equipment Corporation),
2. line printer for hard copies (Versatec - Xerox Company),
3. graphic display screen for online histogram and scatterplot displaying and updating (Tektronix 611),
4. magnetic tape to store the data (decmagtape TU 10 9-channel - Digital Equipment Corporation) and
5. disc drive with RK05 disk which has the data acquisition program. (decpack RK05 - Digital Equipment Corporation)

All the event information is sent to the corresponding TDC, ADC, or scaler registers in the CAMAC crate. Each event contains 74 TDC words from all drift chamber wires, and ADC word from the crystal detector pulse height and several scaler values (one word in PDP-11 is 16 bits).

The CAMAC unit is basically a register-control unit which communicates with the computer through an interface called the BISON box (Fermilab computer document HN-3) developed at Fermilab. When an event interrupt is given to the BISON box from the logic system, it enables the computer to read all pre-defined registers of CAMAC unit into the computer memory in order to transfer them to magnetic tapes or to analyze them on-line. The corresponding CAMAC registers are defined in the file 'CAMAC.DEF' (Fermilab computer document PN-110). The data

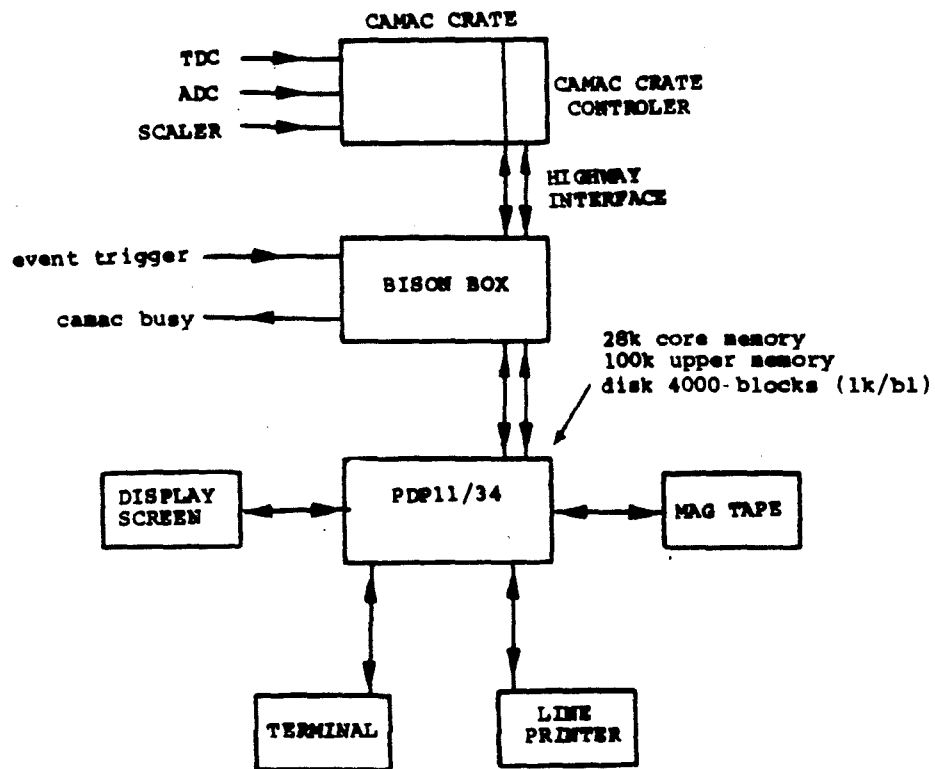


Figure 4.9 On-line data acquisition, system.

logging rate by the computer was about 100 events per second (an event was about 80 sixteen bit words). The limiting factor of the data acquisition rate is the computer busy time which is about 1.2 milliseconds.

MULTI is the computer program used for data acquisition and analysis on PDP-11 computer system which was developed to satisfy the basic requirements needed for high energy experiments. User written analysis programs can be added and the 'MULTI' program can be rebuilt according to the requirements of the experiment. The utility programs are available in the Fermilab computer department. ('MULTI system generation' in document PN-98 and 'MULTI programing references' in document PN-106). This is a FORTRAN-BASED program having well defined interfaces through which it obtains data for analysis, logs the data into magnetic tapes, performs user data analysis and makes graphic displays. The basic algorithm in the user routine is the construction of the incident and outgoing tracks of the particles.

The basic constants necessary to calculate the coordinates are stored in the file INIT.MCM. When MULTI is loaded the initialization sequence includes reading the files CAMAC.DEF, INIT.MCM and other user defined histogram definition files. The basic commands described in the document PN-97.5 are used to control on-line data acquisition program via the user terminal.

CHAPTER 5

CRYSTAL SEPTUM

5.1 Introduction

The purpose of this chapter is to discuss the following.

1. the crystal septum and the control system.
2. setting the correct bend angle of the crystal.
3. through-put studies of the septum crystal.

The septum magnets steer the beam by 8.9 milliradians downward. This bending angle can normally be adjusted by changing the magnet currents. But in the case of the crystal septum we did not have the remote control bending angle adjustment. Once the crystal was installed frequent access to the Front End Hall (FEH) was not permitted. Therefore it was necessary to set the correct bend angle prior to the installation of the crystal septum. The experimental set up discussed in Chapter 4 was used to set the 8.9 milliradians bending angle. After that, through-put studies of the septum crystal were carried out at different energies.

5.2 Crystal

A silicon crystal 0.8 mm thick, 12.0 mm wide and 27.0 mm long with a surface barrier semiconductor detector fabricated near the upstream end of the crystal was used in this application. The crystal with the

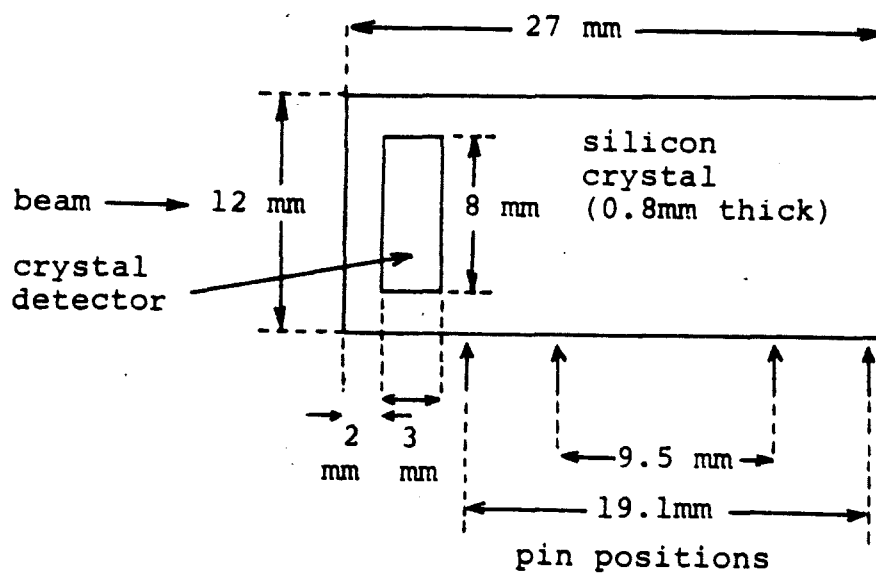


Figure 5.1 Silicon crystal used in septum application to bend the beam in M-Bottom beam line. A surface barrier semiconductor detector was fabricated on the upstream end of the crystal and a (110) plane is parallel to the major face of the crystal.

detector which covers an area of 3.0 mm by 8.0 mm, is shown in Figure 5.1. The crystal was cut such that (110) plane was nearly parallel to the major face of the crystal slab. This silicon crystal was supplied to Fermilab by CERN, Switzerland.

When selecting the correct crystal one has to think about the following:

1. the crystal plane which has a higher angular acceptance, and
2. the material which gives a higher bending fraction.

Table 5.1 shows some calculated critical angles for different crystal planes and axes of different materials at several energies. These values have been calculated by using equation 2.6 for the planar case and equation 2.7 for the axial case. Ellison [13] has numerically calculated the dechanneling fractions for different crystal planes for different bend radii as a function of a universal variable $\Gamma (= pvk/2\pi Z_1 Z_2 e^2 N)$. Figure 5.2 shows the comparison of dechanneling fractions for tungsten (110) and silicon (111) planes. Crystals of higher atomic numbers have higher bending fractions and angular acceptances for a given energy and bent angle as shown in Table 5.1 and Figure 5.2.

The critical angle and dechanneling length are larger for axial channeling than planar channeling for a given energy. Nevertheless planar ~~channeling~~ was chosen here because in the axial case particles are fed into many planes which are bent in different directions and result in different total bend angles [10]. Further, the angular acceptance perpendicular to a plane is infinite and the crystal only needs to be aligned in one direction in the planar case. The septum

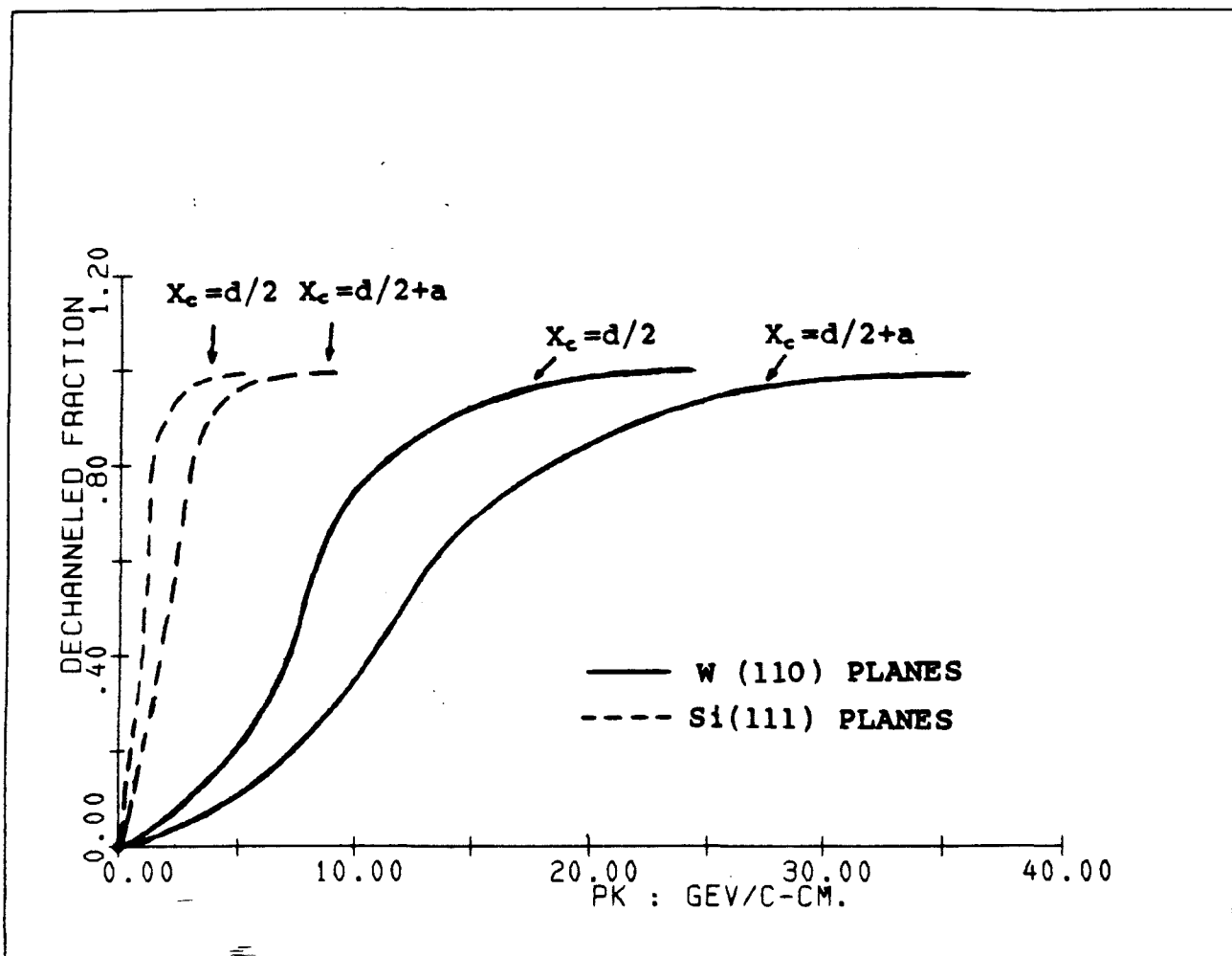


Figure 5.2 Plot of dechanneled fraction versus pk for protons incident on the (111) plane of silicon and the (110) plane of tungsten obtained from reference [13], where p is the momentum and k is the curvature of the bend. Two curves for each case are drawn for $x_c = d/2$ and $x_c = d/2 + a$, where ' d ' is the interplanar spacing, ' a ' is the screening distance and ' x_c ' is the critical distance of approach. The dashed lines are the weighted averages of the si (111) wide and narrow planes.

crystal is needed to be aligned in the experimental pit in order to set the correct bending angle prior to the installation in FEH. A crystal with a detector is easier to align in the experimental pit by using the familiar energy loss scanning method (Chapter 6). As far as the physics is concerned, the results of silicon crystal can be scaled to other materials. For the future it is important to pursue other materials such as germanium and tungsten. However the availability of silicon crystals and the fact that germanium had to be cooled in order to get the detector working and tungsten is not a semiconductor material in order to have a surface barrier detector, we were limited to use silicon crystals.

Table 5.1 Critical angles in microradians for different planes and axes of different materials at 100 GeV. Since critical angle scales as $1/\sqrt{p}$ where p is the momentum one can calculate it for any given energy. For fcc-diamond (111) planes 'n' and 'w' represent the narrow and wider planes respectively.

Material	Planar critical angle (μ r)			Axial critical angle (μ r)			
	(100)	(110)	(111)	$\langle 100 \rangle$	$\langle 110 \rangle$	$\langle 111 \rangle$	$\langle 112 \rangle$
Si(z=14) fcc-diam.	13.3	15.8	10.1n 17.5w	38.5	45.8		41.5
Ge(z=32) fcc-diam.	16.7	19.9	12.7n 22.0w	57.1	67.9		61.3
W(z=74) (bcc)	28.3	33.6	21.4	116.00	97.6	124.7	
Pt(z=78) (fcc)	27.5	32.7	35.2n	107.10	127.3	81.3	

5.3 Bending Device

A four point bending device was used for crystal bending. Figure 5.3 shows the bending device and the crystal mounted on it with the detector outside the pin region. So far there is experience with three point and four point bending devices. In both cases in addition to the forward peak and fully deflected peak, there is a prominent peak due to the center pin for the crystal bent by a three point bender and two small but significant peaks due to the two center pins for the crystal bent by a four point bender [11,15,30,31]. These peaks correspond to dechanneled particles due to the local distortion of the crystal at the pin positions. This effect was examined in detail as the local curvature effect in references [11] and [30].

The stress per unit length (along the width) on the crystal due to the pins of the four point bender can be derived using the theory of elastic bending of beams, as

$$p = \frac{E}{3(1-\nu^2)} t^3 \frac{\theta}{(L^2-b^2)} \quad 5.1$$

where E is the Young's modules, ν is the Poisson ratio, t is the thickness, L is the distance between outer pins, b is the distance between center pins and θ is the bend angle. Note here for $t \ll h$, E is replaced by the effective modules $E/(1-\nu^2)$ [32], where h is the width of the crystal. Figure 5.4 shows the stress on the crystal by the pins of a four point bender as a function of b/L. For the crystal septum four point bender of L=19 mm and t=0.8 mm (shown in Figure 5.3) the calculated stress on the crystal for 8.9 milliradians is 0.85×10^6 dynes/cm. assuming $E=1.3 \times 10^{10}$ dynes/cm² and $\nu=0.386$ for silicon. The

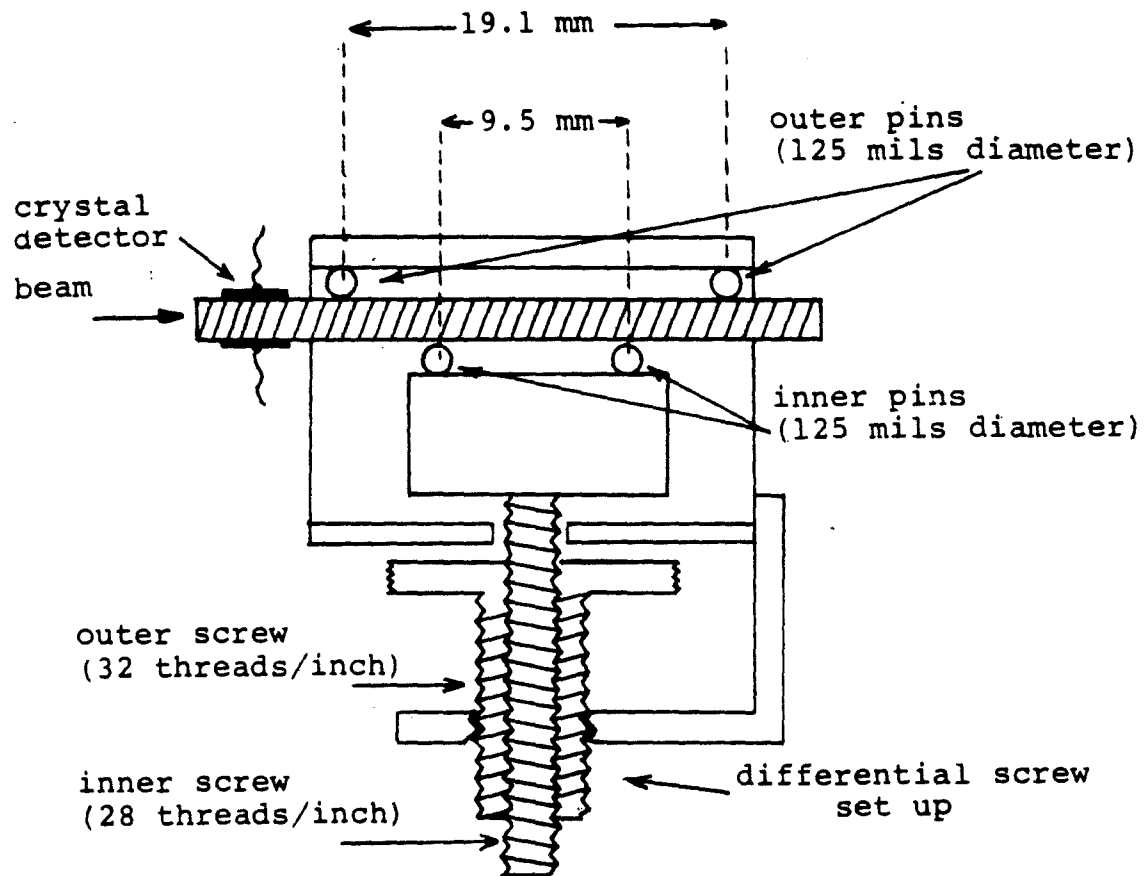


Figure 5.3 Crystal bending device. By turning the differential screw the inner pins can be moved up or down with respect to the outer pins to change the bending angle of the crystal.

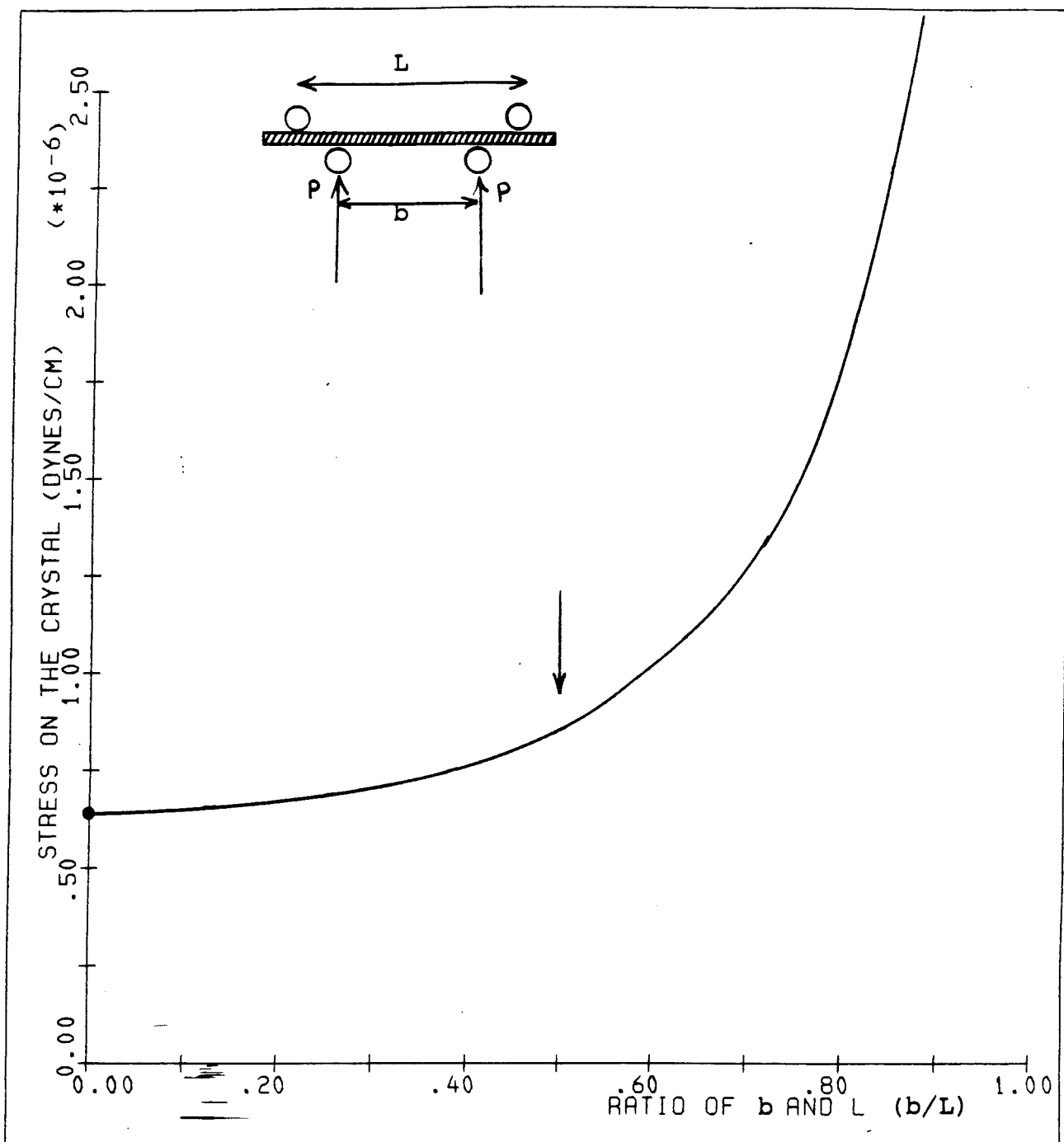


Figure 5.4 The stress per unit length (along the width of the crystal) by each of the middle pins of a four point bender as a function of b/L .

three point bender is a special case of the four point bender in which $b=0$. The calculated stress due to the center pin of an equivalent three point bender case (same L and bending angle) is 1.29×10^6 dynes/cm. The local stress distribution due to the pressure of the pins was discussed in references [11,33,34]. According to reference [11] the local curvature distribution along the thickness is

$$\rho(y) = \frac{-8 P}{\pi \times 0.141 E t^2} \left[\frac{y^2}{2t^2} - \ln(0.824 \frac{2y}{t}) \right] \quad 5.2$$

where $\rho(y)$ is the local curvature at a distance y across the thickness of the crystal from the pin position. Figure 5.5 compares the local curvature distribution across the thickness of the crystal for both the four point and an equivalent three point bender case.

Equation 5.2 and Figure 5.5 show that higher pressure causes higher local curvature effects near the pin positions of the crystal. Less pressure on the crystal corresponds to a smaller effective distorted regions and smaller local curvatures and therefore cause less dechanneling at the pin positions according to the Figure 5.2. Therefore, a four point bender was used instead of a three point bender. From Figure 5.4 one can decide the ratio of b and L when designing a four point bender. A reasonable value of b/L is $1/3$.

A differential screw fixed to the two center pins of the four point ~~bender~~ was used to change the bending angle of the crystal as shown in Figure 5.3. The differential screw set up provides a finer movement than a regular screw since the distance per turn is equal to the difference between the two pitches of both outer and inner screws. The thread sizes of both screws used are 28 turns/inch and 32

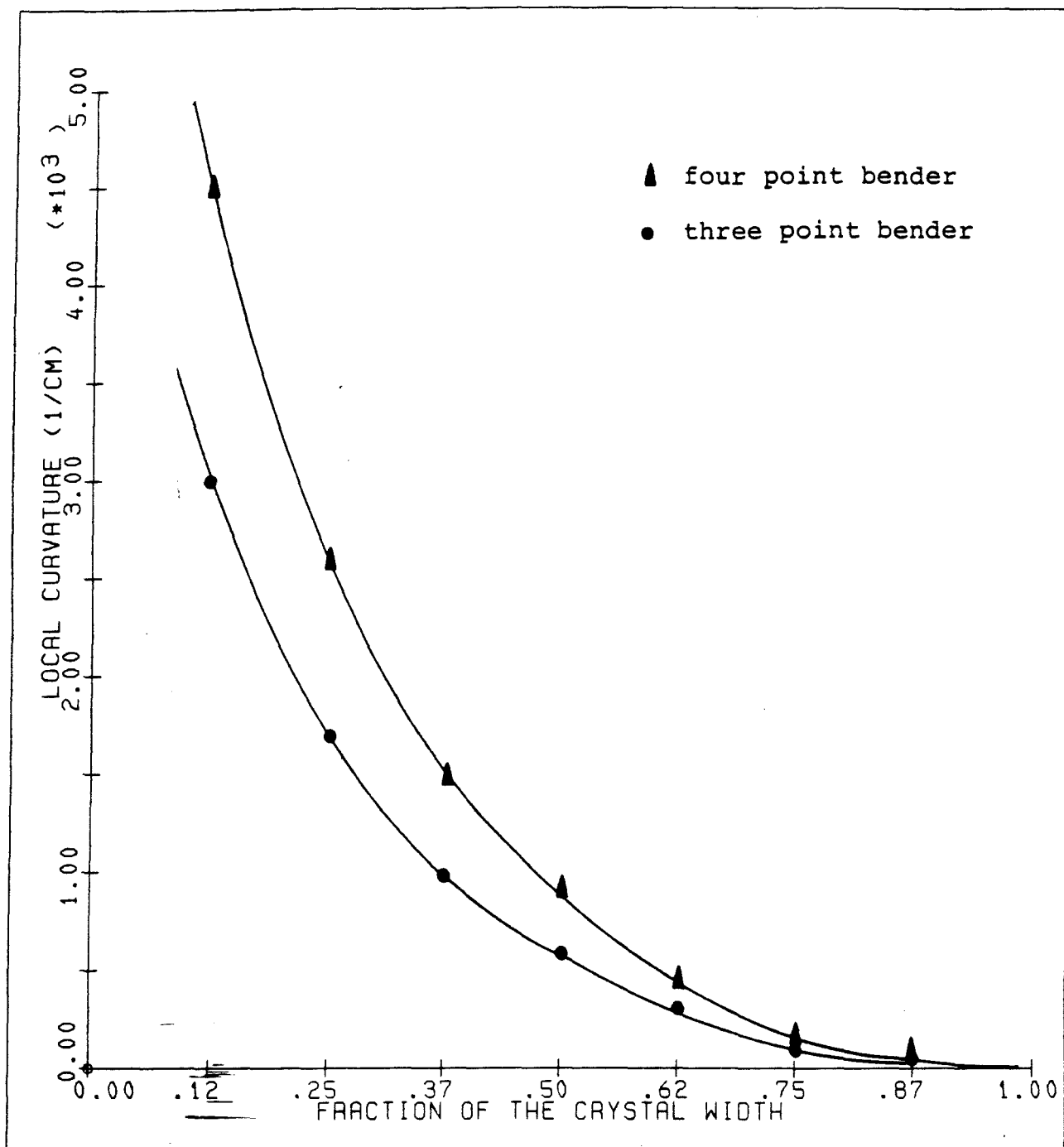


Figure 5.5 Local curvature distribution across the thickness of the crystal for the four point bender and an equivalent three point bender (same length between outer pins and bending angle).

turns/inch and the resultant thread size of the differential screw is $(1/28 - 1/32)^{-1} = 224$ turns/inch.

5.4 Septum Stand

A special stand was designed for the septum as shown in Figure 5.6. This Figure shows the schematic view when looking upstream of the beam. A linear motion in the vertical direction and a rotational motion about a horizontal axis perpendicular to the beam direction were possible in this design. The rotational motion is for crystal alignment and the vertical motion is for moving the crystal in and out of the beam.

The bending device with the horizontally mounted crystal is fixed to the goniometer shaft by a set-screw as shown in Figure 5.7. Repositioning of the bending device by tightening the set-screw does not change the previous orientation of the crystal with respect to the shaft and also to the beam direction. Since the crystal detector is very sensitive to light, the crystal was covered by a light-tight aluminum box with thin aluminum foil (5.0 mils thick) windows for the beam to go through. The goniometer arrangement is fixed to the holder which can be moved vertically up and down. Two reference base plates were installed in the M-Bottom pit and FEH to hold the septum stand. The stand can be locked on to the reference base plate at the correct horizontal position by the adjustable lock. Table 5.2 shows the specifications of both motions of the crystal septum stand.

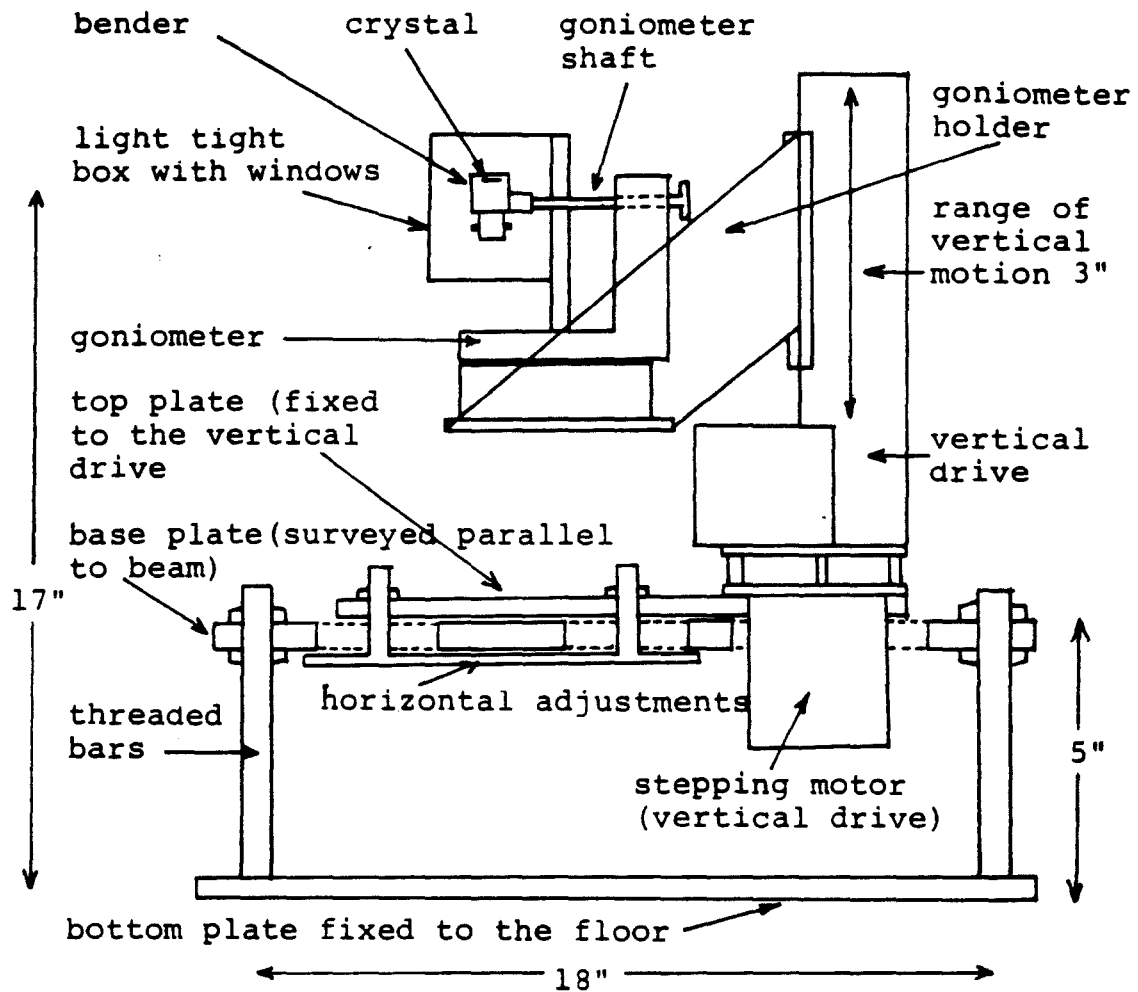


Figure 5.6 Schematic of the crystal septum stand. The beam direction is in to the paper.

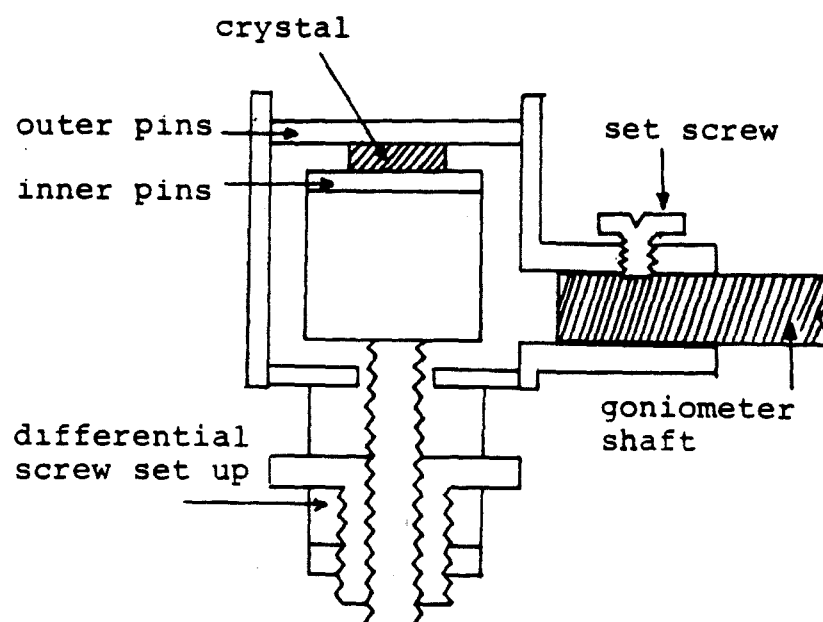


Figure 5.7 The bender and the goniometer shaft assembly of the crystal septum stand. The beam direction is into the paper.

Table 5.2 Operating parameters of the crystal septum.

	Rotational	Vertical
range of travel	12 degrees	3.0 inches
step size	4.8 microradians	2.5 micrometers
maximum speed	1000 steps/sec	1000 steps/sec
motor voltage	28 volts	-25, 12 volts

5.5 Septum Control System

Figure 5.8 shows the schematic of the crystal septum control system. Both motions can be controlled manually by the control box front panel buttons or remotely by EPICS control commands. An interface box links the control box and the two Fermilab made '044M' CAMAC modules. These two units were assigned as two beam line devices with the names MB6SIR (for rotational motion) and MB6SIV (for vertical motion). In the remote control mode the following EPICS command can be used:

SET device = value

where 'device' is the name of the device (MB6SIR or MB6SIV) and 'value' is the final position. When a command is given to make a certain number of steps in either one of the stepping motors, the corresponding '044M' module generates the required number of pulses and sends them to the control box through the interface box and enables the control box to drive the corresponding stepping motor. The final position of either motion (read-back value) is displayed and stored under the specified device name in M-Bottom PAGE FILE (section 3.3).

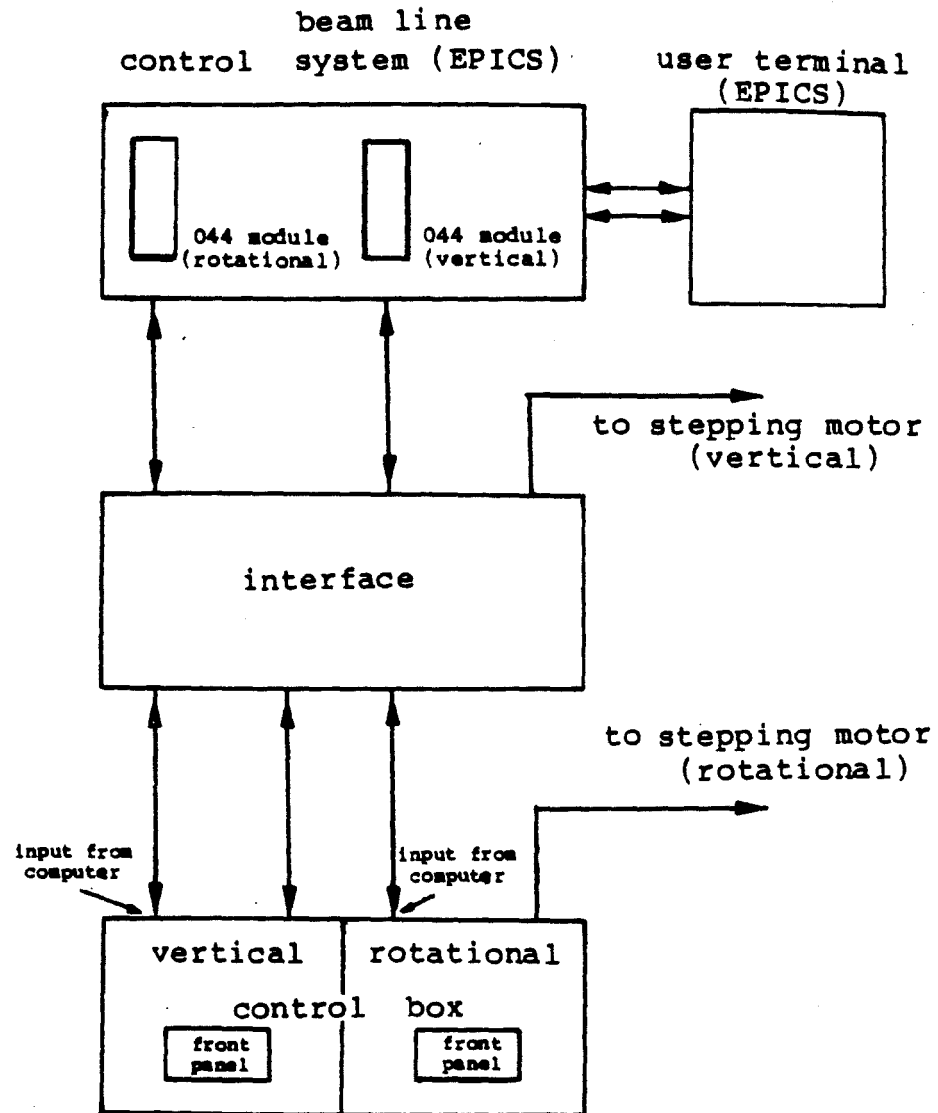


Figure 5.8 Schematic of the crystal septum control system. Both rotational and vertical motions can be controlled (a) manually by front panel switches in control box or (b) remotely by EPICS commands via any user terminal.

5.6 Septum Crystal Scanning Set Up

The septum control system was discussed in section 5.5. The trigger system used for regular scanning is shown in Figure 4.8. In addition to that, the following set up as shown in Figure 5.9 was used for septum crystal computer scanning. The two '044M' modules are basically EPICS compatible CAMAC units. They can be controlled only by EPICS commands as discussed above. Therefore both computers had to be linked together to form the septum scanning system. The EPICS program named 'SEPTUM.BAS' written in Basic language had to execute simultaneously with the regular 'MULTI' scanning program.

The MULTI scanning program in the PDP-11 is first started by the command "RUN MULTI" and then the SEPTUM program in EPICS is executed using the command "RUN SEPTUM". Once the MULTI is loaded the following commands

```
SET YESRUN='140000
```

```
SET NORUN='140000
```

are typed in the regular MULTI terminal. These two commands generate BISON box Daout-14 output signals (TTL) when 'BEGINRUN' and 'ENDRUN' commands are given in MULTI. The 'SEPTUM.MCM' file contains the above two SET commands including the other SET commands for the scanning mode. Then type the starting position and the increment of the goniometer In EPICS terminal (responds to "RUN SEPTUM" command).

The two EPICS CAMAC scalers MB6SI1 and MB6SI2 were assigned to assist the SEPTUM program execution. When the BEGINRUN command is given in MULTI, the BISON box Daout-14 generates a signal which goes to the EPICS MB6SI1 scaler to initiate the SEPTUM program. This TTL

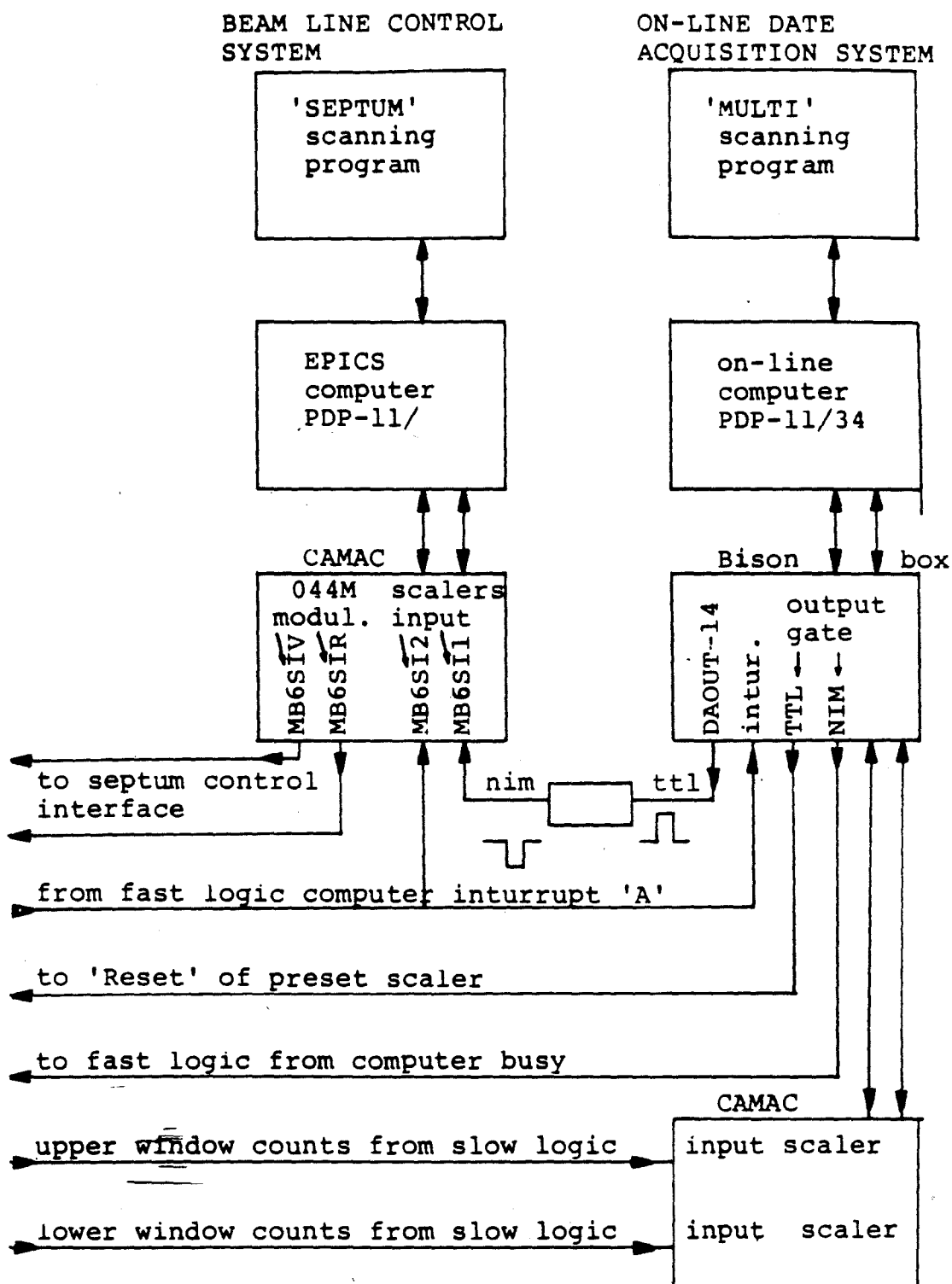


Figure 5.9 Schematic of the septum crystal computer scanning logic used in the M-Bottom experimental pit. This has been done by linking the beam line control system and the on-line scanning system.

signal is converted to a NIM signal before it goes to MB6SI1. In the regular scanning set up the BISON computer interrupt 'A' is generated from the logic set up when the number of upper window counts reaches the set value in the preset scaler. The goniometer is then advanced to the next position before starting the window counts. In this scanning set up the computer interrupt 'A' is sent to MB6SI2 scaler register in addition to the BISON box to enable the SEPTUM program to make the goniometer increment. For each goniometer increment the EPICS terminal displays the position of the crystal and the MULTI program prints the ratio of window counts and updates the display scatter plot. An ENDRUN command in MULTI sends a DAOUT-14 signal to MB6SI2 again to terminate the execution of the SEPTUM scanning program. The ENDRUN command itself terminates the regular 'MULTI' scanning program.

5.7 Setting the Bending Angle

The experimental set up was discussed in chapter 4. The septum stand was placed on the base plate which was surveyed parallel to the beam direction in the M-Bottom pit. The regular energy loss technique was used to align the crystal.

Data was accumulated for some time to see the outgoing angular distribution at 100 GeV/c. On-line data analysis was used to display the outgoing angular distribution. Necessary readjustment of the bending angle was done by turning the differential screw.

Since the upstream end of the crystal was not clamped, realignment of the crystal was needed after changing the bending angle. A laser arrangement as shown in Figure 5.10 was used in addition to the regular

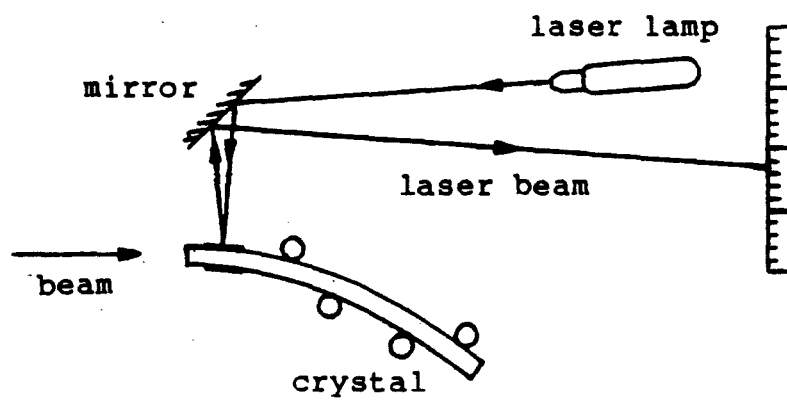


Figure 5.10 Schematic of the laser arrangement used to assist realignment of the plane when a readjustment of the bend angle was done.

experimental set up described in chapter 4.

A reflected laser beam from the upstream surface of the crystal shows a sharp spot on the screen. Once the crystal was well aligned, the spot position was used as the reference position and after each bend readjustment, the crystal was rotated manually to get back to the original orientation. After that, scanning the crystal manually in a short range would be enough to realign the crystal plane. The crystal reorientation was done several times during the bend angle setting. Crystal reorientation using the laser spot was always found to be within 100 microradians.

Figure 5.15 shows the outgoing-y angular distribution after the correct bend was set on the crystal at a beam momentum of 100 GeV/c. Outgoing particles of low energy loss at the crystal detector were selected for the above figure. Figure 5.11 shows the scatter plot of outgoing-x and -y angular distributions. This figure shows that the particles are bent only in the vertical downward direction. Miss-alignment of planes will be discussed in section 6.5. The measured value of the bend angle was 9.8 milliradians. Figure 5.12 was taken by relaxing the bend by one third of a turn in the differential screw. The measured bend angle in this configuration was 8.0 milliradians according to the above figure. These two bending angles imply that one turn of the differential screw corresponds to a change of 2.7 milliradians.

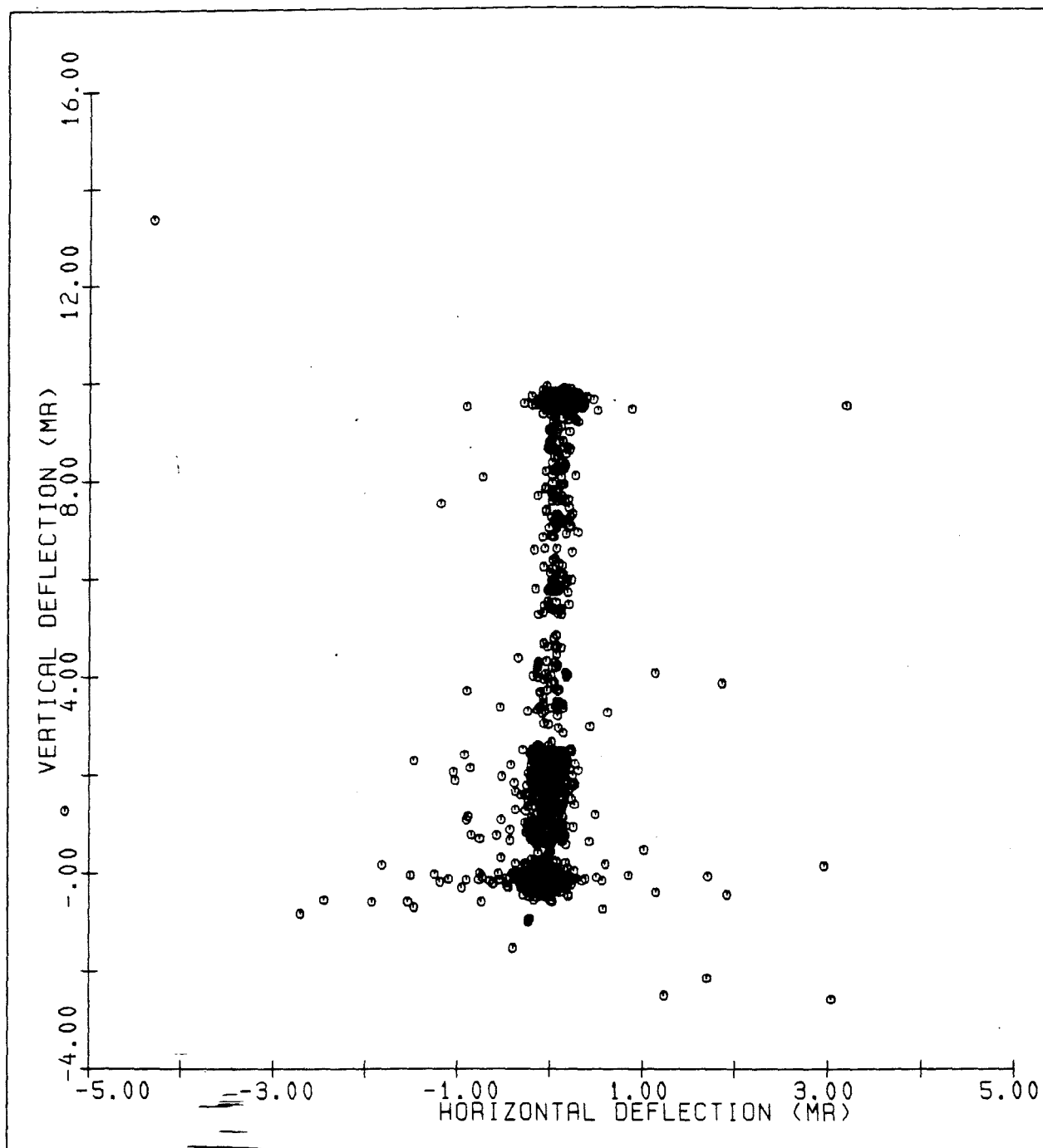


Figure 5.11 Out going -x and -y angular distribution for the crystal obtained at 100 GeV/c after the correct bending angle was set. The positive bend direction is vertically downward.

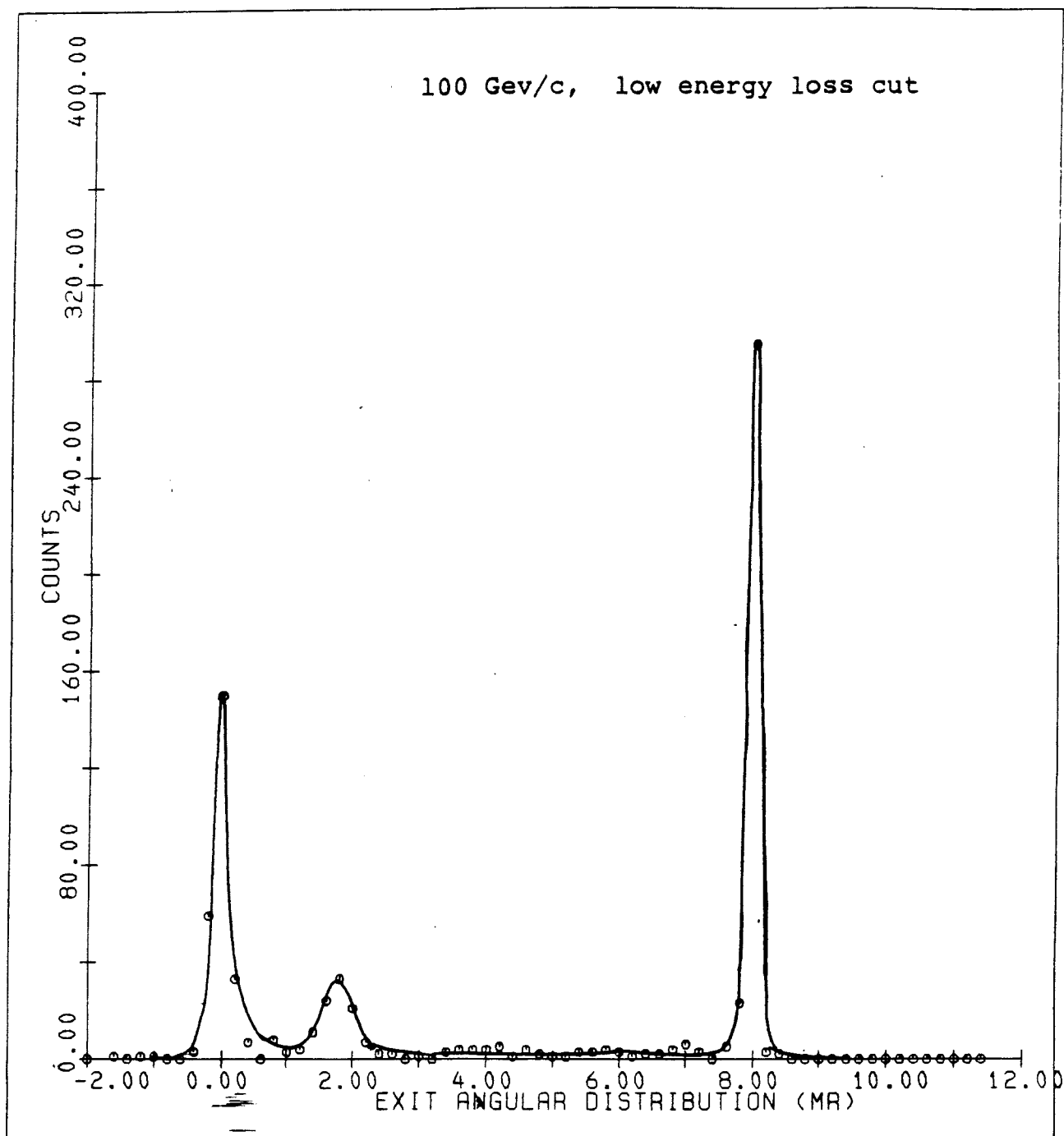


Figure 5.12 Bent particle distribution of the septum crystal at 100 Gev/c after the bend angle was relaxed by one third of a turn of the differential screw. Low energy loss particles at the detector were selected for the spectrum.

5.8 Through-put Studies of the Septum Crystal

After setting the correct bend angle data was accumulated for beam energies of 60, 100, and 200 Gev. The drift chamber data and the energy loss information of the crystal detector were recorded for each event logged. This experiment was done during the January 1984 running period. Table 5.3 shows the summary of through-put data. Off-line analysis has been done to find the transmission properties of the crystal at these energies.

Table 5.3 Summary of data logged during crystal septum application.

Energy	Events logged	Comments
160 Gev	25,000	random orientation of the crystal.
100 Gev	100,000	drift chamber calibration.
100 Gev	95,000	8.0 mr bend angle.
100 Gev	114,000	8.9 mr bend angle through-put studies.
200 Gev	110,000	8.9 mr bend angle through-put studies.
60 Gev	110,000	8.9 mr bend angle through-put studies.
200 Gev	63,000	beam studies during septum operation.

5.8.1 Bending Efficiency (f_b)

Figure 5.13 shows the energy loss distribution of the beam particles at the detector for 100 Gev/c. The region A in Figure 5.13 represents the channeled particles at the detector. Figures 5.14, 5.15 and 5.16 show the outgoing-y (vertically downward) angular distribution of particles which were channeled at the detector for 60, 100 and

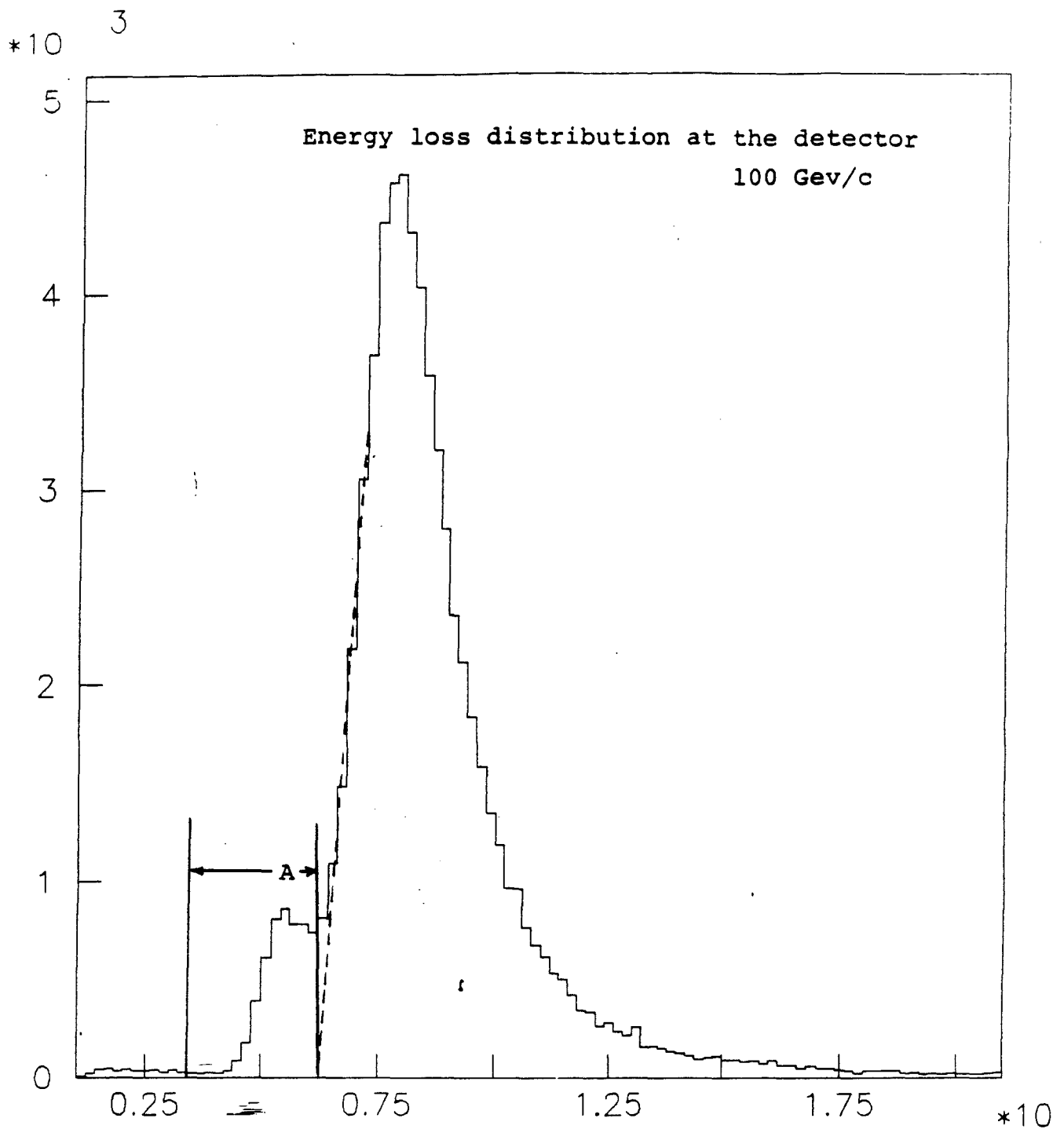


Figure 5.13 Energy loss distribution of the particles at the upstream end of the crystal (before the bend region) measured using the crystal detector. Data was acquired at 100 Gev/c and the energy scale is arbitrary.

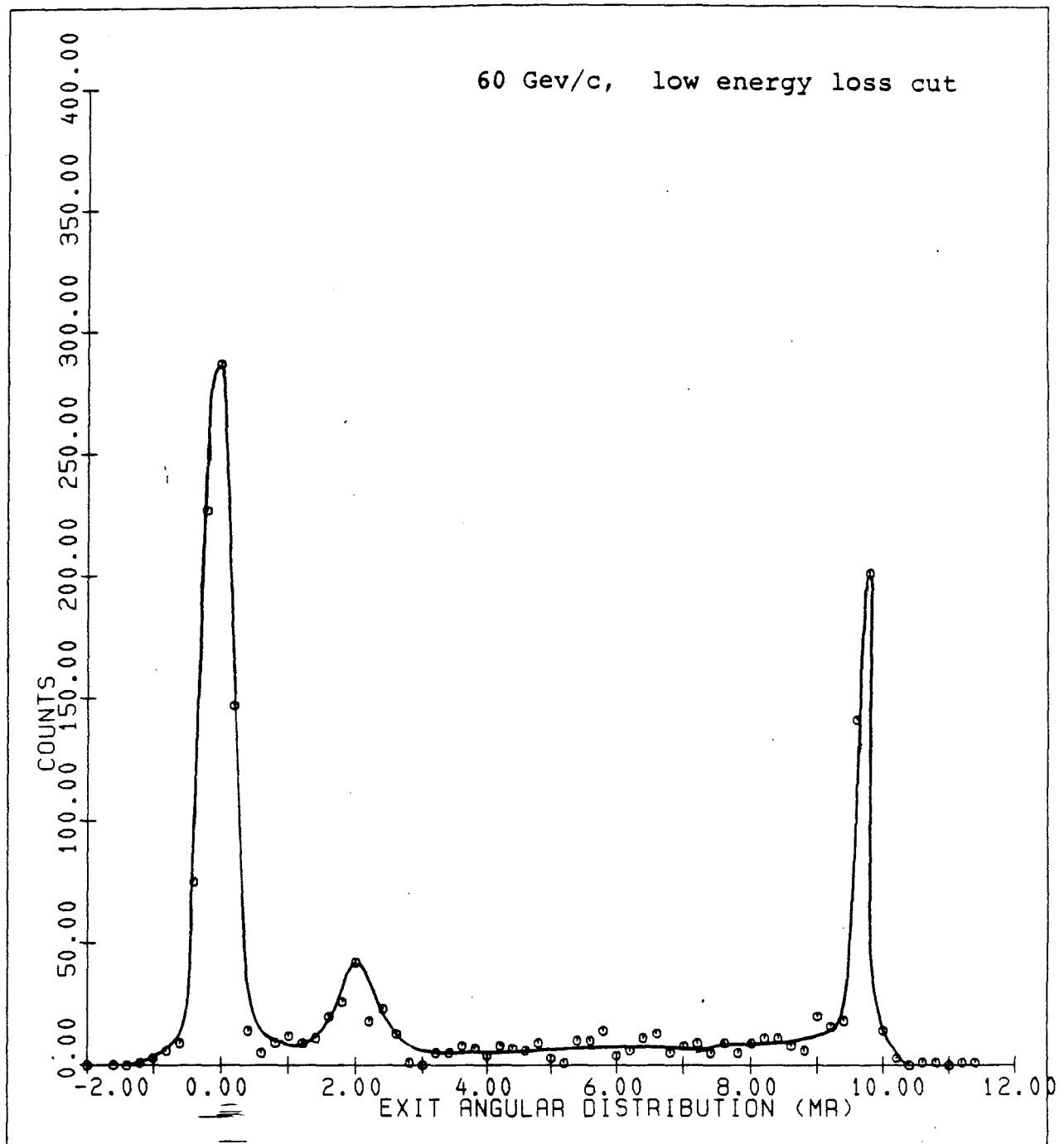


Figure 5.14 Bent particle distribution of the septum crystal at 60 Gev/c, used for through-put calculations. Low energy loss particles at the detector were selected,

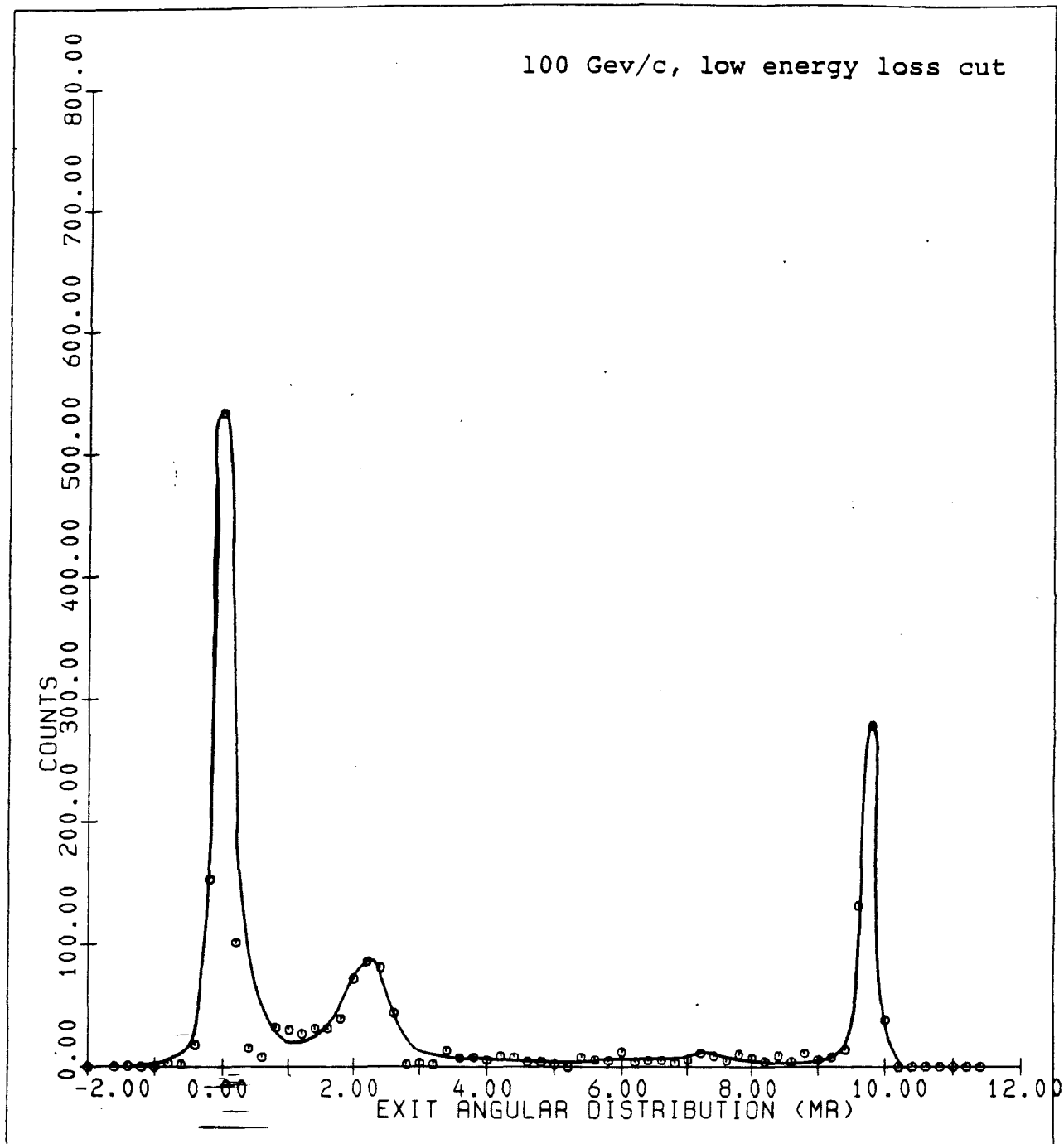


Figure 5.15 Bent particle distribution of the septum crystal at 100 Gev/c; used for through-put calculations. Low energy loss particles at the detector were selected.

200 GeV/c. These particles, channeled at the initial (unbent) portion of the crystal were selected by energy loss discrimination. The 'bending efficiency' (f_b) of the septum crystal is defined as the totally bent fraction of initially channeled particles. Therefore according to the Figure 5.16, f_b is the ratio of counts in the region B to the total counts in the whole distribution (B+C).

$$f_b = B/(B+C) \quad 5.3$$

The bending dechanneling of particles is due to the curvature of the bent regions and the local curvature near the pin positions. Both ordinary dechanneling and bending dechanneling of the septum crystal are included in the calculation of the bending efficiency so that these fractions need not to be calculated separately for the through-put studies of the crystal septum. It should be noted that in this calculation the pin effects have been taken into account. Since the pin effects depend on the bend angle and the pin positions, it is a complicated process to scale the results of bending fractions to an arbitrary case.

5.8.2 Capture Efficiency (f_c)

The 'capture efficiency' [35] (f_c) of a crystal plane is defined as the ~~initial~~ channeled fraction of incident particles within the channeling phase space. Incident angular data and the energy loss information of the particles are needed for the calculation of f_c .

The measured widths of the incident-y angular distribution of channeled particles at the detector were several times larger than the

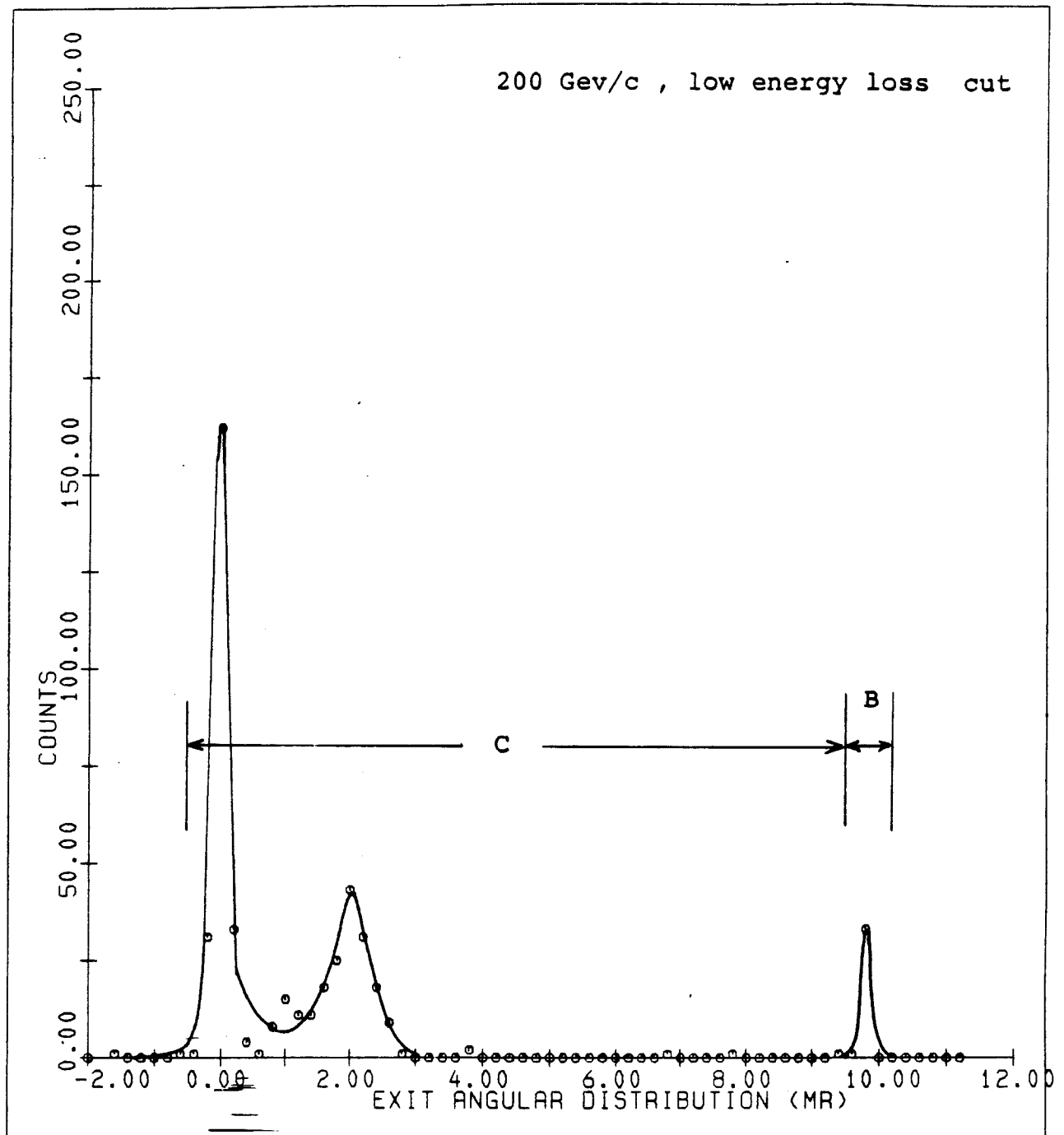


Figure 5.16 Bent particle distribution of the septum crystal at 200 Gev/c; used for through-put calculations. Low energy loss particles at the detector were selected.

critical angle at that energy. This was due to the poor resolution of the y-coordinate measurement of the drift chamber D1. The efficiency of the wire planes 1Y and 1Y' (section 4.2.1) was about 60% and the wire planes were not fired at all about 30% of the time. Therefore, the incident-y angular selections were not possible for the calculation of capture efficiency.

Since in both runs (January and June 1984) the crystal plane used were si(110), June data was used to calculate the initial capture efficiency. The summary of June 1984 run data is shown in Table 9.1.

Figure 5.17, 5.18 and 5.19 show the energy loss distributions of the particles incident within the critical angle for the plane of si(110) at 60, 100 and 200 GeV/c, respectively. The initial channeled fractions for particles incident within the critical angle to the plane are calculated theoretically in section 8.7 and experimentally in section 9.4.3. The results are only presented in this section. The experimental values of f_b and f_c are shown in Table 5.4 for the above energies.

Table 5.4 Bending efficiencies and capture efficiencies of the crystal septum.

Energy <u>Gev</u>	Critical Angle <u>μr</u>	Bending Efficiency (f_b)	Capture Efficiency (f_c)
60	20.6	0.26	0.55
100	16.0	0.23	0.55
200	11.3	0.07	0.55

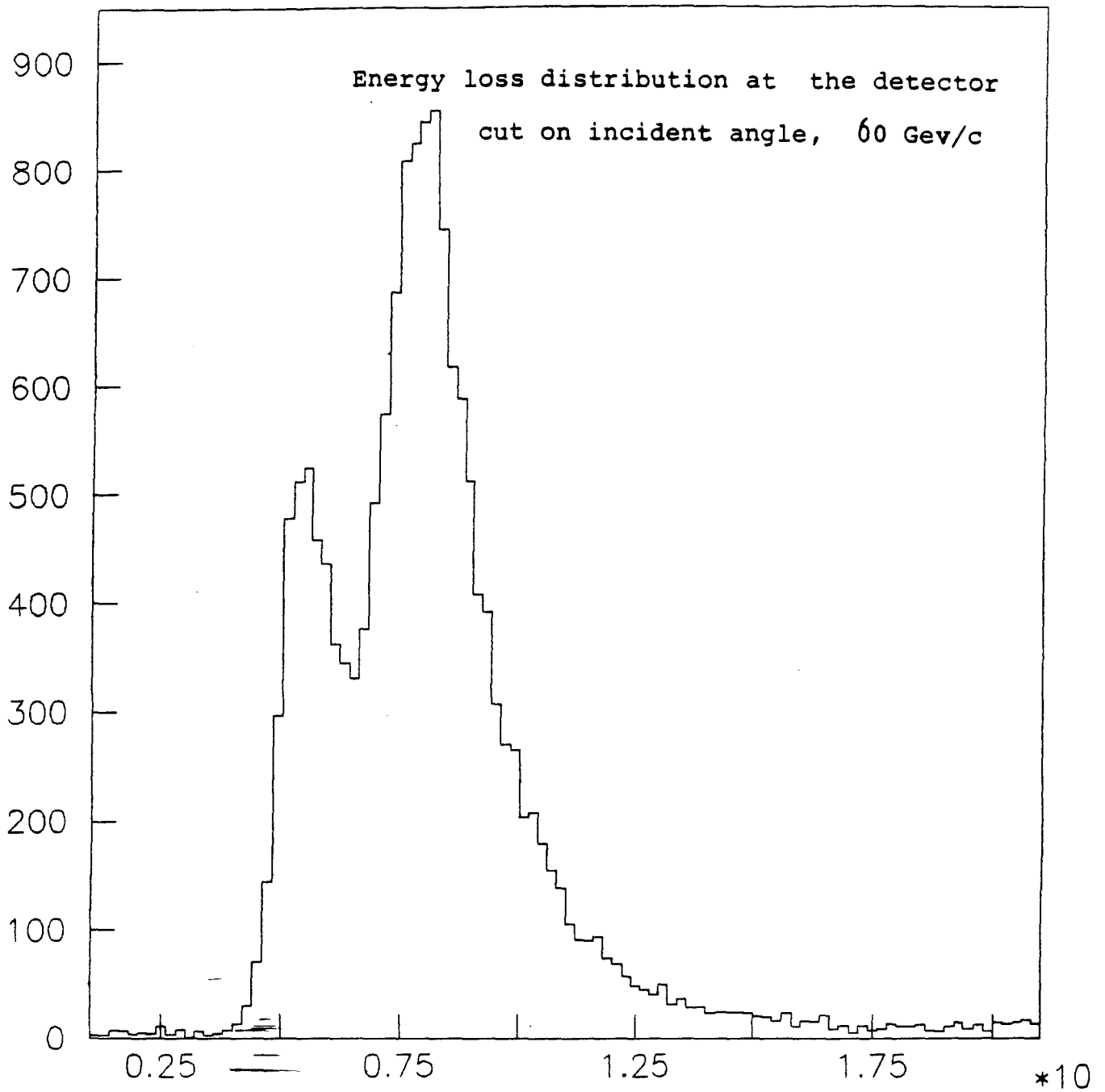


Figure 5.17 Energy loss distribution of the particles at the upstream end of the crystal (before the bend region) incident within the critical angle to the plane in both directions. Data was acquired at 60 GeV/c and the energy axis is an arbitrary scale.

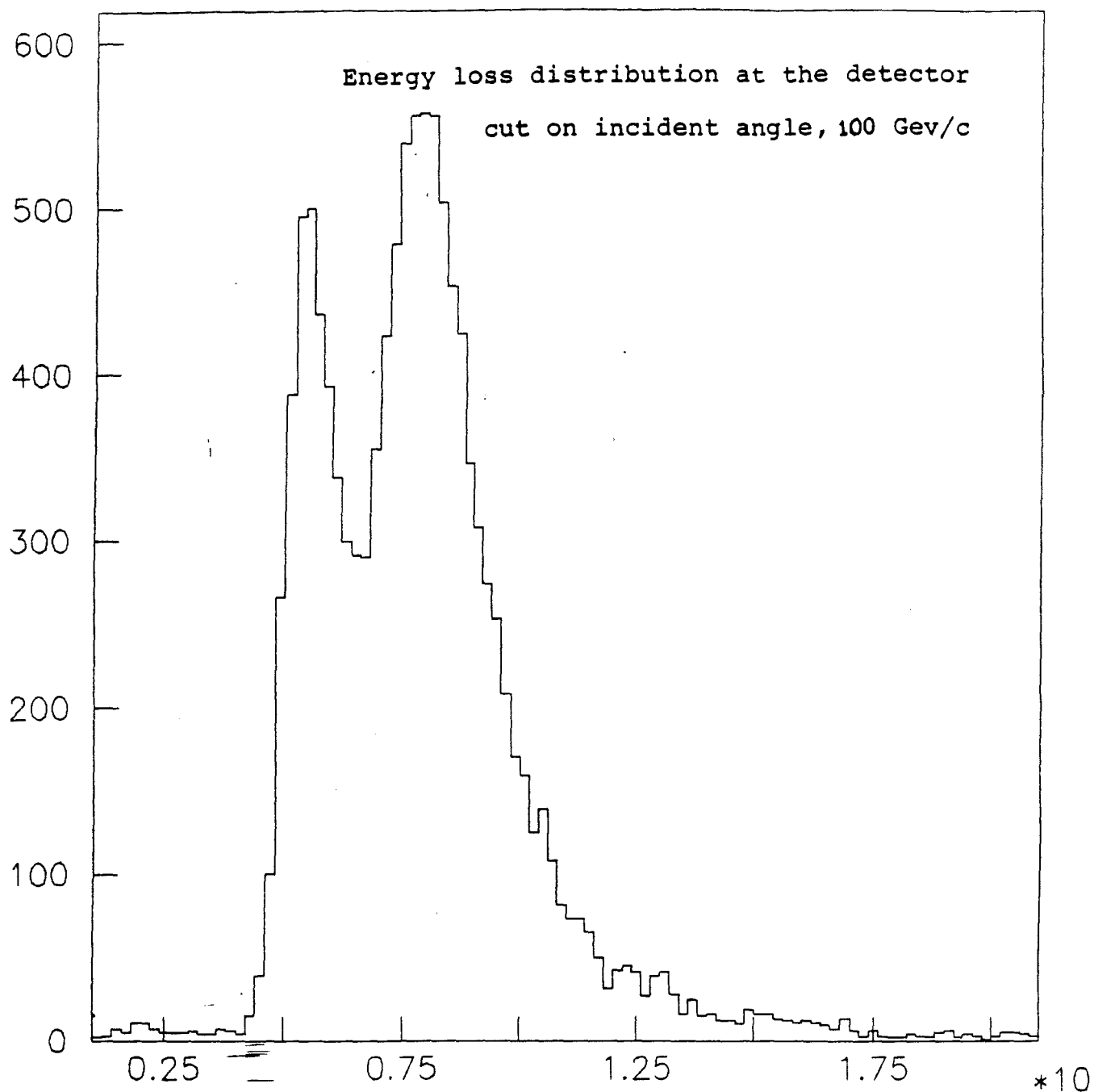


Figure 5.18 Energy loss distribution of the particles at the upstream end of the crystal (before the bend region) incident within the critical angle to the plane in both directions. Data was taken at 100 GeV/c and the energy axis is an arbitrary scale.

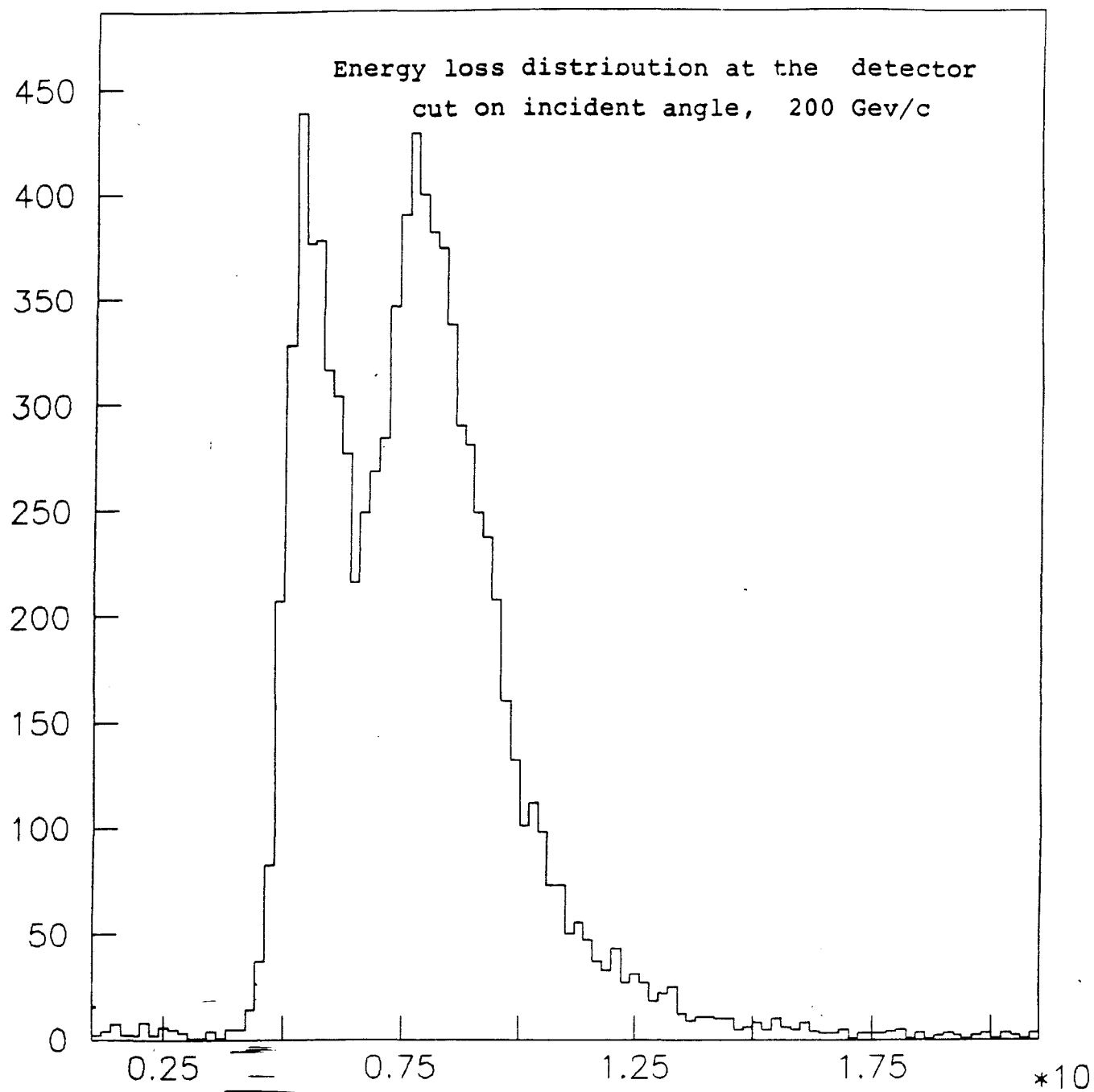


Figure 5.19 Energy loss distribution of the particles at the upstream end of the crystal (before the bend region) incident within the critical angle to the plane in both directions. Data was taken at 200 GeV/c and the energy axis is an arbitrary scale.

5.8.3 Spatial Acceptance (f_s)

The 'spatial acceptance' (f_s) of the crystal is defined as the fraction of the beam going through the crystal. If the horizontal and vertical beam widths are x and y and horizontal and vertical widths of the crystal are a and b , then

$$f_s = \frac{a \cdot b}{x \cdot y} \quad 5.4$$

As one can see in equation 5.4, f_s depends only on the geometry of the beam and the crystal.

5.8.4 Angular Acceptance (f_a)

For planar channeling the angular acceptance perpendicular to the direction of the bend assuming the crystal is bent perpendicular to the plane, is infinite. The angular acceptance in the direction of the bend is determined by the critical angle of the plane. Therefore if θ_c is the critical angle and θ_0 is the half width of the beam in the direction then the 'angular acceptance' (f_a) is defined as

$$f_a = \theta_c / \theta_0, \quad \text{for } \theta_c < \theta_0 \quad 5.5a$$

$$f_a = 1, \quad \text{for } \theta_c \geq \theta_0 \quad 5.5b$$

5.8.5 Transmission Fraction (f_T)

Taking all the fractions together the 'transmission fraction' of the septum crystal can be written as

$$f_T = f_b \cdot f_c \cdot f_s \cdot f_a \quad 5.6$$

If we assume a typical beam of 1.0×10^6 particles per spill, vertical divergence of 0.1 mr and diameter of 1.0 cm, Table 5.5 shows the number of particles one would expect to be bent at different energies.

Table 5.5 Efficiencies and particles transmitted for 1.0×10^6 particles incident on the septum crystal.

Energy Gev	Critical Angle μr	Angular Accept f_a	Spatial Accept f_s	Bending Effici. f_b	Capture Effici. f_c	Number Of bent Particles
60	20.6	0.41	0.10	0.26	.55	6000
100	16.0	0.32	0.10	0.23	.55	4000
200	11.3	0.23	0.10	0.07	.55	900

CHAPTER 6

SCANNING OF CRYSTALS

6.1 Introduction

In channeling experiments we always deal with particles that are incident nearly parallel to the crystal planes or axes. Therefore, crystal alignment plays a major role in high energy channeling. In the multi-Mev energy region back-scattering techniques are used but in the multi-Gev region these yields are very small. Normally low energy loss techniques are used with the assistance of a surface barrier semiconductor detector incorporated in the crystal. However, this method is limited only to semiconductor materials. Heavy materials like tungsten have higher bending efficiencies and angular acceptances. A method has been suggested to scan this kind of bent crystals. This chapter discusses the above scanning methods and techniques to improve the efficiency of scanning.

6.2 Energy Loss Scanning Method

This ~~method~~ can be used for bent or unbent crystals with built-in detectors. —The crystals are normally made such that a major plane or an axis is nearly parallel to the major face of the crystal slab. Since the region outside the two ends of the detector pads are not completely depleted, the charge collection from that region is poor. Therefore, the pulse height due to the particles passing outside the

detector pads does not give the correct energy loss information. The energy loss distribution due to these particles smears over the low energy side of the regular energy loss distribution (Landau distribution). Use of a scintillation detector with a hole of length shorter than the width of the crystal detector as a veto to the fast coincidence avoids this problem and gives a cleaner Landau distribution. The detector hole can be aligned with the crystal by using the drift chamber D2.

The normal random direction energy loss spectrum for 100 Gev particles through a 3.0 mm path length in silicon is shown in Figure 6.1. Figure 6.2 shows the energy loss distribution when the incident beam direction is aligned with the crystal (110) plane. The low energy loss shoulder corresponds to the channeled particles. In this scanning method two windows are set, one around the channeled peak and the other one at the high energy side of the Landau distribution as shown in Figure 6.2.

The crystal is first scanned with step sizes of 5-10 milliradians while observing the ratio of window counts to find the physical plane of the crystal. This scan is called a 'macroscan'. Figure 6.3 shows the septum crystal macroscan spectrum at 100 Gev/c. The macroscan dip position corresponds to the crystal orientation where the physical plane of ~~the~~ crystal is parallel to the beam direction. When the crystal is at a certain angle to the beam direction, particles travel shorter or longer distances within the detector region than the distance they travel when the crystal is parallel to the beam. Therefore, the energy loss distribution is flatter and wider which

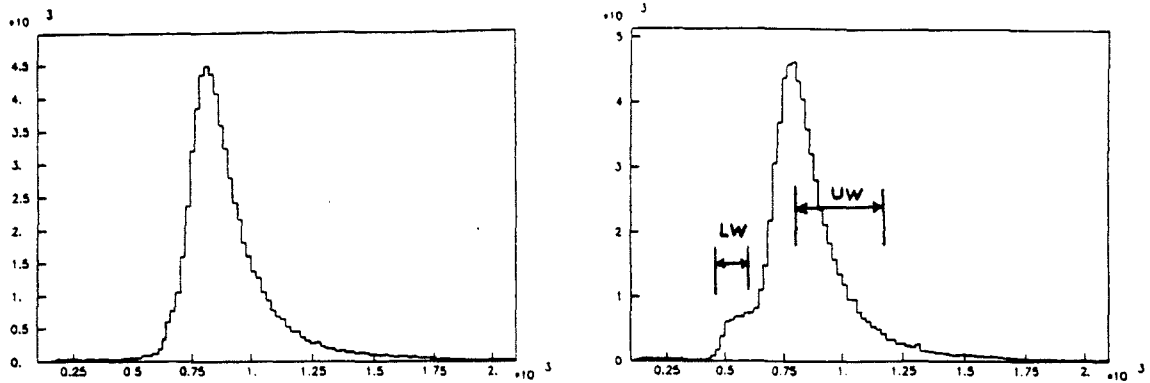


Figure 6.1 (Left) Energy loss distribution of 100 GeV/c charged particles at the crystal detector for an arbitrary incident direction.

Figure 6.2 (Right) Energy loss distribution of 100 GeV charged particles at the crystal detector when a (110) plane is parallel to the beam direction. Channeled particles appear at the low energy shoulder. In both figures the scales for the horizontal energy axes are arbitrary.

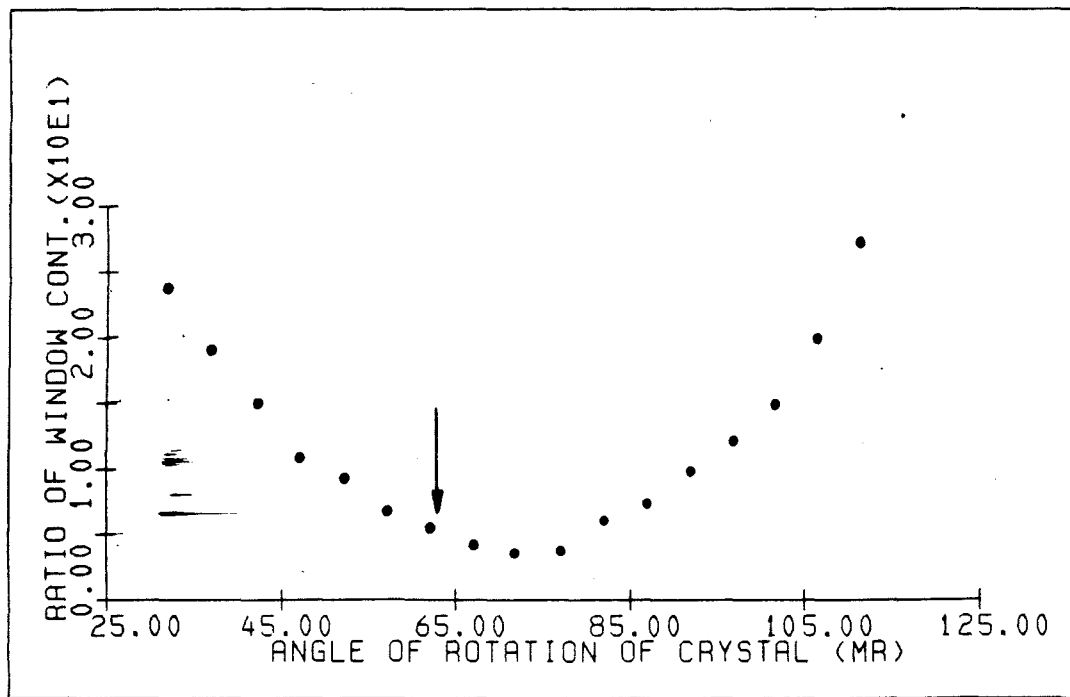


Figure 6.3 Macroscan spectrum of septum crystal. The vertical axis is the ratio of lower window and upper window counts in the energy loss distribution. The vertical arrow shows the position of the (110) plane found later in microscanning.

causes the window ratio to be higher as the crystal is more and more tilted away from the beam direction.

Once the crystal orientation is understood, the crystal is scanned around the macroscan minimum until a peak ratio of lower window counts to upper window counts is found. The angular step size of the scan is kept smaller than one third of the beam divergence so that the crystal plane is within the beam for at least three successive orientation positions. The step sizes are normally of the order of 50 microradians for a beam of angular divergence of 200 microradians. This type of scan is called a 'microscan'. Figure 6.4 shows the microscan spectrum of the septum crystal. The trigger level selected for both these scans is T1.T2.T4.X where X denotes the crystal fast signal.

6.3 Efficiency Tests

After the (110) plane of the septum crystal was found, the following tests were performed at a beam energy of 100 Gev.

(a) It is obvious that the ratio of counts is very sensitive to the position of the upper level of the lower window. This position should be set to catch as many of the channeled particles as possible during scanning without including too many unchanneled particles. The crystal was rescanned over the plane for two different lower window settings as shown in Figure 6.4. About one third of the height of the Landau peak on the low energy side was found to be the better position of the two for the upper level of the lower window. A point to notice is that in both spectra the increase of the ratio from background to the peak has not been changed very much. However, the peak in the lower spectrum is

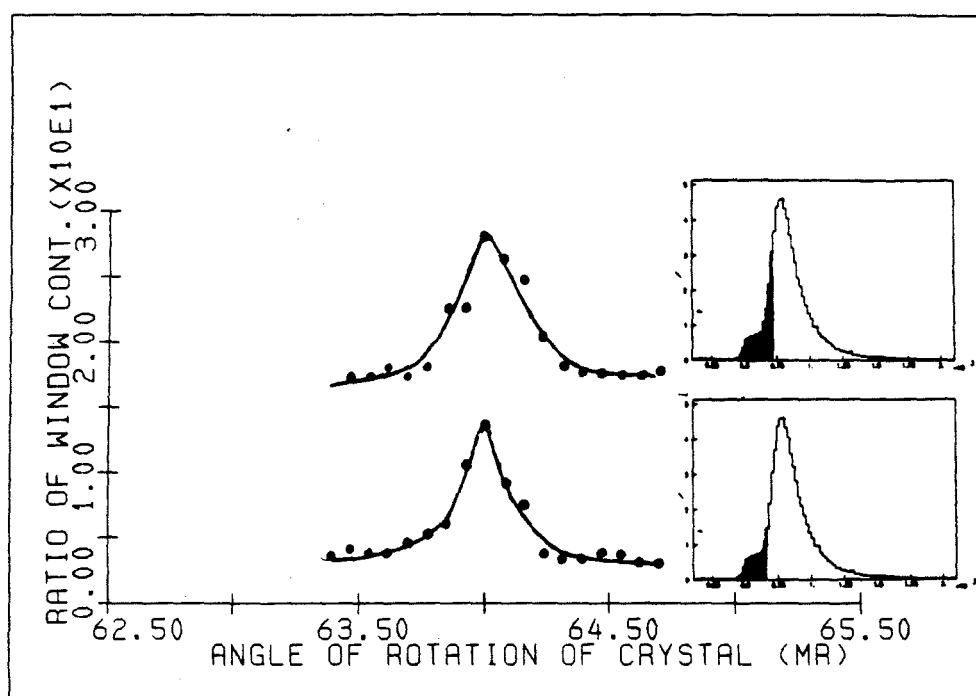


Figure 6.4 Rescan spectra of the bent crystal for two different settings of lower window. Lower window settings are shown next to each scan spectrum. (a) upper level of the lower window is at about two-thirds of the height of the Landau peak. The measured ratio at the peak is about 1.6 times higher than the ratio of the background. (b) Upper level of the lower window is at about one-third of the height of the Landau peak. The measured ratio at the peak is about 3.5 times higher than the ratio of the background.

more prominent over the background.

(b) When scanning a bent crystal, selection of the correct trigger system is important. When the bent crystal is aligned, a fraction of channeled particles follows the bent path. This fraction depends on the bend angle and the energy of the beam (Figure 5.14 through 5.16 in Chapter 5). If the system is unable to trigger on these particles, one may have a hard time finding the scan peak. Therefore, in order to improve the scanning efficiency one has to make sure that the downstream trigger counter catches the bent particles, also. After the plane was aligned, energy loss distribution was accumulated for $T1.\overline{T2}.T3.X$ and $T1.\overline{T2}.T4.X$ fast coincidence levels where the area of $T4$ was 7"x 28" and $T3$ is 2"x 2". Missing bent particles in the $T3$ counter account for the difference between the two Landau distributions in Figure 6.5. Figure 6.6 shows the rescan spectra with these two fast coincidence levels.

(c) As a test the $T2$ anti-detector was replaced by a small scintillation detector $T5$ (Table 5.2) of the size equal to the hole of the $T2$ detector. There was no significant difference observed between the regular scan of $T1.\overline{T2}.T4.X$ and $T1.T5.T4.X$.

(d) The $T5$ detector was moved about 10 cm downstream of the crystal and aligned 1.5 mm below the crystal so that most of the straight going particles miss it, but the bent particles pass through it. Figure 6.7 shows the scan spectrum and Landau distribution obtained in this fast trigger $T1.\overline{T2}.T5.T4.X$. The most significant point to notice concerning

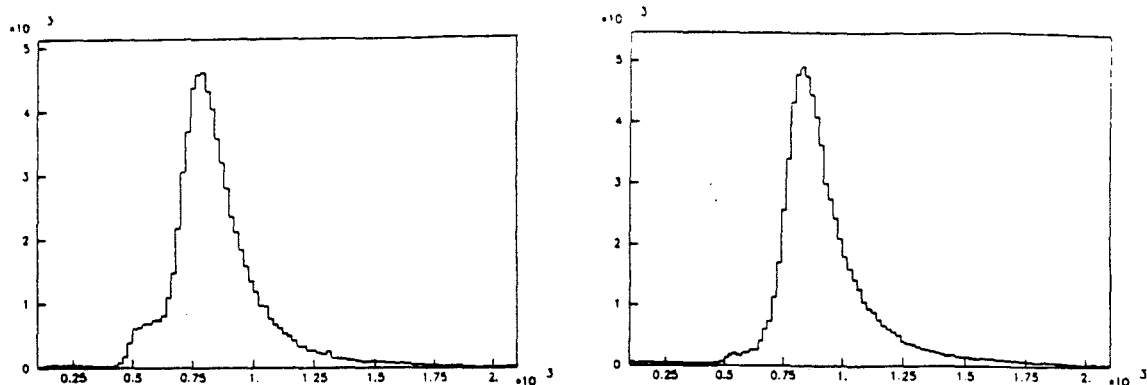


Figure 6.5 Energy loss distributions of charged particles at the detector for two different trigger settings. The figure at the left shows the distribution when the large counter was used downstream of the crystal. The figure at the right shows the distribution when the small counter was used instead of the large counter.

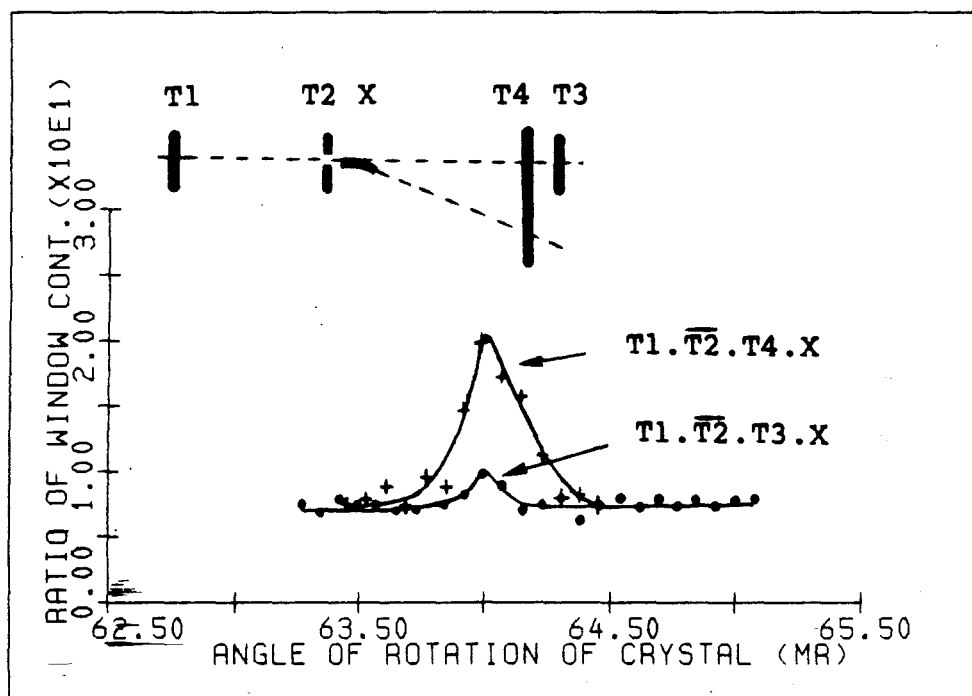


Figure 6.6 Rescan spectra of the bent crystal for two different trigger systems of $T1.T2.T3.X$ and $T1.T2.T4.X$. In the first trigger system the measured ratio at the peak is about 2.1 times higher than the ratio of the background. When the small trigger counter was used, the ratio at the peak is only about 1.3 times higher than the ratio of the background because of the missing bent particles.

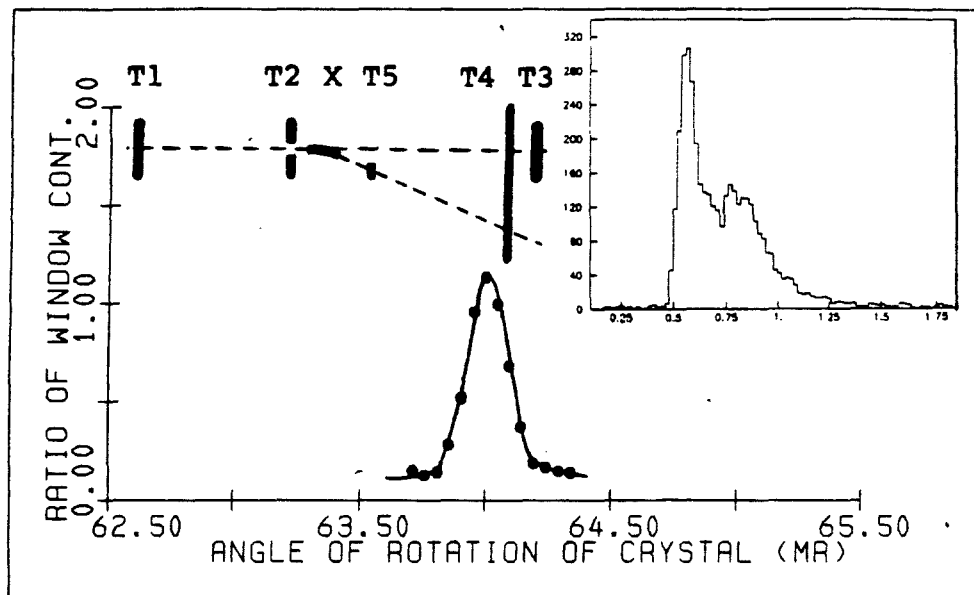


Figure 6.7 Rescan spectrum of the bent crystal with counter T5 in the trigger system. Fast trigger level used is T1.T2.T5.T4.X. Energy loss distribution is also shown with this trigger system. The measured peak height is about 8 times higher than the background. Missing of straight through particles is responsible for the rise of the ratio at the peak.

this method is that the ratio at the peak is very much larger than the background compared to the other methods. In reality this method is very slow because the system triggers only on the particles hitting the T5 detector. If the regular scanning rates were about two points per spill, this method would take a couple of spills to get one point. This method is somewhat similar to the Kim technique which will be discussed in next next section.

6.4 Kim Scan Method

This method was proposed by I. J. Kim for bent crystals without the assistance of a crystal detector. If we scan a bent crystal, it can deflect particles only if it is aligned. Thus by monitoring the deflected particles a bent crystal can be aligned.

The bent septum crystal was used to test this technique. The detector T3 accepts only the forward scattered unbent particles and T4 covers the whole range of the bent spectrum. Therefore, the counts of fast coincidence level $T1.T5.\overline{T3}.T4$ should show the deflected particles. The ratio of $T1.T5.T3$ and $T1.T5.\overline{T3}.T4$ counts was observed while the crystal was being scanned. This had been done in parallel to the regular scanning to compare the efficiency of this method. Figure 6.8 shows the ~~results~~ of Kim scanning. Detector T5 was used in front of the crystal ~~instead~~ of $\overline{T2}$ (anti) in this part of the experiment. The observed peak height was about 1.4 times higher than the the background in Kim method and the number is 1.8 in regular scanning.

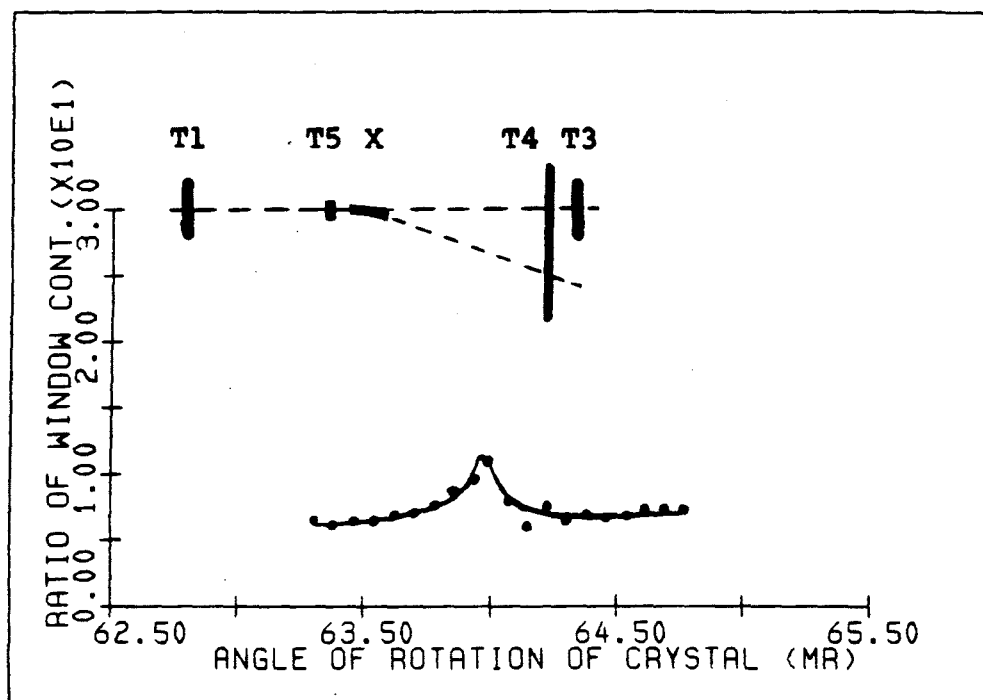


Figure 6.8 Scan spectrum of the bent crystal using Kim method. 'Ratio of window counts' are defined as the ratio of coincidence levels of T1.T5.T3 and T1.T5.T3.T4.

6.5 Some Important Points About Scanning

If an axis is oriented very close to the beam direction accidental alignment of another nearby plane could occur. This can not be identified by the Landau distribution. For an unbent crystal this can be identified by measuring incident or outgoing angular distribution widths of channeled particles. For a bent crystal the orientation of the plane can be identified either by the above method or by looking at the bent particle direction. If a drift chamber is not available downstream of the crystal, a small counter can be used to find the bent particle direction. Moving the counter along the expected bend direction and watching count rates would show whether the correct plane was found or not. In fact, this method can be used to measure the bend angle also.

CHAPTER 7

CRYSTAL SEPTUM OPERATION

7.1 Introduction

The crystal septum installation in the Front End Hall (FEH) and its operation at energies of 200 and 400 GeV/c are presented in this chapter. At 200 GeV/c the beam properties in the experimental pit have been observed. Two computer programs 'TRANSPORT' and 'DECAY TURTLE' which have been written to design beam transport systems, are used to calculate beam element parameters and beam properties. At 200 GeV/c beam properties in the experimental pit are calculated and compared with the observed results. The possibility of momentum recombination and focusing the beam in the experimental pit at 200 GeV/c and 400 GeV/c is also discussed in this chapter.

7.2 Crystal Septum Installation Procedure

The drift chamber set up in M-Bottom experimental pit was used to set the 8.9 milliradian bend on the septum crystal as discussed in section 6.3. The next step was the crystal alignment in FEH after the installation of the septum stand.

7.2.1 Base Plate Alignment

The technique described below was used in order to make crystal

alignment easier in FEH. The base plate in FEH was aligned at an angle of 2.5 milliradians to the horizontal plane and parallel to the beam direction. The other base plate in the M-Bottom pit was also aligned at an angle of 8.25 milliradians to the horizontal plane and parallel to the beam direction. The two angles 2.5 milliradians and 8.25 milliradians are the beam directions with respect to the horizontal plane at the FEH and M-Bottom pit respectively. When the septum stand is transferred from one base plate to the other, the crystal orientation with respect to the beam direction at the second location should remain the same as that at the first location. In other words, if the crystal is aligned in the M-Bottom pit then it should be aligned in FEH also. However, in practice because of the uncertainty of the base plate alignment the crystal may have to be scanned in a short region the size of which depends on the above uncertainty. This is about ± 1.0 milliradian for each base plate so that crystal scanning would be required only over an angular region of ± 2.0 milliradians.

7.2.2 Background Studies in the FEH

During the period of the septum crystal tests in the M-Bottom pit another crystal with a surface barrier semiconductor detector was installed in the beam line at the septum magnets location in the FEH. The particle energy loss in this detector displayed the expected Landau peak but it was superimposed on a large background coming from nearby beam lines. These beam lines are located within several feet of the septum magnets of the M-Bottom beam line. Figure 7.1 shows the energy loss spectrum obtained when the primary beam intensity was 1.0×10^{10}

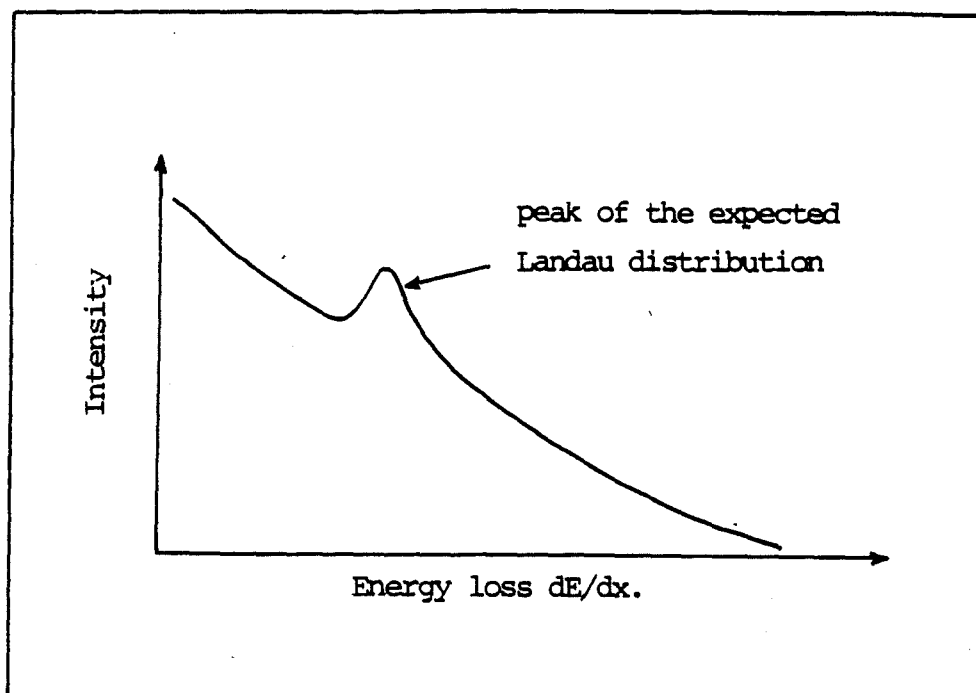


Figure 7.1 A sketch of the energy loss spectrum of the crystal detector mounted in between the two septum magnets (MB2D) during the crystal septum tests in the FEH. The small hump at the center is the expected Landau peak but it had been superimposed on a large background due to the particles that are coming from other beam lines.

particles per spill on the upstream target of M-Center beam line. Note that the detector was located about 160 feet downstream of the target at an angle of 2.5 milliradians to the incident beam direction on the target. The count rates of the detector was of the order of 5.0×10^5 per spill (5 seconds long).

The background in the energy loss distribution was due to particles that were coming from outside the M-Bottom beam line. They would travel across the detector and the lengths of their paths within the detector were shorter than the length of the detector along the beam line. Therefore these particles would deposit low energies in the detector. One possibility that was considered was to install a scintillation detector upstream or downstream of the septum crystal, so that the coincidence of both detector signals (scintillation detector signal and septum crystal fast signal) could be used to eliminate the background. If this method could clean up the low energy side of Landau distribution, the energy loss technique which has been described in section 6.2 could be used to perform the rest of the alignment of the septum crystal.

7.2.3 Decision to Use Kim Technique

Another possibility was to use the Kim technique in which the flux through the M-Bottom beam line itself is used to align the crystal. This method which has been explained in section 6.4 does not need the assistance of a detector incorporated in the crystal. In view of the complications caused by the background in the energy loss distribution in the energy loss scanning method it was decided to use the Kim

technique first. However, the following arrangements were made to use the energy loss scanning method with certain modifications in case the Kim technique failed.

7.2.4 Preparations to Use Energy Loss Technique

The scintillation detector T5 (Table 4.2) was attached to the septum stand about 10 cm downstream of the crystal along the bent direction. The dimensions of this detector are 5.0 mm, 1.0 mm and 3.0 mm in x, y and z directions, respectively, where the x and y axes are the horizontal and vertical axes perpendicular to the beam direction and z axis is along the beam direction. Another crystal with a detector called the 'fixed detector' was fixed vertically inside the septum goniometer box. The surface barrier semiconductor detector was 1.0 mm thick, 5.0 mm long and 3.0 mm wide along the x, y and z directions, respectively. A second scintillation detector T7 (Table 4.2) of 1.0 mm thick, 3.0 mm wide and 5.0 mm long along x, y and z directions, respectively, was installed about 30 cm upstream of the septum crystal. Figure 7.2 shows the schematic of the apparatus set up in FEH after the crystal septum installation. The dashed line shows the central beam line when the septum magnets are in operation. The central beam line for crystal septum in operation is shown by the solid line. The separation between the two central beam lines were calculated to be 0.5 inch at the crystal location. All the detectors were aligned along the central beam line for crystal septum operation.

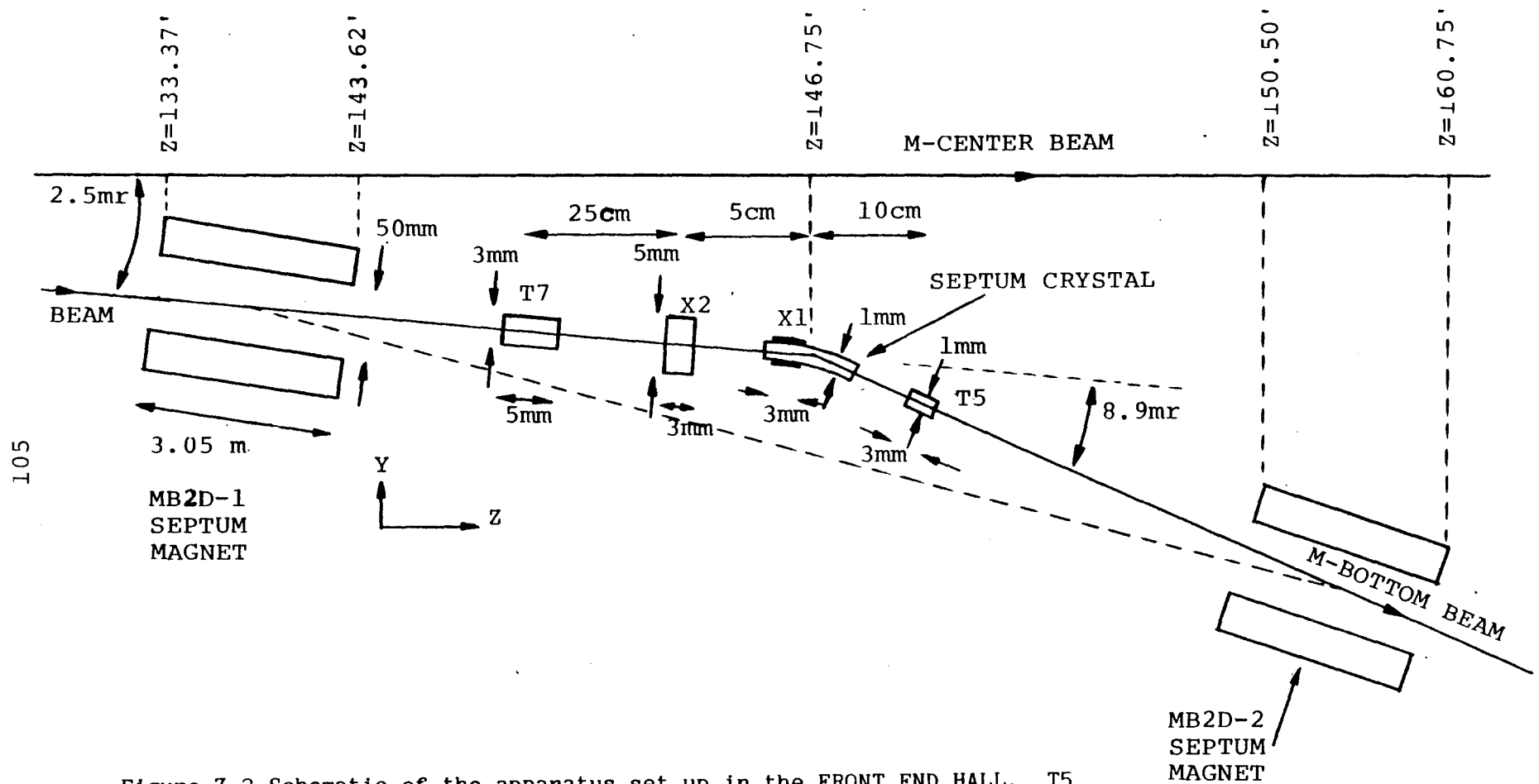


Figure 7.2 Schematic of the apparatus set up in the FRONT END HALL. T5 and T7 are scintillation detectors and X2 is the 'Fixed detector'. The dashed line represents the beam axis for septum magnet operation and solid line represents the beam axis for septum crystal operation.

7.2.5 Installation

The septum crystal was first aligned in the M-Bottom experimental pit using the low energy loss method discussed in section 6.2. Then the septum stand was moved to FEH and installed on the prealigned base plate between the septum magnets. The control system was reinstalled in the MS2 service building which is the nearest service building to the FEH. New cables were laid from the MS2 building to the septum location in FEH for two stepping motors, two scintillation detectors and two crystal detectors. All power supply units for detectors and electronic units were also installed in the MS2 building.

7.3 Input Beam for Crystal Septum Applications

The two computer programs 'TRANSPORT' and 'DECAY TURTLE' were discussed in Chapter 3. These two programs have been used to calculate beam element parameters and beam characteristics for crystal septum operation and the results have been compared with the observations. This section will discuss the input parameters to the above programs.

The crystal position is used as the input beam position in both programs. Crystal dimensions of 0.8 mm thickness and 12.0 mm width are used as the horizontal and vertical widths of the input beam. The angular acceptance normal to the crystal plane for channeling is determined by the critical angle of the crystal plane. Bent particles are assumed to be the channeled particles along the bent crystal length. These particles maintain their transverse energies constant while being channeled between the crystal planes. When channeled particles are transmitted through the channel their transverse energies

are still less than the critical transverse energy for channeling, therefore, the angular divergence normal to the crystal plane of the deflected particles is also determined by the critical angle. The half width of the vertical angular divergence of the input beam is assumed to be the critical angle at a given energy. Note here that the crystal is bent vertically downward. Since the angular acceptance parallel to the crystal planes for channeling is infinite, the half width of the horizontal divergence of the input beam is assumed to be the same as that of the horizontal angular divergence of the regular beam at the crystal location. This has a value of 0.35 milliradian (half width) which is determined by the horizontal aperture of the MB2S magnet for all energies, as discussed in Chapter 3. Table 7.1 gives the summary of the input beam parameters discussed above.

Table 7.1 Input beam parameters for crystal septum runs, used in 'TRANSPORT' and 'DECAY TURTLE' programs.

Horizontal beam width	12.0 millimeters
Vertical beam width	0.8 millimeters
Horizontal angular divergence (half)	0.35 milliradians
Vertical angular divergence (half)	critical angle
Initial beam x-coordinate	0.0
Initial beam y-coordinate	-0.415 inches
Initial beam z-coordinate	+146.75 feet
Initial beam horizontal angle	0.00
Initial beam vertical angle	-11.414 milliradians

7.4 Operation at 200 Gev/c

The first operation of the crystal septum at 200 Gev/c is discussed in this section. The primary beam momentum of the accelerator during the time of the following parts of the experiment was 400 Gev/c.

7.4.1 Crystal Alignment

After the installation of the crystal septum in the FEH the crystal was aligned using the Kim method as follows:

Beam trim elements were tuned with the septum magnets on for the regular 200 Gev/c beam. Then the septum magnets and the quadrupole magnets were turned off and the crystal was substituted. All the collimators were opened to their maximum slit sizes of 3.0 inches. When the crystal septum was in operation, the energy of the transmitted beam was determined by the vertical bending magnet MB2U (section 3.2). The crystal was rotated in steps of 40 microradians (8 goniometer steps) while recording the yield in the experimental pit. The coincidence of T1 and T3 (Figure 5.1) trigger counters were used to record the number of transmitted particles.

The scanning was continued until a peak was obtained in the spectrum. Alignment of the crystal was found to be about 500 microradians away from the expected position (installed position) as shown in Figure 7.3. The beam intensity at the peak was about 10 times higher than the background. The average number of particles outside the peak was always less than 5 per spill. The intensity on the M-Center target was of the order of 3.0×10^{11} particles per spill. The

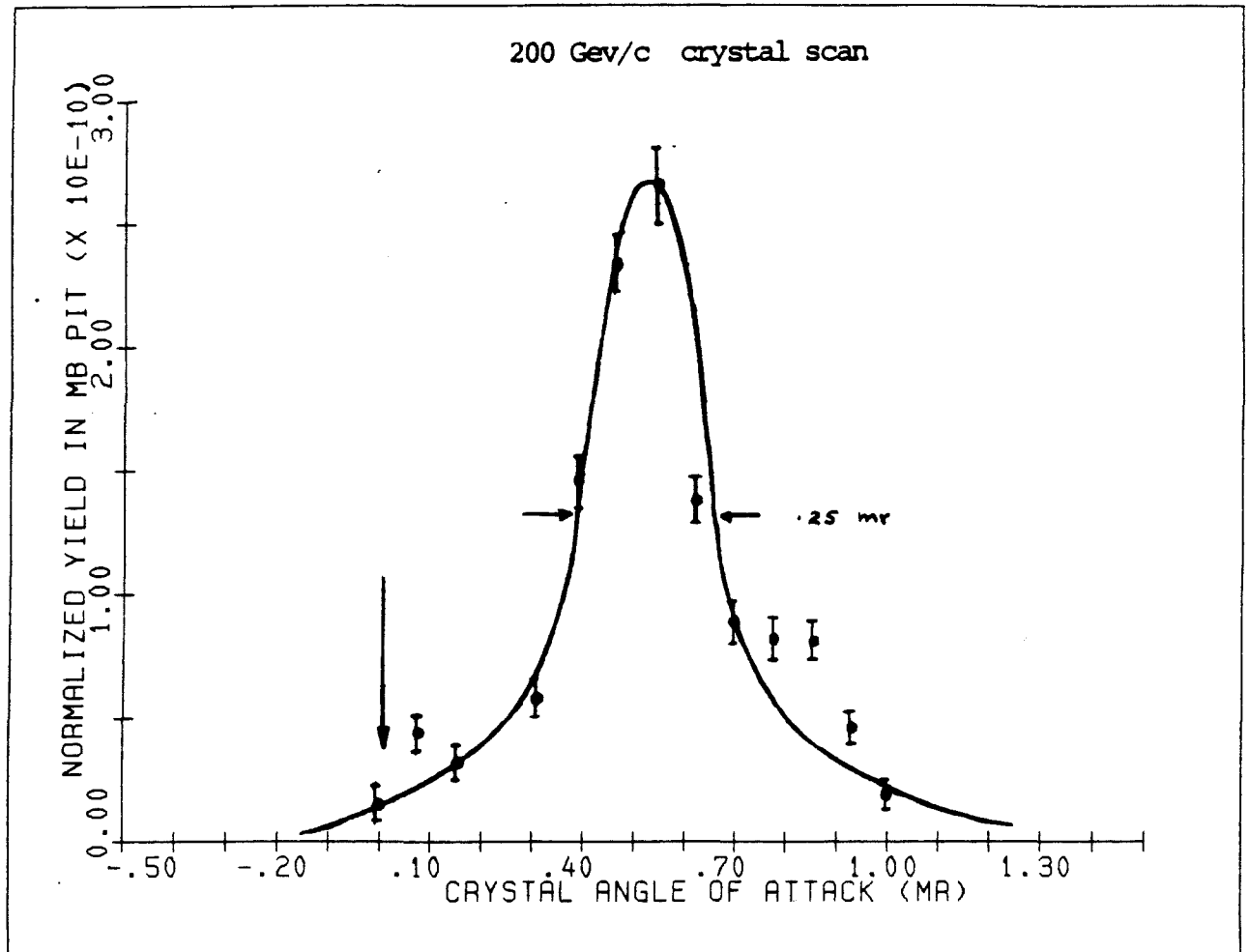


Figure 7.3 Scanning spectrum of the septum crystal in the FRONT END HALL at 200 Gev/c. Transmitted yield into the experimental pit was normalized to the intensity of the particles on the M-Center target. The arrow indicates the installed orientation of the crystal.

angular width of 250 microradians in Figure 7.3 is determined by the vertical angular divergence of the beam at the crystal location.

The program TRANSPORT (run no.1) was used to calculate the beam properties for a 200 GeV/c secondary beam without the quadrupole magnets. The vertical beam divergence at the crystal septum location was calculated to be 240 microradians. This agrees well with the observed vertical angular width of 250 microradians in crystal scanning.

7.4.2 Beam Divergence and Width Studies

Drift chamber data was recorded during the 200 GeV/c operation of the crystal septum (Table 5.5). About 60,000 events were logged on a magnetic tape using the T1.T3 trigger. Results of the off-line analysis are shown in Figure 7.4 (angular distributions), Figure 7.5 (spatial distributions) and Table 7.2 (observed beam properties). Also given in Table 7.2 are the beam properties calculated using the DECAY TURTLE program. According to the Figure 7.5 both beam widths are 2.0 inches (~50 mm) each. But that is the dimension of the T1 and T3 trigger counters used (Table 4.2). Therefore the beam size could not be determined from the data. The only thing certain was that both widths were larger than 2.0 inches.

The DECAY TURTLE program (run No.2) was used to simulate a beam transport system identical to the above case in which all quadrupole magnets were turned off and all collimators were fully opened (3.0 inches each). The input beam was described in section 7.3 for all crystal septum runs. The program was executed for 10,000 pions at

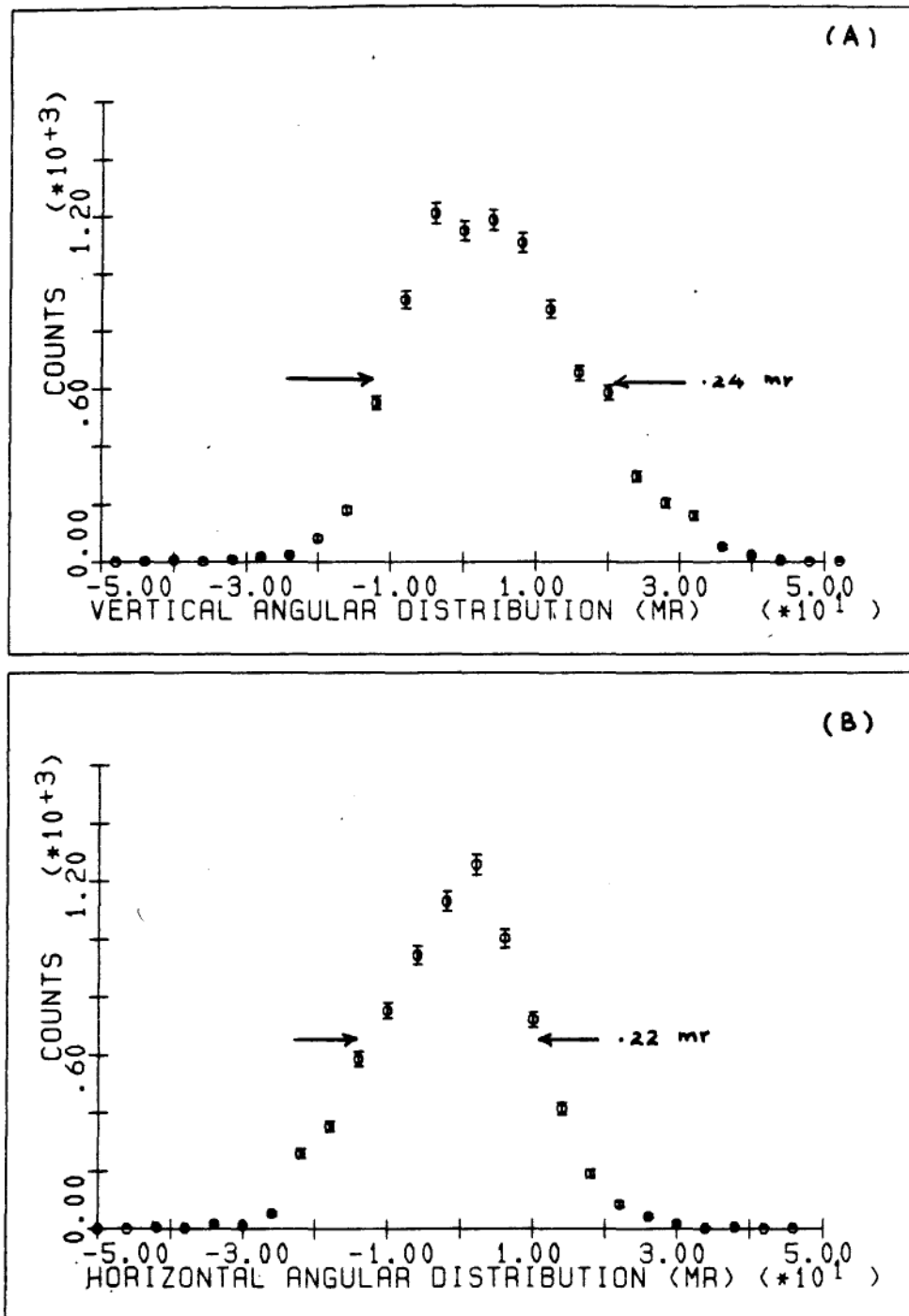


Figure 7.4 Observed (a) vertical and (b) horizontal angular distributions in the experimental pit for 200 GeV/c crystal septum operation. All quadrupole magnets were turned off and the collimators were fully opened during the data acquisition.

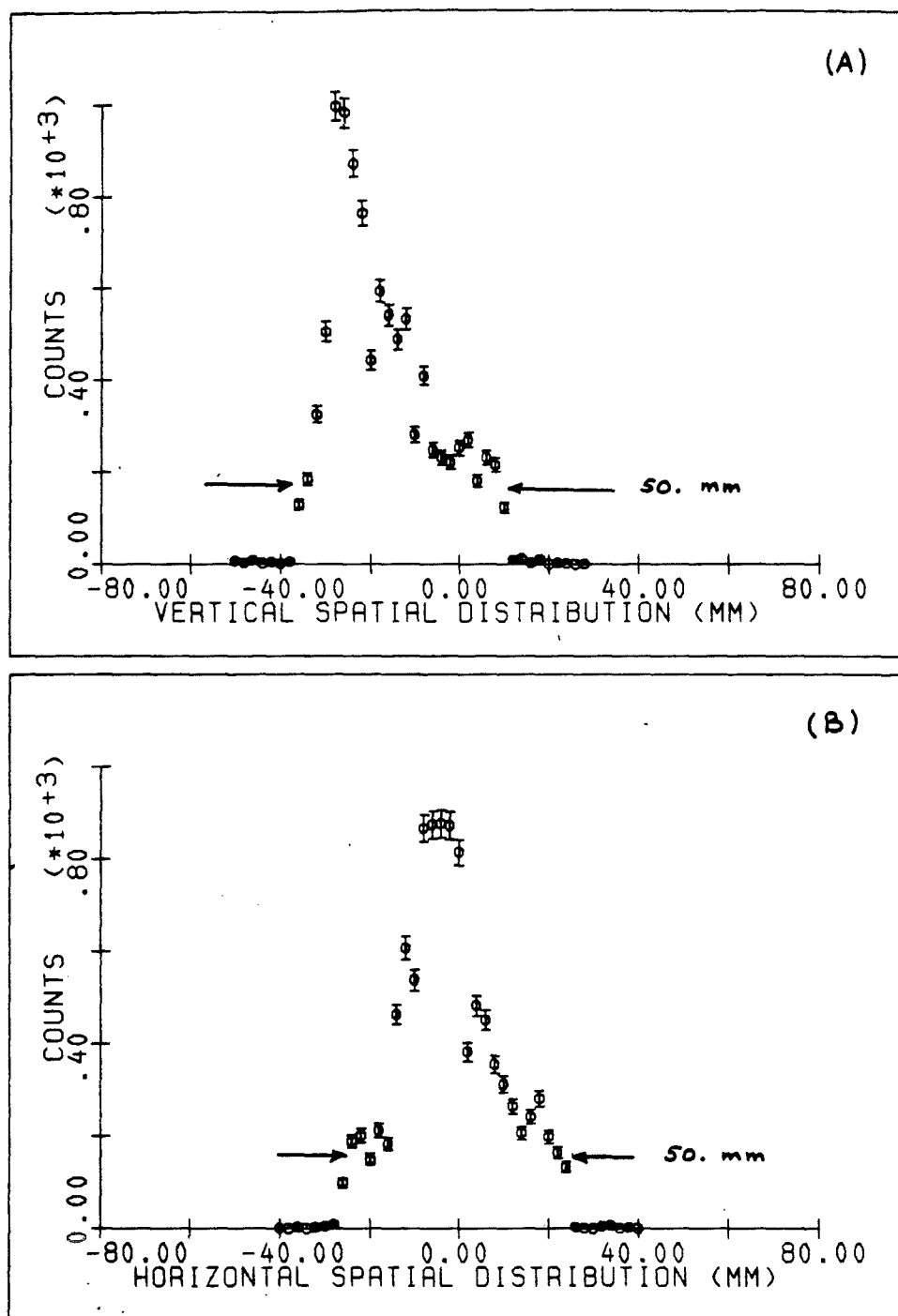


Figure 7.5 Observed (a) vertical and (b) horizontal spatial distributions in the experimental pit for 200 GeV/c crystal septum operation. All quadrupole magnets were turned off and the collimators were fully opened during the data acquisition. The 50 mm width of both distributions are due to the finite size of the T1 trigger counter used.

200 GeV/c with $\pm 5\%$ momentum spread. The histograms of angular and spatial distributions are shown in Figures 7.6 and 7.7. Table 7.2 (calculated without quadrupoles) shows the results. Observed angular divergences are in good agreement with the calculations. Calculated beam widths showed that they were greater than 2.0 inches. But exact comparisons are not possible as the trigger counters were only 2.0 inches wide.

Table 7.2 Observed and calculated beam properties in the experimental pit at 200 GeV/c crystal septum operation. Calculated values were obtained using DECAY TURTLE program.

	Observed	Calculated without Quadrupoles	Calculated with tuned Quadrupoles
horizontal angular divergence (FWHM)	0.22 mr	.23 mr	.40 mr
vertical angular divergence (FWHM)	0.24 mr	.28 mr	.20 mr
horizontal beam width	50.0 mm	95. mm	25. mm
vertical beam width	50.0 mm	105. mm	17. mm

7.4.3 Momentum Studies

Momentum studies were also carried out during 200 GeV/c crystal septum operation. Horizontal momentum spectrometer magnets (MB6EW) downstream of the experimental set up were used in this part of the experiment as shown in Figure 7.8. A scintillation detector T6 (Table 4.2) 6.0 mm wide (horizontally and perpendicular to the beam direction) was located about 15.25 m downstream of the first two MB6EW

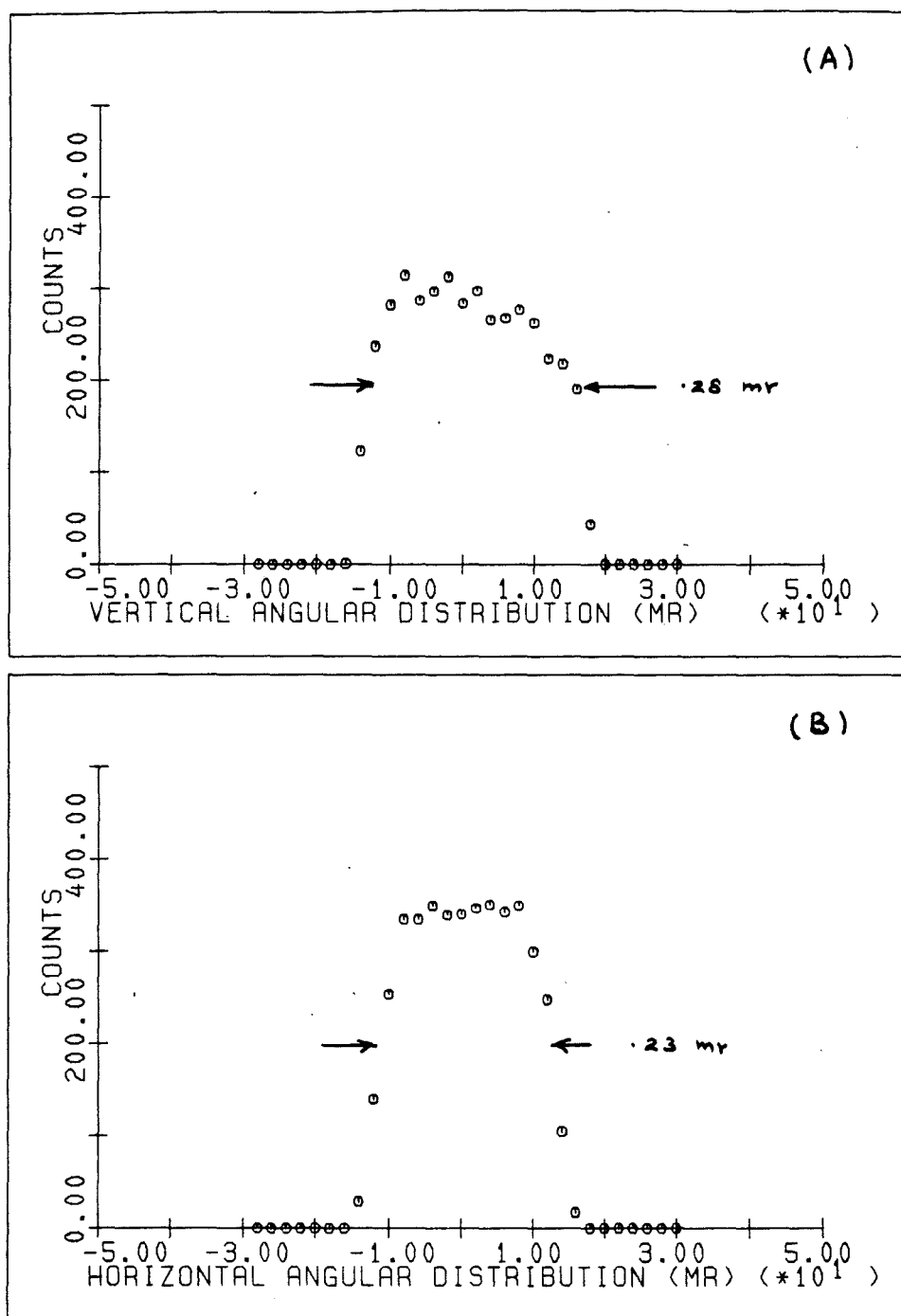


Figure 7.6 Calculated (a) vertical and (b) horizontal angular distributions using DECAY TURTLE program for 200 GeV/c crystal septum operation. Quadrupole magnets were not used and the collimators were opened to their maximum aperture sizes. Fraction of pions reaching the experimental pit was about 40% for a $\pm 5\%$ momentum dispersion.

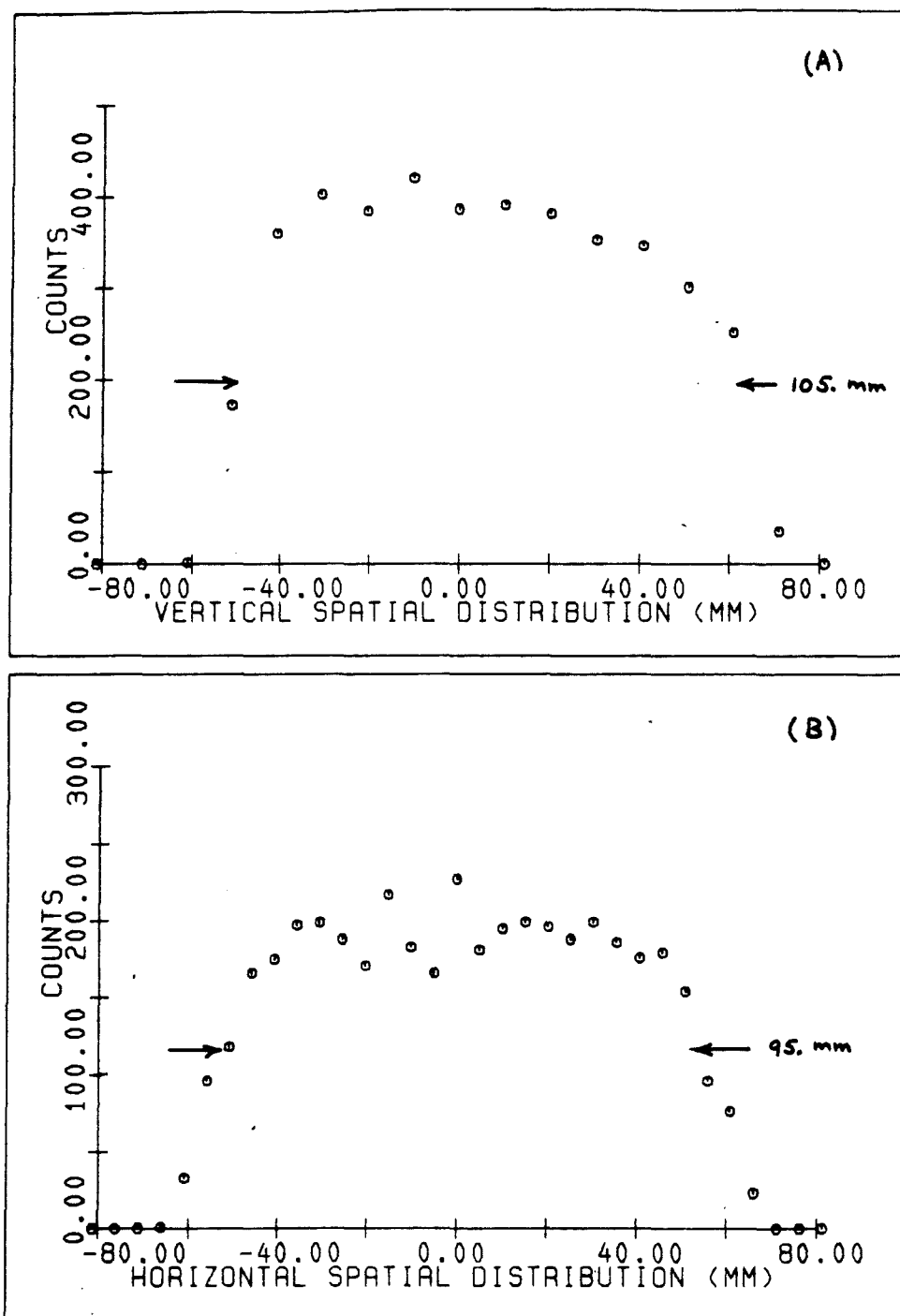


Figure 7.7 Calculated (a) vertical and (b) horizontal spatial distributions using DECAY TURTLE program for 200 GeV/c crystal septum operation. Quadrupole magnets were not used and the collimators were opened up to their maximum aperture sizes. Fraction of pions reaching the experimental pit was about 40% for a $\pm 5\%$ momentum dispersion.

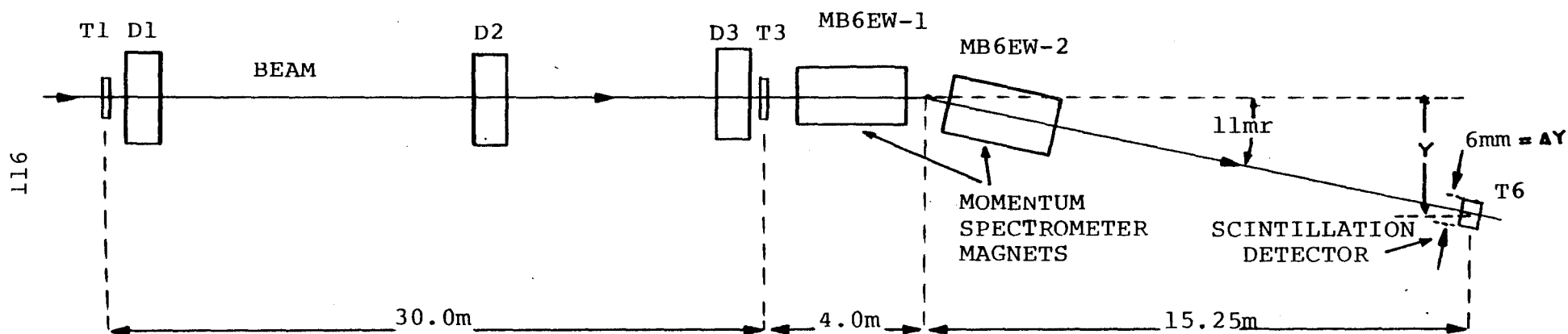


Figure 7.8 Schematic of the apparatus set up used for the momentum studies. The spectrometer magnets MB6EW bend the beam by 11.0 milliradians in regular operation. T6 is a scintillation detector that is 6 mm wide along the bent direction. D1, D2 and D3 are the three drift chambers and T1 and T3 are the trigger counters used in data acquisition.

magnets so that it was centered at an average angle of 11.0 milliradians to the straight beam direction.

The momentum acceptance of the crystal for channeling is very large. The vertical bending magnet (MB2U) controls the mean momentum of the transmitted beam. Figure 7.9(a) shows the distribution of on axis off momentum particles in $x-\Delta p$ space where x is the horizontal axis perpendicular to the beam direction and Δp is the momentum deviation from the mean. After passing through MB6EW magnets (horizontal bend) the same distribution is shown in Figure 7.9(b). Here $x=0$ always refer to the central beam line. The x position of the T6 counter is also shown in Figure 7.9(b). Changing the current in the magnets by an amount of ΔI would move the distribution across the detector (along the x -direction) by a distance Δx as shown in Figure 7.9(c). Then the horizontal displacement Δx with respect to the T6 detector causes the beam particles of momentum deviation Δp to hit the detector. The relationship between ΔI and Δp can be written as

$$\delta(\Delta p) = 0.1717 \Delta I \quad 7.1$$

where p is the momentum of particles which are bent at an angle of 11.0 milliradians (along the central beam line) and I is the corresponding current in MB6EW magnets. This equation was obtained by using the field integral of MB6EW magnets.

By changing the current in the magnets and measuring the yield of particles hitting the T6 detector the width of the momentum dispersion can be measured. A coincidence of T1.T3.T6 was used to measure the fraction of the number of particles hitting the detector with respect

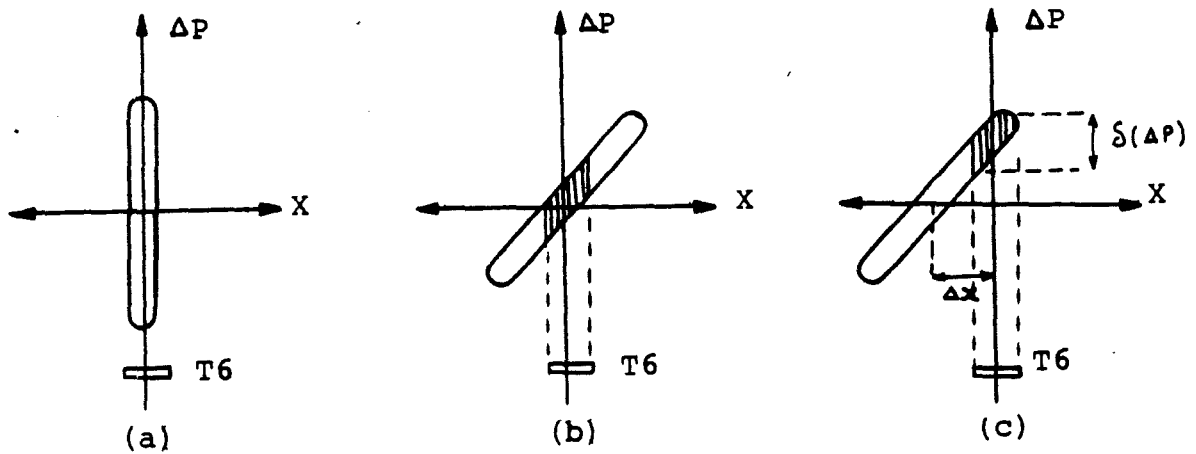


Figure 7.9 (a) Momentum distribution of 'on axis' rays of the beam where x is the horizontal coordinate with respect to the beam axis and Δp is the deviation of momentum from the mean. (b) The same distribution after passing through the spectrometer magnets. The detector T6 sits on the beam axis. (c) The same distribution due to a current change of ΔI in the spectrometer magnets.

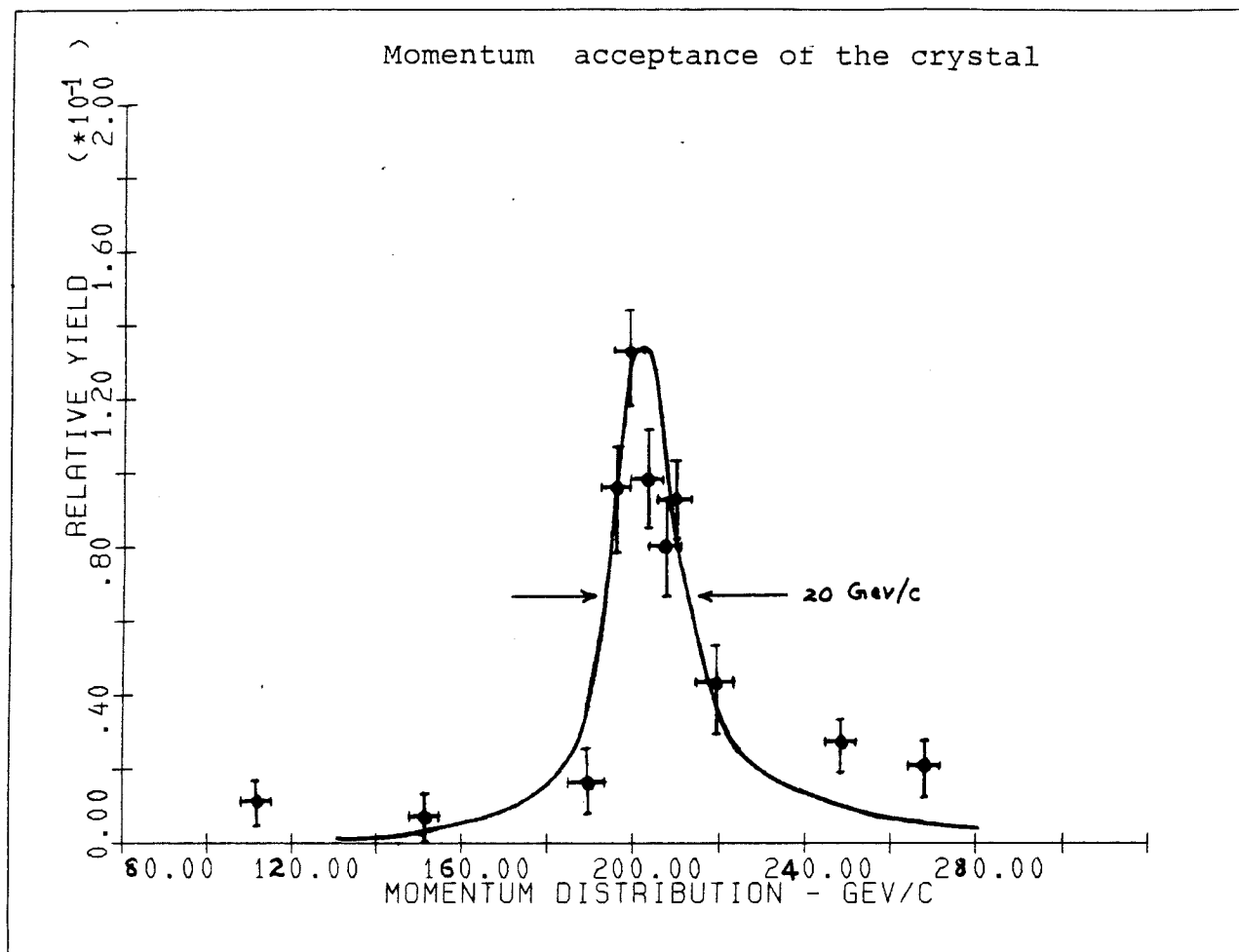


Figure 7.10 Momentum distribution for 200 GeV/c crystal septum operation measured using the momentum spectrometer magnets MB6EW.

to the total number of particle transmitted to the pit which was measured by the coincidence of T1.T3. For a fixed value of the current in the magnet, the momentum p is inversely proportional to the deflection (y) of the beam at the detector position, therefore the momentum resolution due to the thickness of the the detector can be calculated by

$$\delta(\Delta p) = (\Delta y/y)p \quad 7.2$$

where Δy ($=6.0$ mm) is the thickness of the detector. This value is 2.5 Gev/c at a mean momentum of 200 Gev/c. The data is shown in Figure 7.10 according to which the observed fractional momentum deviation is about $\pm(5.00 \pm 1.25)\%$.

The vertical bending magnet MB2U as shown in Figure 7.11 disperses the momentum vertically. Then the momentum collimator MB3CV determines the momentum acceptance of the transmitted beam into the experimental pit. The aperture size of this collimator was 0.5 inch during the data acquisition for momentum studies. TRANSPORT (run No.3) was used to calculate the momentum dispersion for 200 Gev/c crystal septum operation. The results showed that the fractional momentum deviation was $\pm 5\%$ for an opening of 0.5 inch on the momentum collimator slit (MB3CV). This agrees with the observed deviations. Figure 7.11 shows the beam optics for crystal septum operation at 200 Gev/c with all the quadrupole magnets off.

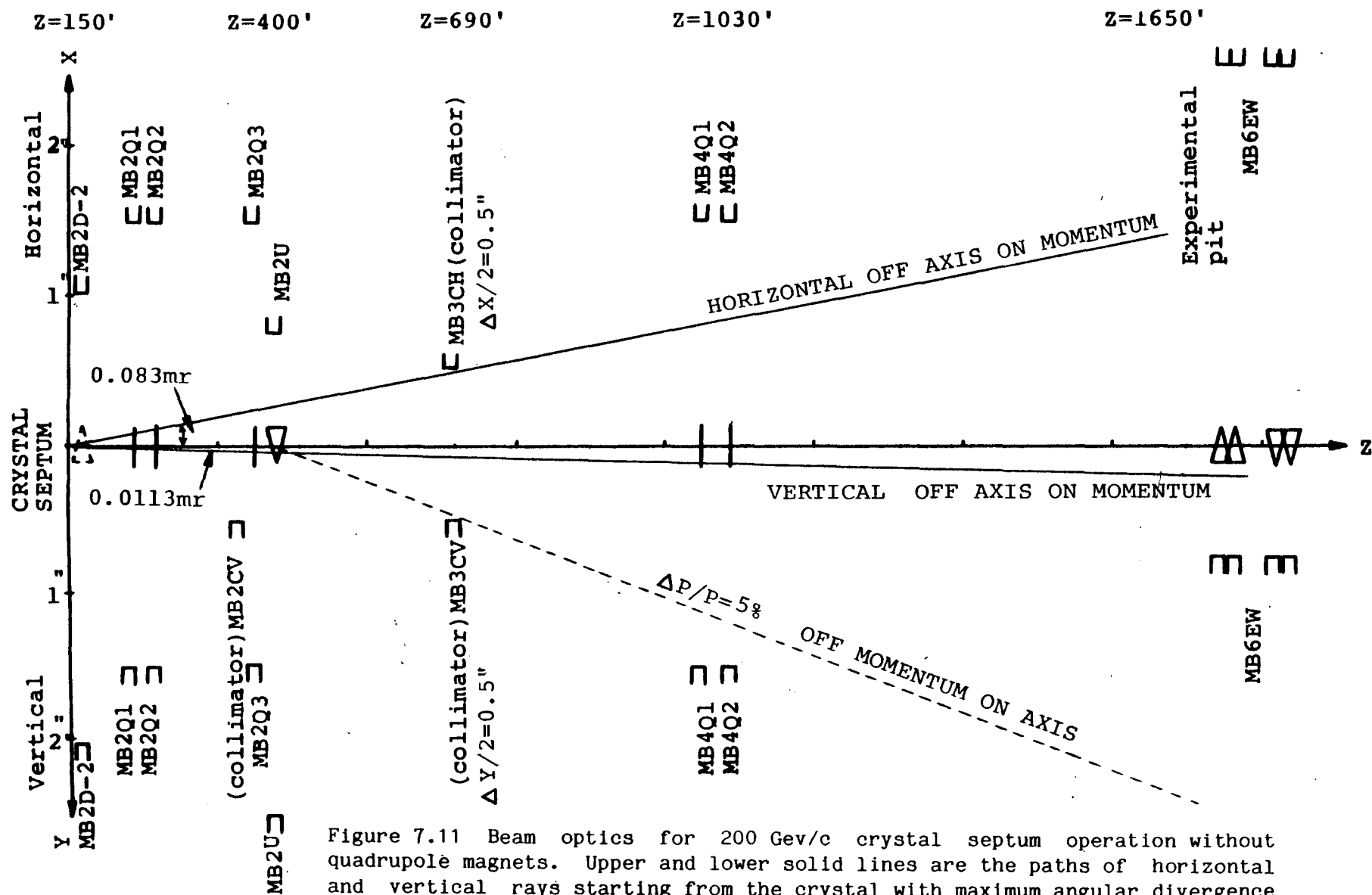


Figure 7.11 Beam optics for 200 GeV/c crystal septum operation without quadrupole magnets. Upper and lower solid lines are the paths of horizontal and vertical rays starting from the crystal with maximum angular divergence (on momentum off axis). The broken line is the momentum dispersion for $\pm 5\%$ change in momentum (off momentum on axis).

7.4.4 Momentum Recombination and Focusing

TRANSPORT (run No.4) was used to calculate the magnetic fields of quadrupole magnets for momentum recombination and focusing the beam for crystal septum operation at 200 GeV/c.

The half width of the vertical angular divergence of the input beam for crystal septum operation is the critical angle of the crystal plane as explained in section 7.3. The critical angle at 200 GeV/c is 11.3 microradians which is very small compared to the regular vertical divergence of 250 microradians at the crystal location. The calculated vertical dispersion due to the vertical angular divergence of 11.3 microradians is 0.4 inch in the experimental pit at 200 GeV/c. Since all vertical apertures in the beam line are greater than 0.4 inch (the minimum is 1.5 inches), focusing of 'off axis' rays in the vertical plane is not necessary as far as the beam intensity is concerned. Since the horizontal angular acceptance of the crystal is infinite, focusing in that plane would increase the transmitted yield. Also in principle the crystal can transmit a large spread in momentum. Therefore, it should be possible to improve the crystal septum momentum acceptance and the transmitted yield by proper tuning of the quadrupole magnets.

The input beam for crystal septum operation was discussed in section 7.3. The following constraints were applied when executing the TRANSPORT program:

1. Intermediate horizontal focusing at momentum collimators (MB3CH) by using the quadrupole triplet MB2Q1, MB2Q2 and MB2Q3.
2. Final horizontal focusing and momentum recombination in the

experimental pit by using the quadrupole doublet MB4Q1 and MB4Q2.

Figure 7.12 shows the beam optics constructed from the results for horizontal point to point to point focusing and momentum recombination at 200 Gev/c. The vertical 'off axis on momentum' ray is defocused by the quadrupole triplet and gives a dispersion of 0.25 inch per $\pm 5\%$ momentum dispersion at the momentum collimator. The horizontal 'off momentum on axis' ray gets focused in the experimental pit while the vertical 'off axis on momentum' ray gets focused about 100 feet upstream of the pit as shown in Figure 7.12. This can be explained by beam optics. Here the quadrupole doublet acts as a convex lens to focus both horizontal and vertical rays. Since the vertical ray has a larger object distance than the horizontal ray it converges at a shorter distance than the horizontal ray. Table 7.3 shows the magnetic fields and corresponding currents in quadrupole magnets.

Table 7.3 Magnetic field gradients and corresponding currents of quadrupole magnets for horizontal point to point to point and momentum recombination at 200 Gev/c crystal septum operation.

Quadrupole Magnet	Magnetic Field B(KG/IN)	Current (Amperes)
MB2Q1	+0.669	12.8
MB2Q2	+1.087	20.8
MB2Q3	+0.667	12.8
MB4Q1	-3.556	68.3
MB4Q2	+3.665	70.0

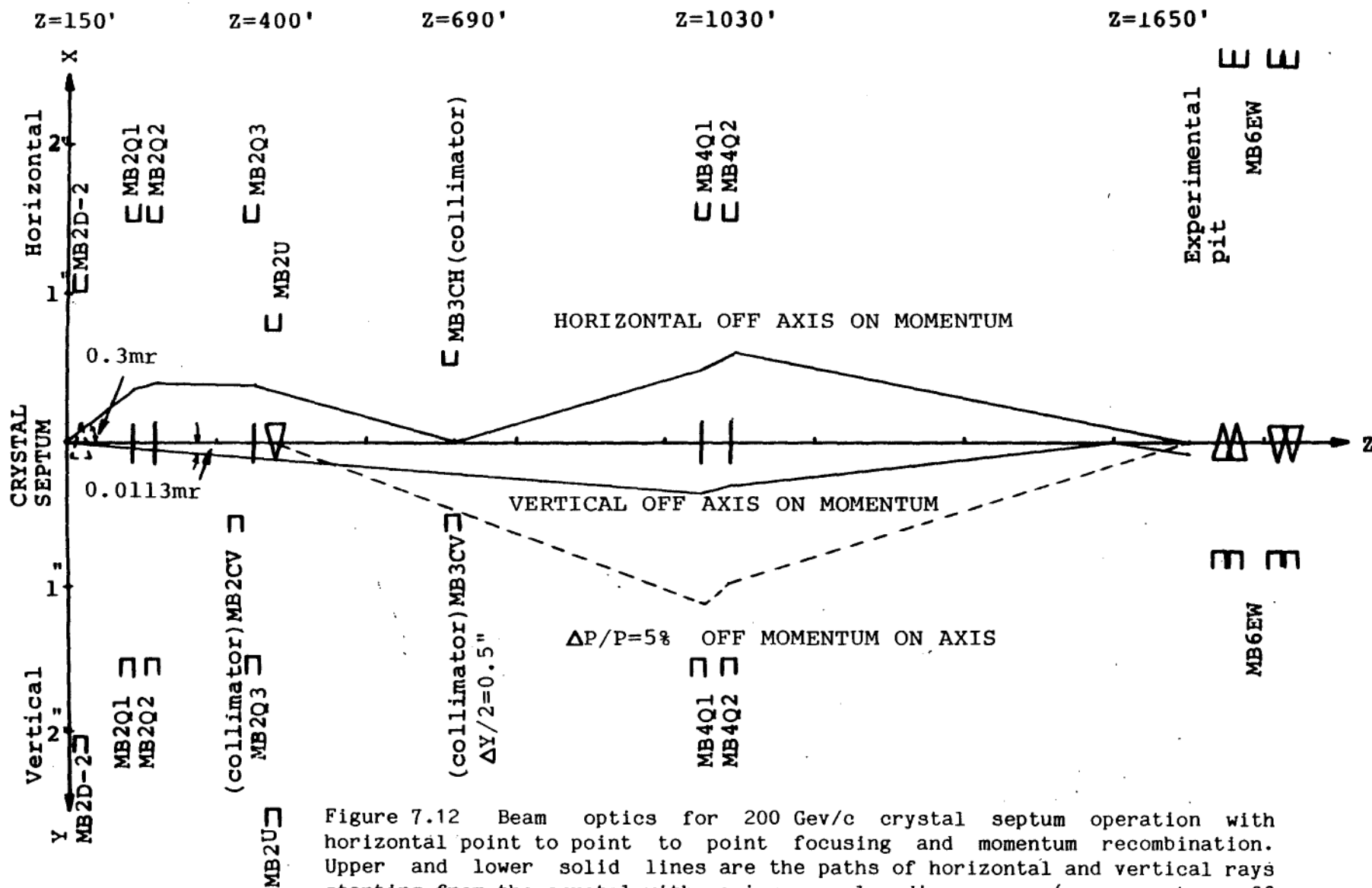


Figure 7.12 Beam optics for 200 GeV/c crystal septum operation with horizontal point to point to point focusing and momentum recombination. Upper and lower solid lines are the paths of horizontal and vertical rays starting from the crystal with maximum angular divergence (on momentum off axis). Broken line is the momentum dispersion for $\pm 5\%$ change in momentum (off momentum on axis).

The calculated magnetic fields were used to run DECAY TURTLE program (run No.5) to find the beam distributions in the experimental pit. The program was executed for 10,000 pions starting from the crystal. Figures 7.13 and 7.14 show the angular and spatial distributions one should expect if the quadrupole magnets were properly tuned. The momentum dispersion was assumed to be $\pm 5\%$ from the mean momentum of 200 GeV/c. The observed and calculated (with and without the quadrupoles) beam characteristics are shown in Table 7.2.

7.4.5 Beam Intensity Studies

According to the TRANSPORT run No.1 (section 7.4.1) beam properties at the crystal location are shown in the second column of Table 7.4. The horizontal and vertical spatial acceptance of the crystal are determined by the physical width and the thickness of the crystal. The vertical angular acceptance for channeling is determined by the critical angle at the given energy while the horizontal angular acceptance for channeling is determined by the angular divergence of the beam at the crystal location (the crystal was bent vertically) as discussed in section 7.3. The third column of Table 7.4 shows the beam acceptance of the crystal at 200 GeV/c (0.08 spatial and 0.09 angular). From the through-put studies of the crystal septum in the M-Bottom pit the bending efficiency and capture efficiency are 0.07 and 0.55 at 200 GeV/c (Table 5.4). Therefore, the fraction of particles transmitted into the beam line is equal to 0.00027 ($= .08 \times .09 \times .07 \times .55$).

During the momentum studies beam intensities were recorded for regular and crystal operation under the identical beam element

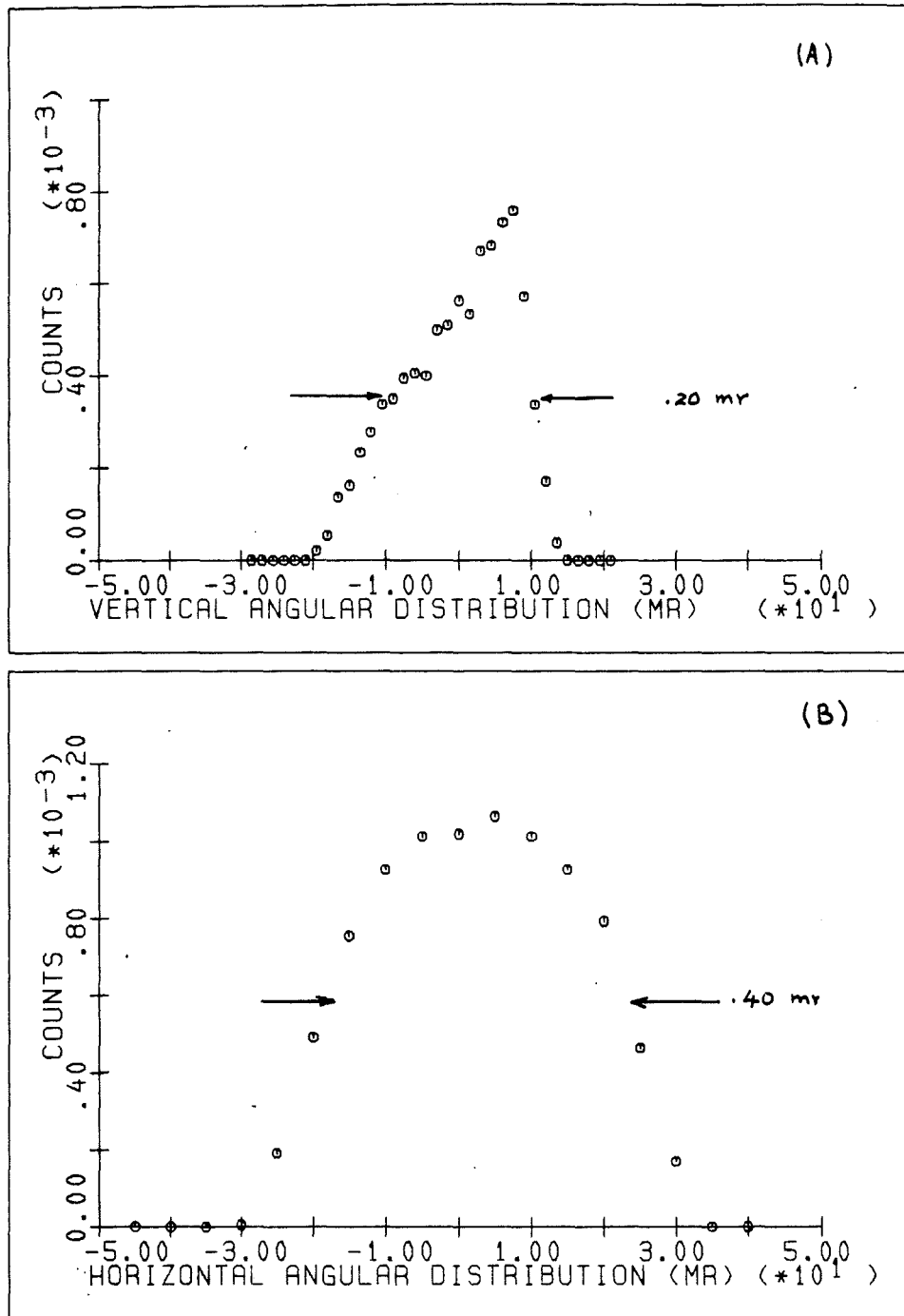


Figure 7.13 Calculated (a) vertical and (b) horizontal angular distributions using DECAY TURTLE program for 200 GeV/c crystal septum operation with tuned quadrupole magnets. The fraction of pions reaching the experimental pit was 80% for a $\pm 5\%$ momentum dispersion.

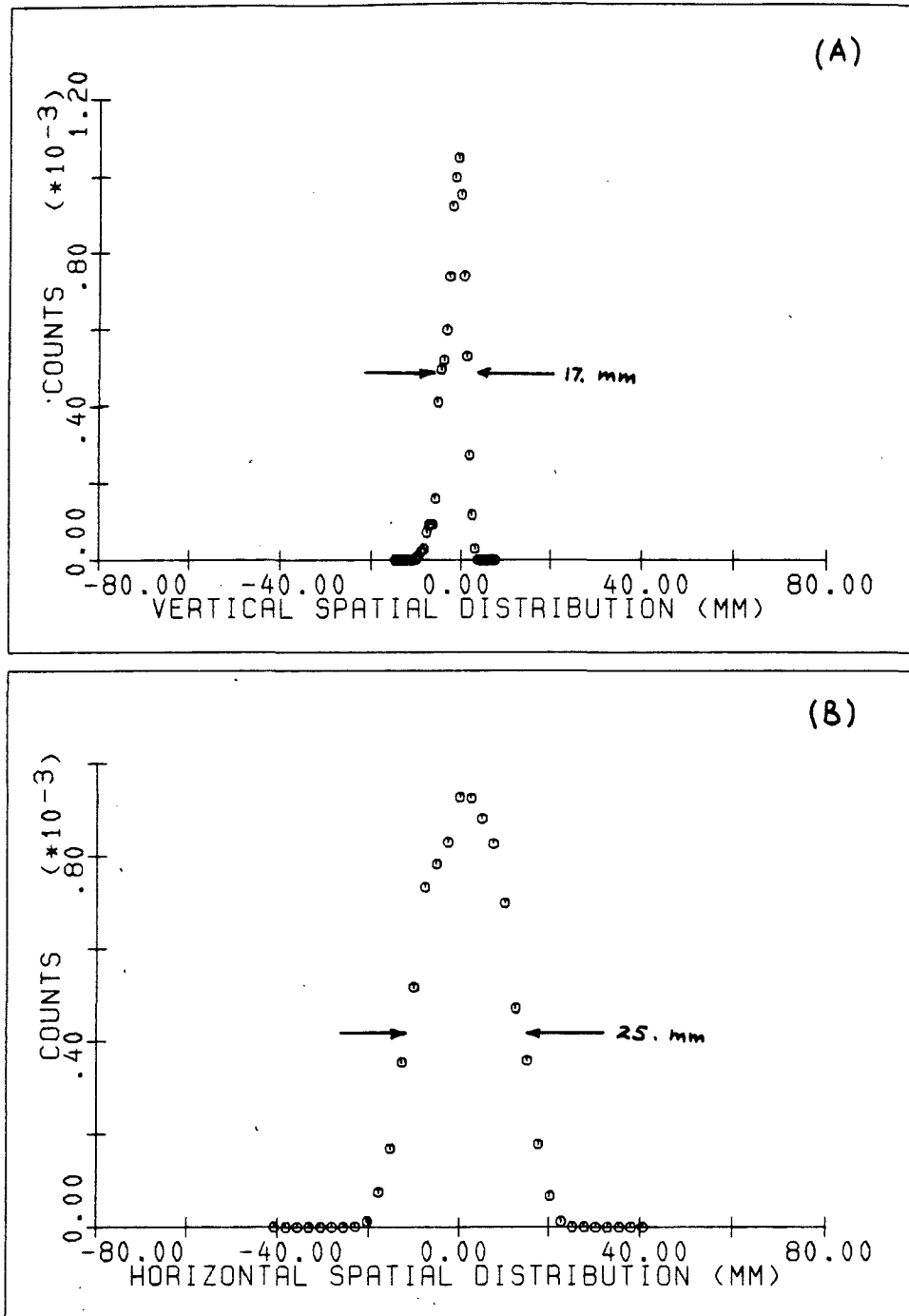


Figure 7.14 Calculated (a) vertical and (b) horizontal spatial distributions using DECAY TURTLE program for 200 GeV/c crystal septum operation with tuned quadrupole magnets. The fraction of pions reaching the experimental pit was 80% for a $\pm 5\%$ momentum dispersion.

settings. The collimators MB3CV and MB3CH were set for a half aperture size of 0.5 inch for both cases and Table 7.5 shows the recorded data for T1.T3 coincidence setting. According to the data the transmission fraction for crystal operation with respect to regular operation was $0.00039 (= 7.30 \times 10^{-10} / 1.88 \times 10^{-6})$.

Table 7.4 Beam divergences and widths at the crystal location and crystal acceptances for channeling at 200 GeV/c.

	Beam at Crystal Location	Crystal Acceptance	Fractional Acceptance
horizontal width	1.00 cm	1.00 cm	1.00
horizontal divergence	0.30 mr	0.30 mr	1.00
vertical width	1.00 cm	0.08 cm	0.08
vertical divergence	0.24 mr	0.022 mr	0.09

Table 7.5 Recorded beam intensities in the experimental pit for regular operation with tuned quadrupole magnets and crystal operation without quadrupole magnets at 200 GeV/c.

	MCISEM	T1.T3	T1.T3/MCISEM
regular operation	2.465×10^{11}	4.63×10^5	1.88×10^{-6}
crystal operation	3.384×10^{11}	2.47×10^2	7.30×10^{-10}

DECAY TURTLE run No.2 and run No.5 were discussed in sections 7.4.2 and 7.4.4. Run No.2 was executed without quadrupole magnets and Run No.5 was executed with tuned quadrupole magnets. In both cases the horizontal half angular width of the input beam and the horizontal half

aperture size of the MB3CH collimator were 0.35 milliradian and 0.5 inch, respectively. According to the calculations about 40% of particles are found to be transmitted in the 'without quadrupole' case while 80% of particles are found to be transmitted in the 'tuned quadrupole' case. About 5% of the pions decay before reaching the experimental pit and the rest are stopped due to the apertures of the elements in the beam line which is a factor of two higher. On the other hand, according to the Figure 7.11 the horizontal angular acceptance (half width) of the system is 0.08 milliradian for the 0.5 inch half width size of MB3CH. This scales to be 0.24 milliradian for a value of 1.5 inches half width of MB3CH. This change in angular acceptance of the system would increase the yield by nearly a factor of two, which agrees with the above calculation.

The observations (without the quadrupoles) were made in an area of 50mm x 50mm (area of T1 and T3 counters). However, the calculations (run no.2) show that the beam should be about 100 mm x 100 mm which is a factor of four higher than the area of T1 detector. Therefore, taking the above two factors into account the properly tuned quadrupole magnets should deliver a yield of about a factor of eight greater than the number observed on the detector T1. This means the crystal septum operation at 200 GeV/c would transmit about 2000 particles per 3.0×10^{11} MC1SEM.

7.5 Operation at 400 Gev/c

Of the two bending magnets (MB2D and MB2U) of the M-Bottom beam line the first, namely the MB2D septum magnet, has an upper limit of 225 Gev/c. Therefore, even though the upper limit of the second bending magnet MB2U (upper limit 500 Gev/c) is above 225 Gev/c the beam line can handle energies up to 225 Gev only. By replacing the MB2D septum magnet with a crystal it would be possible to increase the operational limit of the beam line to about 500 Gev/c. With this in mind the performance of the crystal septum was tested at an energy of 400 Gev.

7.5.1 400 Gev/c Beam in M-Bottom Beam Line

With all the quadrupole magnets off and the MB2U dipole magnet at the 400 Gev/c setting, the crystal was scanned while recording the particle yield in the experimental pit using the coincidence of the T1 and T3 counters. The resulting spectrum is shown in Figure 7.15.

Unlike the previous case of 200 Gev/c in the present case of 400 Gev/c the number of particles that enters the secondary beam are the scattered protons due to target nuclei. Therefore, the elastic scattering has to be taken into account in the computations. The elastic scattering of protons by those of the target nuclei obeys the relation [36].

$$\frac{d\sigma}{dt} = A e^{-bt} \quad 7.3$$

where σ is the elastic cross section of p-p, A and b are constants, $t = (p\theta)^2$, p is the momentum and θ is the scattering angle. The values

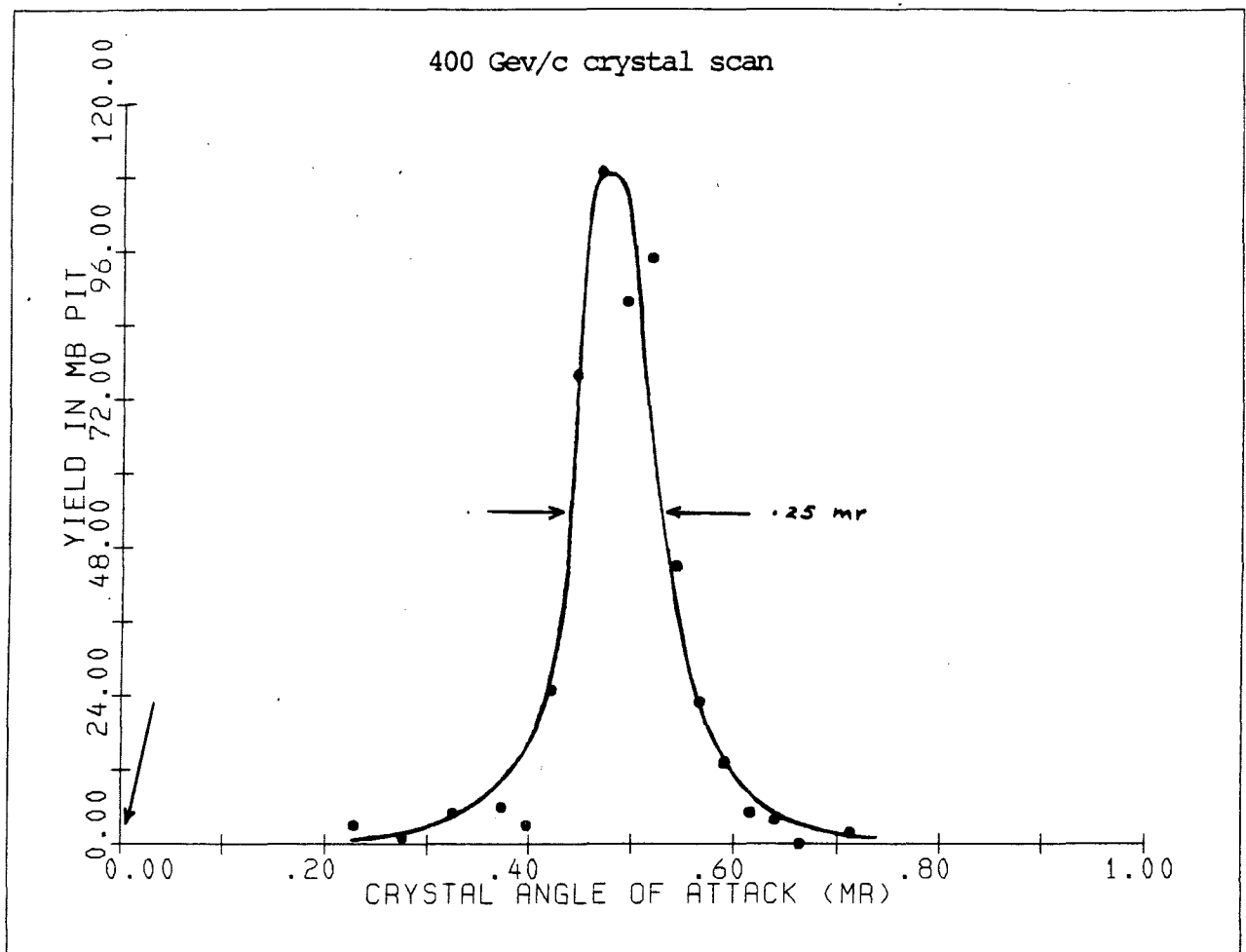


Figure 7.15 Scanning spectrum of the septum crystal in the FRONT END HALL at 400 Gev/c. The arrow indicates the installed orientation of the crystal.

of the constants A and b have been determined from experimental data by different experimenters for different ranges of t [36-42]. In the present case of 2.5 milliradians production angle and 400 GeV/c momentum the value of t is 1.0 (GeV/c)^2 . It should be noted that the experimental data was not reported for this combination of ranges. However, we have been compelled to use values of A and b reported there as more pertinent values have not been reported. This introduces a certain degree of uncertainty in to the calculations. The best fit values for A and b from the above references are $A = 100 \text{ mb/}(\text{GeV/c})^2$ and $b = 11.8 \text{ (GeV/c)}^{-2}$. These were used to compute the scattering yields and the results are presented in Figure 7.16. The crystal location 160 feet downstream of the target folded with the cross sectional area of 12.0 mm by 0.8 mm ($=9.6 \text{ mm}^2$) were used to calculate the solid angle subtended by the crystal on the target which is 0.004 microsteradian. The scattered yield was calculated over this solid angle. The important feature that should be noted is that the scattering yield increases drastically with decreasing angle.

It was felt desirable to acquire data at a smaller angle of scattering because this would cause an increased yield. The angle of scattering could be reduced by using the MC1D magnet upstream of the target. In regular operation it bends the primary beam down so as to make it horizontal and in this configuration (Figure 3.1) it is the secondary particles produced at 2.5 milliradians that are sent through the beam line. By increasing the current in MC1D magnet the primary beam could be bent down further leading to a reduction of the angle of deflection of the particles entering the beam line.

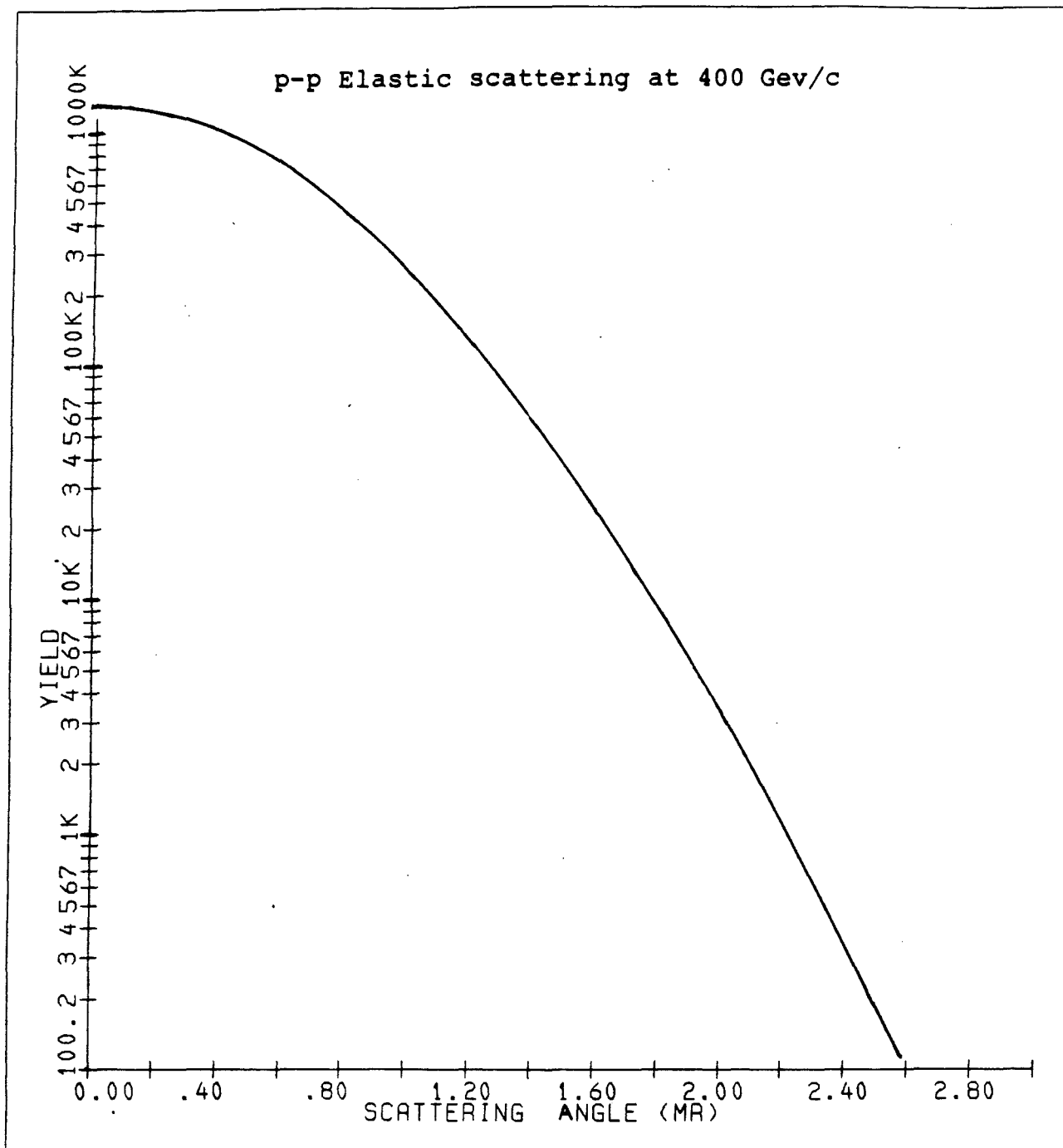


Figure 7.16 Calculated scattered proton yield incident on the crystal septum for different scattering angles for 400 GeV/c incident protons.

In regular operation the current setting of MC1D magnet is 440 Amperes. This value was increased up to the maximum permissible (due to radiation considerations) limit of 980 Amperes. Figure 7.17 shows the configuration after this increase where the beam line is deflected from the primary beam (at the target) by 0.7 milliradian instead of 2.5 milliradians in the regular set up. This arrangement resulted in transmitting about 10,000 particles per spill into the experimental pit at 3.0×10^{11} particles on MC1SEM. This yield is about a factor of hundred higher than the yield observed in the regular set up according to Figure 7.15. The calculated yield at 0.7 milliradian is about a factor of thousand higher than the one at 2.5 milliradians according to Figure 7.16. This would explain the increase of the particle yield going from 2.5 milliradians deflection angle to about 0.7 milliradian, however, the extra factor ten could be due to several reasons, such as (1.) uncertainty of the values of A and b used in equation 7.3, (2.) uncertainty of the angle 0.7 milliradian which is not very well understood and (3.) experimental errors.

7.5.2 Momentum Recombination and Focusing

Momentum recombination and focusing for the 200 GeV/c beam was discussed in section 7.4.4. Similar calculations for 400 GeV/c beam will be discussed in this section. The input beam for crystal septum operation was discussed in section 7.3. The critical angle, which is 8.0 microradians at 400 GeV/c, is assumed for the vertical beam divergence at the crystal location. The following constraints were applied when executing the TRANSPORT program (run No.6).

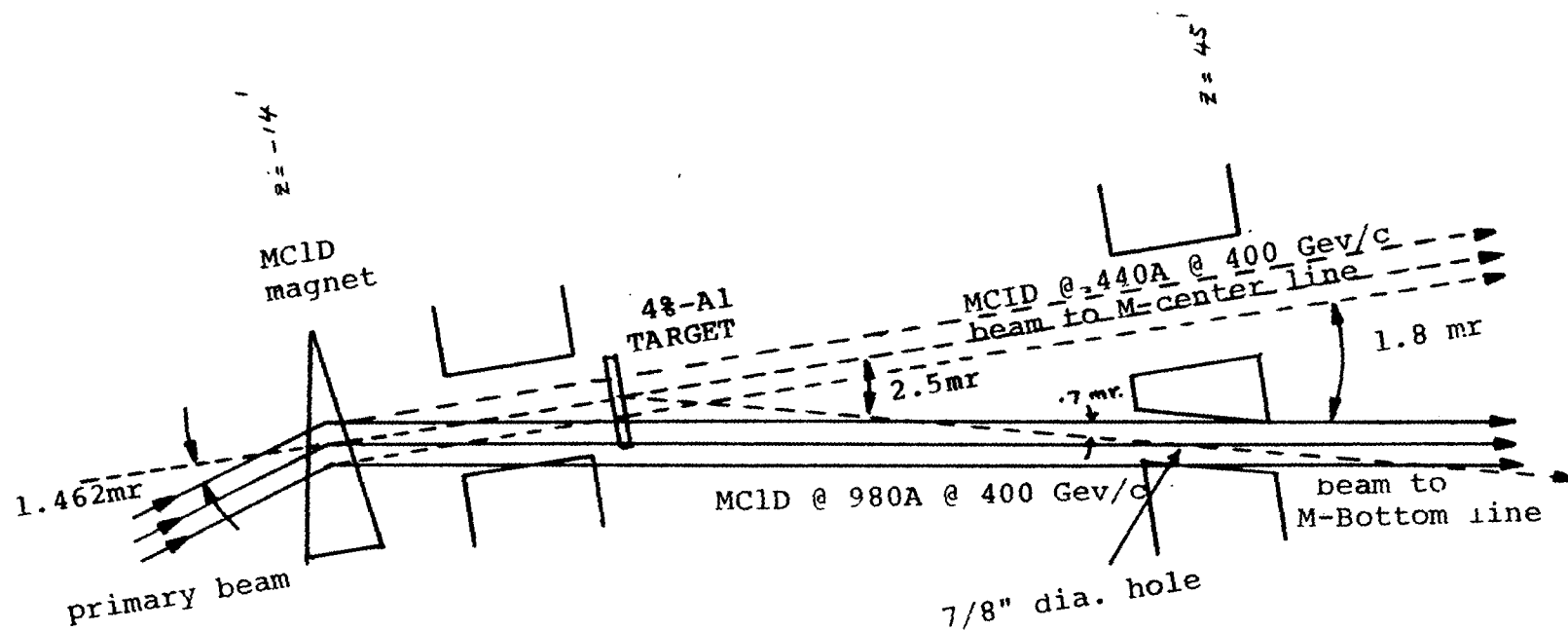


Figure 7.17 The schematic of the set up in the Front End Hall near the MC1D magnet. The solid line shows the beam direction for increased current setting in the MC1D magnet. This configuration reduces the deflection angle of the beam line from 2.5 milliradians to 0.7 milliradians.

1. Intermediate horizontal focusing at the momentum collimators (MB3CH) by using the quadrupole triplet MB2Q1, MB2Q2 and MB2Q3.
2. Final horizontal focusing and momentum recombination in the experimental pit by using the quadrupole doublet MB4Q1 and MB4Q2.

Figure 7.18 shows the beam optics for 400 GeV/c horizontal point to point to point focusing and momentum recombination. Table 7.6 shows the field gradients and corresponding currents of the quadrupole magnets. The second column in this Table shows the maximum possible currents of these magnets. It shows that, since the calculated values of the quadrupole doublet currents are exceeding the maximum currents, this configuration is not practicable.

Table 7.6 Magnetic field gradients and corresponding currents of quadrupole magnets for 400 GeV/c crystal septum operation.

Quadrupole Magnet	Maximum Current Amperes	Horizontal Point-Point-Point and Momentum Recombination		Horizontal Point-Point and Momentum Recombination	
		Magnetic Field B(kG/in)	Current (Amperes)	Magnetic Field B(kG/in)	Current (Amperes)
MB2Q1		+3.58	69.	+1.74	33.
MB2Q2		+0.67	13.	+1.28	25.
MB2Q3		+0.67	13.	+0.87	17.
MB4Q1	80.0	-7.13	136.	-4.32	80.
MB4Q2	80.0	+7.03	134.	+3.54	68.

Instead of horizontal point to point to point focusing, horizontal

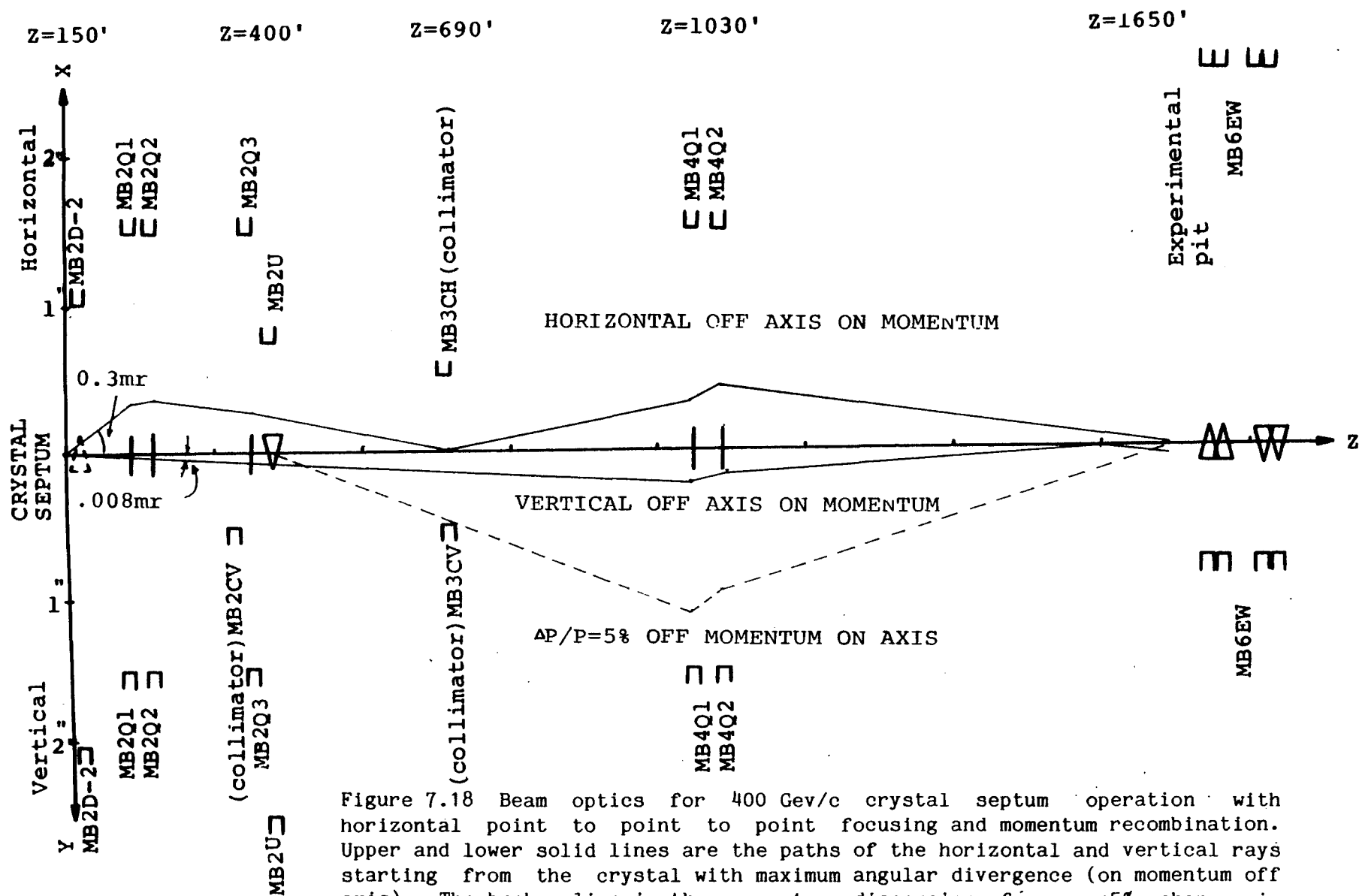


Figure 7.18 Beam optics for 400 GeV/c crystal septum operation with horizontal point to point to point focusing and momentum recombination. Upper and lower solid lines are the paths of the horizontal and vertical rays starting from the crystal with maximum angular divergence (on momentum off axis). The broken line is the momentum dispersion for a $\pm 5\%$ change in momentum (off momentum on axis). Current settings of the quadrupole magnets are shown in Table 7.6.

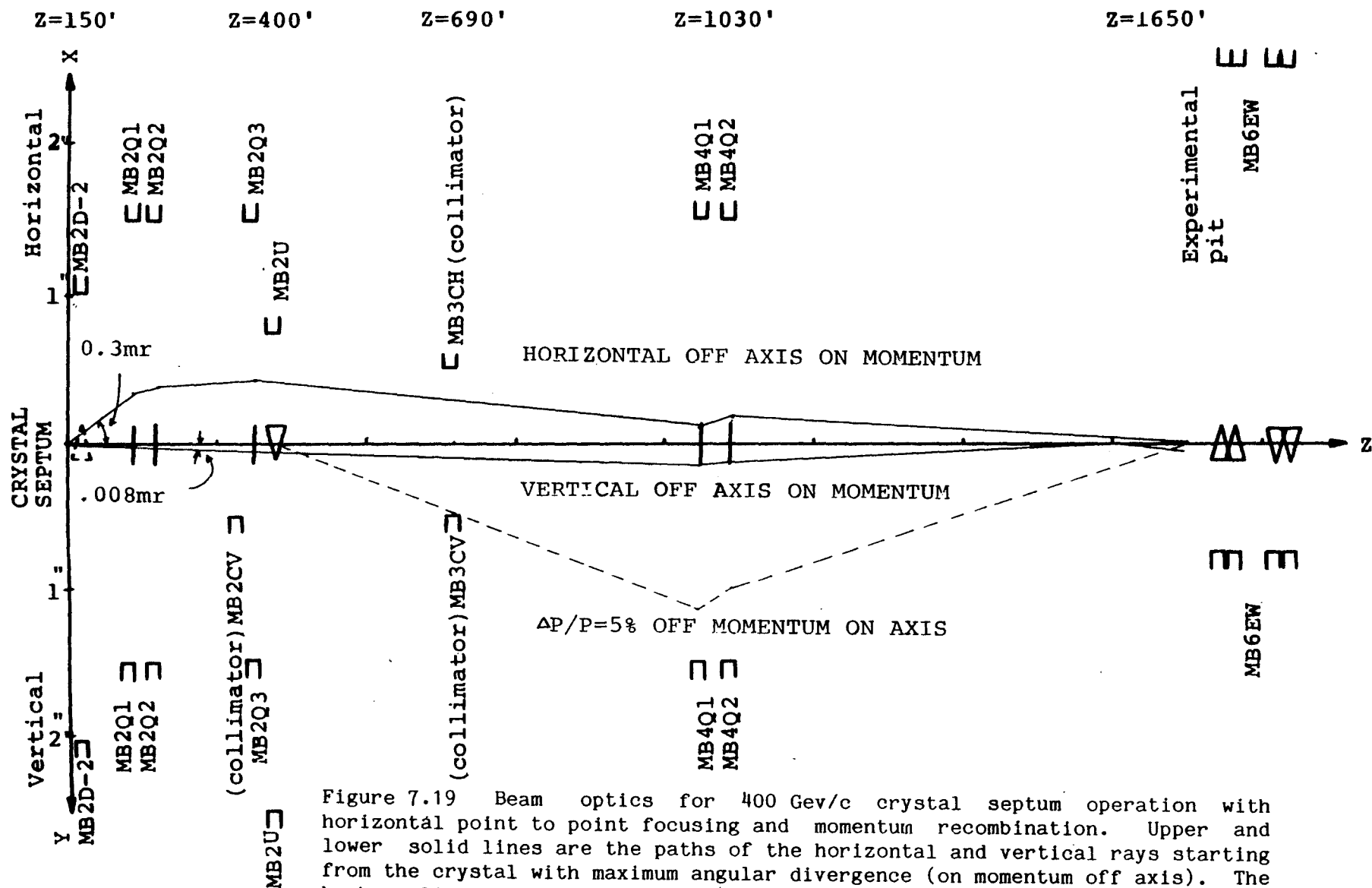


Figure 7.19 Beam optics for 400 GeV/c crystal septum operation with horizontal point to point focusing and momentum recombination. Upper and lower solid lines are the paths of the horizontal and vertical rays starting from the crystal with maximum angular divergence (on momentum off axis). The broken line is the momentum dispersion for a $\pm 5\%$ change in momentum (off momentum on axis). Current settings of the quadrupole magnets are shown in Table 7.6.

point to point focusing was applied when calculating the magnet parameters again (run No.7). Since no intermediate focusing is required in this calculation, both quadrupole triplet and doublet are combined to give the final focus in the experimental pit, which reduces the magnetic field requirements of each magnet. Table 7.6 shows the results of this calculations and the Figure 7.19 shows the beam optics.

PART 2

CHAPTER 8

THEORY OF DECHANNELING AND FEEDING-IN

8.1 Introduction

The classical theory of channeling was discussed in chapter 2. There the transverse energy of a channeled particle was assumed to be a constant of its motion. This assumption is not reasonable when considering channeling depth, typically over a few thousands of angstroms. As the channeled particles move through the crystal they undergo multiple scattering by electrons and the thermally vibrating nuclei of the target, and also by the defects and impurities in the target. Therefore the transverse energy becomes significantly changed which causes the transverse energy of some particles to become larger than the critical transverse energy for channeling. These particles escape from their channeled paths to the random beam. This process is called dechanneling. This was first described theoretically by Lindhard [1].

The reverse process in which a random particle gets trapped into the channel paths as it moves along the crystal nearly parallel to a major axis or plane, is called feeding-in. If a random particle is to be scattered into the channeled path, a close collision of impact parameter much less than the screening length, is required. The impact parameter of a channeled particle is normally greater than the

screening length. Therefore the scattering from random beam to channeled beam is prohibited. This effect of feeding-in is large enough to be observed [17] for 12 GeV/c protons, however no theoretical explanations were reported so far. This chapter discusses the derivation of a simple model to explain the observed feeding-in effects.

A probabilistic equation governing transverse energy distribution with depth of an incident beam distribution is derived first in this chapter. This equation is identical to the master equation of Bonderup et al.[43] which was used to derive a diffusion equation for axial dechanneling. Ellison showed that a feeding-in process is also built into this basic probabilistic equation and separated the equation into dechanneling and feeding-in parts. This chapter reviews his work of deriving the simple model to study the characteristic dechanneling and feeding-in lengths.

8.2 Derivation of the Probabilistic Equation

Consider a beam of positive particles of energy E , incident on a crystal nearly parallel to a major axial or a planar direction. If $g(E_t, Z)$ is the normalized transverse energy density of the beam at a depth Z , then

$$\int_0^{\infty} g(E_t, Z) dE_t = 1 \quad 8.1$$

where, E_t is the transverse energy at a depth Z . If θ is the incident angle with the major direction of the crystal then the initial transverse energy is $E\theta^2$. The initial transverse energy density $g(E_t, 0)$

of the beam is determined by the beam divergence outside the crystal. Let $P(E'_t, E_t, Z) dZ dE'_t$ be the transition probability for a particle with transverse energy E_t to scatter to $(E'_t, E'_t + \Delta E'_t)$ on a path length dZ . Then the change in transverse energy density at E_t from Z to $Z + \Delta Z$ is given by

$$\begin{aligned} d[g(E_t, Z)]dE_t &= [g(E_t, Z + \Delta Z) - g(E_t, Z)]dE_t \\ &= \int_0^\infty g(E'_t, Z) dE'_t [dZ P(E_t, E'_t, Z) dE_t] \\ &\quad - \int_0^\infty g(E_t, Z) dE_t [dZ P(E'_t, E_t, Z) dE'_t] \end{aligned} \quad 8.2$$

where the first term represent the transition from the outside to $(E_t, E_t + \Delta E_t)$ and the second term from $(E_t, E_t + \Delta E_t)$ to the outside. As dZ tends to zero this equation can be written as

$$\frac{d}{dZ}[g(E_t, Z)] = \int_0^\infty dE'_t [P(E_t, E'_t, Z)g(E'_t, Z) - P(E'_t, E_t, Z)g(E_t, Z)] \quad 8.3$$

This equation is discussed in detail by Lindhard et al.[49] and used in axial case by Bonderup et al.[43].

8.3 Derivation of the Basic Equation

If E_{tc} is the critical transverse energy for channeling, the channeled and random fractions at a depth Z is given respectively by

$$C(Z) = \int_0^{E_{tc}} g(E_t, Z) dE_t \quad 8.4(a)$$

$$1 - C(Z) = \int_{E_{tc}}^\infty g(E_t, Z) dE_t \quad 8.4(b)$$

By integrating equation 8.3 from $0 \rightarrow E_{tc}$ one gets

$$\begin{aligned} \frac{d}{dZ} \left[\int_0^{E_{tc}} g(E_t, Z) dE_t \right] &= \int_0^{E_{tc}} dE_t \int_0^{\infty} dE'_t [P(E_t, E'_t, Z) g(E'_t, Z) \\ &\quad - P(E'_t, E_t, Z) g(E_t, Z)] \end{aligned} \quad 8.5$$

Since the function inside the right hand side integral is symmetric with respect to E_t and E'_t ,

$$\int_0^{E_{tc}} dE_t \int_0^{E_{tc}} dE'_t [P(E_t, E'_t, Z) g(E'_t, Z) - P(E'_t, E_t, Z) g(E_t, Z)] = 0 \quad 8.6$$

Therefore equation 8.5 can be written as

$$\begin{aligned} \frac{d}{dZ} [C(Z)] &= \int_0^{E_{tc}} dE_t \int_{E_{tc}}^{\infty} dE'_t P(E_t, E'_t, Z) g(E'_t, Z) \\ &\quad - \int_0^{E_{tc}} dE_t \int_{E_{tc}}^{\infty} dE'_t P(E'_t, E_t, Z) g(E_t, Z) \end{aligned} \quad 8.7$$

We now assume that the transition probability P is such that the mean value theorem applies; thus the first term in equation 8.7 is

$$\begin{aligned} \int_0^{E_{tc}} dE_t \int_{E_{tc}}^{\infty} dE'_t P(E_t, E'_t, Z) g(E'_t, Z) \\ = \int_0^{E_{tc}} dE_t P(E_t, E_2(Z, E_{tc}), Z) \int_{E_{tc}}^{\infty} g(E'_t, Z) dE'_t \end{aligned} \quad 8.8(a)$$

where, $E_{tc} \leq E_2(Z, E_{tc}) < \infty$ and the second term in equation 8.7 is

$$\begin{aligned} \int_{E_{tc}}^{\infty} dE'_t \int_0^{E_{tc}} dE_t P(E'_t, E_t, Z) g(E_t, Z) \\ = \int_{E_{tc}}^{\infty} dE'_t P(E'_t, E_1(Z, E_{tc}), Z) \int_0^{E_{tc}} dE_t g(E_t, Z) \end{aligned} \quad 8.8(b)$$

where, $0 \leq E_1(Z, E_{tc}) \leq E_{tc}$. Let

$$p_1(Z, E_{tc}) = \int_{E_{tc}}^{\infty} dE'_t P(E'_t, E_1(Z, E_{tc}), Z) \quad 8.9(a)$$

$$p_2(Z, E_{tc}) = \int_{E_{tc}}^{\infty} dE_t P(E_t, E_2(Z, E_{tc}), Z) \quad 8.9(b)$$

Then by using equation 8.4, equation 8.7 can be written as

$$C'(Z) = - p_1(Z, E_{tc}) C(Z) + p_2(Z, E_{tc}) [1 - C(Z)] \quad 8.10$$

where, $C'(Z) = \frac{d}{dZ}[C(Z)]$. By suppressing the dependence of p_1 and p_2 on E_{tc} , equation 8.10 becomes

$$\frac{dC}{dZ} = - p_1(Z)C + p_2(Z)(1 - C) \quad 8.11$$

It should be mentioned that no approximations have been made on going from the basic probabilistic equation 8.3 to equation 8.11.

8.4 Analysis of the Basic Equation

In the above basic model $p_1(Z)$ and $p_2(Z)$ are complicated functions of Z once E_{tc} is given and depend on the basic probabilistic functions $P(E_t, E'_t, Z)$ and $g(E_t, Z)$. All the physics is contained in this function which $P(E_t, E'_t, Z)$ which is unknown at this time. For our purpose it is reasonable to assume that $P(E_t, E'_t, Z)$ is a slowly varying function of Z , so we can replace $p_1(Z)$ and $p_2(Z)$ by two constants $1/\lambda_1$ and $1/\lambda_2$. From the theoretical point of view these two constants can be defined as

$$1/\lambda_1 = \frac{1}{d} \int_0^d p_1(Z) dZ \quad 8.12(a)$$

and

$$1/\lambda_2 = \frac{1}{d} \int_0^d p_2(Z) dZ \quad 8.12(b)$$

where d is the length of the crystal. This might be a crude approximation but it does lead to an easy way of analyzing the experimental data using the above model. Therefore the equation 8.11 can be written as

$$dC = -C dZ/\lambda_1 + (1-C)dZ/\lambda_2 \quad 8.13$$

This equation can be interpreted as follows: if λ_1 and λ_2 are the characteristic dechanneling and feeding-in lengths, then the two terms in the right hand side, $[-C dZ/\lambda_1]$ and $[(1-C)dZ/\lambda_2]$ are the increase in channeled fractions, going from Z to $Z+\Delta Z$ as ΔZ tends to zero, due to dechanneling and feeding-in processes. A method of extracting λ_1 and λ_2 from the experimental data will be discussed in the next chapter. Now, equation 8.13 can be arranged as

$$dC/dZ = -(1/\lambda)C + 1/\lambda_2 \quad 8.14$$

where $(1/\lambda) = (1/\lambda_1) + (1/\lambda_2)$. Let $C(0)$ be the initial channeled fraction at $Z=0$. By integrating equation 8.14 one gets

$$C(Z) = [C(0) - \lambda/\lambda_2]e^{-Z/\lambda} + \lambda/\lambda_2 \quad 8.15$$

As Z tends to infinity the above equation 8.15 has the limiting steady state channeling fraction, which is given by,

$$C_\infty = \lambda/\lambda_2 = \lambda_1/(\lambda_1 + \lambda_2) \quad 8.16(a)$$

$$\text{for } \lambda_1 = \lambda_2, \quad C_\infty = 1/2 \quad 8.16(b)$$

$$\text{and for } \lambda_1 \ll \lambda_2, \quad C_\infty = \lambda_1/\lambda_2 \quad 8.16(c)$$

Also if the feeding-in probability is zero (ie., $p_2 = 0$ and $\lambda_2 \rightarrow \infty$) then equation 8.15 becomes

$$C(Z) = C(0) e^{-Z/\lambda_1} \quad 8.17$$

which predicts the observed exponential dechanneling behavior [44,45].

8.5 Alternative Method of Deriving the Basic Equation

The basic equation (equation 8.13) can be derived by using the following two assumptions:

1. Rate of dechanneling along the length of the crystal is proportional to the number of channeled particles.
2. Rate of feeding-in along the length of the crystal is proportional to the number of random particles.

If C is the channeled fraction at a depth Z then $(1-C)$ is the random fraction at Z , and the first assumption can be written as,

$$-(dC/dZ)_d \propto C$$

where $(dC/dZ)_d$ is the rate of increase of channeled fraction due to the dechanneling, and the second assumption can be written as,

$$+(dC/dZ)_f \propto (1-C)$$

where $(dC/dZ)_f$ is the rate of increase of the channeled fraction due to feeding-in.

By introducing characteristic dechanneling and feeding-in lengths λ_1 and λ_2 respectively, the resultant change of channeling fraction can be written as,

$$dC/dZ = (dC/dZ)_d + (dC/dZ)_f = -C/\lambda_1 + (1-C)/\lambda_2 \quad 8.18$$

This equation is the same as the basic equation (equation 8.13) derived using the probabilistic equation.

8.6 Dechanneling

For a perfect crystal without dislocations and impurities, the dechanneling is due to:

(1) Multiple scattering by electrons. As the channeled particles proceed into the target, multiple scattering due to the target electrons increase the transverse energy of incident particles. As the transverse energy increases, the channeled particles approach the target nuclei and eventually become scattered.

(2) Multiple scattering by thermally vibrating target nuclei. The force fluctuations produced by thermal vibrations of the lattice nuclei contribute to the increase of transverse energy of channeled particles. The nuclei of a static row or plane do not affect the transverse energy of channeled particles.

The average rate of increase of transverse energy of channeled particles can be written as

$$d\langle E_t \rangle / dz = d\langle E_t \rangle_n / dz + d\langle E_t \rangle_e / dz \quad 8.19$$

The nuclear contribution is given by [44]

$$d\langle E_t \rangle_n / dz = \frac{1}{4E\sqrt{(Nd_p)}} u^2 \langle -dV(x)/dx \rangle \quad 8.20$$

and the electronic contribution is given by [44]

$$d\langle E_t \rangle_e / dz = \frac{\pi Z_1^2 e^4}{E} L_e \langle \rho(r) \rangle \quad 8.21$$

where d_p is the planar separation, u is the component of the mean square vibrational amplitude of lattice atoms normal to the plane, $V(x)$ is the continuum planar potential, Z_1 and Z_2 are the atomic numbers of the projectile and the target nuclei respectively, e is the electronic charge, m is the rest mass of an electron (in eV), $\rho(r)$ is the electron density, r is the position vector of an electron, density and $L_e = \ln(2mv^2\gamma^2/I)$ denotes the logarithm in Bethe's formula for the electronic stopping power where $I = 10Z_2 \text{ eV}$, v is the velocity of the projectile and γ is the relativistic constant.

Because of the statistical description of the elementary processes, the changes of the transverse energy distribution can be described [1] by the planar diffusion equation with a diffusion coefficient $D(E_t)$,

$$\frac{\partial}{\partial z} g(E_t, z) = \frac{\partial}{\partial E_t} D(E_t) \frac{\partial}{\partial E_t} g(E_t, z) \quad 8.22$$

with the boundary conditions $g(E_t, z) = g_0(E_t)$ and $g(E_{tc}, z) = g(-E_{tc}, z) = 0$ where $g_0(E_t)$ is the initial transverse distribution of channeled particles and E_{tc} is the critical transverse energy.

The diffusion coefficient is related to the scattering through the increase in the average transverse energy by the following differential equation,

$$D(E_t) + p_t D'(E_t) = M_1 \frac{d}{dz} \langle E_t \rangle \quad 8.23$$

where p_t is the transverse momentum and M_1 is the mass of the incident particle. The prime denotes differentiation with respect to E_t .

Once $\langle E_t \rangle$, $g_0(E_t)$ and E_{tc} are known, the diffusion coefficient can be calculated using equation 8.23. It should be noted that an analytical function for $D(E_t)$ is difficult to obtain due to the complicated forms of $V(x)$ and $\rho(r)$. The transverse energy distribution can then be found by solving equation 8.22, and the channeled fraction at a depth z can be calculated using equation 8.4(a).

8.6.1 Planar Dechanneling

Campisano et al.[44] solved equation 8.23 for $D(\epsilon_t)$ analytically using a polynomial approximation for the planar continuum potential where ϵ_t is a dimensionless quantity for the transverse energy given by $\epsilon_t = E_t/ACa$ where $A = 2\pi Z_1 Z_2 e^2 N d_p$, $C = \sqrt{3}$ and a is the Thomas-Fermi screening distance. The nuclear and electronic contributions were treated separately where and found that the nuclear contribution to the diffusion coefficient is about a factor of twenty less than the electronic contribution in the transverse energy range of channeled particles. Therefore, by neglecting the nuclear part the obtained diffusion coefficient can be written as

$$D(\epsilon_t) = \frac{M_1 A Z_1 e^2 L_e}{16 E C a} D_e(\epsilon_t) \quad 8.24$$

where $D_e(\epsilon_t)$ is a linear function of ϵ_t which starts from a nonzero value at $\epsilon_t=0$ and changes by a factor of one or two for channeled particles.

Because of the complicated procedure of solving equation 8.22 with

this diffusion coefficient, Campisano et.al. assumed a constant diffusion coefficient D_0 , the value of which corresponds to the value of $D(\epsilon_t)$ calculated at the average transverse energy ϵ_{t0} of the channeled beam. The obtained solution to the equation 8.22 showed an exponential channeled fraction with Z where the dechanneling length is given by

$$\lambda_1 = \frac{16^2 C^2 a^2 E}{\pi^2 Z_1 e^2 L_e D_e(\epsilon_{t0})} \quad 8.25$$

Figure 8.1 shows their theoretical $\chi_1 (= \ln(2) \lambda_1)$ depth for MeV range protons through Si(110), which agrees quite well with their experimental results. The experimental results of Feldman and Appleton[45] are also shown in the figure.

One can extrapolate this nonrelativistic result to the relativistic region as follows. E in equation 8.25 is the kinetic energy of incident particles which is $\frac{1}{2}pv$ where p is the momentum and v is the velocity. For relativistic particles $pv = E$. Therefore E in equation 8.25 should be replaced by $E/2$ for relativistic particles. The calculated dechanneling lengths for 100 GeV/c protons through Si(110) is about 140 mm. According to equation 8.25, for different materials, dechanneling lengths will vary with the fraction a^2/L_e , which is .0036 for Si, .0024 for Ge and .0016 for W. Using these results, the calculated dechanneling lengths for Ge(110) and W(110) are 93 mm and 62 mm respectively. The results of planar dechanneling length determination for Si(110) in this experiment will be presented in the next chapter.

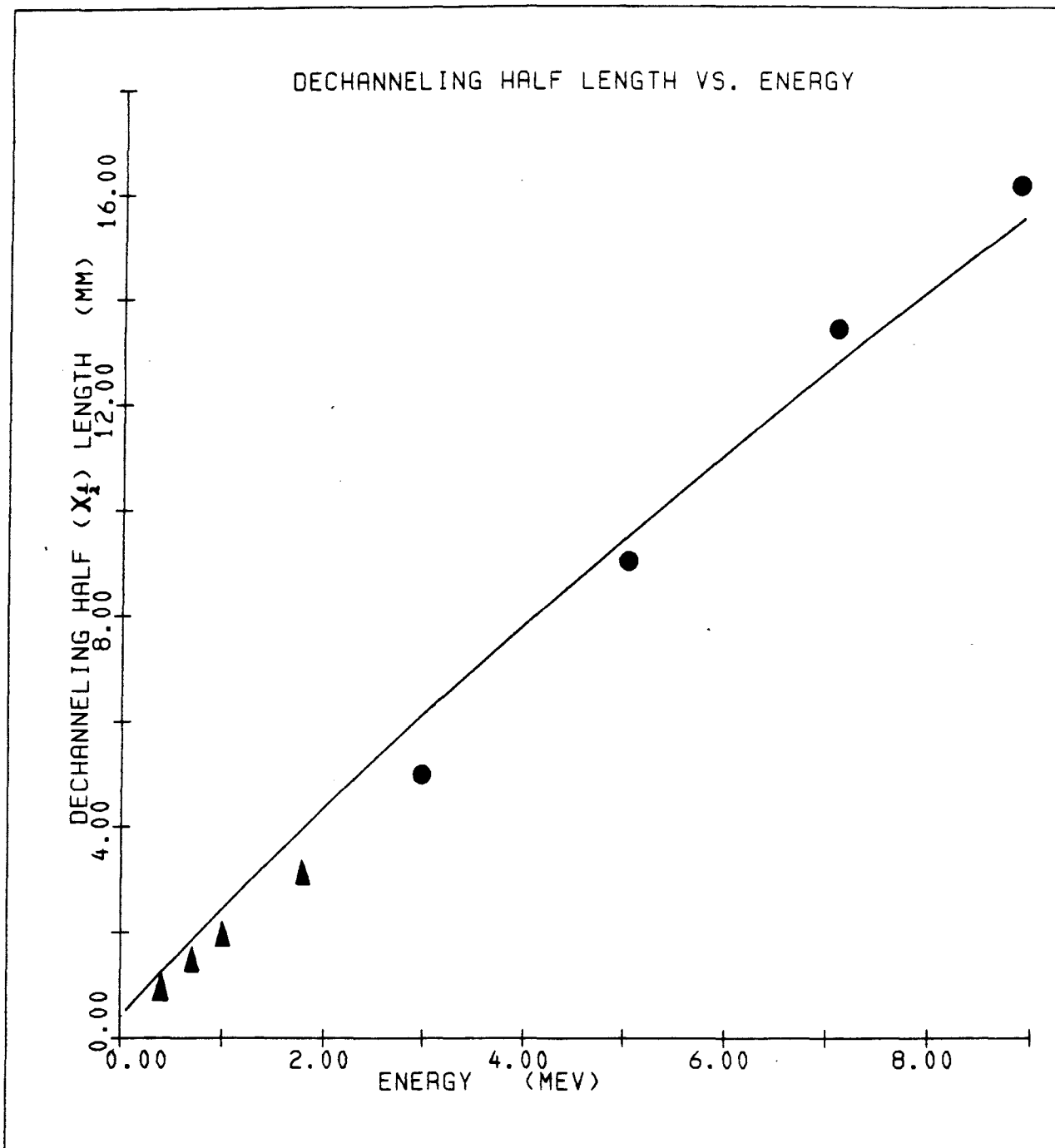


Figure 8.1 Comparison of experimental (dots- Campisano et al.[44] and triangles- Feldman et al.[45]) and theoretical (by Campisano et.al.) dechanneling half lengths (χ_1) for si (110) planar channeling of Mev protons.

8.6.2 Axial dechanneling

Bonderup et al.[43] numerically solved the differential equation (8.23) for $D(E_t)$ where he used the formula derived by Lindhard[1] for the average transverse energy loss of aligned beams in which the electronic contribution is given by

$$d\langle E_t \rangle_e / dz = \frac{E\theta_c^2}{2Z_e} [1 - \exp\{-(\epsilon_t + \epsilon_t')\}] \quad 8.26a$$

and the nuclear contribution by

$$d\langle E_t \rangle_n / dz = \frac{E\theta_c^2}{4Z_n} \left[\frac{1}{2} \exp(\epsilon_t + \epsilon_t') + \frac{1}{3} \right] [1 - \exp\{-(\epsilon_t + \epsilon_t')\}]^3 \quad 8.26b$$

where ϵ_t is defined by $\epsilon_t = E_t / \frac{1}{2} E\theta_c^2$, $\epsilon_t' = C^2 a^2 / r_0^2$, $\pi r_0^2 = 1 / Nd_a$ and Z_e and Z_n are the characteristic lengths for electronic and nuclear diffusion.

The calculation showed that the electronic contribution to $D(E_t)$ dominates at lower transverse energies, whereas the nuclear contribution takes over at higher values of E_t . Subsequent numerical calculations of the diffusion equation (8.22) for Si<110> and W<100> showed that the calculated values of dechanneling fractions were approximately one third of the experimental values of Pedersen et al.[46].

The characteristic dechanneling lengths Z_e and Z_n in equation 8.26 can be extrapolated to the relativistic region and are given by

$$Z_n = \frac{(Ca)^2}{2u^2} \frac{pv}{4\pi e^2 Z_1 Z_2 Nd_a} \quad 8.27a$$

$$Z_e = \frac{pv}{2\pi Z_1 e^2 L_e Nd_a} \quad 8.27b$$

where N is the density of the target material and d_a is the lattice

spacing along the string. The exact relationship between the dechanneling length λ_1 and the combined characteristic diffusion length is quite difficult to obtain because of the complicated form of $D(\epsilon_t)$. However one can use these two characteristic lengths as a guide to compare the effects in different materials (for example Si with Ge and W). The calculated values of Z_e and Z_n for Si, Ge and W are given in Table 8.1. As one can see, in this table the electronic effect stays the same for all materials while the nuclear effect is higher for heavier materials.

Table 8.1 Electronic and nuclear diffusion lengths calculated using equation 8.27 for Si, Ge and W at 100 GeV/c.

		<100> cm	<110> cm	<112> cm
Si	Z_n	6.4	9.0	7.4
	Z_e	4.7	6.6	5.4
Ge	Z_n	1.6	2.1	1.7
	Z_e	5.6	7.9	6.5
W	Z_n	1.4	1.0	
	Z_e	7.8	5.5	

8.7 Initial Channeled Fraction

Consider a beam of charged particles entering a crystal parallel to a major crystal plane. As the particles enter the crystal their transverse energies are modified due to the continuum potential between the crystal planes and are given by

$$E_t = E\theta^2 + V(x)$$

8.28

where θ is the incident angle, $V(x)$ is the continuum potential and x is the distance from the point midway between the crystal planes.

The condition for a particle to be channeled is governed by how closely it can approach the atomic plane without large angle scattering. Lindhard[1] assumed this distance to be the Thomas Fermi screening distance ($a = a_0.8853(Z_1^{2/3} + Z_2^{2/3})^{-1/2}$) where a_0 is the Bohr radius. The condition for planar channeling can therefore be written as

$$E_{tc} = V(d_p/2-a) > E\theta^2 + V(x) \quad 8.29$$

where E_{tc} is the critical transverse energy and d_p is the inter planar distance. This can be represented clearly by a phase space diagram as shown in Figure 8.2. θ_c in the figure is the maximum incident angle a channeled particle could have at the entrance to the crystal plane. This is defined as the planar critical angle and is given in equation 2.6. Table 5.1 gives calculated critical angles for different materials.

All particles satisfying the channeling condition given in equation 8.29 lie inside the region surrounded by the solid oval in Figure 8.2. The initial channeled fraction $C(0)$ (called f_c in section 5.8.2) of these particles is therefore given by the ratio of the areas of the solid oval to the dashed rectangle, where the area inside the dashed rectangle is the total phase space of the incident beam. This can be written as

$$C(0) = \pi(d_p/2-a) \times \theta_c / d_p \times 2\theta_c$$

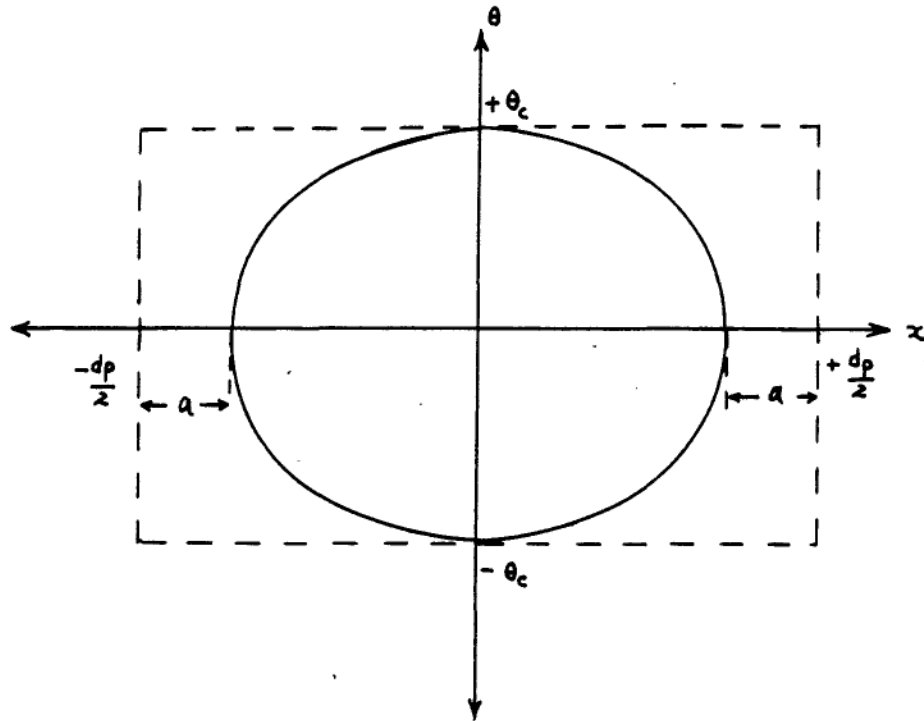


Figure 8.2 Phase space of the crystal acceptance (solid oval) for channeling of particles incident between two crystal planes and within the critical angle to the planar direction (dashed rectangle).

$$= \frac{\pi}{4}(1-2a/d_p)$$

8.30

using the area of an ellipse. This gives a result of .64 for silicon and .67 for germanium independent of the energy.

CHAPTER 9

STUDY OF DECHANNELING AND FEEDING-IN

9.1 Introduction

This part of the experiment was performed during the month of June, 1984, in the Meson area M-Bottom beamline at Fermilab. As a result, strong dechanneling and feeding-in effects were observed. First the experimental set up is briefly presented and then the algorithm of the analysis used to calculate the feeding-in and dechanneling probabilities is discussed. Next the results of dechanneling and feeding-in lengths, the angular dependence of feeding-in and initial channeled fraction at different energies are presented.

9.2 Data Acquisition

A detailed set up of the experiment was given in chapter 4. Figure 9.1 gives a schematic view of the multi-detector silicon crystal that was used. The crystal was made and fabricated with five ion-implanted surface barrier semiconductor detectors at Chalk River Nuclear Laboratories, Chalk River, Canada. The silicon crystal was cut such that the (110) plane was parallel to the major face of the crystal and the $\langle 112 \rangle$ axis was parallel to the length of the crystal so that the (110) plane is perpendicular to the major face of the crystal. Out

of the five surface barrier detectors namely A, B, C, D and E only B, D and E were in working condition during the experiment, where the detector positions are shown in Figure 9.1.

Data was acquired at 30, 60, 100 and 200 GeV/c for silicon (110) planar channeling and at 60 and 100 GeV/c for silicon <112> axial channeling. Table 9.1 shows the summary of data logged during the experiment. For each event, the drift chamber data and ionization energy losses at the three detectors were recorded. Drift chamber information was used to calculate the incident and exit angles of the beam particles.

Table 9.1 Summary of three detector data logged during June 1984 run.

energy	events logged	comments
200 GeV/c	89,000	Si 110 planar.
100 GeV/c	102,000	Si 110 planar.
60 GeV/c	102,000	Si 110 planar.
30 GeV/c	30,000	Si 110 planar.
100 GeV/c	80,000	Si 112 axial.
60 GeV/c	65,000	Si 112 axial.

9.3 Algorithm

9.3.1 Determination of Channeled Particles

One of the difficulties in this analysis is to separate the channeled particles from the random particles. The channeled particles have lower energy losses than the random particles, because they do not make close collisions with the target nuclei, so that the most probable

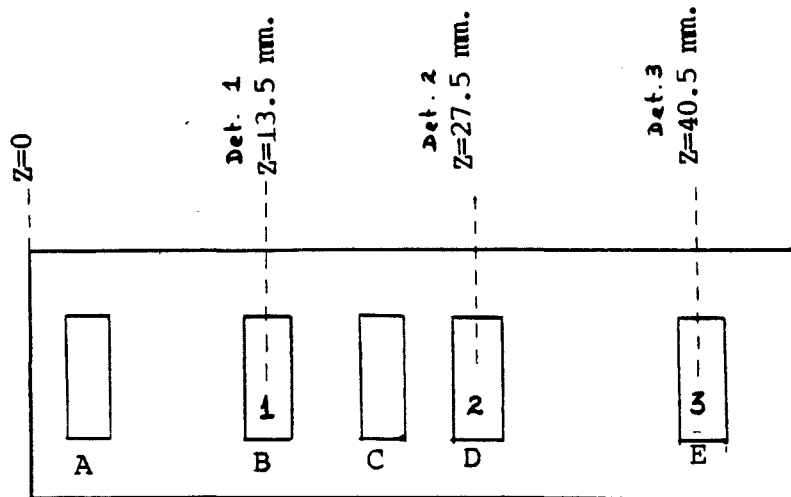


Figure 9.1 Schematic diagram of the multi detector crystal used in dechanneling and feeding-in studies. The positions of the detectors used during the data acquisition are shown with respect to the upstream end ($Z=0$) of the crystal. The detector pads are 3 mm wide along the beam direction and 8 mm perpendicular to the beam.

energy loss value of the channeled particles is less than the most probable energy loss value of the random particles. Lindhard [1] suggested that stopping power experienced by a channeled particle should be at most a factor of 2 less than that of a random particle.

Esbensen and Golovchenko [47] have calculated the average energy loss suffered by the channeled particles as a function of impact parameter in the Born approximation. The results of the calculations, which were originally nonrelativistic, have been extrapolated to the relativistic region by Uggerhoj [48], but no theoretical work has yet been reported in deriving the energy loss distribution of channeled particles.

The experimentally determined energy loss spectrum for planar channeling is shown in Figure 9.2. Note that the distributions corresponding to random and channeled particles overlap each other. Two Landau-like curves are drawn over the random distribution and the channeled distribution, respectively, to illustrate the overlapping of the two distributions. Therefore one can not completely separate the channeled particles from the random particles; however one can make a low energy loss window to separate a fraction of channeled particles from the total beam distribution as shown in Figure 9.2. The lower edge of the random distribution can roughly be estimated by drawing a Landau like curve as shown in Figure 9.2 whereby the window can then be set below the random distribution.

In order to find the distribution of channeled particles the following method was used. By keeping two low energy loss windows at the first and the third detectors, the energy loss distribution of the

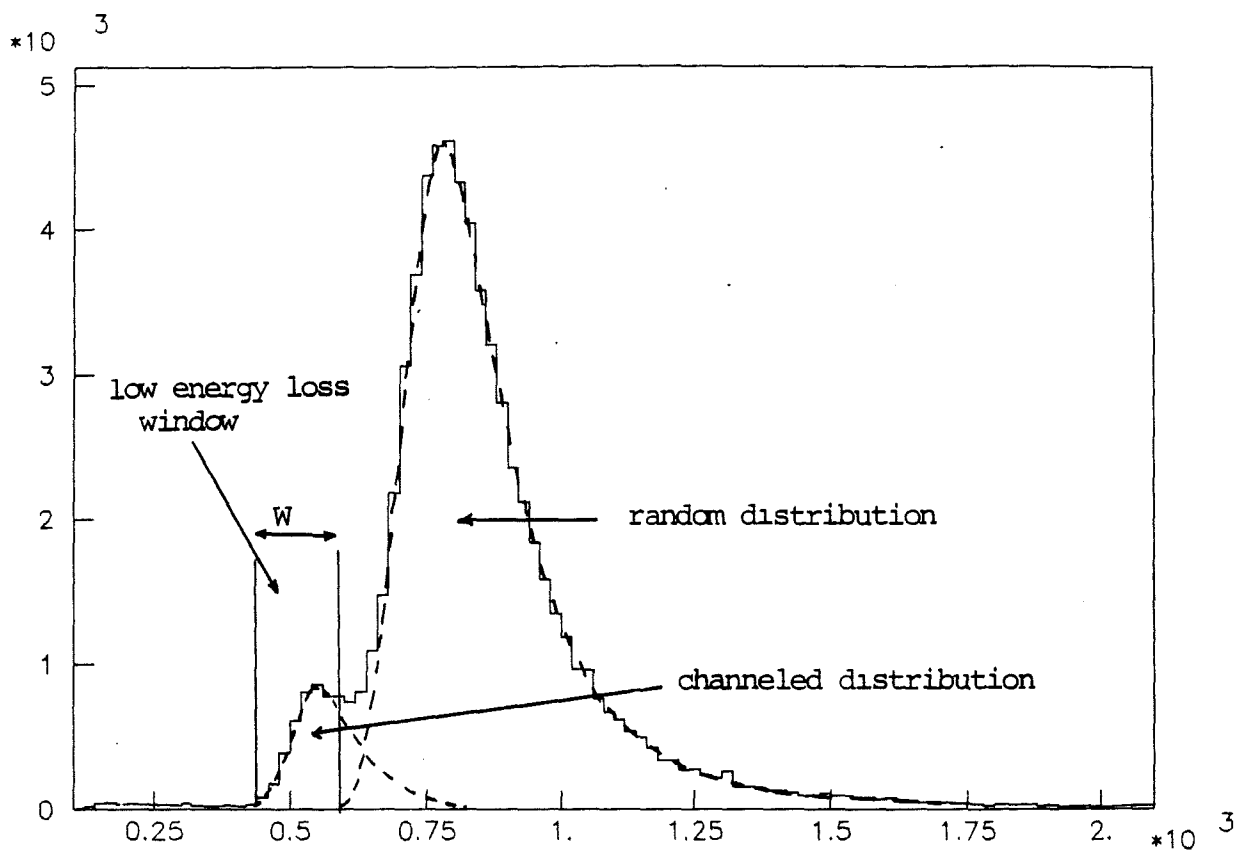


Figure 9.2 A typical ionization energy loss spectrum of positive charged particles at the detector when the beam direction is parallel to the major direction of the crystal. The dashed lines are drawn to show the channeled and random (Landau) distributions separately. A window W can be set to select a fraction of channeled particles in data analysis.

second detector was obtained for particles incident within the critical angle. Figure 9.3 shows these distributions for the second detector for both planar and axial cases at all energies. Horizontal scales of all distributions are identical and proportional to the channel number of the Analog to Digital Converter (ADC) used in data acquisition. The calibration of the ADC is not necessary and one can use the channel numbers of the units as an arbitrary scale for the data analysis. The most probable energy loss of the random distribution is also shown in Figure 9.3 by the vertical arrows.

Since the dechanneling lengths and feeding-in lengths are either of the same order or longer than the length of the crystal at the above energies, it was reasonable to assume that a dechanneled particle is never fed-in and a fed-in is never dechanneled again within the distance between the first and third detectors. Under these assumptions the obtained energy loss distribution can be used as the energy loss distribution of channeled particles at the second detector. But this method is not valid for the first detector (having low energy loss windows at the second and third detectors) and the third detector (having low energy loss windows at the first and second detectors), because the fed-in and dechanneled particles are also included in the distributions of the first and the third detectors, respectively.

Since all three detectors are identical, the distributions of channeled particles at all detectors were assumed to be identical. Once the energy loss distributions of channeled particles were known, the following method was used to determine the number of channeled particles for a given arbitrary energy loss distribution which contains

ENERGY LOSS DISTRIBUTIONS OF CHanneled PARTICLES

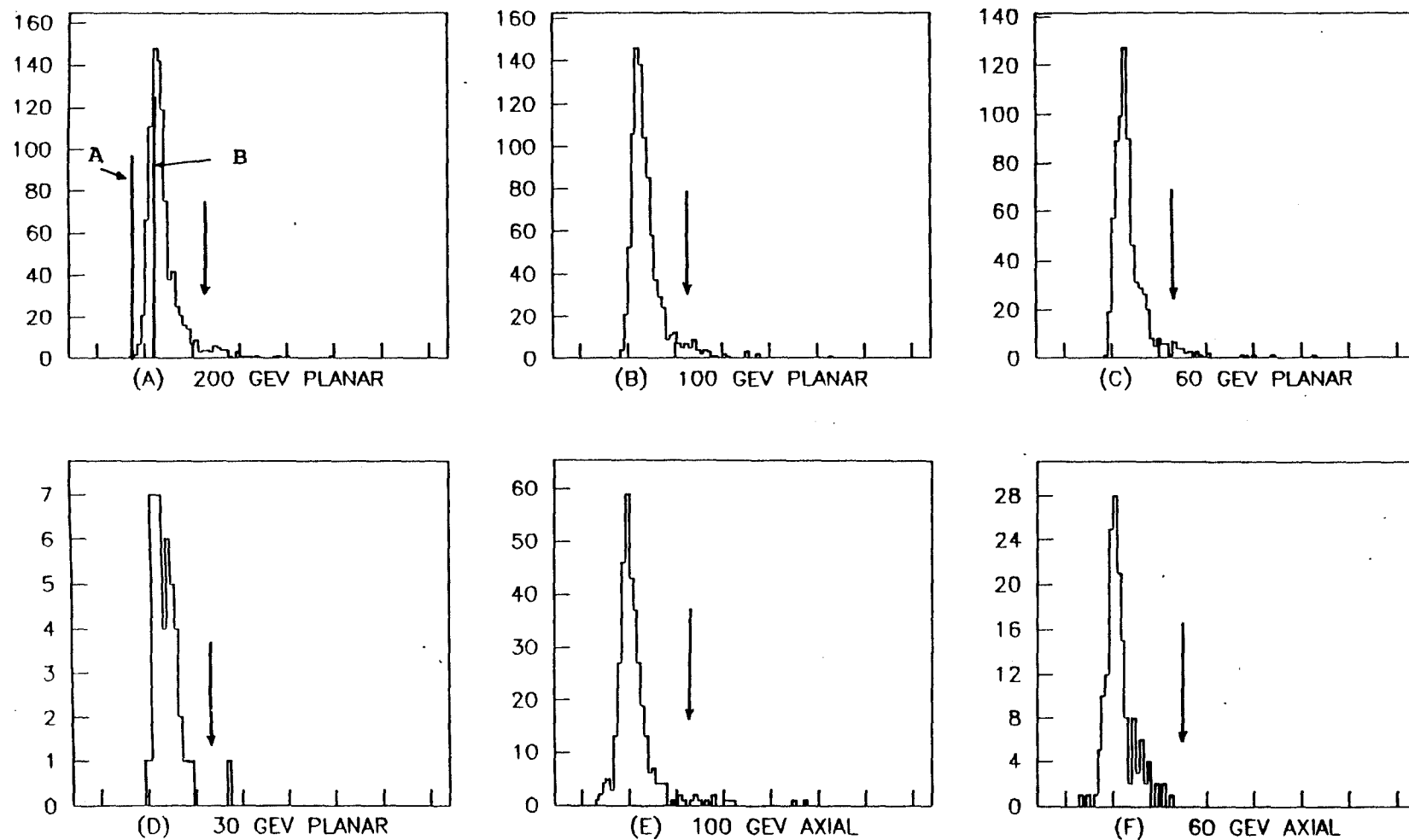


Figure 9.3 Energy loss distribution of channeled particles at the middle detector, obtained by keeping low energy loss windows at the first and the third detectors for particles incident within critical angle to the major direction of the crystal. The arrow indicates the position of the peak of the random distribution.

both channeled and random particles: Table 9.2 shows the ratio (α) of the total number of particles and the number of particles in the region between A and B in the channeled spectrum (Figure 9.3A), where B corresponds to the peak of the channeled distribution. Since the region AB in any given distribution is normally below the random distribution as shown in Figure 9.2, the total number of particles in region AB was multiplied by the corresponding factor α at the given energy (Table 9.2) to calculate the total number of channeled particles.

Table 9.2 The factor α used to calculate the total number of channeled particles in a given distribution.

Energy	Factor(α)
200 Gev/c planar	$2.64 \pm .31$
100 Gev/c planar	$2.84 \pm .26$
60 Gev/c planar	$2.81 \pm .29$
30 Gev/c planar	2.67 ± 1.0
100 Gev/c axial	$2.22 \pm .22$
60 Gev/c axial	$1.94 \pm .27$

In the above procedure when calculating the factor α one has to be very careful when selecting the low energy loss windows at the first and the third detectors. First the upper level of the windows are kept at a reasonable position and the factor α is calculated. Then the position of the upper level is gradually moved towards the low energy

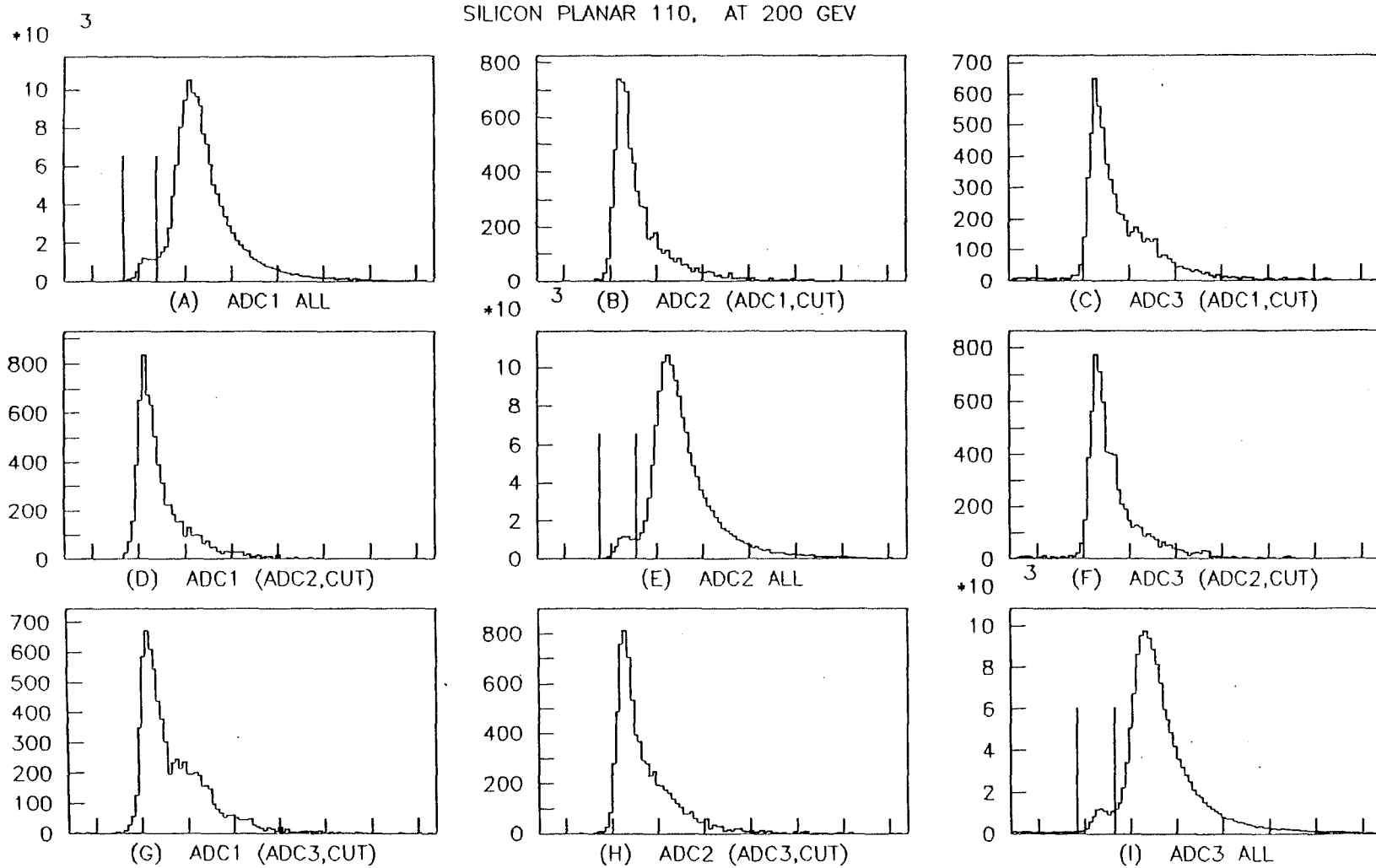


Figure 9.4 Ionization energy loss spectra at the three detectors for pions and protons transmitted through the silicon crystal parallel to 110 plane at 200 GeV/c.

*10 3

SILICON PLANAR 110, AT 100 GEV

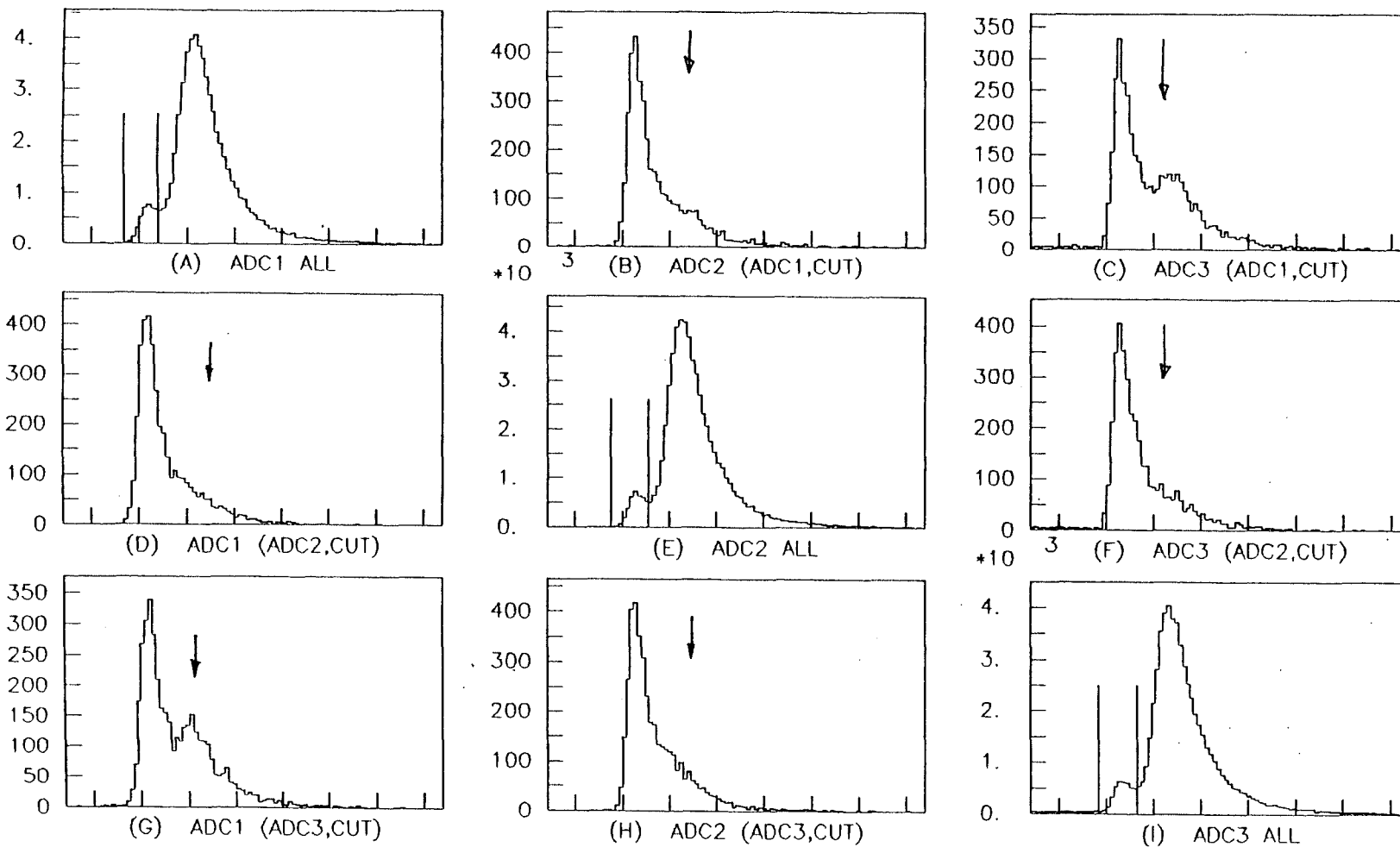


Figure 9.5 Ionization energy loss spectra at the three detectors for pions and protons transmitted through the silicon crystal parallel to 110 plane at 100 GeV/c.

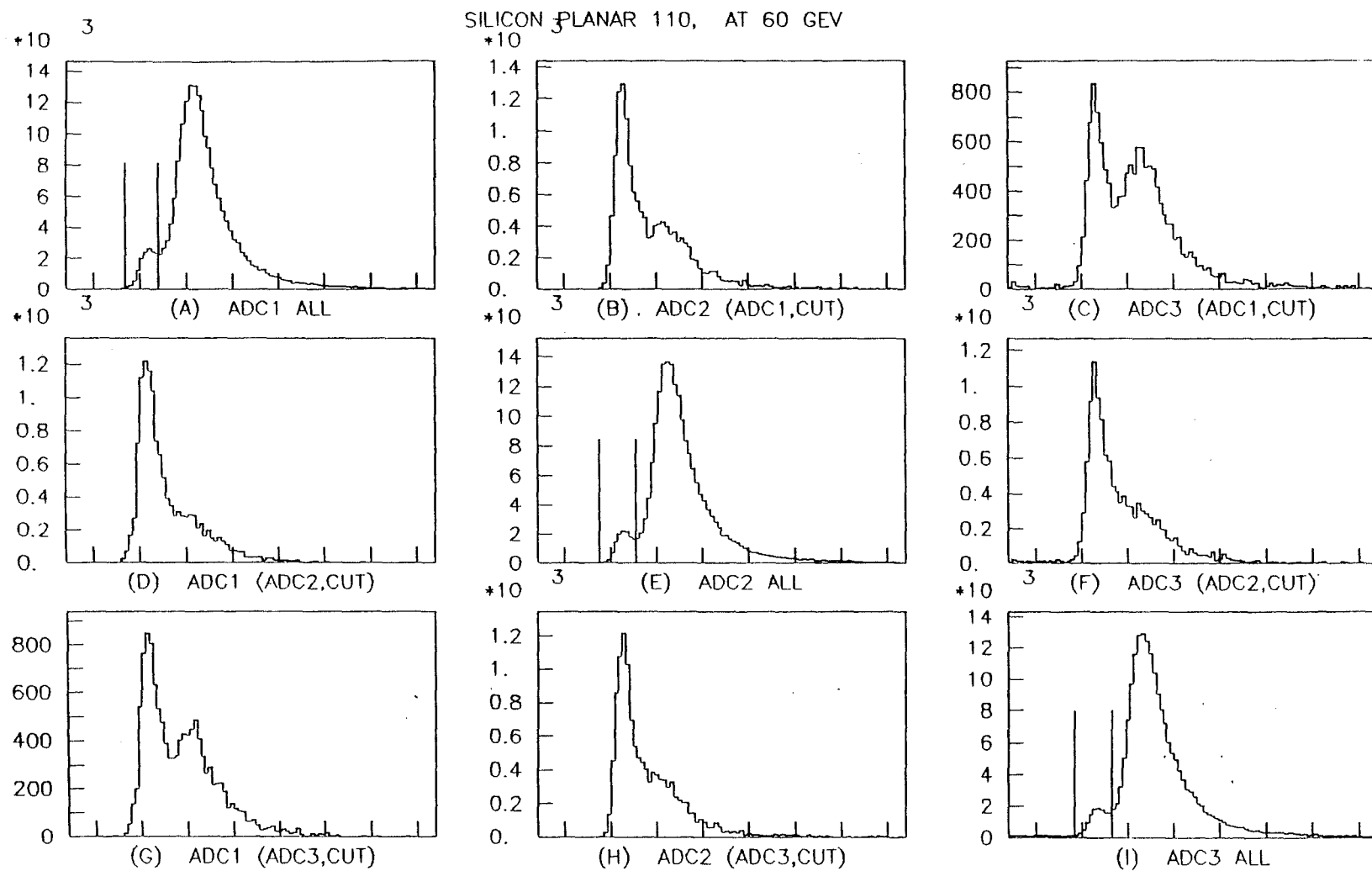


Figure 9.6 Ionization energy loss spectra at the three detectors for pions and protons transmitted through the silicon crystal parallel to 110 plane at 60 GeV/c.

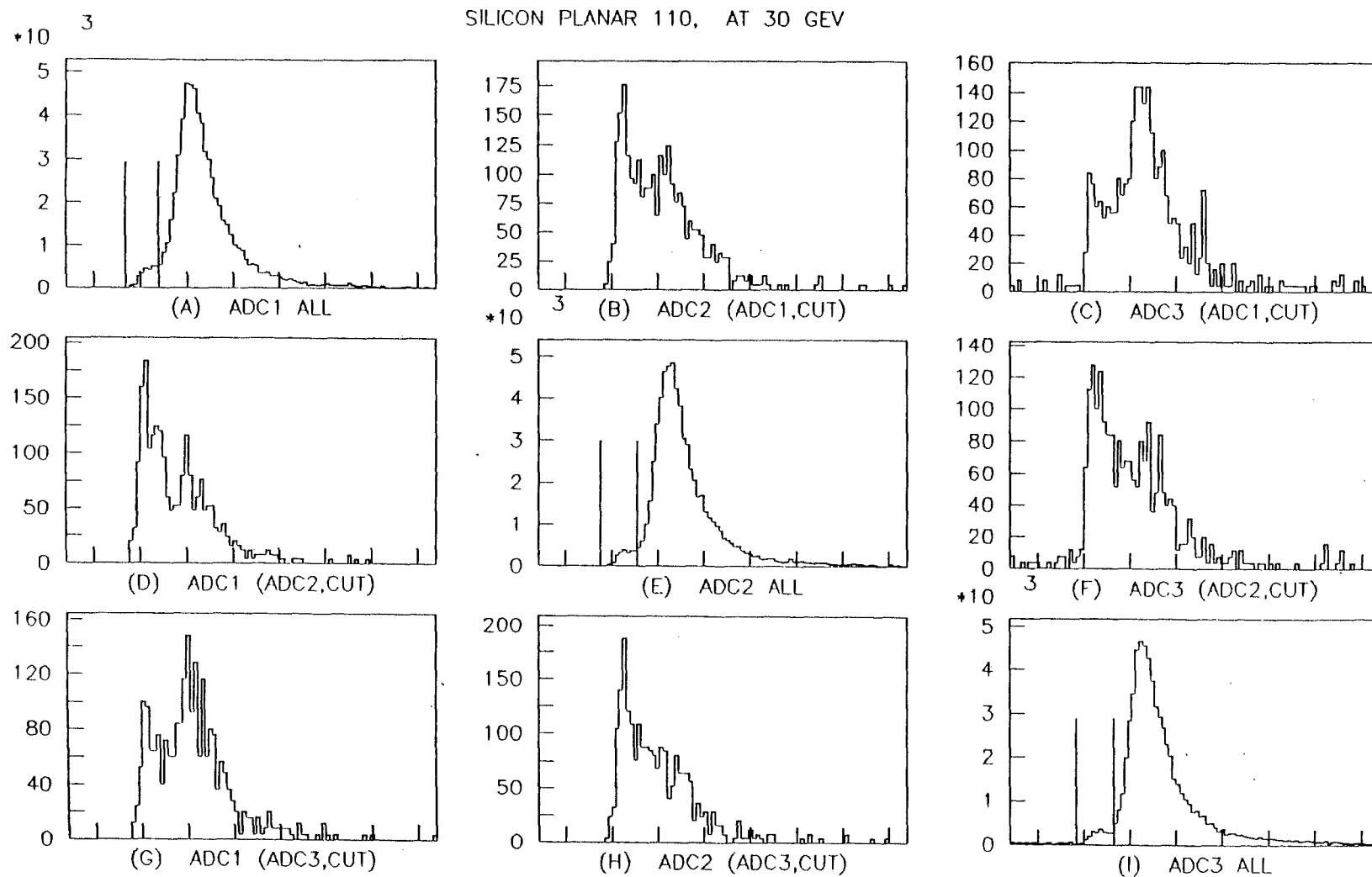


Figure 9.7 Ionization energy loss spectra at the three detectors for pions and protons transmitted through the silicon crystal parallel to 110 plane at 30 GeV/c.

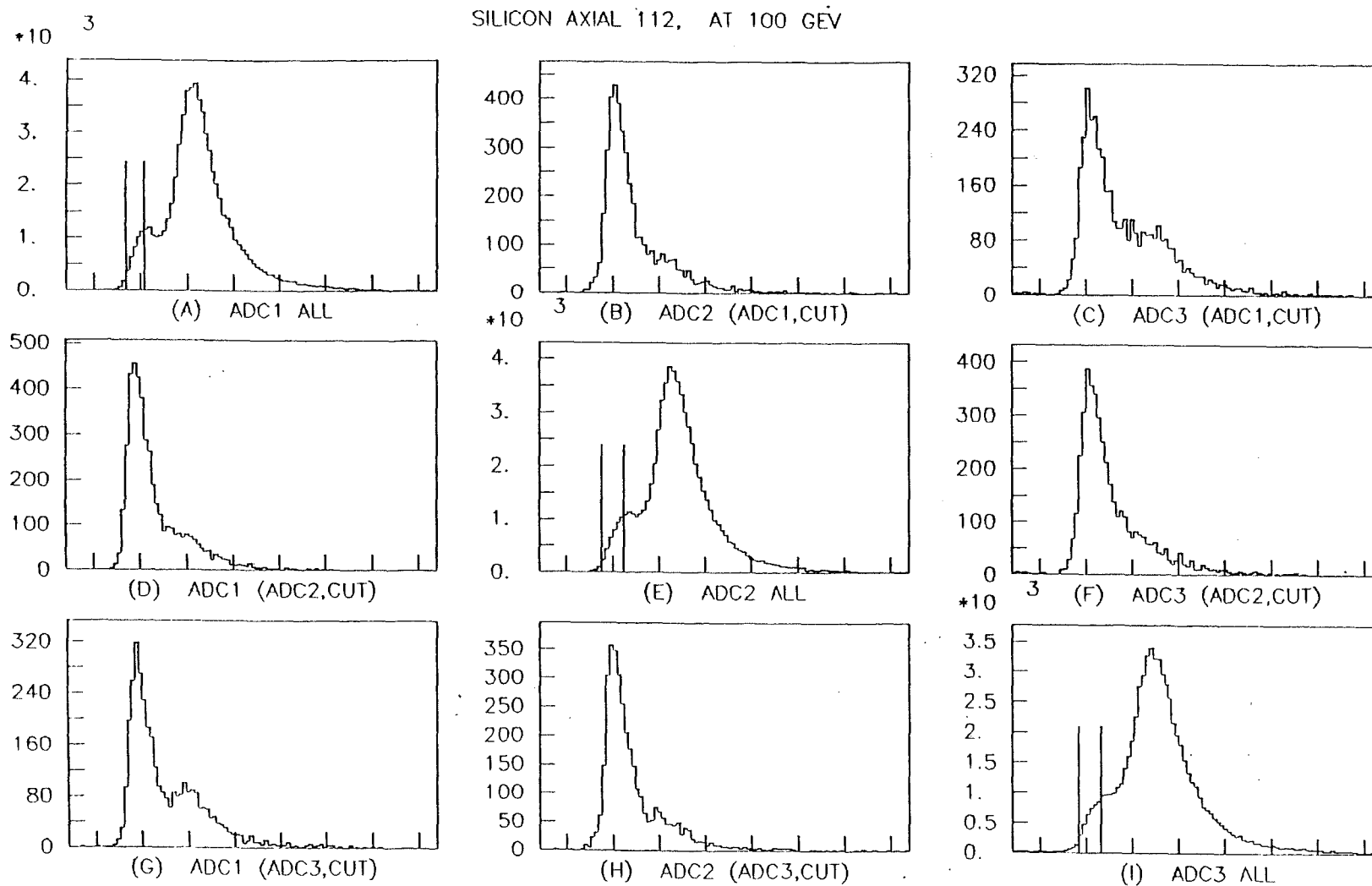


Figure 9.8 Ionization energy loss spectra at the three detectors for pions and protons transmitted through the silicon crystal parallel to 112 axis at 100 GeV/c.

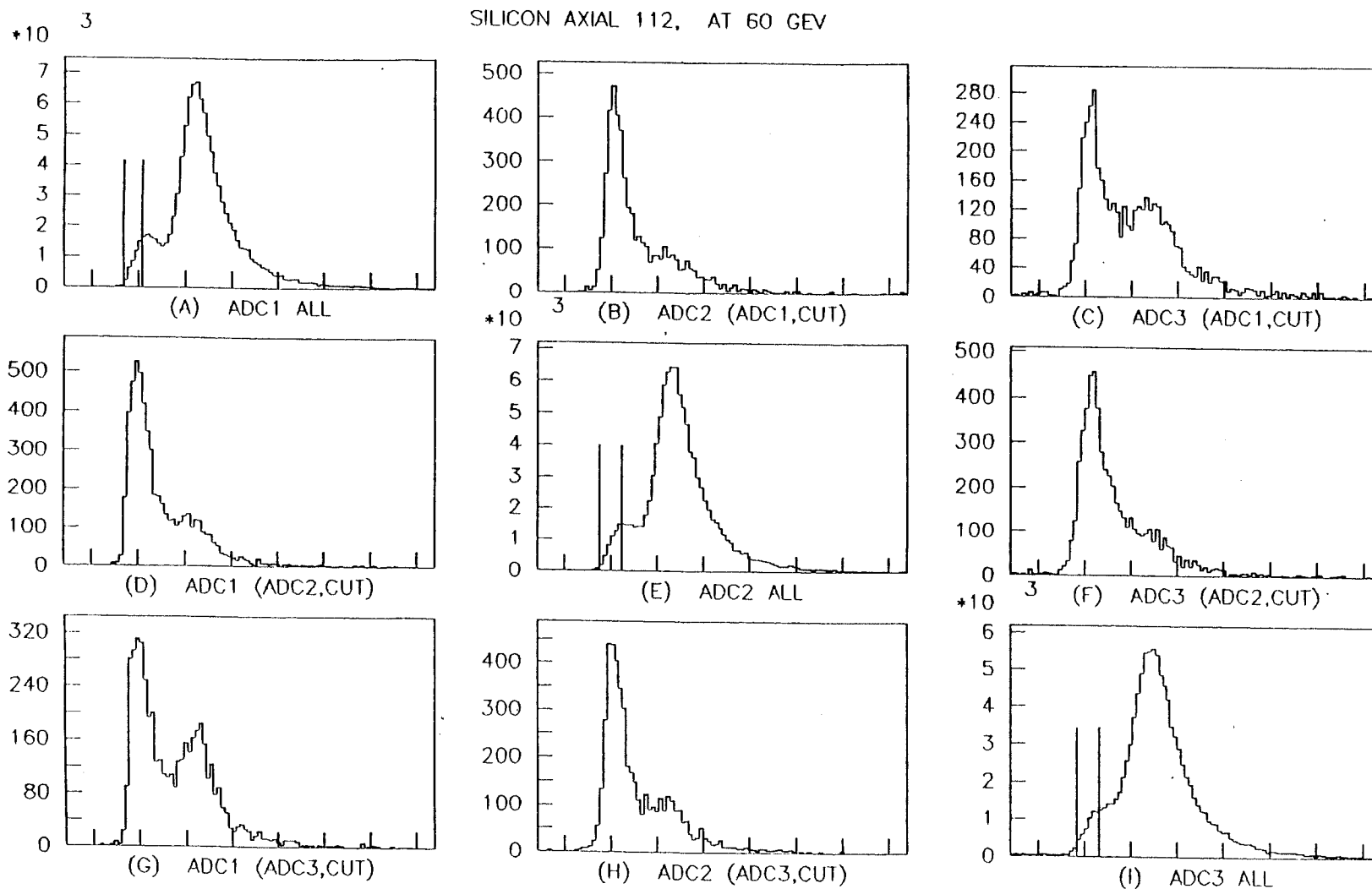


Figure 9.9 Ionization energy loss spectra at the three detectors for pions and protons transmitted through the silicon crystal parallel to 112 axis at 60 GeV/c.

side while calculating the factor α until a steady number is found. In this process until the window is completely below the random distribution the factor α varies because of the acceptance of random particles in the windows. The window positions of all detectors are shown in Figures 9.4 through 9.9 for both planar and axial channeling. The upper level of the windows for the axial case was found at a lower energy compared to the planar case and the most probable energy loss of the channeled distribution was also found lower than the peak of the channeled shoulder, as one can see in the above figures.

9.3.2 Calculation of Dechanneling Lengths

Figure 9.10 shows the energy loss distributions for pions and protons transmitted through the three detector crystal. Figure 9.10 (A), (E) and (I) are the spectra for all the particles at the three detectors and the vertical lines show the low energy loss windows made to select the channeled particles, where W_1 , W_2 and W_3 are the total number of channeled particles inside the windows respectively. {(B) and (C)}, {(D) and (F)} and {(G) and (H)} in Figure 9.10 are the spectra for those particles which have had low energy losses (cut on low energy window) in first, second and third detectors respectively. The shaded areas represent the channeled particle distribution in each spectra and the total number was calculated by using the method described in Section 9.3.1.

If W_{1C2} , W_{1C3} and W_{2C3} are the calculated total number of channeled particles in Figure 9.10(B), (C) and (F), then the channeled fractions d_{12} , d_{13} and d_{23} between the detectors 1 and 2, detectors 1

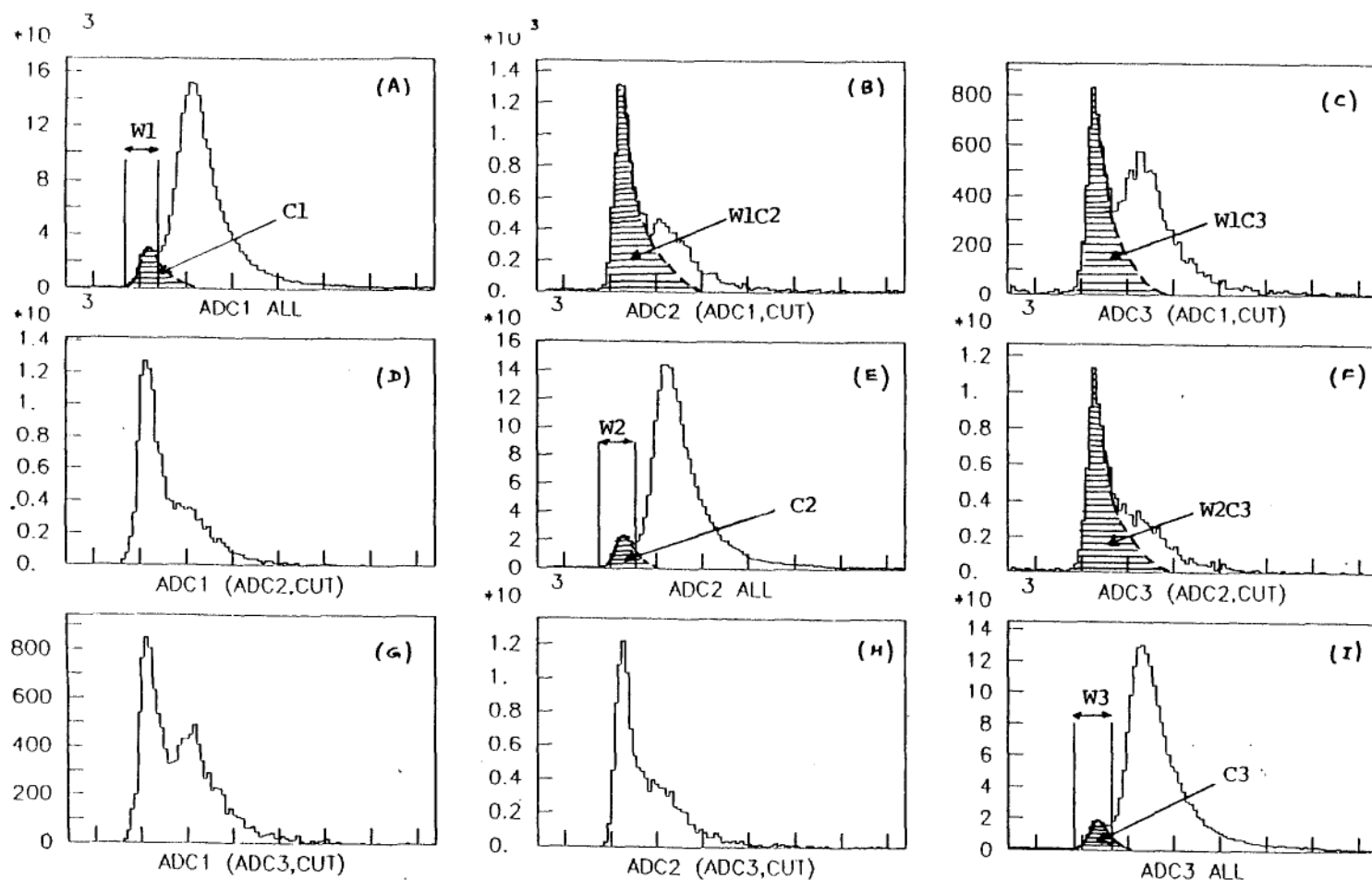


Figure 9.10 (A), (E) and (I) are the ionization energy loss distributions of pions and protons at the first, second and third detectors respectively. (B) and (C) are the energy loss distributions at the second and third detectors of particles selected from window $W1$ in the first detector, (D) and (F) are the distributions at the first and third detectors of particles selected from window $W2$ and (G) and (H) are the distribution at the first and second detectors of particles selected from window $W3$ in the third detector. The shaded areas of all figures are the channeled distributions.

and 3 and detectors 2 and 3 are given by

$$d_{12}=W1C2/W1, \quad d_{13}=W1C3/W1 \quad \text{and} \quad d_{23}=W2C3/W2 \quad 9.1$$

and the corresponding dechanneling lengths can be calculated by using Equation 8.17. Let λ_1 be the dechanneling length and t_1 , t_2 and t_3 be the positions of the detectors with respect to the upstream end of the crystal then the average value of dechanneling length λ_1 can be calculated by using the following equation

$$\lambda_1 = 1/3 [-(t_2-t_1)/\ln(d_{12})-(t_3-t_1)/\ln(d_{13})-(t_3-t_2)/\ln(d_{23})] \quad 9.2$$

Note that feeding-in is not included because only particles which were initially channeled in the first detector are counted in subsequent detectors.

9.3.3 Calculation of Feeding-in Lengths

Now consider the energy loss distribution at the first and the second detectors. If $C1$ and $C2$ (Figure 9.10) are the total number of channeled particles and d_{12} is the dechanneled fraction between the detectors which are (t_2-t_1) apart, then the fed-in particles at the second detector is given by $(C2-C1.d_{12})$. Since $(T-C1)$ was the total available number of random particles at the first detector, the fed-in fraction is $(C2-C1.d_{12})/(T-C1)$, where T is the total number of particles going through the crystal.

Let f_{12} , f_{13} and f_{23} be the fraction of fed-in particles from the random beam between the detectors 1 and 2, detectors 1 and 3 and detectors 2 and 3 respectively and $C1$, $C2$ and $C3$ the total calculated

number of channeled particles at the three detectors (in Figures 9.10(A), (B) and (C)) then the feeding-in fractions can be written as

$$f_{12} = (C2 - C1 \cdot d_{12}) / (T - C1) \quad 9.3a$$

$$f_{13} = (C3 - C1 \cdot d_{13}) / (T - C1) \quad 9.3b$$

$$f_{23} = (C3 - C2 \cdot d_{23}) / (T - C2) \quad 9.3c$$

The average value of feeding-in length λ_2 can then be calculated using the equation

$$\lambda_2 = 1/3 \left[-(t_2 - t_1) / \ln(1 - f_{12}) - (t_3 - t_1) / \ln(1 - f_{13}) - (t_3 - t_2) / \ln(1 - f_{23}) \right] \quad 9.4$$

9.4 Results and Calculations

The results of planar and axial dechanneling and feeding-in are discussed in this section. The data was acquired at 30, 60, 100 and 200 GeV/c for Si(110) planar channeling and 60 and 100 GeV/c for Si<112> axial channeling. A summary of all data is given in Table 9.1.

Figures 9.4 through 9.33 show the energy loss spectra spectra at the detectors for pions and protons transmitted through the crystal for both planar and axial channeling at all energies. (A), (E) and (I) in Figures 9.4 through 9.33 are the spectra for all the particles at the three detectors and the vertical lines show the low energy loss windows made to select the channeled particles. {(B) and (C)}, {(D) and (F)} and {(G) and (H)} are the spectra for those particles which have had

SILICON PLANAR 110, AT 200 GEV

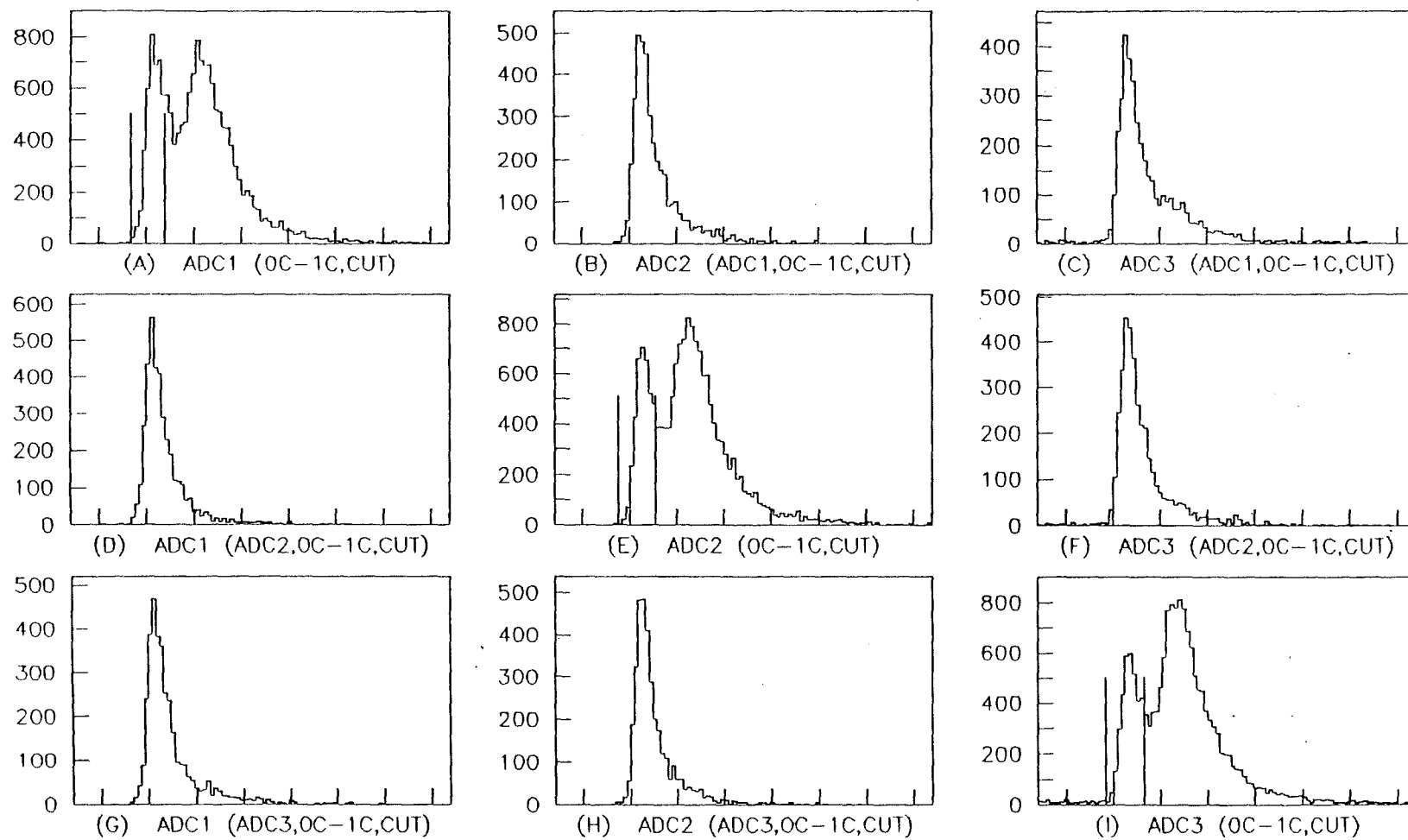


Figure 9.11 Ionization energy loss spectra at the three detectors for pions and protons transmitted through the silicon crystal parallel to 110 plane at 200 GeV/c. Particles incident in the angular region $0 < \theta < \theta_c$ with respect to the plane are selected.

SILICON PLANAR 110, AT 200 GEV

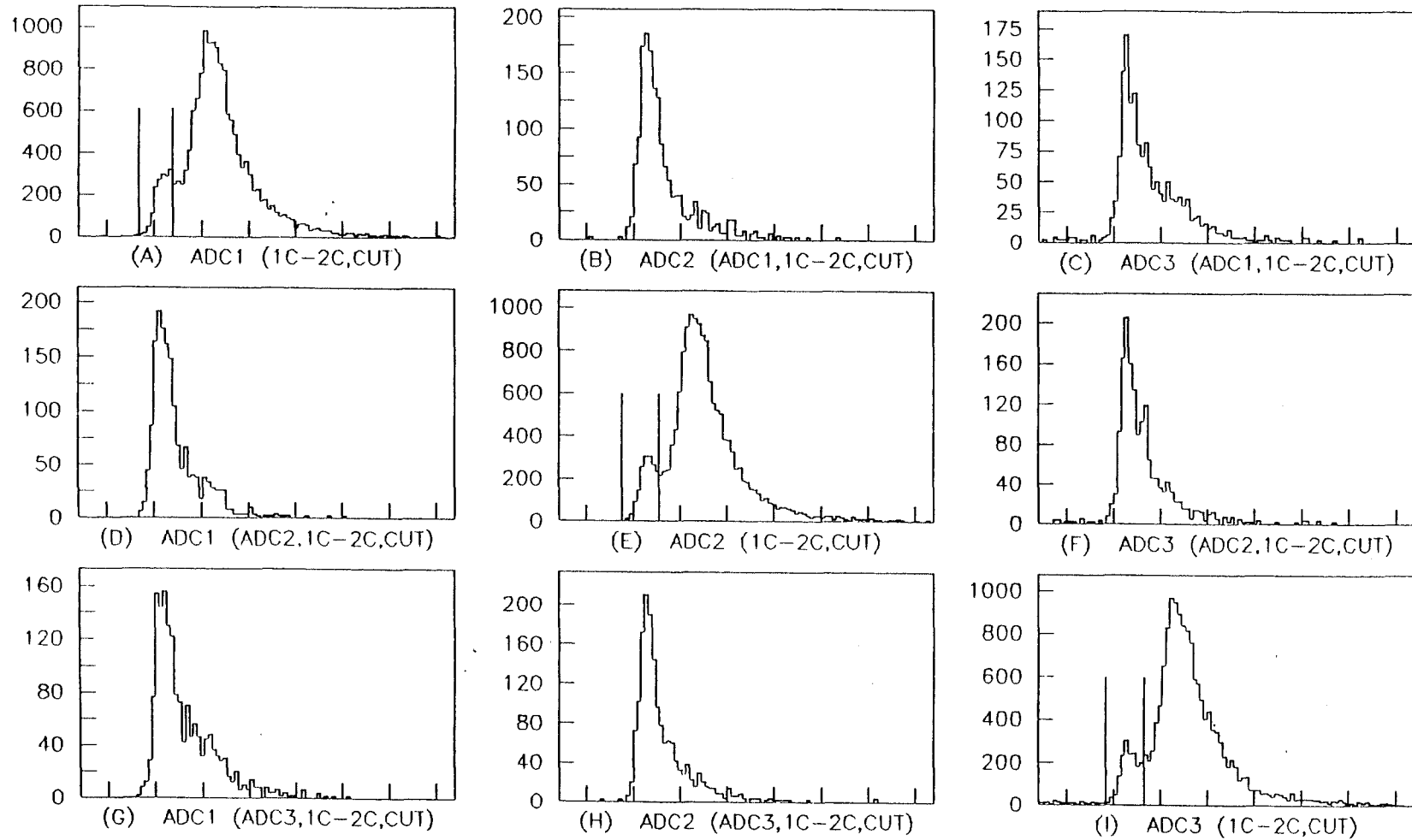


Figure 9.12 Ionization energy loss spectra at the three detectors for pions and protons transmitted through the silicon crystal parallel to 110 plane at 200 GeV/c. Particles incident in the angular region $\theta_c < \theta < 2\theta_c$ with respect to the plane are selected.

SILICON PLANAR 110, AT 200 GEV

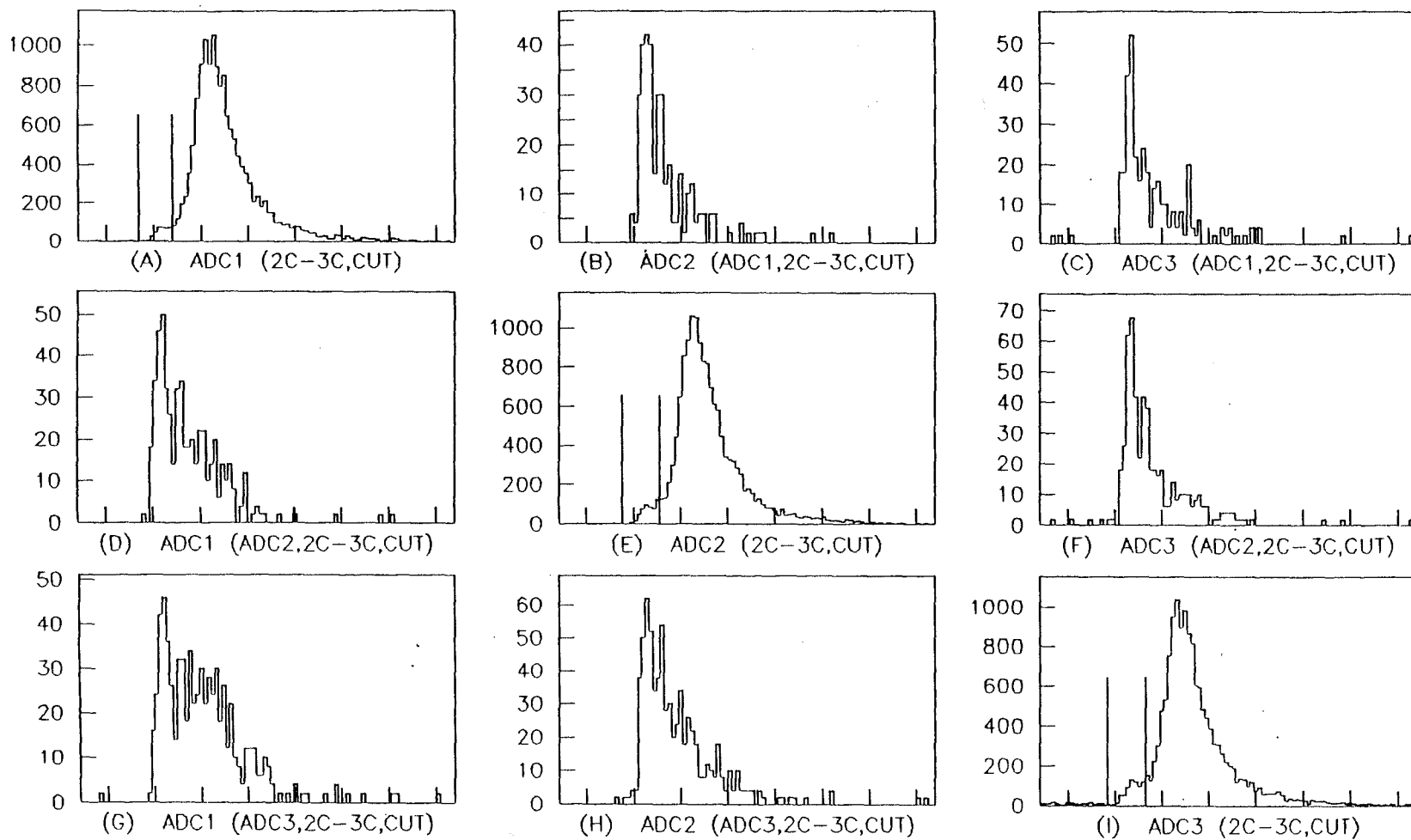


Figure 9.13 Ionization energy loss spectra at the three detectors for pions and protons transmitted through the silicon crystal parallel to 110 plane at 200 GeV/c. Particles incident in the angular region $2\theta_c < \theta < 3\theta_c$ with respect to the plane are selected.

SILICON PLANAR 110, AT 200 GEV

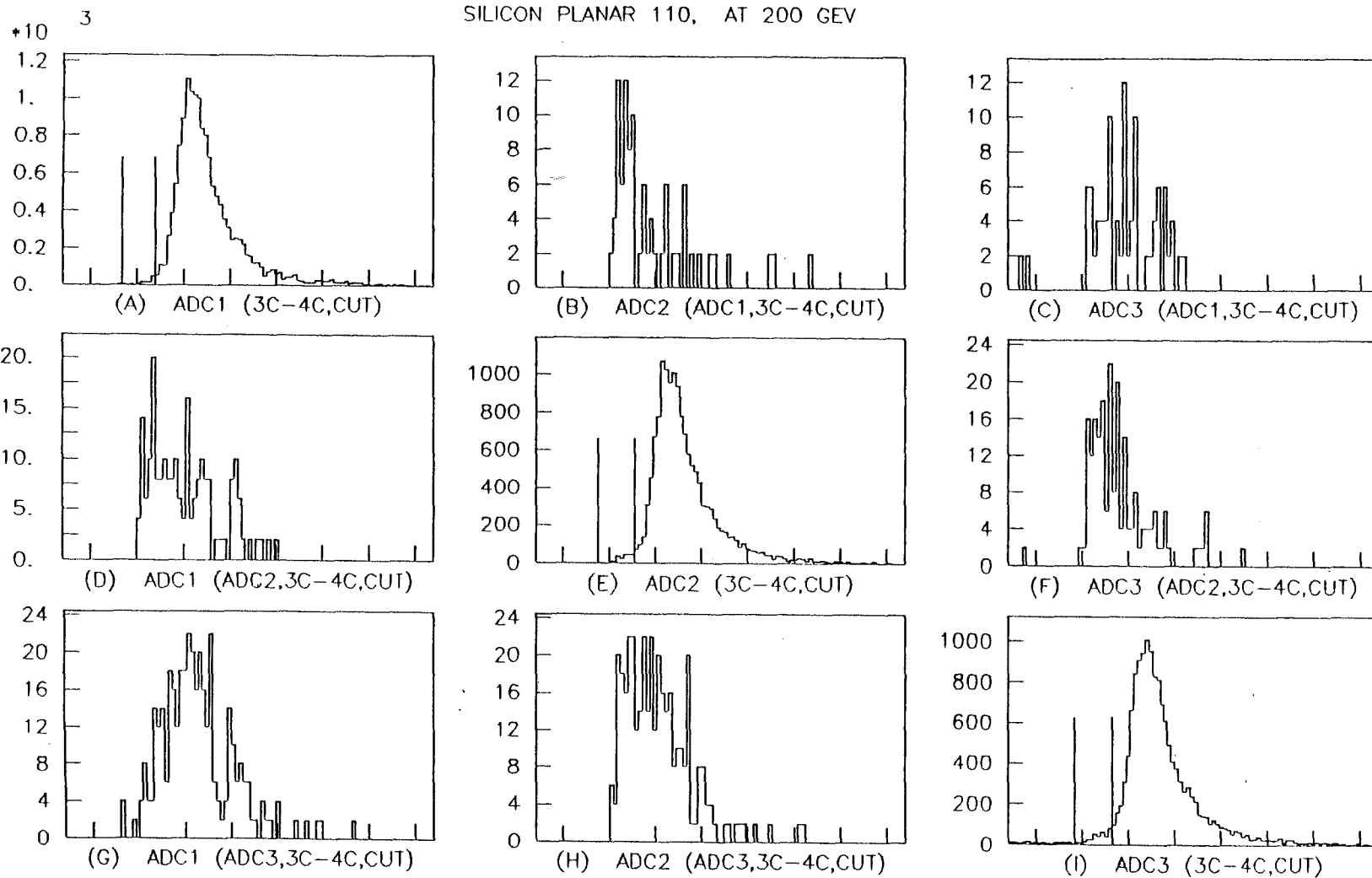


Figure 9.14 Ionization energy loss spectra at the three detectors for pions and protons transmitted through the silicon crystal parallel to 110 plane at 200 GeV/c. Particles incident in the angular region $3\theta_c < \theta < 4\theta_c$ with respect to the plane are selected.

SILICON PLANAR 110, AT 100 GEV

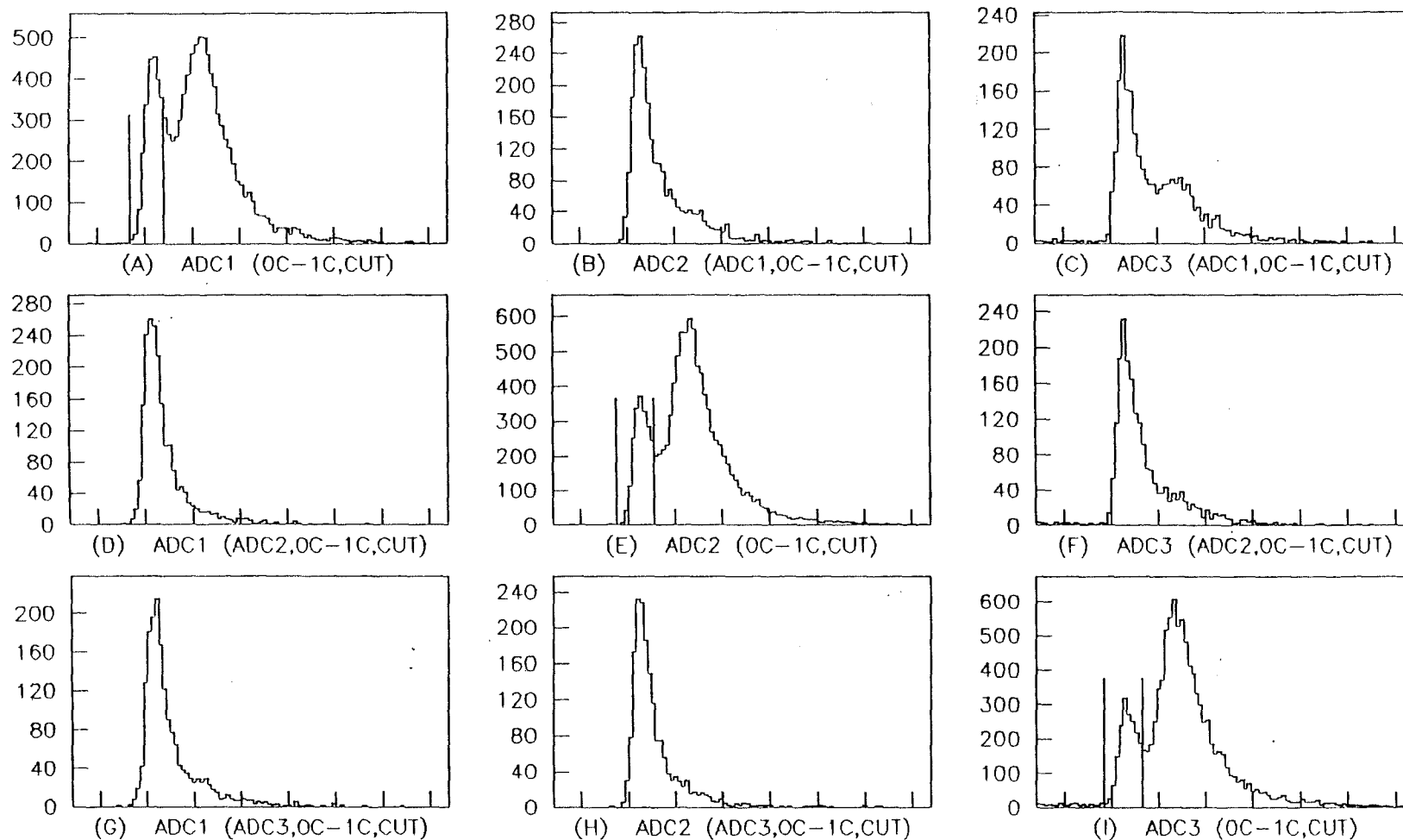


Figure 9.15 Ionization energy loss spectra at the three detectors for pions and protons transmitted through the silicon crystal parallel to 110 plane at 100 GeV/c. Particles incident in the angular region $0 < \theta < \theta_c$ with respect to the plane are selected.

SILICON PLANAR 110, AT 100 GEV

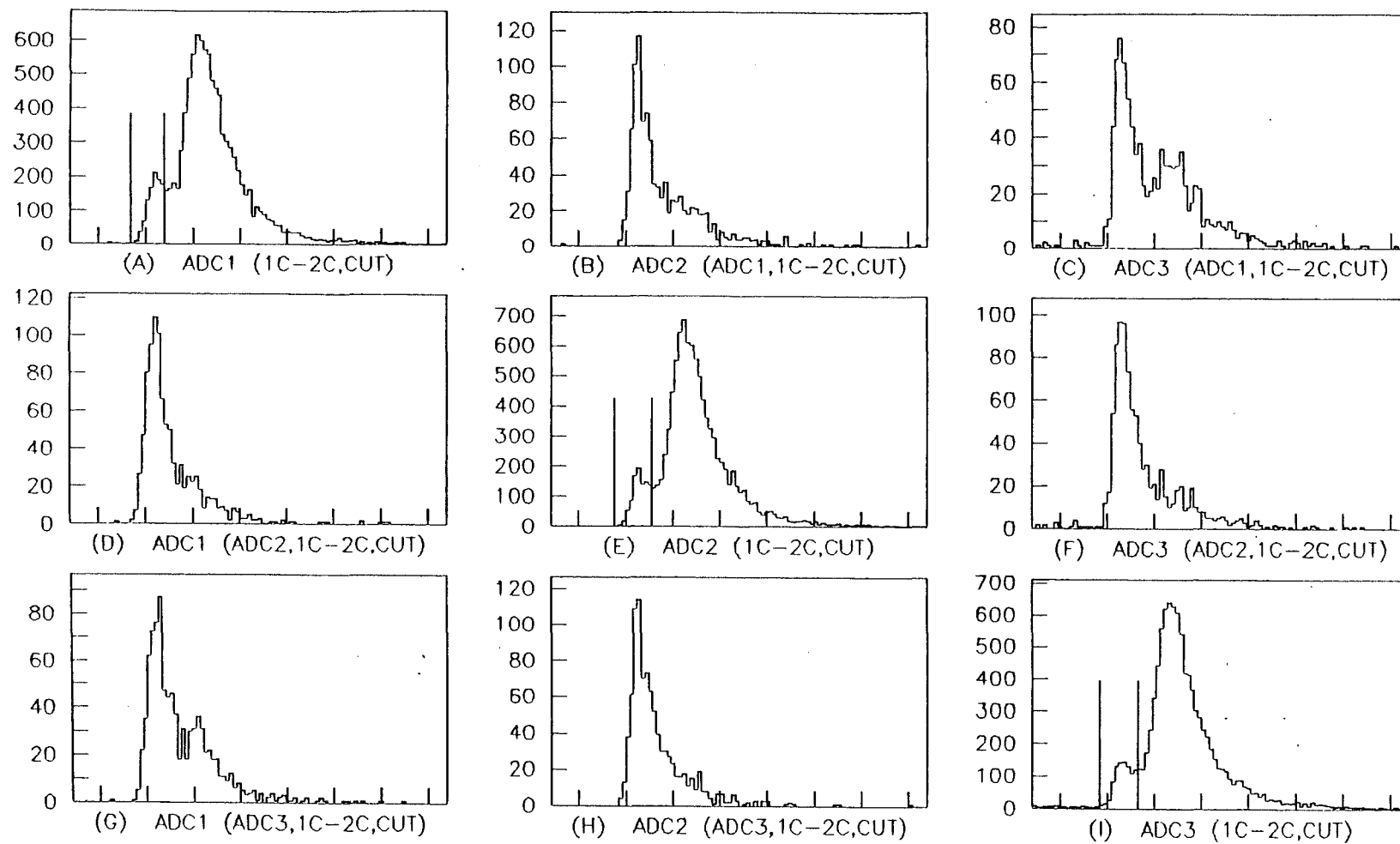


Figure 9.16 Ionization energy loss spectra at the three detectors for pions and protons transmitted through the silicon crystal parallel to 110 plane at 100 GeV/c. Particles incident in the angular region $\theta_c < \theta < 2\theta_c$ with respect to the plane are selected.

SILICON PLANAR 110, AT 100 GEV

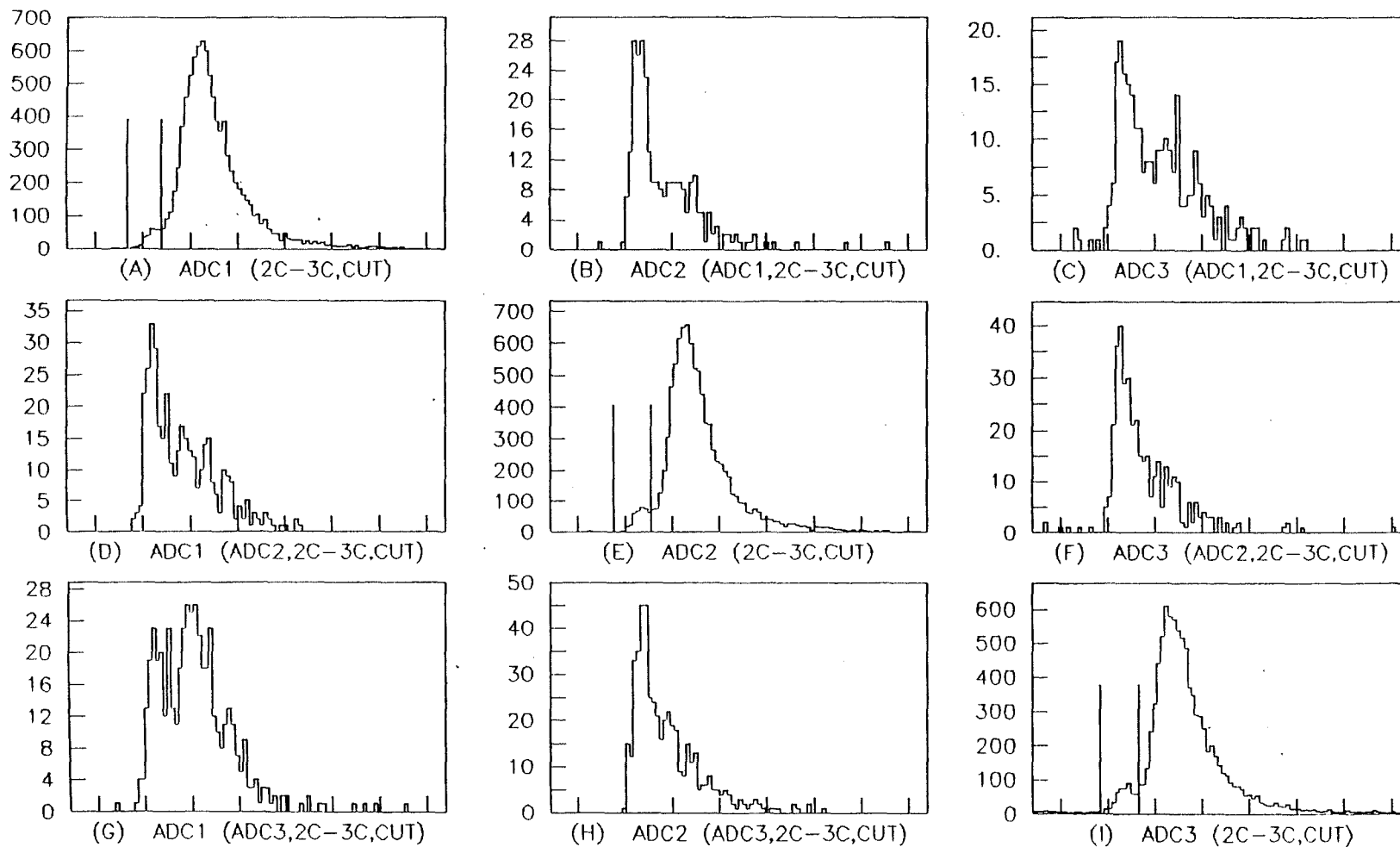


Figure 9.17 Ionization energy loss spectra at the three detectors for pions and protons transmitted through the silicon crystal parallel to 110 plane at 100 GeV/c. Particles incident in the angular region $20^\circ < \theta < 30^\circ$ with respect to the plane are selected.

SILICON PLANAR 110, AT 100 GEV

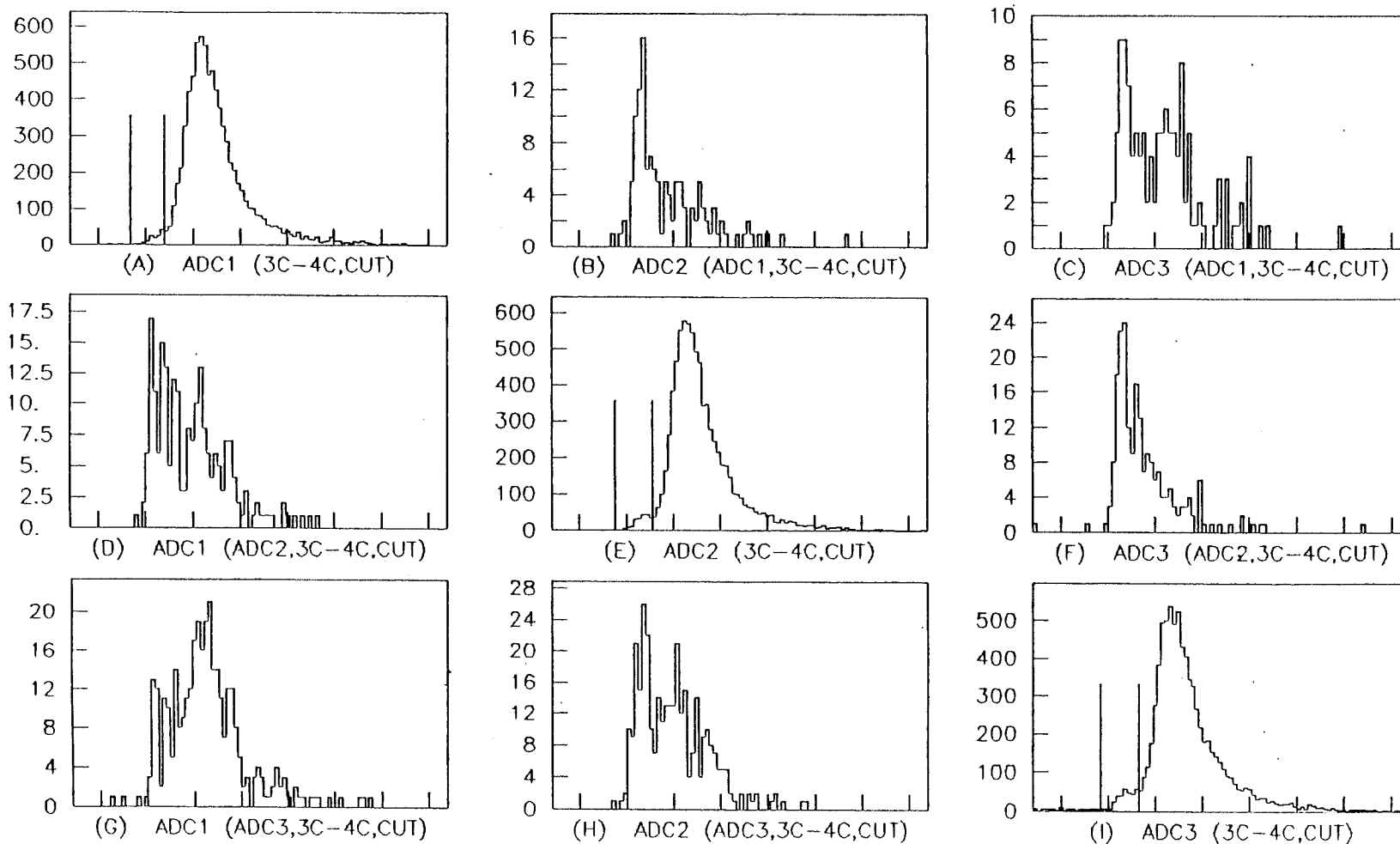


Figure 9.18 Ionization energy loss spectra at the three detectors for pions and protons transmitted through the silicon crystal parallel to 110 plane at 100 GeV/c. Particles incident in the angular region $3\theta_c < \theta < 4\theta_c$ with respect to the plane are selected.

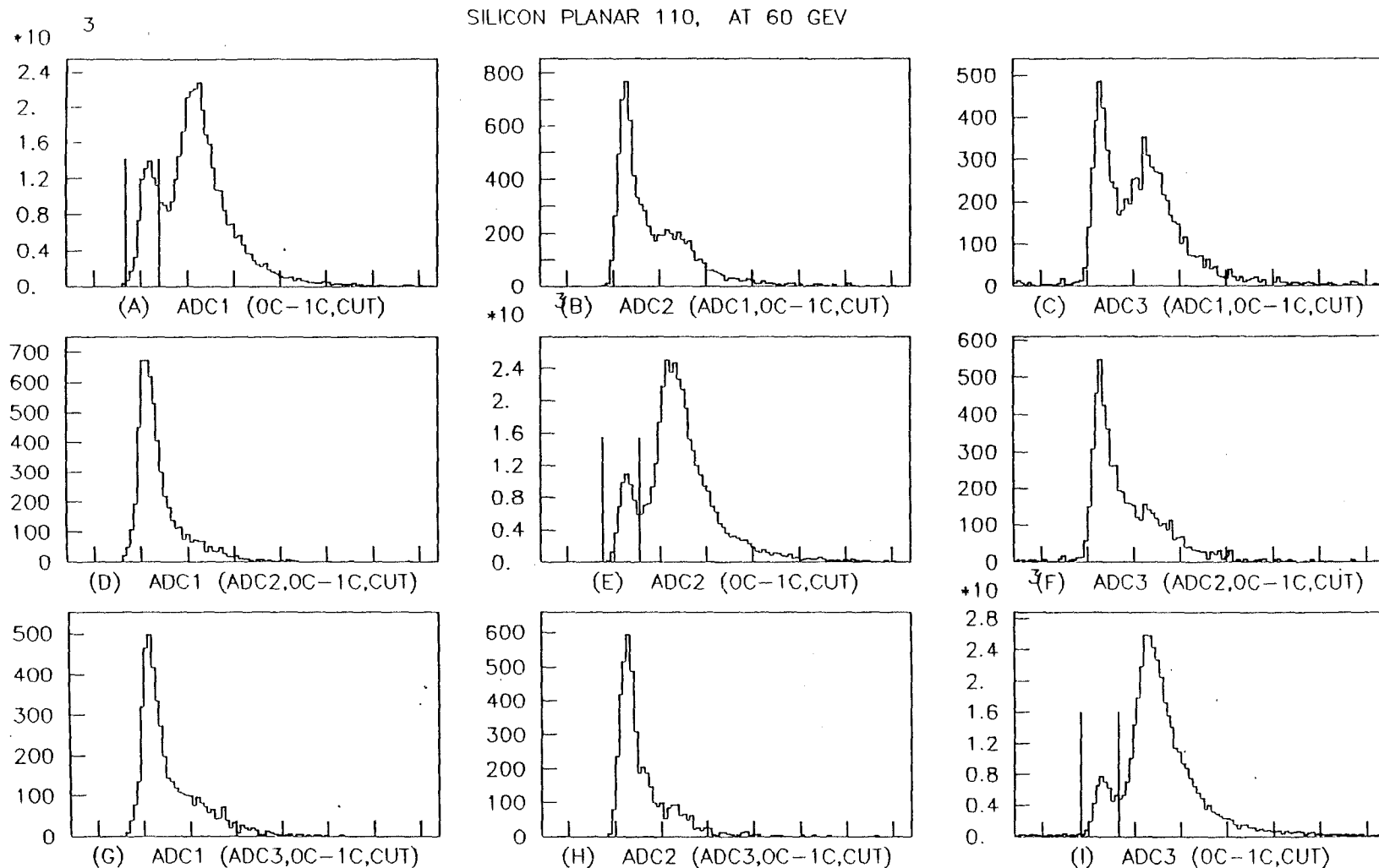


Figure 9.19 Ionization energy loss spectra at the three detectors for pions and protons transmitted through the silicon crystal parallel to 110 plane at 60 GeV/c. Particles incident in the angular region $0 < \theta < \theta_c$ with respect to the plane are selected.

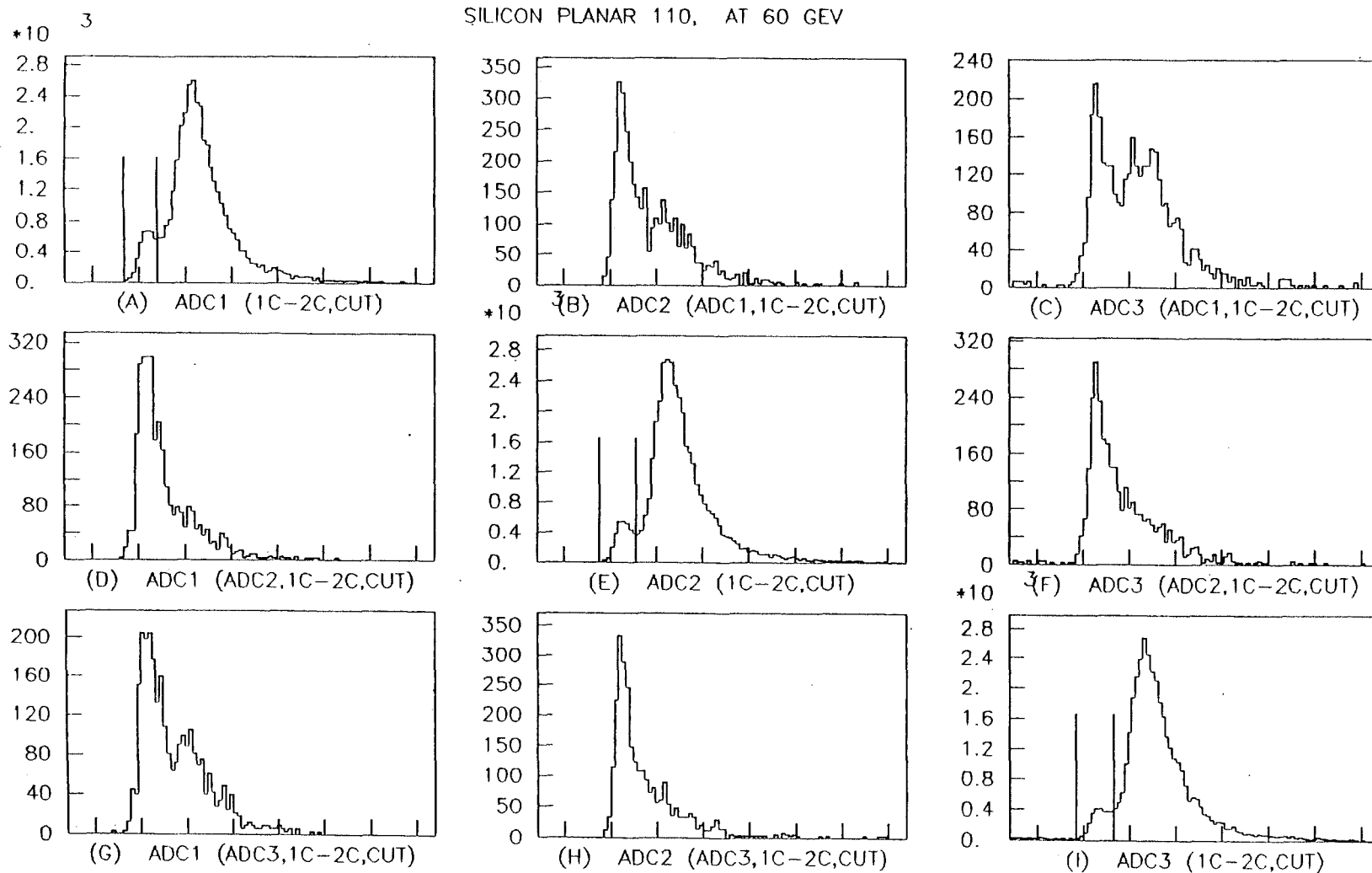


Figure 9.20 Ionization energy loss spectra at the three detectors for pions and protons transmitted through the silicon crystal parallel to 110 plane at 60 GeV/c. Particles incident in the angular region $\theta_c < \theta < 2\theta_c$ with respect to the plane are selected.

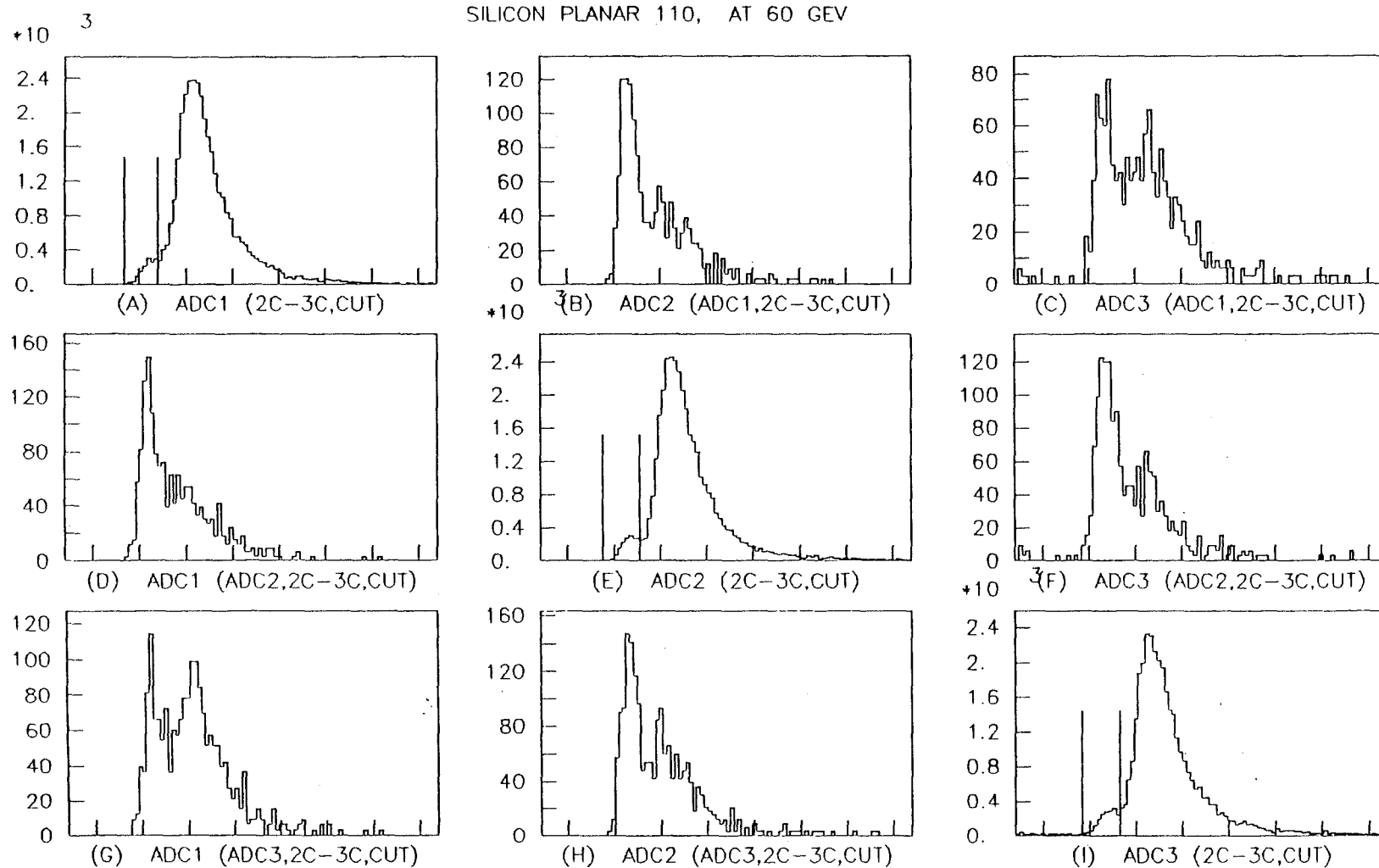


Figure 9.21 Ionization energy loss spectra at the three detectors for pions and protons transmitted through the silicon crystal parallel to 110 plane at 60 GeV/c. Particles incident in the angular region $20^\circ < \theta < 30^\circ$ with respect to the plane are selected.

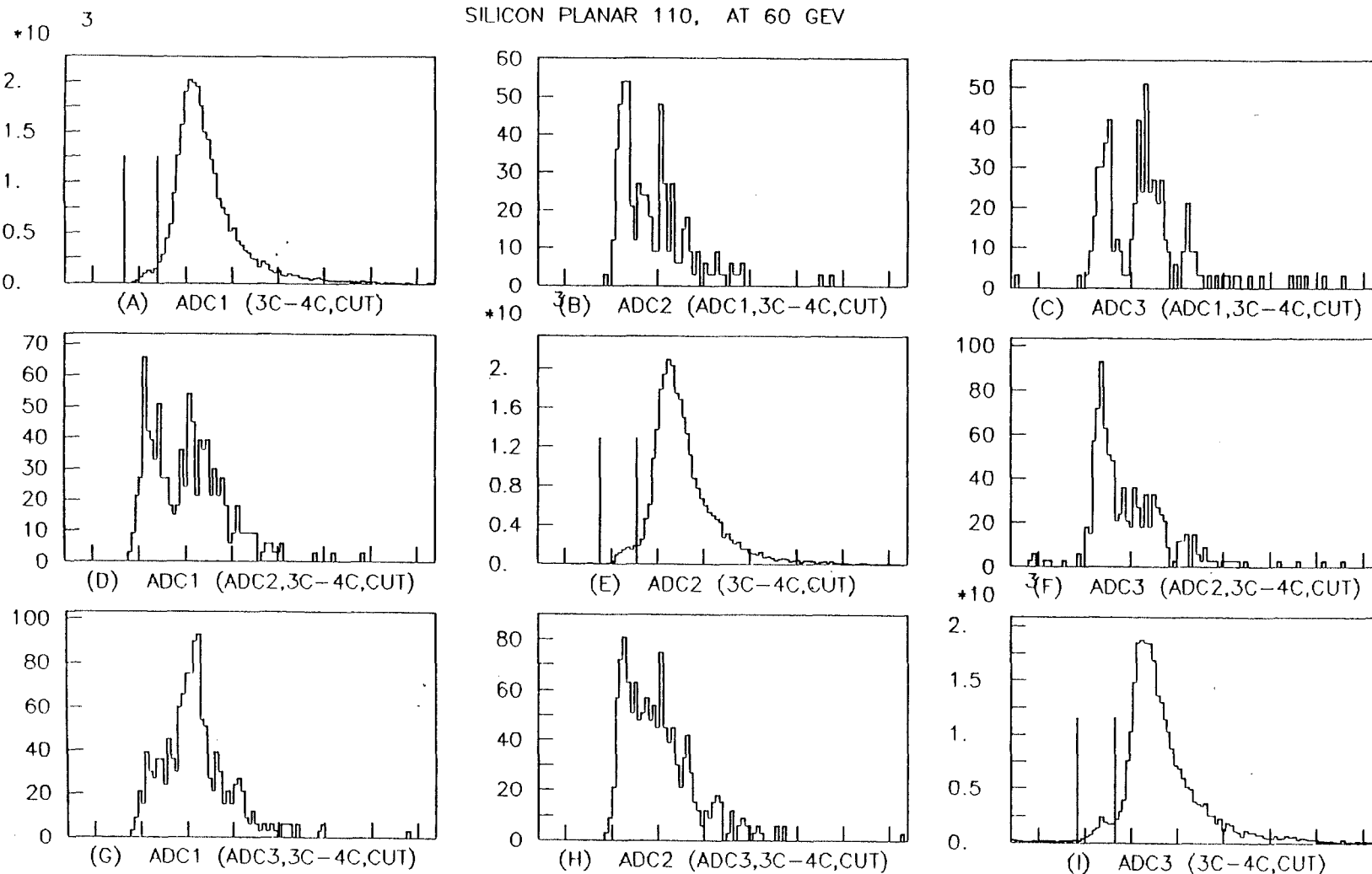


Figure 9.22 Ionization energy loss spectra at the three detectors for pions and protons transmitted through the silicon crystal parallel to 110 plane at 60 GeV/c. Particles incident in the angular region $30^\circ < \theta < 40^\circ$ with respect to the plane are selected.

SILICON PLANAR 110, AT 30 GEV

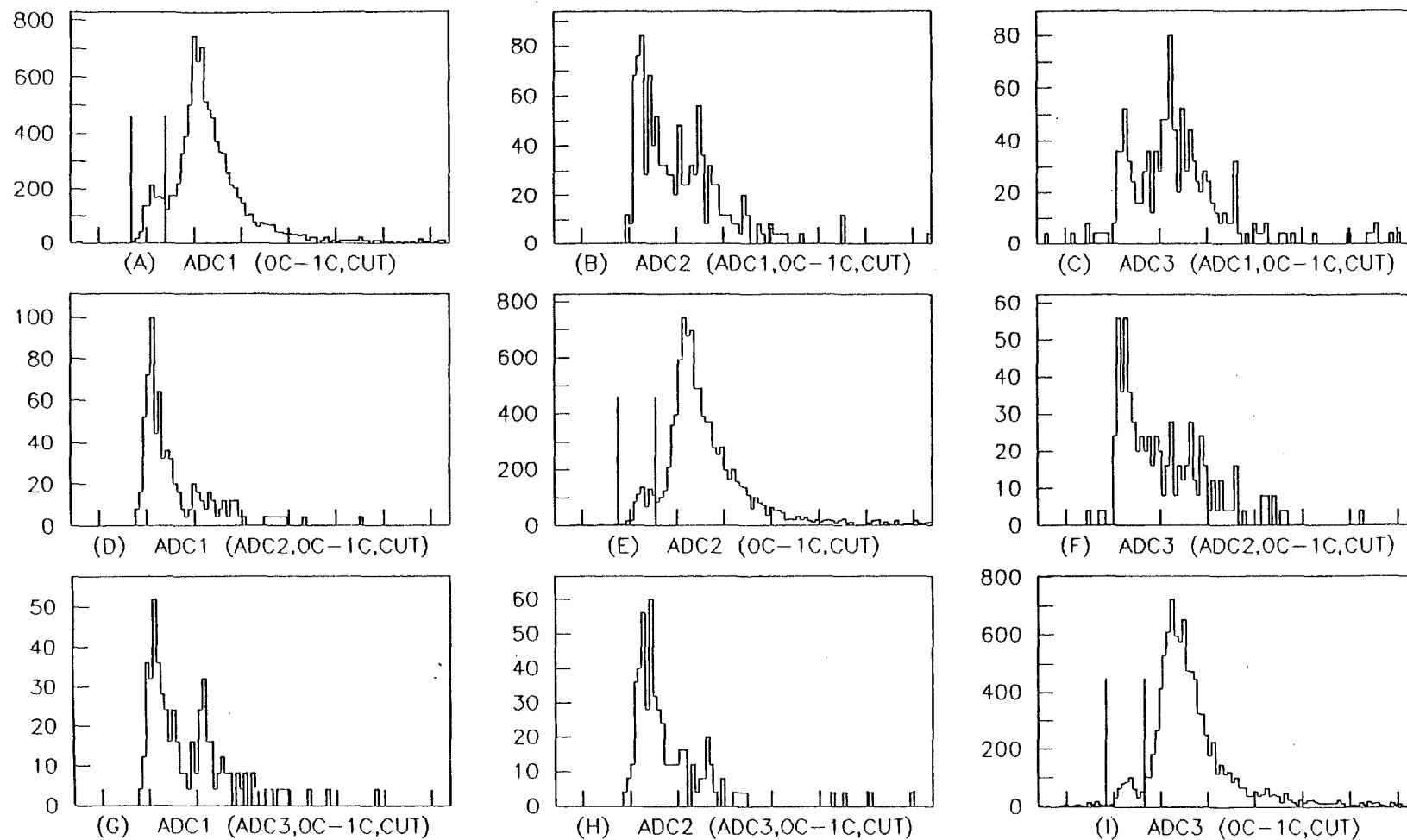


Figure 9.23 Ionization energy loss spectra at the three detectors for pions and protons transmitted through the silicon crystal parallel to 110 plane at 30 GeV/c. Particles incident in the angular region $0 < \theta < \theta_c$ with respect to the plane are selected.

SILICON PLANAR 110, AT 30 GEV

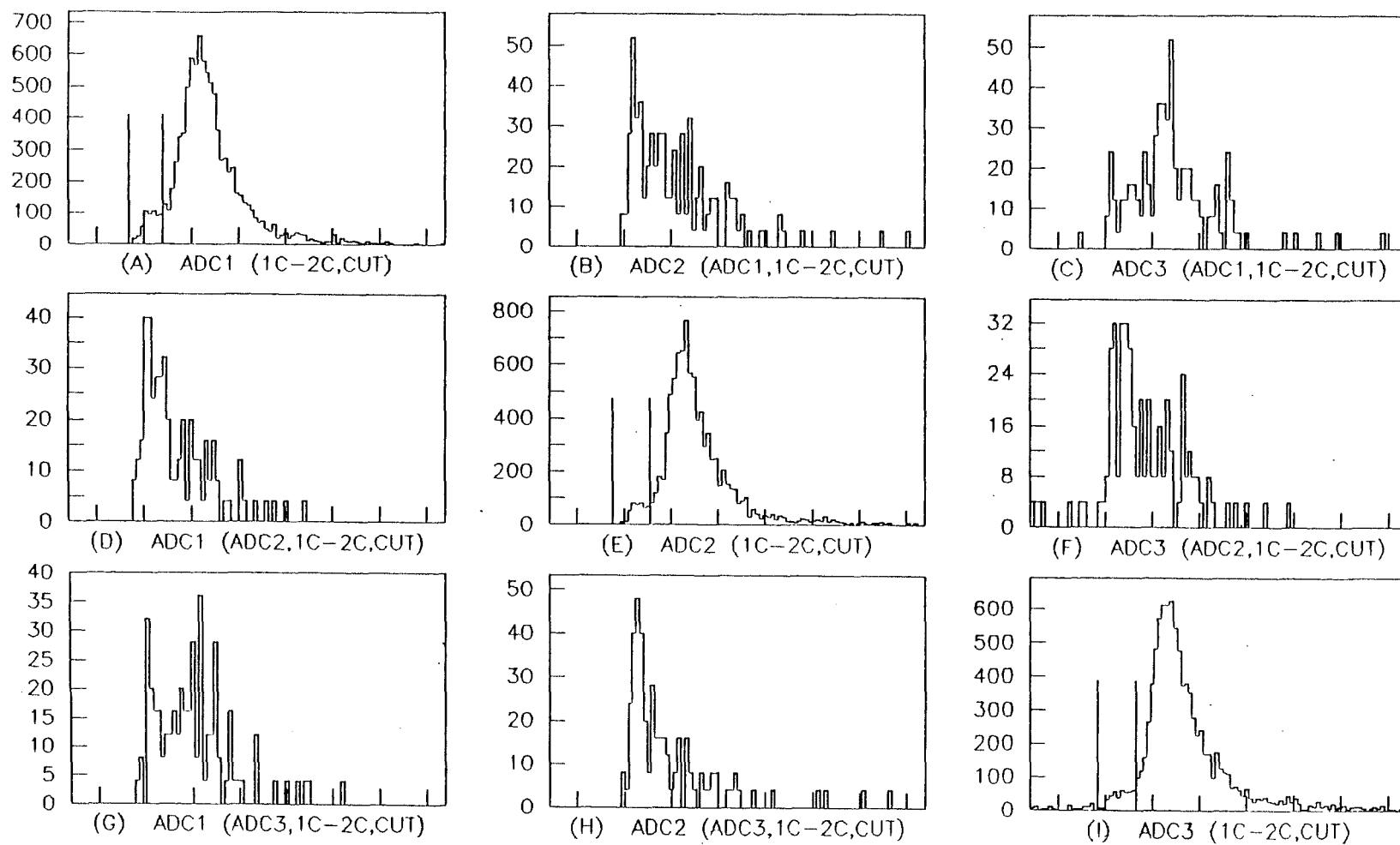


Figure 9.24 Ionization energy loss spectra at the three detectors for pions and protons transmitted through the silicon crystal parallel to 110 plane at 30 GeV/c. Particles incident in the angular region $\theta_c < \theta < 2\theta_c$ with respect to the plane are selected.

SILICON PLANAR 110, AT 30 GEV

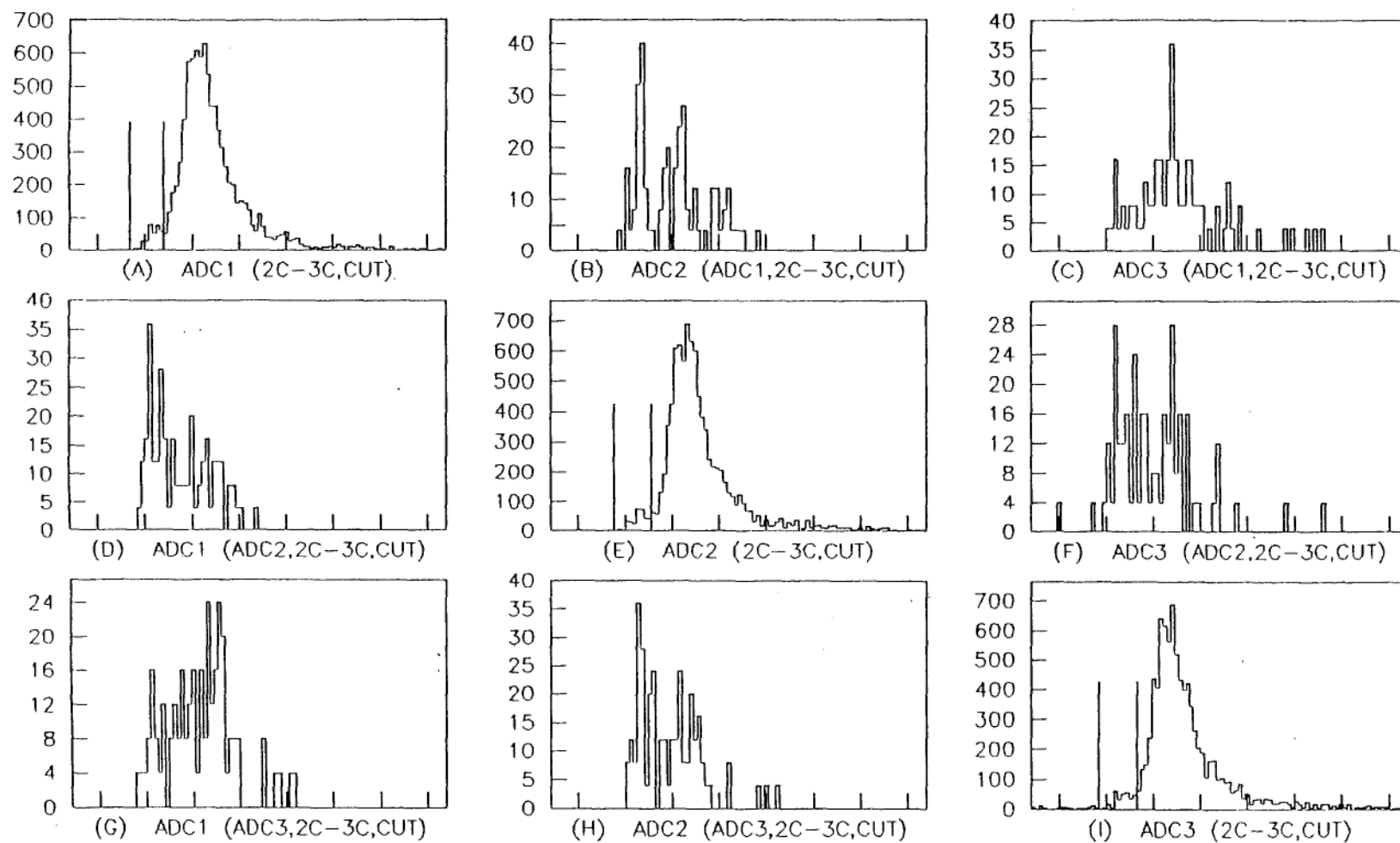


Figure 9.25 Ionization energy loss spectra at the three detectors for pions and protons transmitted through the silicon crystal parallel to 110 plane at 30 GeV/c. Particles incident in the angular region $2\theta_c < \theta < 3\theta_c$ with respect to the plane are selected.

SILICON AXIAL 112, AT 100 GEV

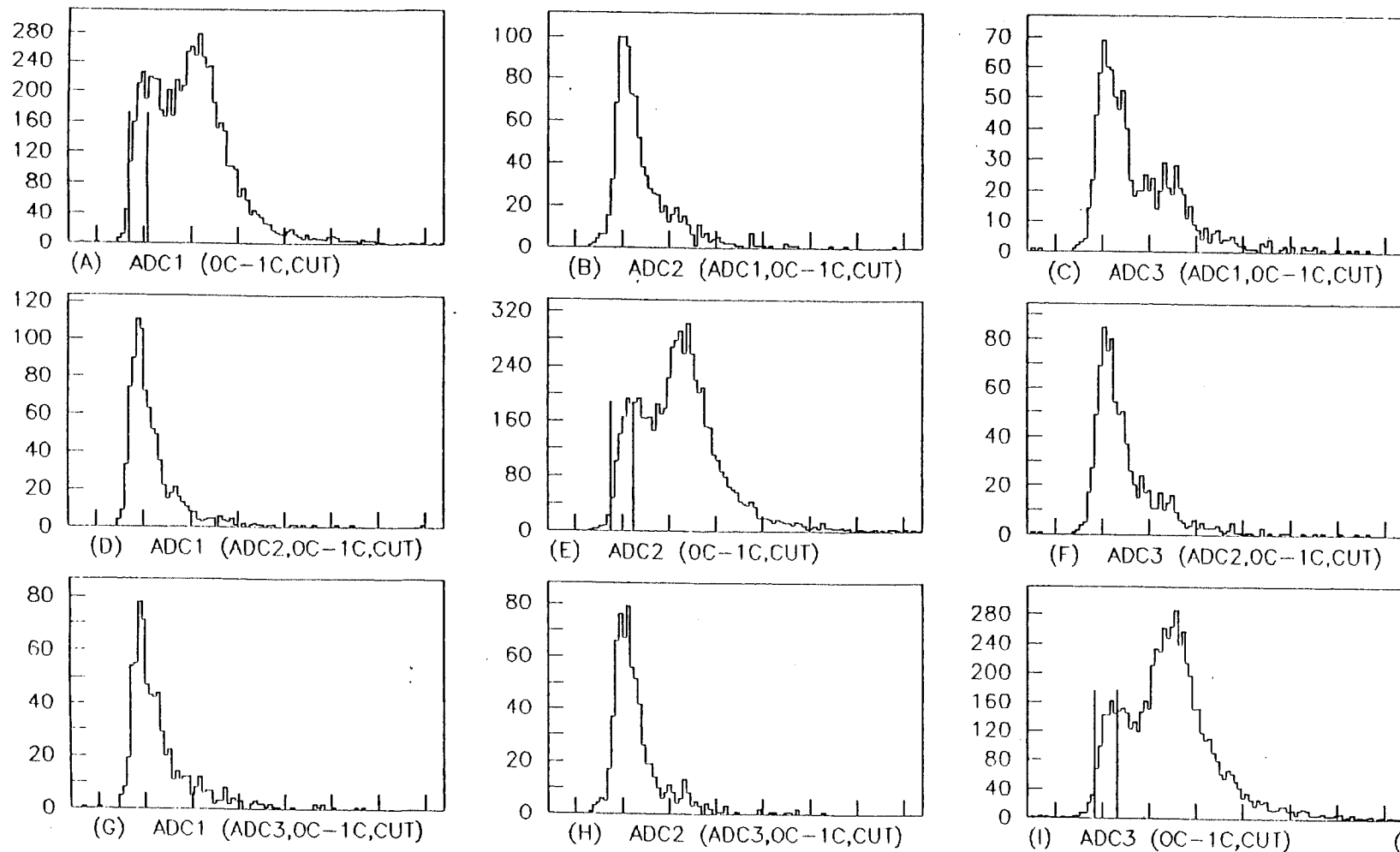


Figure 9.26 Ionization energy loss spectra at the three detectors for pions and protons transmitted through the silicon crystal parallel to 112 axis at 100 GeV/c. Particles incident in the angular region $0 < \theta < \theta_c$ with respect to the plane are selected.

SILICON AXIAL 112, AT 100 GEV

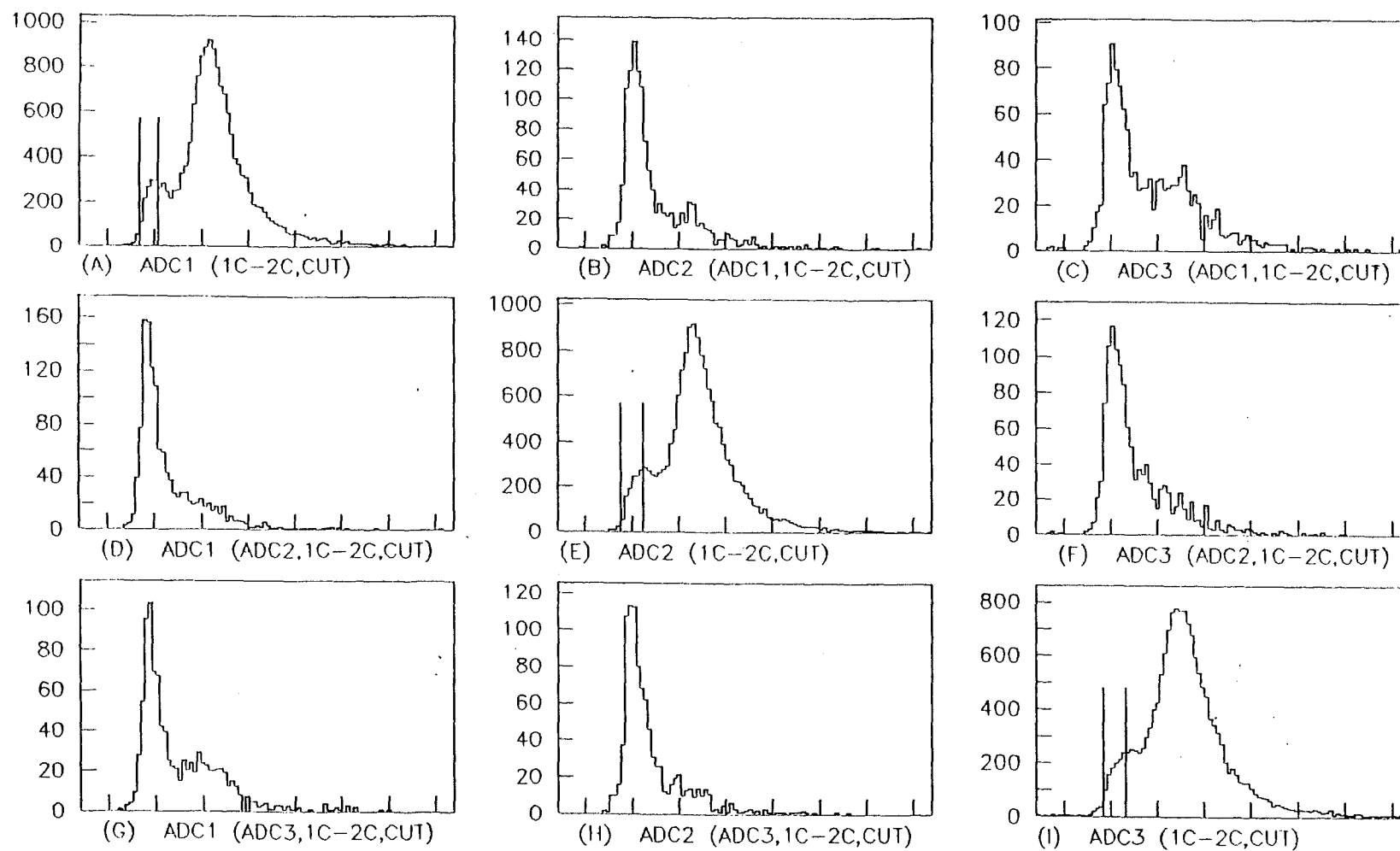


Figure 9.27 Ionization energy loss spectra at the three detectors for pions and protons transmitted through the silicon crystal parallel to 112 axis at 100 GeV/c. Particles incident in the angular region $\theta_c < \theta < 2\theta_c$ with respect to the plane are selected.

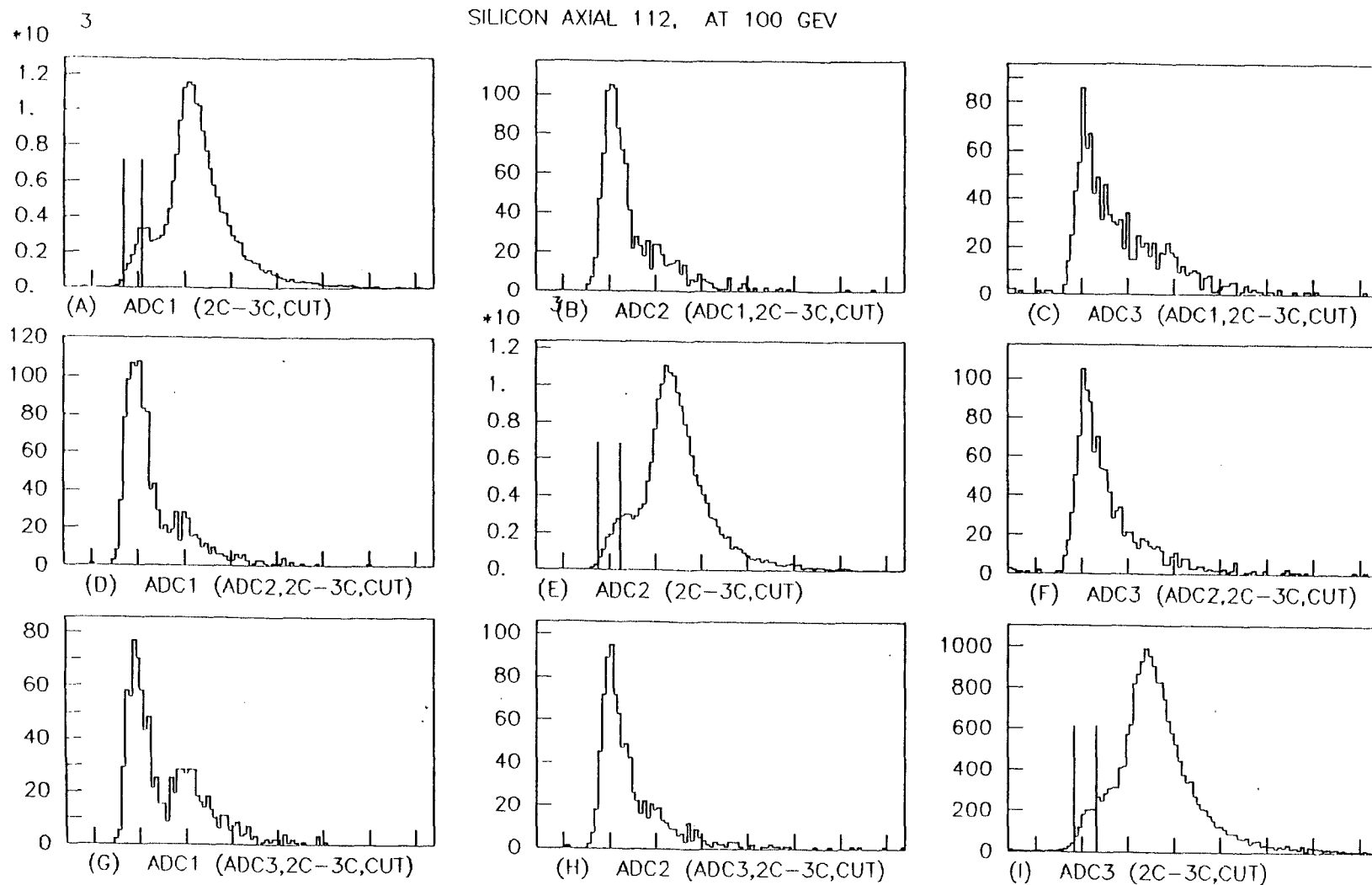


Figure 9.28 Ionization energy loss spectra at the three detectors for pions and protons transmitted through the silicon crystal parallel to 112 axis at 100 GeV/c. Particles incident in the angular region $2\theta_c < \theta < 3\theta_c$ with respect to the plane are selected.

SILICON AXIAL 112, AT 100 GEV

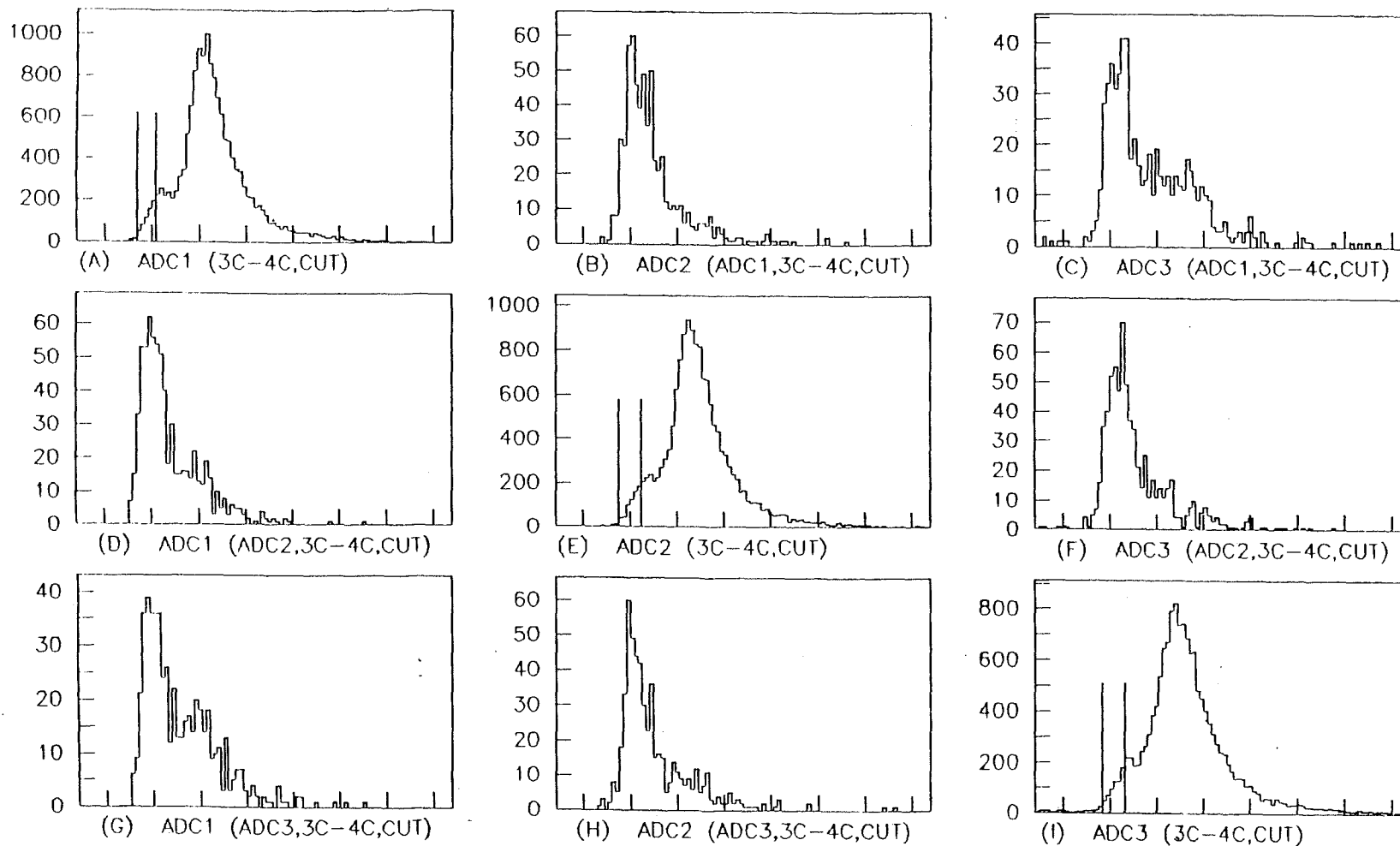


Figure 9.29 Ionization energy loss spectra at the three detectors for pions and protons transmitted through the silicon crystal parallel to 112 axis at 100 GeV/c. Particles incident in the angular region $3\theta_c < \theta < 4\theta_c$ with respect to the plane are selected.

SILICON AXIAL 112, AT 60 GEV

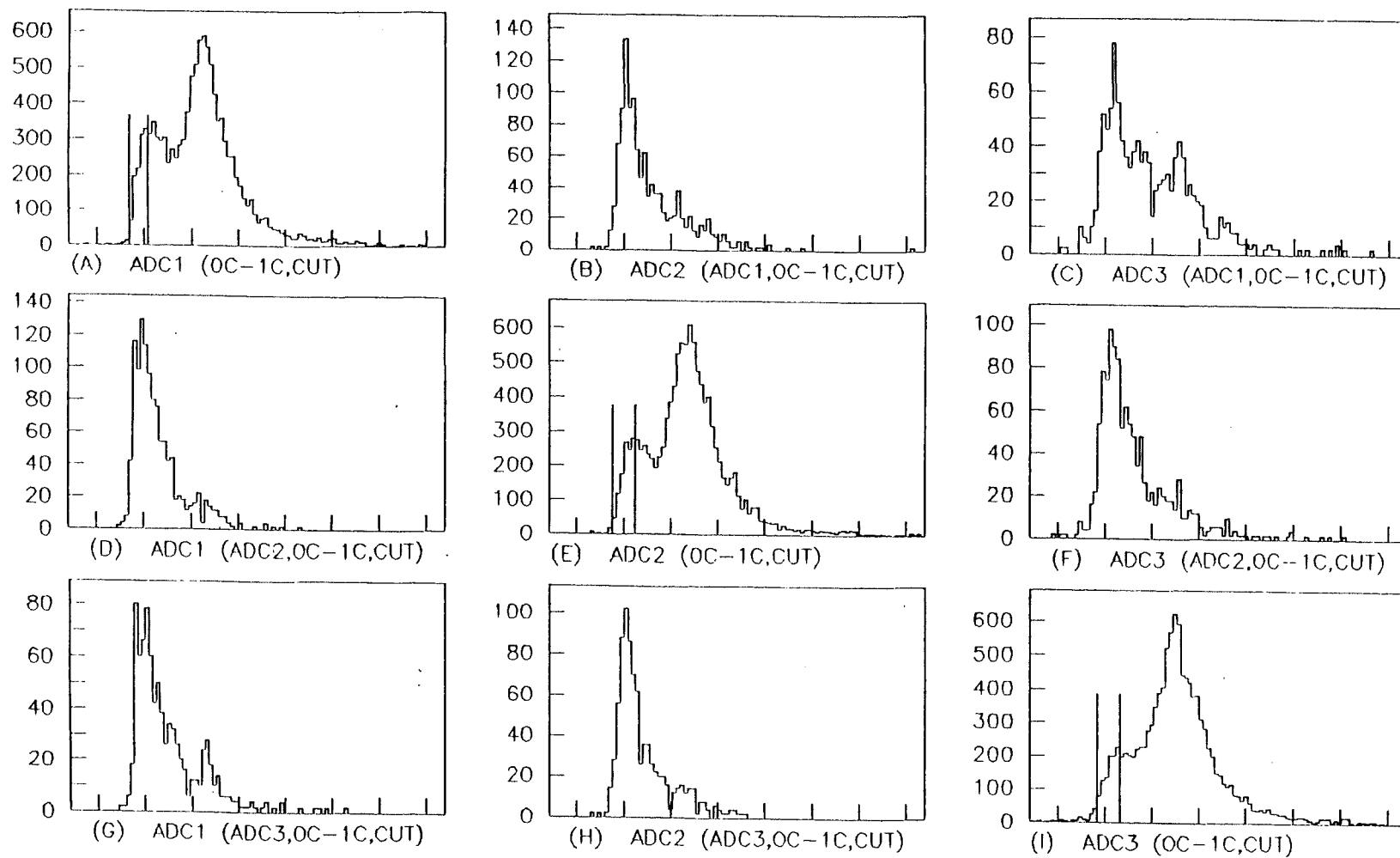


Figure 9.30 Ionization energy loss spectra at the three detectors for pions and protons transmitted through the silicon crystal parallel to 112 axis at 60 GeV/c. Particles incident in the angular region $0 < \theta < \theta_c$ with respect to the plane are selected.

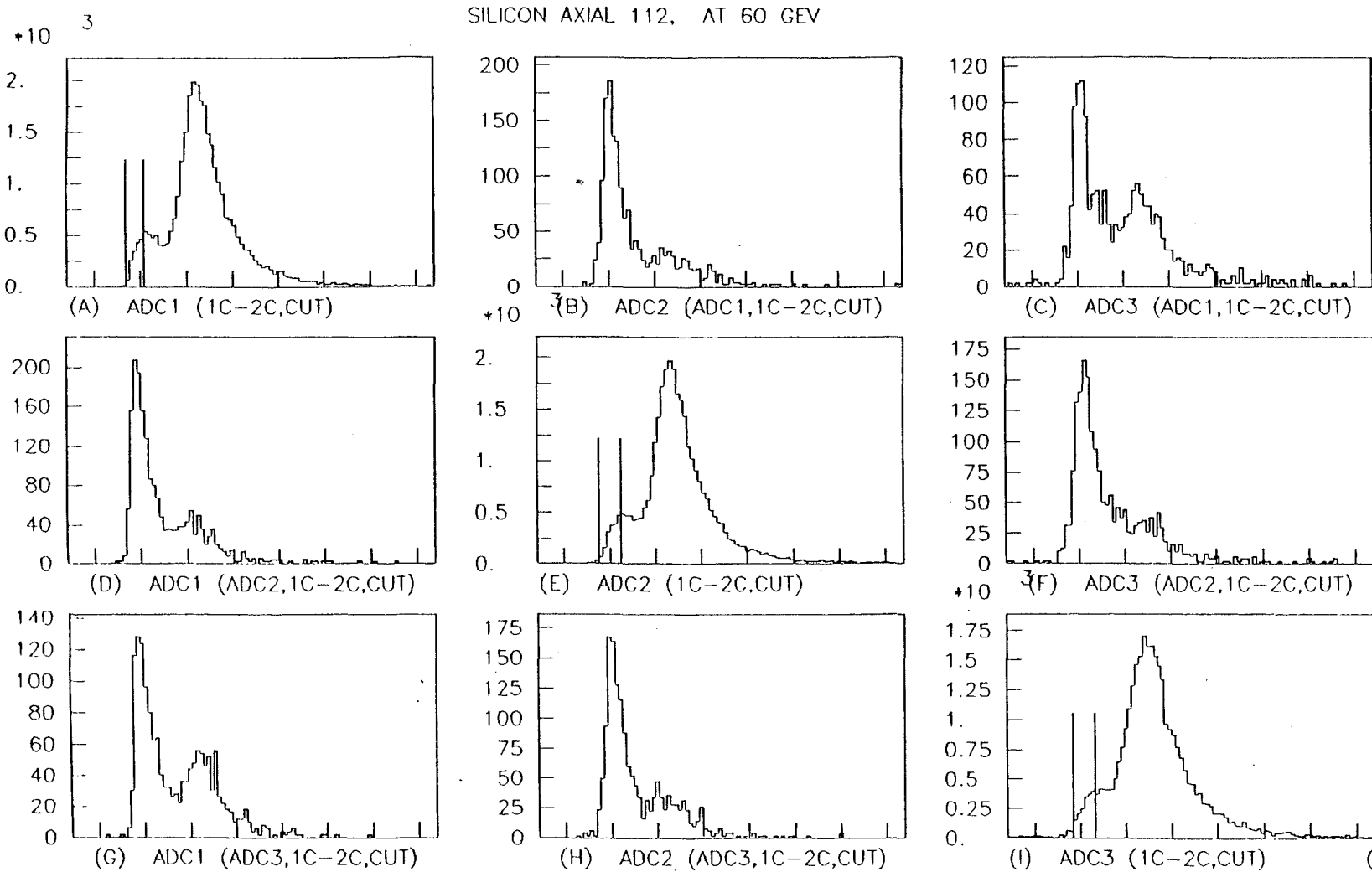


Figure 9.31 Ionization energy loss spectra at the three detectors for pions and protons transmitted through the silicon crystal parallel to 112 axis at 60 GeV/c. Particles incident in the angular region $\theta_c < \theta < 2\theta_c$ with respect to the plane are selected.

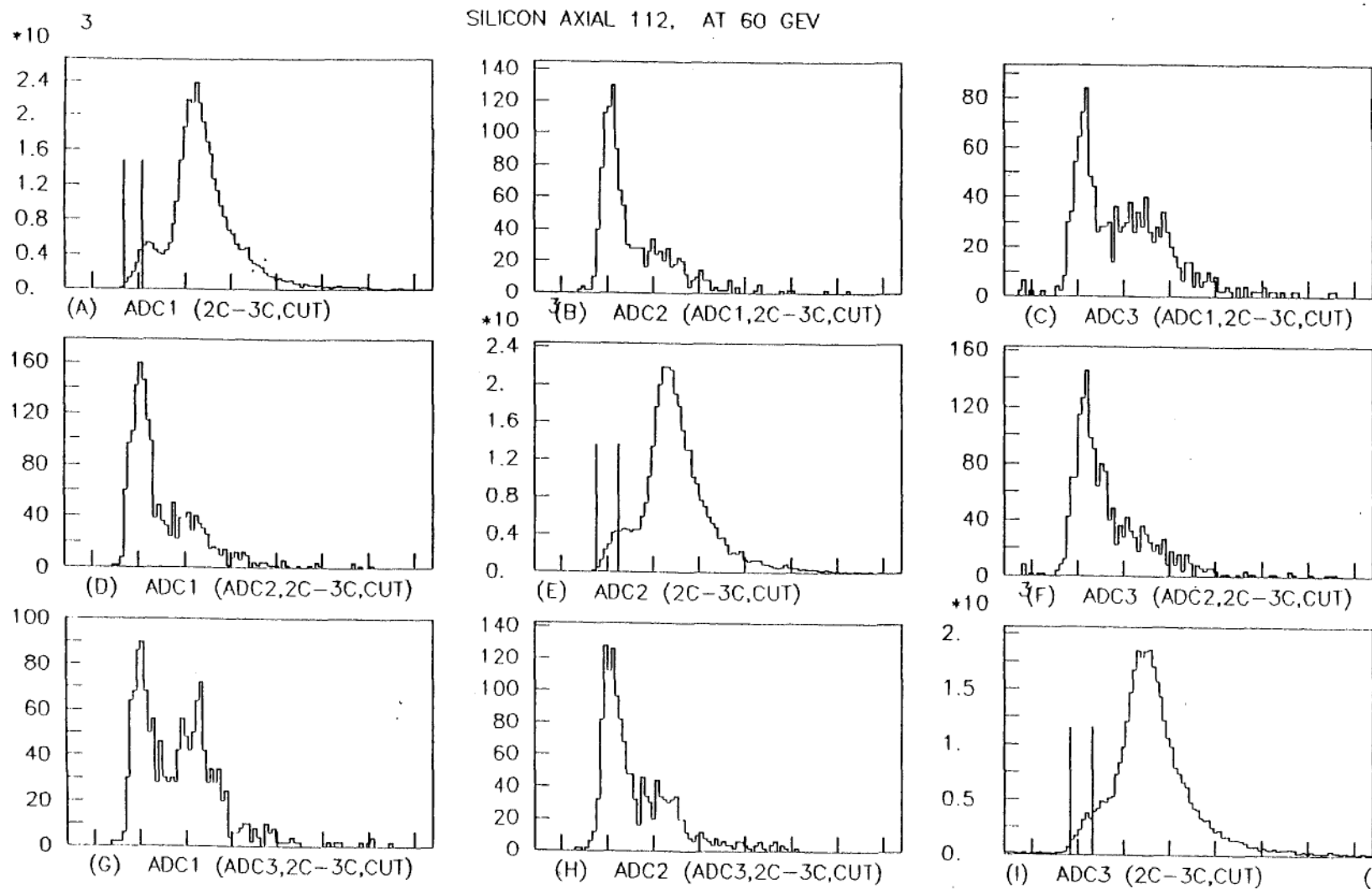


Figure 9.32 Ionization energy loss spectra at the three detectors for pions and protons transmitted through the silicon crystal parallel to 112 axis at 60 GeV/c. Particles incident in the angular region $2\theta_c < \theta < 3\theta_c$ with respect to the plane are selected.

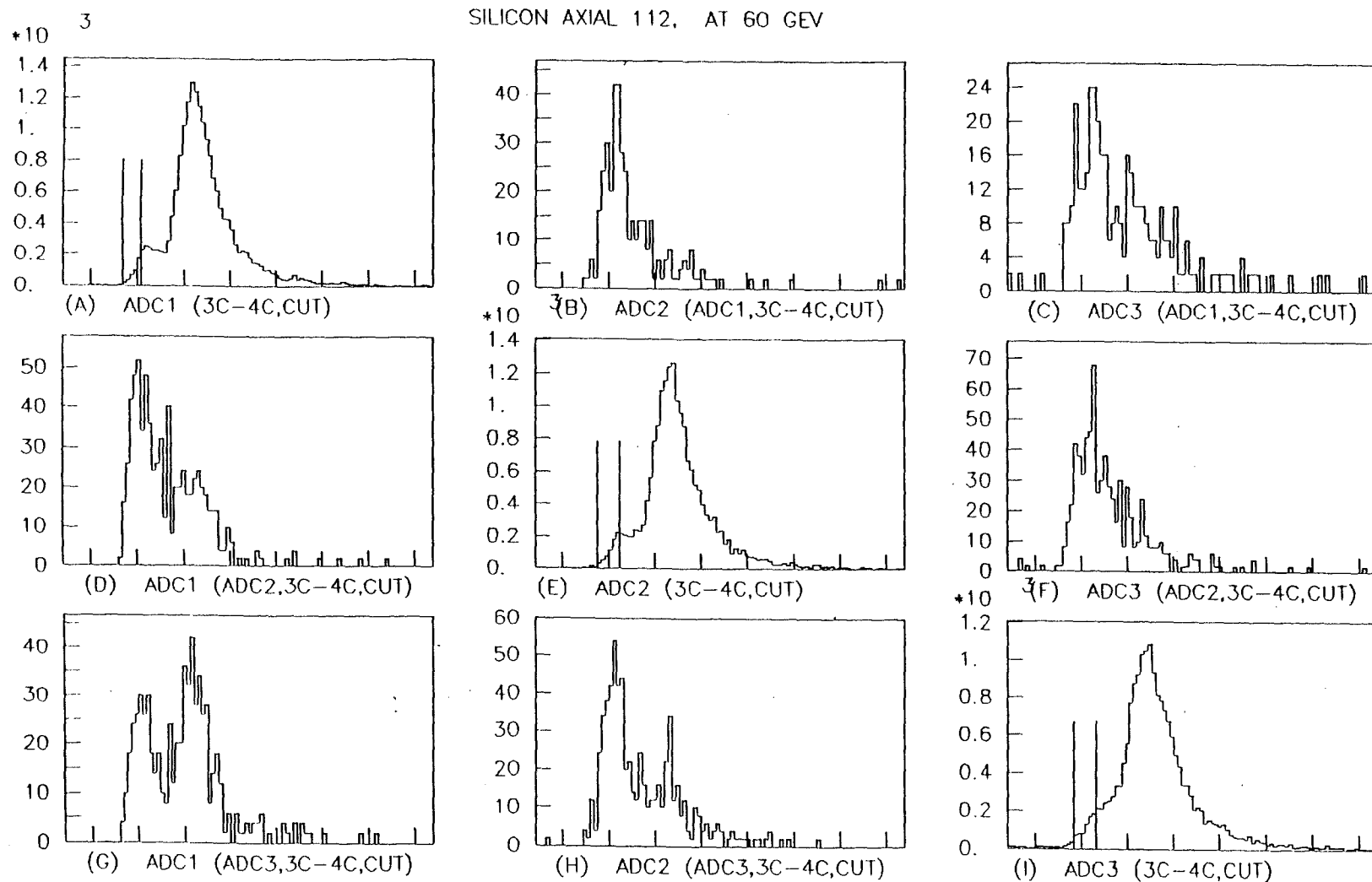


Figure 9.33 Ionization energy loss spectra at the three detectors for pions and protons transmitted through the silicon crystal parallel to 112 axis at 60 GeV/c. Particles incident in the angular region $30^\circ < \theta < 40^\circ$ with respect to the plane are selected.

low energy losses (cut on low energy window) in the first , second and third detectors respectively.

Figures 9.4 through 9.7 are for planar channeling while Figures 9.8 and 9.9 are for axial channeling. Figures 9.11 through 9.33 are for different incident angle cuts where the cuts are made in steps of critical angles at the given energy.

Table 9.3 shows the angular resolution of incident beam at different incident particle energies. This is due to two parts: (a) the drift chamber resolution, which is about $10 \mu r$ (obtained from reference[11]) and (b) the multiple scattering due to the material between the first drift chamber and the crystal which corresponds to a total fraction, 0.005 of a radiation length.

Table 9.3 Angular resolution of the incident beam due to drift chamber resolution and multiple scattering of material between the first drift chamber and the crystal.

Energy	Critical angle(μr)	Incident angular resolution(μr)
200 Gev/c	11.3	15.0
100 Gev/c	16.0	20.0
60 Gev/c	20.6	26.0
30 Gev/c	29.3	42.0

9.4.1 Dechanneling Lengths

The figures labeled (B), (C) and (F) show the strong dechanneling effects of pions and protons through the crystal. The random particles in these figures are the dechanneled particles. One could argue that

these are the random particles which were in the low energy loss window, but the increase of the number of random particles from (B) to (C) clearly shows the dechanneling effect.

A calculation of dechanneling lengths was performed using the data contained in Figures 9.4 through 9.9. No angular cut was considered in this calculation. The channeled fractions $d_{1,2}$, $d_{1,3}$ and $d_{2,3}$ between the three sets of detectors were calculated using the method described in section 9.3.2, and the average dechanneling length was calculated using Equation 9.2, the results of which with the statistical error bars are shown in Figure 9.34 for both planar and axial channeling.

9.4.2 Feeding-in Lengths

The figures (D), (G) and (H) show a strong feeding-in mechanism which is the important observation of this experiment. The decrease of the number of random particles from (G) to (H) shows the feeding-in effect clearly. This was first observed in CERN [17] at 12 GeV/c but no quantitative results were reported. This experiment has data for both planar and axial with energy dependence.

The angular dependence of the feeding-in length also has an interesting property in the determination of the process. This is because the fed-in particles are scattered into a known direction from an arbitrary direction. This section discusses the results of angular dependence of feeding-in lengths for different energies.

In order to calculate the feeding-in lengths one needs to determine the total number of channeled particles in each distribution using the method described in Section 9.3.1. Although not a very

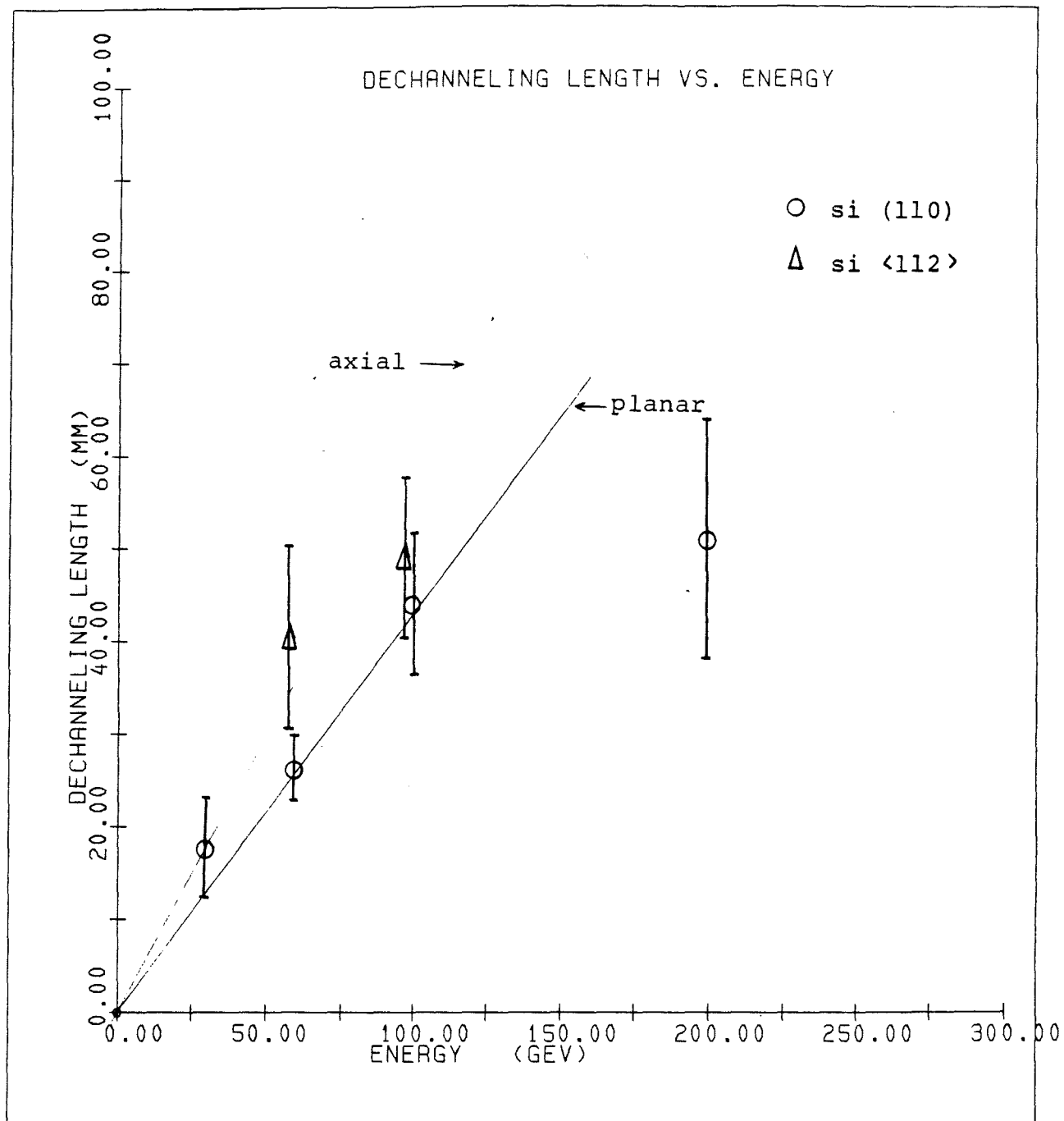


Figure 9.34 Planar and axial dechanneling lengths versus energy.

precise method, one can nevertheless identify the channeled particles with reasonable accuracy. The data in Figures 9.11 through 9.33 were used for the calculation as described in section 9.3.3. Figure 9.35 shows the results for different incident angular regions defined in steps of critical angles for planar channeling.

The low energy region of the energy loss distribution up to the peak of the channeled shoulder in all the spectra could be fit with the channeled distribution found in Figure 9.3 for planar channeling. This is not the case, however, for axial channeling, as one can see in Figures 9.8 through 9.9 and 9.26 through 9.33. The peak of the channeled distribution found in Figure 9.3 does not match with the channeled shoulder of all detectors (figures labeled (A), (E) and (I)) and, in fact, the channeled shoulders are much wider than the channeled distributions in Figure 9.3.

The calculated number of channeled particles gave a wide range of results for axial feeding-in lengths. For example, in some cases the total number of fed-in particles between the first set of detectors (namely the first and second) was a negative number while it was a large positive number between the next set of detectors (namely the second and third). Because of this uncertainty the calculation of feeding-in lengths for axial channeling was ignored. It is uncertain whether this effect is possibly due to experimental conditions such as the noise of the crystal detector.

The angular cut of the incident beam was performed only up to three critical angles away from the planar direction with good statistics, except at 30 GeV/c. This can be seen in Figures 9.14,

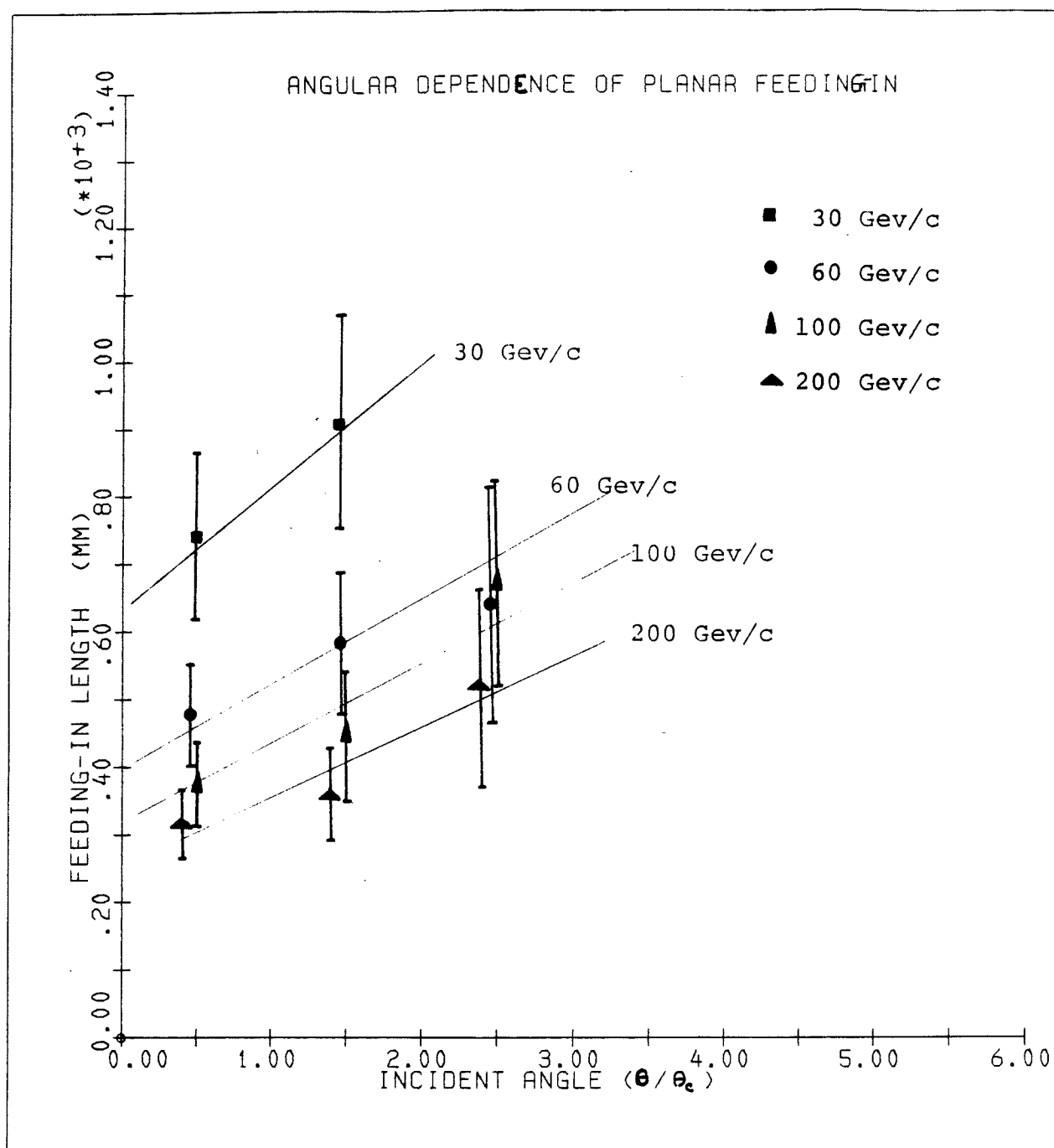


Figure 9.35 Planar feeding-in length versus incident angle (θ/θ_c) for silicon (110) at 200, 100, 60 and 30 GeV/c, where θ_c is the planar critical angle. The lines are drawn to guide the eye.

9.18, 9.22 and 9.25 and also the increasing of the statistical error bar in Figure 9.35. For 30 GeV/c because of the low statistics of the collected data (Table 9.1), it was not possible to make beyond two critical angles.

9.4.3 Channeled Fraction

The calculated channeled fractions at the detectors with the statistical error bars are plotted in Figure 9.36 for particles incident within the critical angle to the silicon (110) plane. The governing equation (Equation 8.15) can be written as

$$C(Z) = [C(0) - \lambda/\lambda_2]e^{-Z/\lambda} + \lambda/\lambda_2 \quad 9.5$$

where $C(0)$ is the initial channeled fraction and λ is given by $1/\lambda = 1/\lambda_1 + 1/\lambda_2$. Here λ_1 is the dechanneling length and λ_2 is the feeding-in length of particles incident within the critical angle to the plane.

The data contained in Figure 9.36 was used to calculate the initial channeled fraction $C(0)$. The least square fit of equation 9.5 was used and the results are shown in Table 9.4. The dechanneling lengths and feeding-in lengths for particles incident within the critical angle to the plane are also shown in Table 9.4. The steady state channeled fraction which was discussed in section 8.4 can be written as

$$C_{\infty} = \lambda/\lambda_2 \quad 9.6$$

The calculated values are given in Table 9.4.

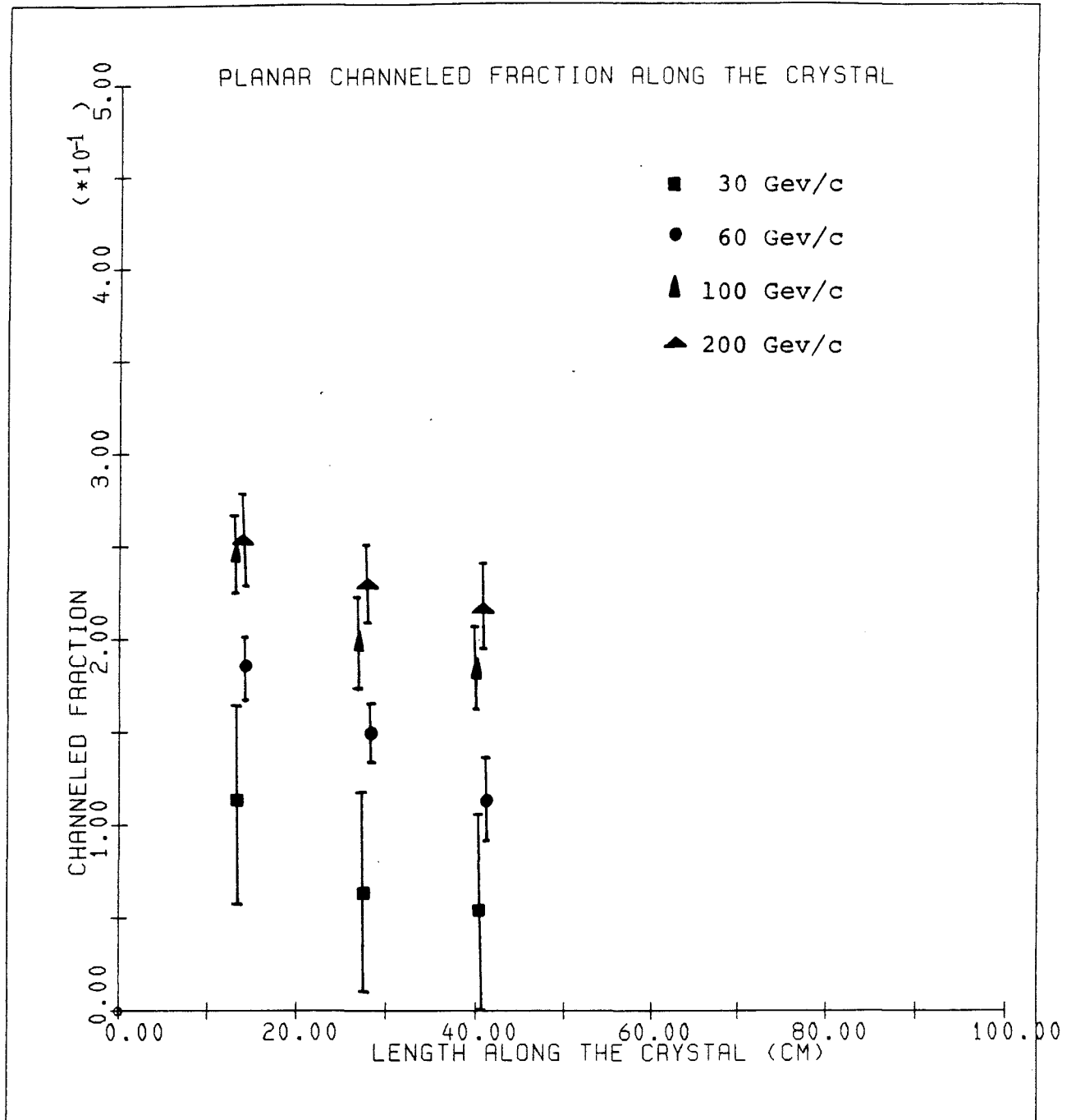


Figure 9.36 Measured channeled fraction versus the crystal length along silicon (110) planar direction for pions and protons incident within the critical angle at 200, 100, 60 and 30 GeV/c.

Table 9.4 Initial channeled fractions and the steady state channeled fractions for silicon (110) planar channeling. Average dechanneling lengths and feeding-in lengths for particles incident within critical angle are also given. The error is only due to the statistical fluctuations.

Energy	Initial Channeled fraction	Steady state Channeled fraction	Dechanneling length λ_1 (mm)	Feeding-in length λ_2 (mm) ($0 < \theta < \theta_c$)
200 GeV/c	$0.30 \pm .03$	$.14 \pm .03$	$50. \pm 12.$	$322. \pm 60.$
100 GeV/c	$0.28 \pm .03$	$.13 \pm .03$	$44. \pm 7.$	$383. \pm 70.$
60 GeV/c	$0.29 \pm .02$	$.06 \pm .02$	$26. \pm 3.$	$476. \pm 85.$
30 GeV/c	$0.24 \pm .08$	$.03 \pm$	$17. \pm 5.$	$745. \pm 130.$

The initial channeled fraction as discussed in section 8.7 is independent of the energy of the incident particles. The experimental values show the energy independence within the statistical uncertainty. The measured value of initial channeled fraction is about .30 which is a factor of two less than the theoretical prediction (section 8.7). This is due to the low resolution of incident angle compared to the width of the angular cut as shown in Table 9.3. Because of this, some of the particles actually going outside the region of the angular cut have been included in the analysis which causes the reduction of the fraction. This can be treated as follows.

Consider only those particles incident on the crystal with $\theta > \theta_c$ as shown in Figure 9.37a. A uniform angular distribution is assumed within a region of several critical angles around the planar direction. If one measured the above particles, then the observed distribution should look like Figure 9.37b with a Gaussian type of edge. The shaded

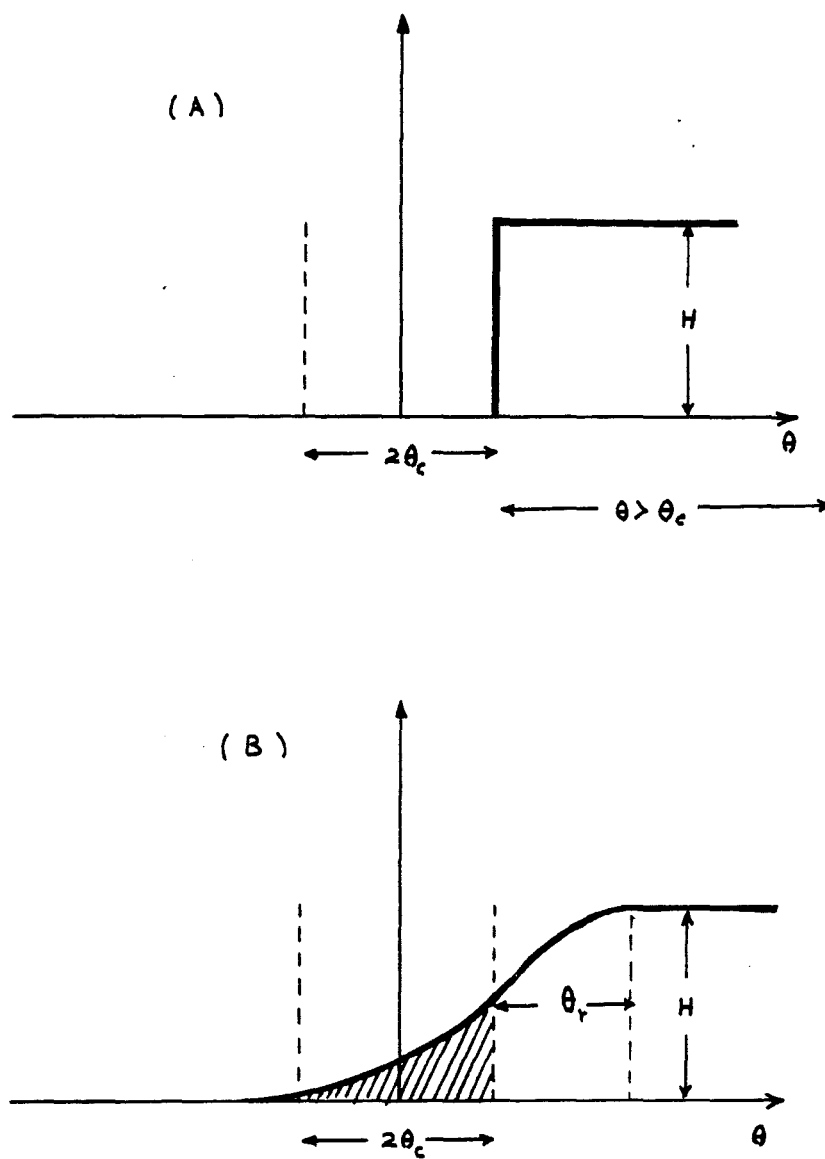


Figure 9.37 (A) The absolute distribution of particles incident on the crystal with $\theta > \theta_c$. (B) The same distribution measured in a typical experiment. The Gaussian type of edge is due to the angular resolution.

area in Figure 9.37b represents the particles distributed from outside into the region of angular cut. This number can be calculated by using the following integral.

$$N = \int_{\theta_r}^{\theta_r + 2\theta_c} H \exp(-\theta^2/2\theta_r^2) d\theta \quad 9.7$$

where H is the height of the incident angular distribution and θ_r is the angular resolution of the incident beam. The value of the integral is about $.32\theta_r H$ and the total from both side (namely $\theta \geq \theta_c$ and $\theta \leq -\theta_c$) becomes about $.64\theta_r H$. Since the total measured number of particles inside the region of the angular cut is $2\theta_c H$, one has to subtract a fraction of $.64\theta_r H/2\theta_c H (= .32 \theta_r/\theta_c)$ from the total incident particles. With this correction the obtained initial channeled fraction is about .55 which is in good agreement with the theoretical value of .64.

Table 9.5 Observed feeding-in and dechanneling probabilities for Si(110); between the first and the second detectors which are 14.mm apart. The feeding-in probability is given for different incident directions where θ_c is the planar critical angle.

Energy	Dechanneling probability	Feeding-in probability		
		$0 < \theta < \theta_c$	$\theta_c < \theta < 2\theta_c$	$2\theta_c < \theta < 3\theta_c$
200 Gev/c	0.24	.043	.038	.026
100 Gev/c	0.27	.036	.031	.022
60 Gev/c	0.42	.029	.024	.018
30 Gev/c	0.55	.018	.015	

9.5 Conclusion

The theoretical calculations using the diffusion model show a linear energy dependence of dechanneling lengths for both planar and axial channeling which agrees quite well with the results of this experiment with the exception of 200 GeV/c planar case. The extrapolated MeV Si(110) planar results are about a factor of three higher than the experimental results in reference [44,45]. The axial Si<112> dechanneling lengths are larger than the Si(110) planar by about 30%.

The observed feeding-in of pions and protons through a silicon crystal (which is the focusing effect of random particles along a major crystal direction) shows the following interesting properties in high energy planar channeling: The observed feeding-in probability (Table 9.5) increases as the energy increases and the incident angle to the plane decreases. The feeding-in probabilities are found to be smaller than the dechanneling probabilities in the energy range of this experiment. The observed feeding-in and dechanneling probabilities between the first and the second detector are shown in Table 9.5. The dechanneling probability decreases while feeding-in probability increases as the energy increases. In the nonrelativistic region (MeV) one could expect negligible feeding-in effects compared to the dechanneling. However in GeV channeling this effect is not quite negligible. The increase of the steady state channeled fraction (Table 9.4) with energy is due to the increase of feeding-in probability.